Wrocław University of Technology
Centre of Advanced Materials and Nanotechnology

Materials Science-Poland

Vol. 28 • No. 2 • 2010

Oficyna Wydawnicza Politechniki Wrocławskiej

Materials Science-Poland is an interdisciplinary journal devoted to experimental and theoretical research into the synthesis, structure, properties and applications of materials.

Among the materials of interest are:

- glasses and ceramics
- sol-gel materials
- photoactive materials (including materials for nonlinear optics)
- laser materials
- photonic crystals
- semiconductor micro- and nanostructures
- piezo-, pyro- and ferroelectric materials
- high-T_c superconductors
- magnetic materials
- molecular materials (including polymers) for use in electronics and photonics
- novel solid phases
- other novel and unconventional materials

The broad spectrum of the areas of interest reflects the interdisciplinary nature of materials research. Papers covering the modelling of materials, their synthesis and characterisation, physicochemical aspects of their fabrication, properties and applications are welcome. In addition to regular papers, the journal features issues containing conference papers, as well as special issues on key topics in materials science.

Materials Science-Poland is published under the auspices of the Centre of Advanced Materials and Nanotechnology of the Wrocław University of Technology, in collaboration with the Institute of Low Temperatures and Structural Research of the Polish Academy of Sciences and the Wrocław University of Economics.

All accepted manuscripts are placed on the Web page of the journal and are available at the address: http://MaterialsScience.pwr.wroc.pl

All published papers are placed on the Web page of the journal and are **freely accessible** at the address: http://MaterialsScience.pwr.wroc.pl

Materials Science-Poland is abstracted/indexed in: Chemical Abstracts, Materials Science Citation Index, Science Citation Index Expanded, Scopus.

The Journal is supported by the State Committee for Scientific Research

Editorial Office

Daniel Davies
Marek Łata

Printed in Poland

Drukarnia Oficyny Wydawniczej Politechniki Wrocławskiej
Zam. nr 276/2010.

Materials Science-Poland, *Vol. 28*, *No. 2*, *2010*

Synthesis of nano-SnO_2 and neural network simulation of its photocatalytic properties

A. E. KANDJANI, P. SALEHPOOR, M. F. TABRIZ*, N. A. AREFIAN, M. R. VAEZI

Materials and Energy Research Center (MERC), Karaj, Iran

Decolouration of Acid Red 27 (AR27) was investigated using UV irradiation in the presence of SnO_2 nanoparticles synthesized via the hydrothermal method. The average crystallite size of SnO_2 nanoparticles synthesized for 2 h was about 3.73 nm, according to X-ray analysis, and the specific surface area, which was estimated from the Halsey based *t* plot, was about 288 m^2/g. The effects of UV irradiation in the absence of a photocatalyst and in the presence of pure SnO_2 nanoparticles without any light source were negligible. An artificial neural network (ANN) was used to build an empirical model for the results. The results of neural network analysis are in good agreement with the experimental data which show that AR27 decolouration exhibits pseudo-first-order kinetic behaviour.

Keywords: *heterogeneous photocatalyst; advanced oxidation process; artificial neural network (ANN)*

1. Introduction

Dye wastewater has become one of the major by-products of several industries, especially the textile and paper industries. These hazardous materials introduce toxicity to their environments and water sources. Due to their simple dyeing procedure and good stability during washing processes, demands for the use of textile dyes are increasing drastically. Thus elaboration of procedures reducing harmful environmental effects of these dyes seems to be inevitable [1–3].

Many various methods of wastewater treatment have been applied, including: electroflotation, membrane filtration, electrocoagulation, ion exchange, irradiation, etc. [4]. Using solid catalysts, especially semiconductor photocatalysts, involves adsorption of pollutant molecules on a solid surface [5–7] and advanced oxidation processes (AOP). AOPs are the main processes involved in the photocatalytic decolouration of azo dyes. Oxide semiconductor photocatalysts are the most promising

*Corresponding author, email: Meisam.fa@gmail.com

semiconductors, which have been used successfully in the photocatalytic decolouration of azo dyes [8–12].

SnO_2 is a wide bandgap semiconductor, having the bandgap of about 3.65 eV at bulk state. SnO_2 has been reported as a suitable gas sensing oxide and recently its composites have been studied as promising semiconductors in the photocatalytic decolouration of wastewaters [13–17].

In the present paper, SnO_2 nanoparticles with small crystallite sizes and high specific surface area have been synthesised. Photocatalytic reactions involving these nanoparticles have been studied in detail, using Acid Red 27 as a pollutant. The results of experimental tests were analysed using artificial neural network (ANN) models. Also ANN has proved an important role for predicting a model based on the decolouration kinetics of AR27 by SnO_2 nanoparticles. To authors' best knowledge there are few papers which apply ANN in order to investigate decolouration kinetics in the presence of a heterogeneous photocatalysts [18–20].

2. Experimental

Materials. NaOH and $SnCl_4$ were purchased from Merck and were used without further purification. AR27 was purchased from Boyakh Saz Company (Iran). It is a commercial dye and was used without further purification. Its chemical structure and UV absorption spectra are shown in Fig. 1.

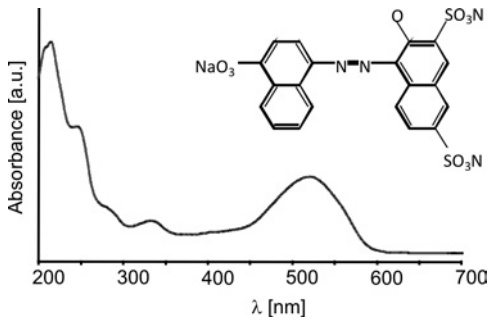

Fig. 1. The UV absorption spectrum and structure of AR27

Method of synthesis. The sample (SP-1) was prepared via the hydrothermal route. Firstly, 29.5 cm^3 of $SnCl_4$ was added dropwise to a 100 cm^3 of 1 M NaOH solution. The mixture was stirred continuously until a transparent solution formed. Then it was poured into a 35 cm^3 Teflon-lined autoclave and maintained at 170 °C for 2 h. After that, the autoclave was cooled to room temperature naturally and then the precipitates were filtered and washed several times with distilled water and ethanol. Finally, the obtained powder was dried at 50 °C for 24 h.

Photocatalytic decolouration procedure. All experiments were carried out in a 200 cm^3 batch photoreactor. The irradiation source was two mercury UV lamps

emitting light at 254 nm (15 W, UV-C, Philips, Holland) placed 15 cm above the bath photoreactor. In each experiment, 100 cm^3 of the dye solution with double the nominal concentration was prepared. Then, the photocatalyst powder was added to in 100 cm^3 of distilled water and sonicated for 30 min to achieve a homogeneous dispersion which was added to the dye solution to get the desired concentration. After very vigorous stirring, the mixture was left for 30 min to enable adsorption of AR27 on the surfaces of SnO2 powders in each reactor. The calculations of AR27 decolouration efficiency after the photochemical process were performed using the following formula:

$$X = \frac{C_0 - C}{C_0} \tag{1}$$

where C_0 and C are the concentrations of the dye before and after irradiation, respectively.

Analysis. Crystallographic structures of the materials was studied using a Siemens D-5000 X-ray diffractometer (XRD) with CuK_α radiation (λ = 0.154178 nm). Transmission electron microscope (Philips CM200) was used to study the morphologies of the prepared samples. The AR27 concentration was analyzed with a UV–Vis spectrophotometer (Aquarius-CECIL CE9500) at λ = 521nm. It was used to monitor the decolouration of the dye and also to calculate the bandgap of the prepared SnO_2. The specific surface area of the nano-SnO_2 particles were determined by the Brunauer –Emmett–Teller and Halsey method (BET-N_2 adsorption, Micromeritics Gemini 2375). Also, the *t*-plot method was used to estimate the median pore size of the obtained sample. The powder was degassed at 200 °C in vacuum for 1.5 h before adsorption.

Neural networks strategy. In this study, our main goal was to identify an optimal ANN architecture. Due to the nonlinear behaviour of the input data, the architecture which produced the most accurate results was found to be a three-layer, feed-forward network. The first layer represents the input data which is fed into the system in a vector form. The hidden layer receives the results from the first layer and after processing, they are sent to third layer to be the desirable output for the system modelled with ANN. Figure 2 shows the scheme of this architecture. The activation functions were considered to be linear for the first and third layers

$$U_i = \sum_{j=1}^{n} W_{ij} X_j \tag{2}$$

A linear activation function was not the best type to be used in the second layer, and after testing various activation functions, the logarithmic sigmoid was found to be the best type to deliver the desired results [21]

$$F\left(U_i = \frac{1}{1+e^{-U_i}}\right) \tag{3}$$

For the sake of simplicity, the training algorithm used for the ANN was a basic back propagation algorithm implemented in C++. This algorithm enabled one to achieve the best possible result, with the accuracy of about 10^{-4}. By using this algorithm, errors will decrease to reach a reasonable range by changing weights to reflect errors.

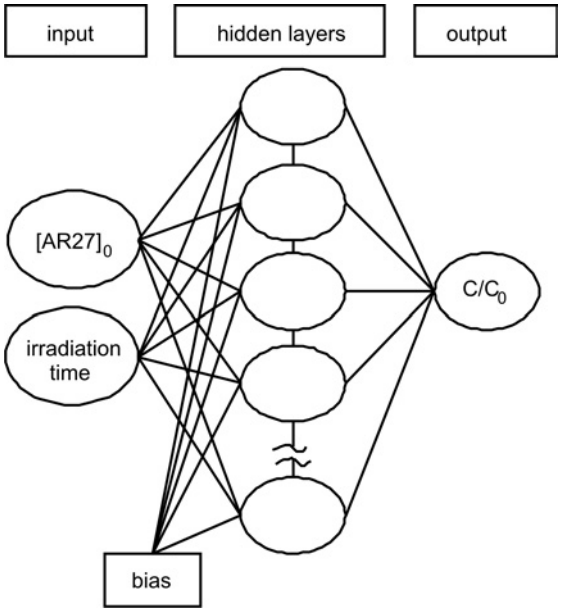

Fig. 2. Architecture of a feed-forward neural network with three layers and two inputs for decolouration analysis

Figure 3 shows the effect of number of neurons in the hidden layer on the overall performance of the neural network.

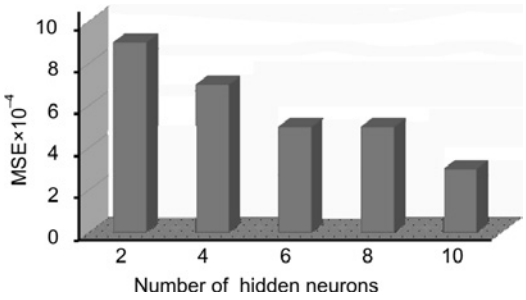

Fig. 3. Effect of number of neurons in the hidden layer on the overall performance of the neural network

3. Results and discussion

3.1. Synthesis

X-Ray diffraction patterns of samples are shown in Fig. 4. The Bragg peaks in all samples are in good agreement with those of cassiterite SnO_2 having a rutile structure (space group *p*42/*mnm*) with $a = 4.73727$ Å and $c = 3.186383$ Å.

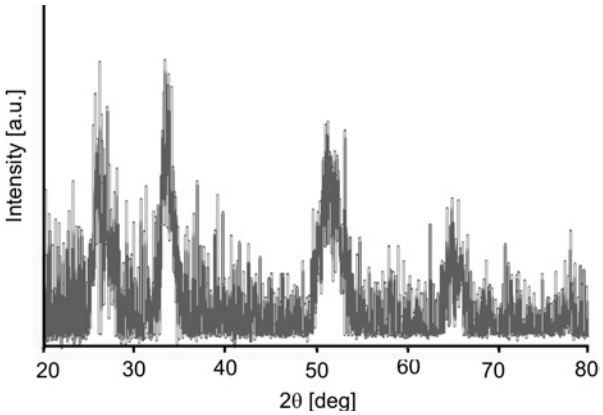

Fig. 4. XRD Pattern of SP-1

The average crystallite sizes were calculated from the full width at half maximum (FWHM) of the diffraction peaks of (101) planes using the Debbye–Scherrer formula:

$$D = \frac{k\lambda}{\beta \cos\theta} \tag{4}$$

where D is the mean crystallite size, k is a grain shape dependent constant (assumed to be 0.89), λ is the wavelength of the incident beam, θ is the Bragg reflection peak and β is the full width at half maximum [22]. The obtained results are listed in Table 1.

Table 1. The properties of SP-1 sample

Average crystallite-size [nm]	Specific surface area [m^2/g]	Initial absorbance of AR27 after 30min
3.73±0.05	188	0.071

In Figure 5, TEM images of SP-1 sample are shown. Under low magnification (Fig. 5a), it can be seen that the grid was covered by thin layers of SnO_2, also some agglomerates with median sizes of about 300 nm are visible. The selected area electron diffraction pattern (SAED) taken from these fine particles is shown in Fig. 5b.

The four indicated diffusion rings were identified as diffractions from the (211), (310), (312) and (411) planes of rutile type SnO_2. These types of diffused rings are attributed to extremely fine grain structures. A higher magnification image (Fig. 5b) shows that these layers and agglomerates are composed of fine spherical particles, typically having diameters smaller than 5 nm. Due to the extremely fine particles and strong agglomeration tendency in these samples, estimation of the true particle size distribution would involve high statistical errors. Therefore the median size of particles has not been indicated here.

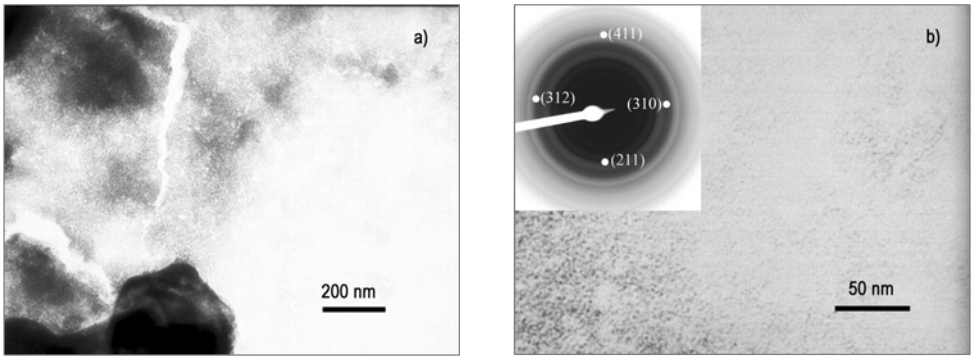

Fig. 5. TEM Images of SP-1

The direct bandgap values of the SnO_2 nanoparticles were estimated using UV absorption spectra. Figure 6 shows the UV-Vis absorption data. The sample shows a blue shift in comparison with its bulk state. Such a shift in the onset of absorption indicates a decreasing optical bandgap of the semiconductor, which is attributed to size quantization effects. The bandgap of the prepared sample was estimated to be ca. 4.15 eV.

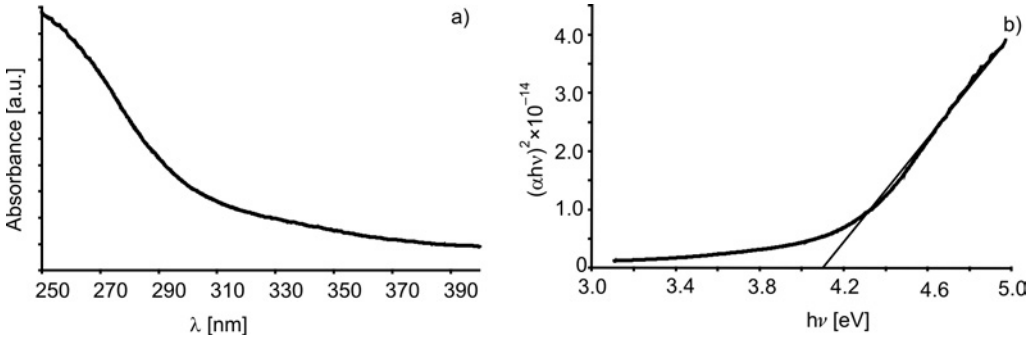

Fig. 6. UV absorption spectrum (a) and bandgap of the prepared SnO_2

The specific surface areas of the obtained samples were calculated from the Brunauer–Emmett–Teller (BET) equation. The obtained results are listed in Table 1. The high

surface area of these samples makes them good candidates as absorbents. Adsorption isotherms of the sample correlate strongly with a type I isotherm, as shown in Fig. 7a.

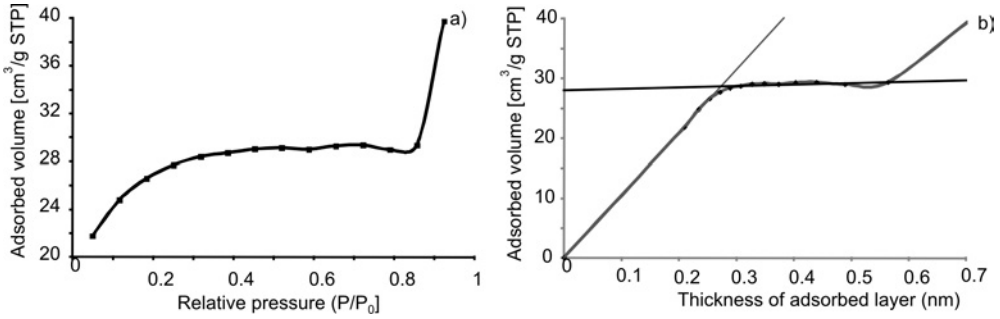

Fig. 7. BET adsorption isotherm (a) and t-plot of the sample (b)

It has been shown that if a solid contains micropores, its adsorption isotherm tends to resemble a type I isotherm. This phenomenon is attributable to overlapping of potential fields of neighbouring walls of porosities and corresponding by the increase in interaction energy of solid with gas molecules [23, 24].

The Halsey equation is generally used as estimation for the statistical thickness of adsorbed film as a function of nitrogen adsorption pressure at 77 K (the *t*-method) [25]

$$t = 0.354\left(\frac{5}{\ln\frac{P_0}{P}}\right)^{1/3} \quad [\text{nm}] \tag{5}$$

It can be used for calculating the monolayer surface area and the micropore volume size of the powders, as shown in Fig. 7b. The results are listed in Table 2.

Table 2. Results of the *t*-method for surface area and micropore volume of the SP-1 sample

Slope 1 [cm^3 STP/(g·nm)]	Slope 2 [cm^3 STP/(g·nm)]	Intercept [cm^3 STP/g]	Total area [m^2/g]	External area [m^2/g]	Micropore volume [cm^3/g]
187.4780	2.5968	47.0607	288.9462	4.0023	0.0729

This type of adsorption can be observed in many solids like xerogel of silica [26], titania [27] and zeolites [28]. Due to the fine particle sizes of these samples and their high agglomeration tendency, the resultant agglomerates act as microporous hosts.

During the hydrothermal process each mole of Sn^{4+} ions react with 4 moles of OH^- ions to form crystals [29]:

$$Sn^{4+} + 4OH^- \longrightarrow Sn(OH)_4 + 4H^+ \tag{6}$$

$$Sn(OH)_4 \longrightarrow SnO_2 + H_2O \tag{7}$$

Formation of crystalline SnO_2 during the hydrothermal process can be described using the growth unit model, first proposed by Zhong [30]. It is assumed in the model that during the crystallization process cations are in the form of complexes with OH^- ions as ligands. The growth units are complexes whose coordination numbers are the same as those of the crystal. It has been shown that during the hydrothermal formation of SnO_2, the growth units are complexes of $Sn(OH)_6^{2-}$ [31, 32].

3.2. Experimental data for decolouration of AR27

Figure 8 Shows the UV-Vis spectra of AR27 dissolved in water with SP-1 colloidal nanoparticles.

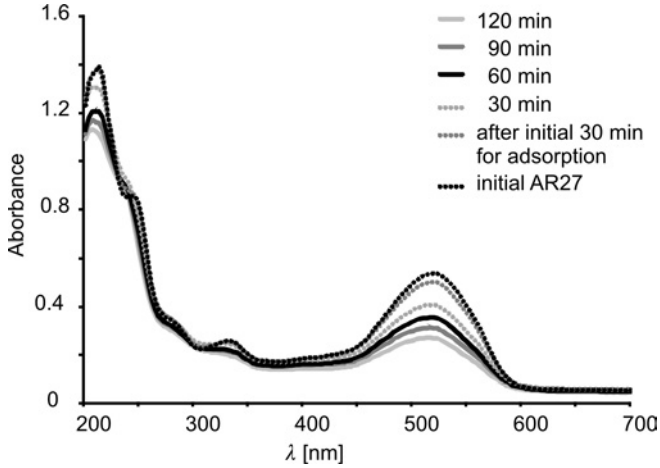

Fig. 8. UV-Vis spectra of $[AR27]_0$= 60 ppm in aqueous SnO_2 colloids $[SP-1]_{SnO2}$ = 20 ppm after various irradiation periods

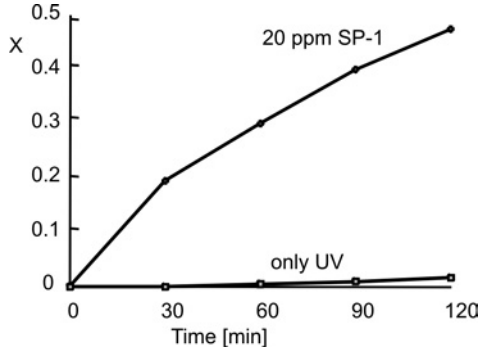

Fig. 9. Effect of irradiation with UV light and SnO_2 nanoparticles of $[SP-1]_{SnO_2}$ = 20 ppm on the photocatalytic decolouration of $[AR27]_0$= 60 ppm

The spectra indicate that the intensities of the spectral peaks depend on the irradiation time. The concentration of AR27 in the solution is lower if no irradiation is applied, even if an initial period of 30 min is given for absorbance of the azo dye layer

on the surface of the SnO_2 particles. If this step was omitted, the photocatalytic efficiency would be decreased due to insufficient interaction of the dye with the active sites on the surface of the nanoparticles. The change in the dye concentration versus time profile during the photocatalytic decolouration of AR27 with SP-1 nanoparticles is shown in Fig. 9.

The removal of AR27 under irradiation without using any photocatalysts was negligible. The procedure steps of decolouration are as follows [33–36]:

$$SnO_2 + h\nu \longrightarrow SnO_2 \text{ excited (pair electron–hole)} \quad (8)$$

$$h_{VB}^{+} + H_2O \longrightarrow H^{+} + OH^{\bullet} \quad (9)$$

$$h_{VB}^{+} + OH^{-} \longrightarrow OH^{\bullet} \quad (10)$$

$$e_{CB}^{-} + O_2 \longrightarrow O^{2-\bullet} \quad (11)$$

$$O^{2-\bullet} + \text{dye} \longrightarrow \text{dye–OO}^{\bullet} \quad (12)$$

$$O^{2-\bullet} + 2OH^{\bullet} + H^{+} \longrightarrow H_2O_2 + O_2 \quad (13)$$

$$H_2O_2 + h\nu \longrightarrow 2OH^{\bullet} \quad (14)$$

$$OH^{\bullet} + \text{dye} \longrightarrow \text{decolouration of the dye} \quad (15)$$

$$h_{VB}^{+} + \text{dye} \longrightarrow \text{oxidation of the dye} \quad (16)$$

3.3. Development of the neural network model

To obtain the optimal network, we tested 132 various neural network architectures with different activation functions and different number of neurons. The data was divided into regions; for each region, training input and test input were selected. This was done continuously, beginning with big regions and reaching smallest possible one. For testing accuracy, the obtained experimental data were plotted versus ANN data in Fig. 10.

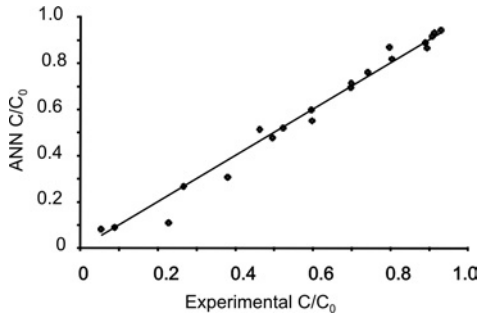

Fig. 10. Calculated and experimental values of the output

Experimental results are in good agreement with a root mean square errors (RMSE) of 0.04053. If the experimental and ANN data have the same values, the bi-

sector line which is shown in Fig. 10 will be carried out. These results confirm that the neural network model could accurately predict the results.

Table 3. Matrix of weights; W1: weights between input and hidden layers; W2: weights between hidden layers and output layers

W1				W2
Neuron	Variables		Bias	Weight
	Time	$[AR27]_0$		
1	–12.177	11.2939	15.2658	–0.62608
2	4.0292	–22.6975	–14.5133	–0.07613
3	6.6108	17.036	–13.1714	–0.77583
4	8.2375	–12.972	–12.1513	–0.03141
5	–28.0891	–6.5282	10.8794	–0.1265
6	15.4685	–1.9166	–10.2164	–0.55046
7	–3.3571	2.8618	–8.9042	1.1693
8	2.5164	1.9812	7.9623	–0.02208
9	11.3862	–14.7485	–7.0389	0.60311
10	–16.8626	–0.61672	5.7468	0.12029
11	–13.3589	–8.4081	4.7322	–1.0515
12	16.5848	9.1167	–3.7837	–0.12174
13	10.8791	8.8175	–2.5057	–0.35808
14	12.7837	8.2848	–1.5429	0.77107
15	9.054	–9.1145	–0.40496	0.022744
16	–17.1134	5.5002	–0.55457	0.522
17	15.6028	2.4898	1.3464	0.83982
18	11.455	–13.1046	2.5528	–0.06878
19	2.7418	–11.1861	3.6116	–0.22561
20	19.567	2.5307	4.5889	–0.15973
21	7.7435	10.0099	5.0492	–0.28686
22	–7.6892	–13.1195	–7.2321	1.5975
23	11.4763	10.1527	8.0373	–0.2725
24	–13.0984	–9.4735	–8.9793	–0.12483
25	10.7286	14.0612	9.9007	–0.97063
26	–11.6994	–8.8096	–11.298	–0.36194
27	–15.5001	2.3851	–12.3374	–0.10918
28	–12.3388	7.7683	–13.2593	–0.02288
29	–11.1478	10.7477	–14.3433	0.77464
30	7.5182	12.9188	15.2121	–0.07348

A neural network with thirty neurons in the hidden layer was used with 800 iterations, providing the weights listed in Table 3. The weights are the coefficients between artificial neurons being analogous to synapse strengths between the axons and dendrites in real biological neurons. Therefore, each weight decides what proportion of the incoming signal will be transmitted into the neuron body. In the neural network, the connection weights between neurons are the links between the inputs and the out-

puts, and therefore are the links between the problem and the solution. The relative contributions of the independent variables to the predictive output of the neural network depend primarily on the magnitude and direction of the connection weights. Input variables with larger connection weights represent greater intensities of signal transfer, and therefore are more important in the prediction process compared to variables with smaller weights. Negative connection weights represent inhibitory effects on neurons (reducing the intensity of the incoming signal) and decrease the value of the predicted response, whereas positive connection weights represent excitatory effects on neurons (increasing the intensity of the incoming signal) and increase the value of the predicted response [37].

Garson [38] proposed a method for partitioning the neural network connection weights in order to determine the relative importance of each input variable in the network. It is important to note that his algorithm uses the absolute values of the connection weights when calculating variable contributions, and therefore is insensitive to the direction of changes between the input and output variables. The Garson equation is based on partitioning the weights

$$I_j = \frac{\sum_{m=1}^{m=N_h}\left(\frac{\left|W_{jm}^{ih}\right|}{\sum_{k=1}^{N_i}\left|W_{km}^{ih}\right|}\left|W_{mn}^{ho}\right|\right)}{\sum_{k=1}^{k=N_i}\left(\sum_{m=1}^{m=N_h}\left(\frac{\left|W_{km}^{ih}\right|}{\sum_{k=1}^{N_i}\left|W_{km}^{ih}\right|}\left|W_{mn}^{ho}\right|\right)\right)} \tag{17}$$

where I_j is the relative importance of the jth input variable on the output variable, N_i and N_h are the numbers of input and hidden neurons, respectively, the (W)s are the connection weights, the subscripts i, h and o refer to input, hidden and output layers, respectively, and subscripts k, m and n refer to input, hidden and output neurons, respectively, and in this particular case $n = 1$, because there is only one output neuron in the neural network used here.

Table 4. Relative importance of input variables

Input variables	Importance [%]
Initial AR27 concentration	43.8
Irradiation time	56.2
Total	100

The relative importance of the variables based on this equation is listed in Table 4. The obtained data using normal inputs between 0 and 1 for training ANN show the

influence of the variables on the decolouration process in which the radiation time is the most influential parameter.

3.4. Kinetics of AR27 photocatalytic decolouration

Once the performance of the network was tested, a set of ANN results were obtained from the corresponding variables of AR27 initial concentration and time. Figure 11 shows the output of the ANN as a surface, which enables understanding of the kinetic behaviour of the system.

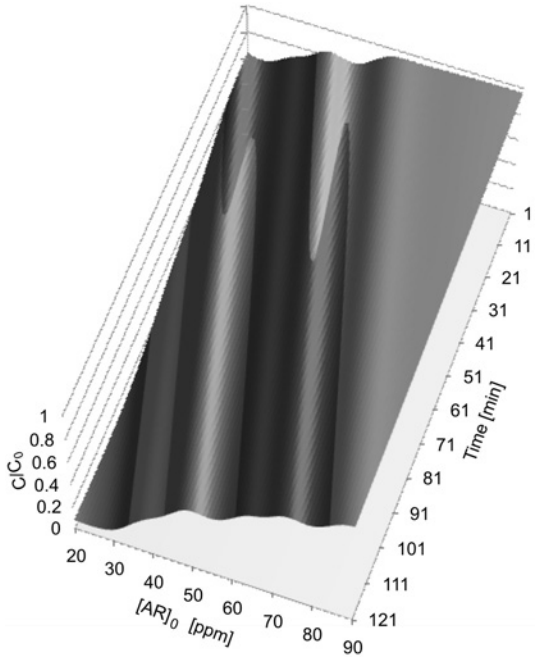

Fig. 11. ANN simulation: effects of the initial pollutant concentration and irradiation time on the decolouration of AR27

It can be easily seen that as has been reported, this pollutant has pseudo-first-order kinetics with respect to the azo dye concentration. Its kinetic profile can be described by:

$$-\ln\frac{[\mathrm{AR27}]}{[\mathrm{AR27}]_0} = k_{\mathrm{obs}}t \tag{18}$$

where k_{obs} is the pseudo-first-order constant. By applying the least square regression analysis, the values of k_{obs} were obtained.

From Figure 12, which is same as Fig. 11 but from other point of view, it is evident that at various initial concentrations of AR27, due to changing the concentration of active organic azo dyes in the vicinity of the photocatalysts and at constant rate of

electron-hole creation on its surface, it is possible to change k_{obs} [39]. By increasing the AR27 concentration k_{obs} decreases.

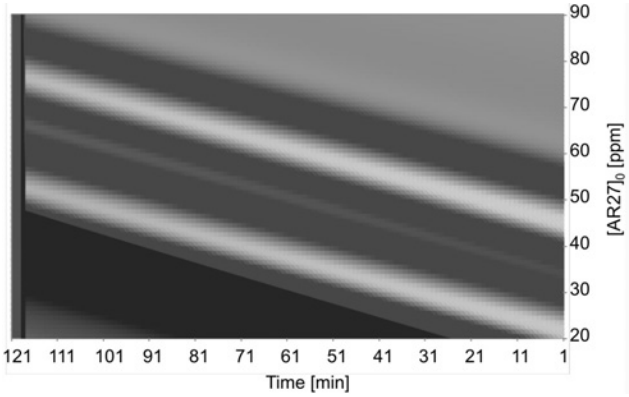

Fig. 12. Irradiation time versus AR27 initial concentration with contour plot of C/C_0

The pseudo-first-order kinetics of the decolouration process of azo dye under UV irradiation in the presence of a photocatalyst can be related to the surface adsorption without saturation of active sites. By assuming the Langmuir–Hinshelwood kinetic model, the decolouration reaction rate of AR27 should be proportional to the surface coverage of photocatalytic particles by an organic substance

$$k_c \frac{K_{\mathrm{AR27}}}{1+K_{\mathrm{AR27}}[\mathrm{AR27}]_0} = k_{\mathrm{obs}} \tag{19}$$

$$\frac{1}{k_{\mathrm{obs}}} = \frac{1}{k_c K_{\mathrm{AR27}}} + \frac{[\mathrm{AR27}]_0}{k_c} \tag{20}$$

where K_{AR27} is the adsorption equilibrium constant, k_c is the kinetic rate constant of surface reaction and $[\mathrm{AR27}]_0$ is the initial concentration of AR27 [40].

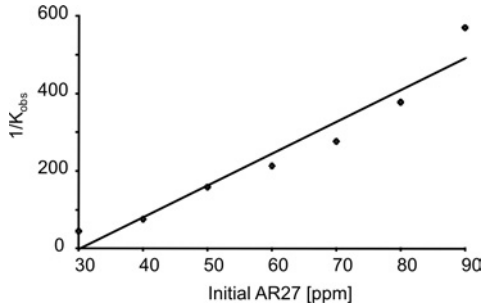

Fig. 13. Dependence of K_{obs} (1/min) calculated from ANN on the initial concentration of AR27

Figure 13 shows the dependence of $1/k_{obs}$ on initial concentration of AR27, from the ANN data. In the Langmuir–Hinshelwood equation, k_c is related to the limiting

rate of the reaction at the maximum coverage under the experimental conditions and K_{AR27} represents the equilibrium constant for adsorption of AR27 on the surface of an active photocatalysts [40]. By means of a least square best fitting procedure, the values of the adsorption equilibrium constant K_{AR27} and the kinetic rate constant of surface reaction k_c were calculated to be 0.0331 dm^3/mg and 0.1218 mg/(min·dm^3), respectively.

4. Conclusions

The synthesis of SnO_2 nanoparticles with relatively high specific surface area and small crystallite sizes has been reported. The synthesized nano-SnO_2 exhibited mesoporous-like behaviour. The statistical film thicknesses of materials adsorbed were used for estimating pore sizes which showed a decrease with increase in hydrothermal period. In addition, the photocatalytic decolouration efficiency of these particles for decolouration of AR27 has been investigated. Results indicated that the decolouration rate and efficiency were highly affected by the initial AR27 concentration and the specific surface area of the photocatalyst. The photocatalytic decolouration of AR27 can be explained in terms of the Langmuir–Hinshelwood kinetic model. The results obtained from this model are in good agreement with the experimental data. The mechanism of the photochemical decolouration of Acid Red 27 solution by using SnO_2 nanopowders was successfully predicted by applying a three-layered neural network with thirty neurons in the hidden layer, and using a back-propagation algorithm. Simulations based on the ANN model were performed in order to estimate the behaviour of the system under various conditions. The parameters investigated in this work (i.e., initial concentration of the dye and reaction time) have considerable influence on the decolouration efficiency and, as expected, the irradiation time with a relative importance of 56.2%, appeared to be the more influential factor. The results of data modelling confirmed that neural network modelling could effectively predict the behaviour of the system.

References

[1] KONSTANTINOU I.K., ALBANIS T.A., Appl. Catal. B. Environ., 49 (2004), 1.
[2] STOLZ A., Appl. Microbiol. Biotechnol., 56 (2001), 69.
[3] O'NEILL C., HAWKES F.R., HAWKES D.L., LOURENCO N.D., PINHEIRO H.M., DELÉE W., J. Chem. Tech. Biotechnol., 74 (1999), 1009.
[4] ROBINSON T., MCMULLAN G., MARCHANT R., NIGAM P., Bioresource Technol., 77 (2001), 247.
[5] BAHNEMANN D., CUNNINGHAM J., FOX M.A., PELIZZETTI E., PICHAT P., SERPONE N., *Photocatalytic Treatment of Waters in Aquatic and Surface Photochemistry*, Lewis Publishers, Boca Raton, 1994.
[6] VALSARAJ K.T., RAVIKRISHNA R., LIN H., YUAN Q., Proc. Symp. ICMAT 2001: *Advances in Environmental Materials, Vol. I. Pollution Control Measures*, Materials Research Society (Singapore), Singapore, 2001.
[7] SAFARIK I., NYMBURSKA K., SAFAIKOVA M., J. Chem. Tech. Biotechnol., 69 (1997), 1.

[8] KUO W.G., Wat. Res., 26 (1992), 881.
[9] MORISSON C., BANDARA J., KIWI J., LOPEZ A., J. Adv. Oxid. Technol., 1 (1996), 160.
[10] SILVA C.G., WANG W., FARIA J.L., J. Photochem. Photobiol. A: Chem., 181 (2006), 314.
[11] STYLIDI M., KONDARIDES D.I., VERYKIOS X.E., Appl. Catal. B: Environ., 47 (2004), 189.
[12] HERRMANN J.M., Catal. Today, 53 (1999), 115.
[13] XI L., QIAN D., TANG X., CHEN C., Mater. Chem. Phys., 108 (2008), 232.
[14] WANG H.C., LI Y., YANG M.J., Sensor. Actuat. B: Chem., 119 (2006), 380.
[15] NAYRAL C., VIALA E., COLLIÈRE V., FAU P., SENOCQ F., MAISONNAT A., CHAUDRET B., Appl. Surf. Sci., 164 (2000), 219.
[16] MUKHOPADHYAY A.K., MITRA P., CHATTERJEE A.P., MAITI H.S., Ceram. Int., 26 (2000), 123.
[17] TEERAMONGKONRASMEE A., SRIYUDTHSAK M., Sens. Actuators, B, Chem., 66 (2000), 256.
[18] EMILIO C.A., MAGALLANES J.F., LITTER M.I., Anal. Chim. Acta, 595 (2007), 89.
[19] DURAN A., MONTEAGUDO J.M., Water Res., 41 (2007), 690.
[20] TOMA F.L., GUESSASMA S., KLEIN D., MONTAVON G., BERTRAND G., CODDET C., J. Photochem. Photobiol. A: Chem., 165 (2004), 91.
[21] MORGAN D.P., SCOFIELD C.L., *Neural Networks and Speech Processing*, Kluwer, London, 1991.
[22] CULITY B.D., Elements of X-ray diffraction, 2nd Edition, Addison-Wesley Company, USA, 1978.
[23] DUONG D.D., *Adsorption Analysis: Equilibria and Kinetic*s, Imperial College Press, Australia, 1998.
[24] GREGG S.J., SING K.S.W., *Adsorption, Surface Area and Porosity*, 2nd Ed., Academic pRess, London, 1982.
[25] HALSEY J., J. Chem. Phys., 16 (1948), 931.
[26] YANG M., WANG G., YANG Z., Mater. Chem. Phys., 111 (2008), 5.
[27] MOHAMMADI M.R., FRAY D.J., MOHAMMADI A., Micropor. Mesopor. Mater., 112 (2008), 392.
[28] CHUNG K.H., CHANG D.R., PARK B.G., Bioresource Tech., 99 (2008), 7438.
[29] WEN Z., WANG Q., ZHANG Q., LI J., Adv. Funct. Mater., 17 (2007), 2772.
[30] ZHONG W.Z., LIU G.Z., Sci. China (B), 24 (1994), 394.
[31] LI W.J., SHI E.W., ZHONG W.Z., YIN Z.W., J. Cryst. Growth, 203 (1999), 186.
[32] WANG W.W., Mater. Res. Bull., 43 (2008), 2055.
[33] BEHNAJADY M.A., MODIRSHAHLA N., HAMZAVI R., J. Hazard. Mater. B, 133 (2006), 226.
[34] KHODJA A.A., SEHILI T., PILICHOWSKI J., BOULE P., J. Photochem. Photobiol. A: Chem., 141 (2001), 231.
[35] DANESHVAR N., SALARI D., KHATAEE A.R., J. Photochem. Photobiol. A: Chem., 162 (2004), 317.
[36] HOFFMANN M.R., MARTIN S.T., CHOI W., BAHNEMANN D., Chem. Rev., 95 (1995), 69.
[37] SLOKAR Y.M., ZUPAN J., MARECHAL A.M.L., Dyes Pigments, 42 (1999), 123.
[38] GARSON G.D., AI Expert, 6 (1991), 47.
[39] MILLS A., DAVIS R.H., WORSELY D., Chem. Soc. Rev., 22 (1993), 417.
[40] OLLIS D.F., Top. Catal., 35 (2005), 217.

Received 29 July 2008
Revised 17 June 2009

Materials Science-Poland, *Vol. 28*, *No. 1*, *2010*

A combined numerical-experimental method for determining the spatial distribution of a residual stress in a notch

E. RUSIŃSKI, P. MOCZKO*

Wroclaw University of Technology, Faculty of Mechanical Engineering, Institute of Machine Design and Operation, Wrocław University of Technology, Wybrzeże Wyspiańskiego 27, Wrocław, Poland

A combined numerical-experimental method for determining the spatial distribution of residual stress has been presented, which allows defining of the state and gradient of stress. The method is based on test measurements and numerical simulations by the finite elements method.

Keywords: *residual stress, finite elements method, deformation measurements*

1. Introduction

A review of dimensioning standards appertaining to immediate strength and durability shows that it is common practice to ignore residual stresses. Such stresses can occur as ta result of machining, forming moulding, welding, heat treatment, casting or phase changes of a given material [1–4]. The practice of ignoring residual stresses might be attributed to a lack of methods for determining its spatial distribution, especially in areas of maximum strain such as notches. It is even suggested [5] that the influence of residual stress should be ignored when dimensioning complicated welded objects, because of the lack of satisfactory methods for determining the condition of such objects after being subjected to such stress processes.

The influence of the manufacturing processes on the initial distribution of stresses within load bearing elements of machine components (i.e. as distinct from strain occurring later, during exploitation) is vital in view of the immediate strength as well as the ultimate durability of these elements. When these strain forces are later superimposed by strain forces occurring during exploitation, this often leads to premature failures or lower durability. Of course, in certain cases residual stress can also have

*Corresponding author, e-mail: przemyslaw.moczko@pwr.wroc.pl

a beneficial effect on durability – for example, shot peening or rolling can improve surface durability and surface resistance to fatigue stress.

Considering the above, the methods have been presented for determining the spatial distribution of a residual stress and for applying them in the design and dimensioning of machine components and load bearing elements. The method for determining the residual stress distribution in the notch areas of a cam shaft has also been presented.

2. Methods of measurement of residual stress

The methods of measurement of residual stresses can be divided into destructive and non-destructive ones. The non-destructive methods are following:

Acoustic methods relying on measurement of sound wave propagation through a material. These methods are generally used only for single axis loads and homogenous materials having a uniform structure.

Methods based on the Barkhausen effect. In magnetic materials, the Barkhausen noise is generated by movement of ferromagnetic domains. A change in this noise is a result of a mechanical stress. In practice, the method is useful for determining the strain direction (at lower stress levels).

Light diffraction methods. There are a variety of various methods based on light diffraction/interference. The application principles are the same as for the Newton ring apparatus. The method can be used for estimating the speed of crack propagation.

Moiré pattern method. A photographic method, where a pattern of parallel lines is printed onto a tested material. The method is difficult in use.

Elastooptic methods. The methods are based on the interference of electromagnetic waves (polarized light) after passing through a deformed, optically active transparent plastic material. In general, the method is only used for modeling, and has rather limited application.

X-ray and neutron diffraction based methods. The only methods providing the most accurate stress distribution measurements, having practically unlimited applications.

The most often used destructive methods of measurement of residual stresses are:

Methods based on exploiting a change in the shape of the material, after removing the deflection. This is a popular method for assessing residual stress in surface layers. When the upper material layer with residual stress is removed, this leads to a geometrical change in the object, and based on these changes it is possible to determine the distribution pattern of the earlier residual stress.

The hole-drilling method [6]. In this method, surface stress around a hole drilled in the material is relaxed. By measuring the stress relaxation (material extension) at appropriate spots distributed around a drilled hole (electric resistance strip strain gauges) it is also possible to determine the distribution pattern of the earlier residual stress. This is a destructive method (creating discontinuities in the material), used for material surface layers. The method consists of measurements of material extension around a small hole (ca. 2 mm in diameter) drilled in the tested element.

All of the discussed methods of measurement of residual stresses [6] have limited application, as they generally require flat or slightly curved, easily accessible surfaces. This basically disqualifies them for notch areas, as in our case, of a cam shaft and the transition areas between different shaft diameters. Nevertheless, these methods can be used to determine residual stress in the areas adjoining the notch, which was applied in the present work.

3. Method for determining residual stress in the notch shape area

The method is based on the assumption that in order to define residual stress in the notch area, it is sufficient to know its state and the gradient of the residual stress around this area. A two stage approach is used. First, experimental measurements on the test object are performed. The measurements of the residual stress may be based on any of the earlier mentioned destructive or nondestructive methods. The obtained results are then used as the input data for a numerical model of the object, where the finite elements method (FEM) is used [7–9] to define the residual stress in the notch shape area. A general diagram of this method is presented in Fig. 1.

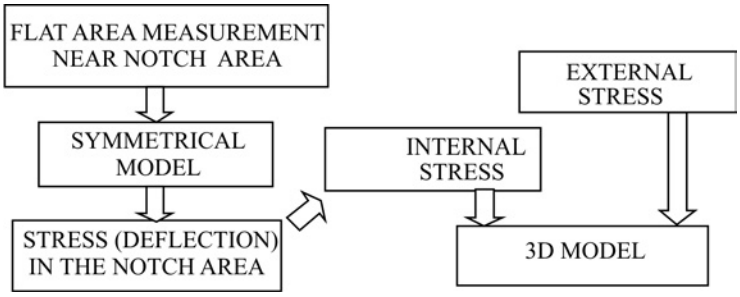

Fig. 1. Diagram presenting the method for creating a 3D model of a residual stress in the notch area

4. Application of the method

Forged elements with varying cross-sections often have significant residual stresses resulting from the technology of their manufacture. Considering this fact, we

have chosen a cam shaft as a prime example, for describing the spatial distribution of residual stress in the notch area – the transition of the cylindrical shaft into the cam shape.

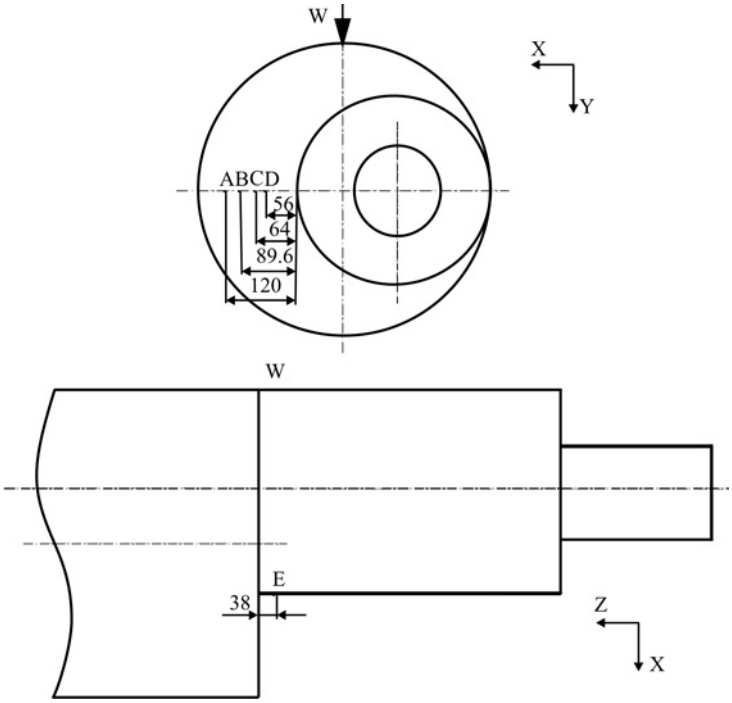

Fig. 2. Distribution of the measurement points

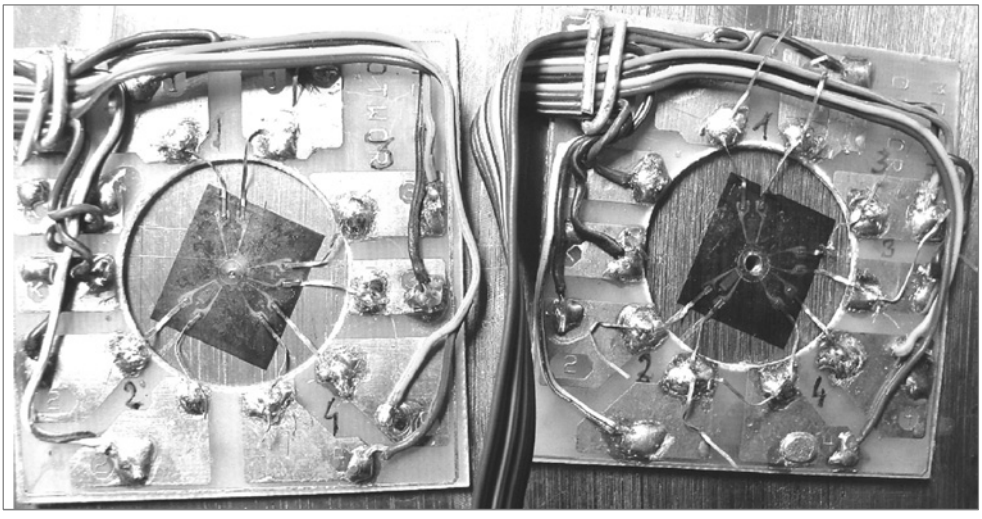

Fig. 3. Exemplary measurements points (A and B, cf. Fig. 2)
before (left) and after (tight) drilling of the relaxing hole

The first step requires measurement of residual stress near the notch. In our case, the hole-drilling stress relaxation method has been applied. Measurements were taken at points specified in Fig. 2, whilst Fig. 3 presents a picture of points A and B with strain gauges installed in a star arrangement, before and after drilling the hole in the shaft. Measurement data showed the presence of high compressive forces, with the gradient oriented towards the notch area. The maximum σ_{min} value was –146 MPa. The measured principal stress levels (σ_{max}, σ_{min}) as well as the stress direction α related to axis x_1 (see Fig. 3) for the individual points shown in Fig. 2 are given in Table 1.

Table 1. Measured residual stress levels for points shown in Fig. 2

Measurement point	σ_{max} [MPa]	σ_{min} [MPa]	α [deg]
D	–126	–146	–10
C	–79	–129	–9
B	44	2	–2
A	24	–4	3
E	–24	–53	–2

We then built a numerical model of the shaft. It was symmetric with respect to the axis. The loads of compressive forces at the cross sections were representative of data obtained from experimental measurements. The dimensions of the shaft model as well as the dimensions of the notch areas under investigation are exactly the same as in the investigated object. The loaded and restrained fragment of the model, as shown in Fig. 4, was then analysed numerically to ascertain the spatial distribution of residual stress in the notch area.

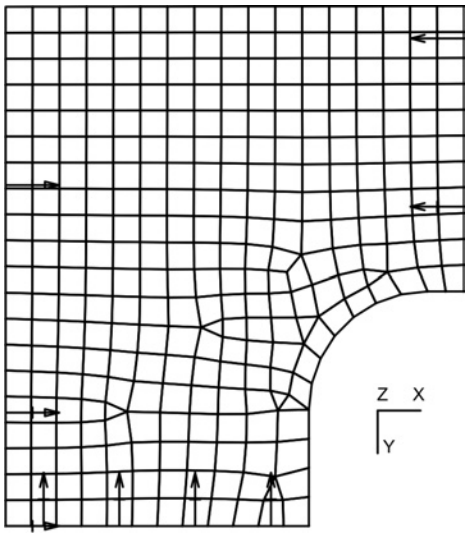

Fig. 4. Axis-symmetrical model of the shaft, showing the view of the notch area, along with the input forces

In Figures 5 and 6, prsent the main stress distribution patterns σ_{max} and σ_{min} are shown on an axis-symmetrical model of the analyzed cam shaft notch area.

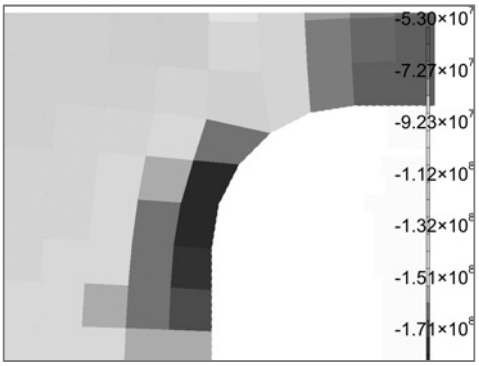

Fig. 5. Stress σ_{min} in the notch area

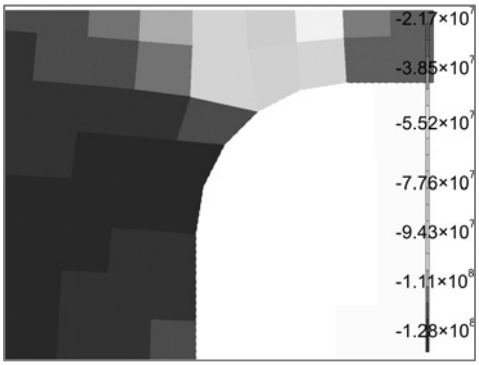

Fig. 6. Stress σ_{max} at the notch area

Figures 7 and 8 present plots of σ_{min} and σ_{max} stresses in function of the distance from the notch area, as determined from the numerical model, with superimposed strain gauge measurement values. Point 'zero' on the plot represents the geometrical centre of the notch curve (the bottom of the notch). The stress measurements and the stresses predicted by the numerical model are clearly marked by arrows and a short textual description. As one can see, the plot based on physical measurements (strain gauge) matches the predictions of the numerical model. The maximum stress level noted in the notch area is $\sigma_{min} = -184$ MPa.

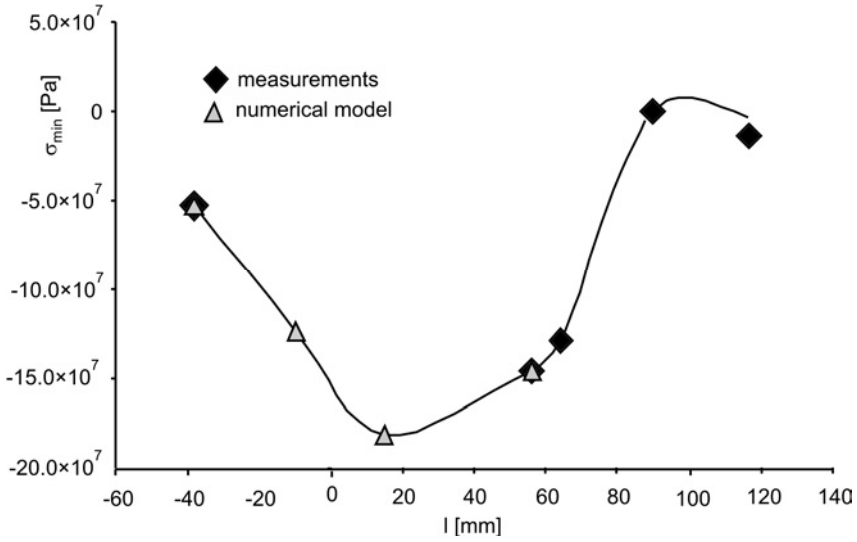

Fig. 7. Stress plot σ_{min} for the notch area [Pa]

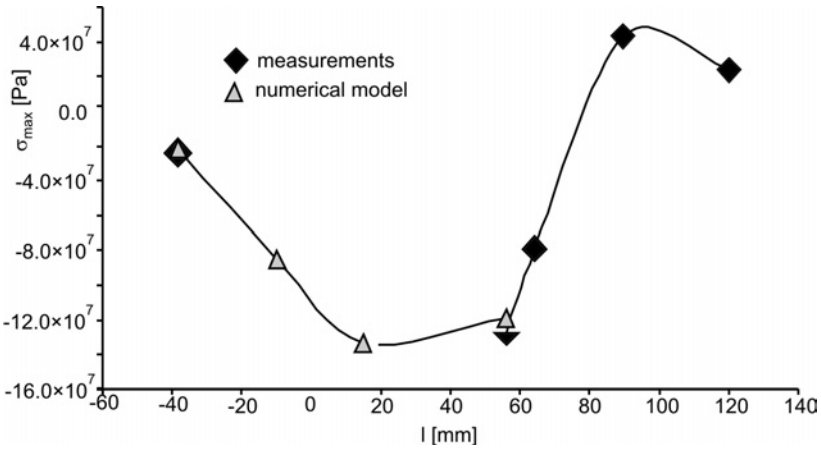

Fig. 8. Stress plot σ_{max} for the notch area [Pa]

5. Summary

The numerical–experimental method presented in the paper makes it possible to determine the spatial distribution of a residual stress in cam shaft notch areas. The method may also be generalized to include other objects. The method requires verification by using destructive testing. It can be applied to assess the strength and durability of load bearing elements, as well as for dimensioning purposes. An advantage of the method is, that knowing the residual stress in the notch area, it is possible to take it into account when assessing fatigue stress exploitation durability, for the notch area where failure is most likely to occur. An example of such analysis is given in [10].

References

[1] PN -87/M-06515, *Cranes. Main rules of load carrying structures design* (1987).
[2] DIN 22261-2, *Excavators, spreaders and auxiliary equipment in opencast lignite mines* (1997).
[3] SOBCZYKIEWICZ W., Przegl. Mech., 18 (1987), 61.
[4] TASAK E., *Welding Metallurgy*, JAK Andrzej Chorzewski, Cracow, 2008.
[5] HOBBACHER A., *Recommendations for fatigue design of welded joints and components*, Int. Inst. Welding, Paris, 2003.
[6] *Standard test method for determining residual stresses by the hole-drilling strain gauge method.*, ASTM Designation E 837-94.
[7] RUSIŃSKI E., CZMOCHOWSKI J., SMOLNICKI T., *Advanced Finite Element Method*, Publ. Wrocław University of Technology, Wrocław 2000.
[8] RUSIŃSKI E., *Finite Element Method System*, COSMOS/M, WKŁ, Warsaw, 1994.
[9] ZIENKIEWICZ O.C., TAYLOR R.L., *The Finite Element Method*, McGraw-Hill, London, 1991.
[10] MOCZKO P., *Numerical/experimental method for determining spatial distribution of residual stress in a notch*, PREPR. No. 009/03, Wroclaw, 2003.

Received 11 August 2008
Revised 2 October 2009

Materials Science-Poland, *Vol. 28*, *No. 2*, *2010*

Effect of long duration intercritical heat treatment on the mechanical properties of AISI 4340 steel

M. R. AKBARPOUR*, F. NEMATZADEH, S. E. HASEMI AMIRI, H. REZAII

Materials and Energy Research Center, P.O. Box, 14155-4777 Tehran, Iran

Ferrite-bainite dual phase (FBDP) steels are a class of steels characterized by a microstructure consisting of a soft ferrite matrix with hard bainite islands. The holding time in the dual phase ($\alpha + \gamma$) region is an important parameter in the intercritical annealing at constant temperature and influencing mechanical properties of this steel. Dual phases with various ferrite volume fractions (45–65 vol. %) were fabricated by changing the holding time. Samples of these steels with ferrite-bainite structure were tensile tested at room temperature. Results showed that as the ferrite volume fraction increased, the yield strength decreased but a different type of behaviour was observed for ultimate tensile strength (UTS) tests. UTS increased when the ferrite volume fraction (V_f) increased above ca. 55%. The tensile flow stress data for this steel, obtained from samples with various ferrite volume fractions, were analyzed in terms of the Hollomon equation. Two or three Hollomon equations can describe the flow behaviour adequately, and it was found that with increasing V_f the work hardening occurs in three stages, each equation belonging to one of these stages. Finally, variations of Hollomon equation parameters were used to explain the deformation mechanisms activated at various stages.

Keywords: *dual phase steels; ferrite; bainite; mechanical properties; work hardening*

1. Introduction

Dual phase steel is currently a material of commercial interest for certain automotive applications. The interest originates from the demand for lighter, more fuel efficient vehicles and the fact that the dual phase steels combine superior ductility, with good tensile strength, and in this regard their properties are very similar to plain carbon steels [1–3].

Dual phase steels usually contain some volume fractions of high-strength phase such as martensite or bainite, within a softer matrix, ferrite [4]. The ferrite matrix provides the ductility while the high strength particles provide strength. Besides these properties, other useful properties of these steels are low yield strength, continuous

*Corresponding author, e-mail: Mreza.akbarpour@gmail.com

yielding behaviour, and highly uniform total elongation [5–8]. Mechanical properties of dual phase steels are affected by several factors, including; the volume fraction, the morphology of hard phase [9], and the ferrite grain size [4].

Investigations on ferrite-martensite steels are extensive compared with those on the structure–property correlations of ferrite-bainite dual phase (FBDP) steels. Only a few papers report on the salient aspects of the structure–property relations of ferrite -bainite (F-B) steels. Sudo et al. [10, 11] examined a few F-B steels, and reported that an increase in the bainite content generally increases their yield ratio (the ratio of yield strength to tensile strength), reduces the area and fatigue endurance limit.

The effect of the bainite content on ferrite-bainite-martensite steels has been examined by Sudo et al. [10, 11], Kim et al. [12] and Choi et al. [13]. Sudo and Iwai [10] indicated that a decrease in the bainite content in ferrite–bainite–martensite steels causes a lowering of the strength and yield ratio but leads to improved percentage elongation and strain hardening exponent. Kim et al. [12] suggested that small amounts of bainite in ferrite–martensite dual phase (FMDP) steels lead to an improvement in the yield strength and the ductility but to a deterioration in the tensile strength. These investigators have also reported the occurrence of discontinuous yielding behaviour in these multiphase steels.

Discontinuous yielding in three phase steels at slow strain rates has also been observed by Choi et al. [13]. In addition, attempts also were made to study the effect of bainite on TRIP aided dual phase steels [14, 15]. However, systematic studies on F-B dual phase steels with a wide range of bainite content are lacking.

In our previous investigations [16, 17] on ferrite-bainite DP steels with $V_f < 0.34$, it was concluded that with increasing ferrite volume fraction, the yield and ultimate tensile strength decrease, while elongation increases. Furthermore, for the considered range of V_f values, the existence of two distinct work hardening stages was ascertained for this particular steel under study. The ferrite and bainite strength is not unique value over any range of V_f but it may be functions of chemical composition, shape and continuity of phases, internal stresses due to phase transformation and plastic incompatibility etc. Some of these parameters such as phase chemical composition, shape and continuity of phases change with increasing V_f and other such as internal stresses due to phase transformation and plastic incompatibility change during deformation and affect the strength of DP steels.

The present research is aimed at understanding the structure–property (tensile) dependences of ferrite-bainite steels having ferrite volume fractions ranging from 45% to 65 %.

2. Experimental

The steel used was a AISI 4340 type steel collected locally in the form of a bar. The chemical composition of the steel is given in Table 1. Cylindrical bars of 10 mm in diameter and 120 mm long were cut and first subject to heat treatment in order to

obtain the desired ferrite-bainite structures. This heat treatment consisted of the following sequential steps: (a) austenitizing the steel at 1100 °C for 1 h, (b) performing intercritrical annealing at 730 °C while adjusting the annealing durations, in order to obtain samples with various V_f values, (c) soaking in a salt bath at 350 °C for 40 min and finally (d) cooling in air.

Table 1. Chemical composition of the investigated steel

Element	Content [wt. %]
C	0.442
Si	0.292
Ni	1.840
Mo	0.246
Mn	0.722
P	0.024
Al	0.027
Cu	0.262
S	0.010
Cr	0.782
Co	0.012
V	0.002
Fe	Base

Samples for microstructural studies were fabricated and etched with 2% Nital solution and then examined under an optical microscope. Volume fractions of the phases were measured by an image analyzer. Tensile specimens were fabricated with a gauge length of 36 mm. Tensile tests were carried out at room temperature using an Instron tensile machine with a cross head speed of 1 mm/min (strain rate of 4.6×10^{-4} 1/s). The relationship between the ferrite volume fraction and the deformation mechanism was predicted using tensile test data and the Hollomon equation. Finally, the fracture surfaces of the specimens were studied using a Philips XL30 scanning electron microscope.

3. Results and discussion

3.1. Microstructure

Ferrite-bainite dual phase steels were fabricated by isothermal treatment in the bainitic transformation range. Transformation temperatures were selected based on the calculated Ac1 and Ac3 transformation temperatures and martensitic start temperatures (Ms) from the empirical formula given in [18]. The Ac1, Ac3 and the Ms Transformation temperatures for the selected steel were found to be 710, 770 and 285 °C, respectively.

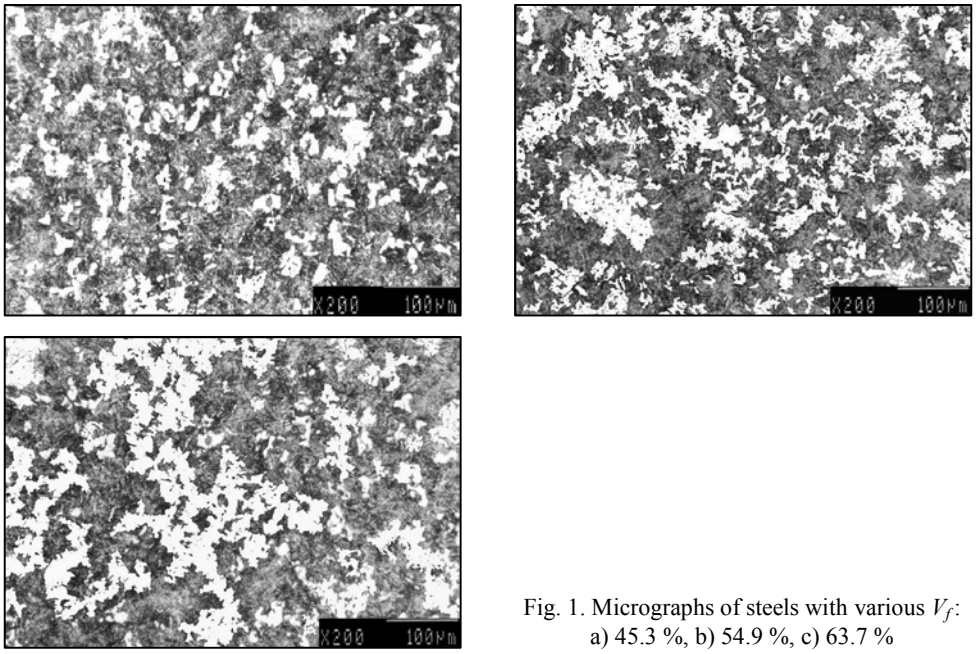

Fig. 1. Micrographs of steels with various V_f: a) 45.3 %, b) 54.9 %, c) 63.7 %

Light micrographs of steels with various V_f are shown in Fig. 1. The ferrite volume fractions of dual phase microstructures produced by intercritical annealing at 730 °C at various holding times of 80,120, 150 min are 0.453, 0.549 and 0.637, respectively.

3.2. Tensile properties

Engineering stress–strain curves for ferrite-bainite dual phase steels exhibited continuous yielding behaviour in the studied range of the ferrite volume fractions. The continuous yielding behaviour of ferrite–martensite dual phase steels has been attributed to the presence of unpinned dislocations introduced into ferrite by plastic deformation during the formation of martensite from austenite [19, 20].

The reason for the occurrence of continuous yielding in ferrite-bainite dual phase steels is not straightforward. Barbacki [21] reported that continuous yielding occurs in ferrite-bainite dual phase steels. Bhadeshia [22], however, mentioned that one may get either continuous or discontinuous yielding in ferrite-bainite dual phase steels, depending on the nature of the system. The factors which govern discontinuous yielding in steels are [20, 23, 24]: (i) low mobile dislocation density of the order of 10^2–10^4 cm^{-2} prior to deformation, (ii) a rapid rise in the number of dislocations that occur during deformation and (iii) a strong dependence of the dislocation rate on the applied stress. The amount and type of the harder constituent in a dual phase steel control the dislocation density, whereas the number of dislocations and the change in the dislocation rate depend on the morphology and the chemistry of the ferrite phase.

In ferrite-bainite dual phase steels, a considerable number of dislocations can be generated in ferrite by the transformation of austenite to bainite; therefore, to achieve continuous yielding in ferrite-bainite dual phase steels, the amount of bainite has to be increased to achieve a high dislocation density in ferrite. Interestingly, Barbacki [21] reported that the majority of dislocations produced during bainitic transformation are mobile in nature. Therefore, the observed continuous yielding behaviour of this dual phase steel may be attributed to the possibility that a high density of mobile dislocations is produced due to the higher volume fraction of bainite in the microstructures of the steels under consideration.

The tensile stress–strain curves have been analyzed to obtain estimations for the yield strength (YS), ultimate tensile strength (UTS), uniform elongation (UEL) and total elongation (TEL) from the tested specimens. The dependences of strengths and elongation of the investigated steel on the volume fraction of ferrite are shown in Figs. 2 and 3.

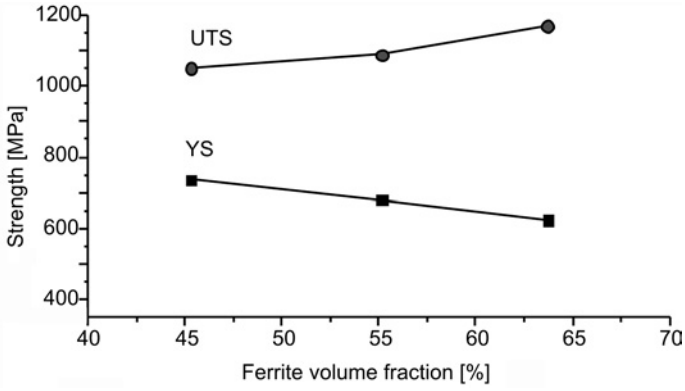

Fig. 2. Effect of the ferrite volume fraction
on the yield strength and the ultimate tensile strength

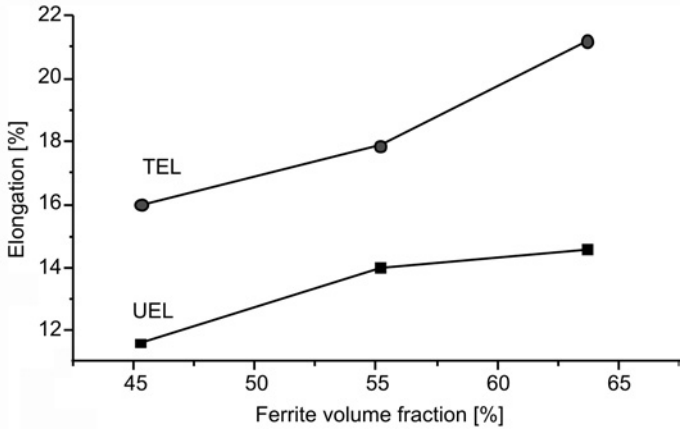

Fig. 3. Effect of ferrite volume fraction on ductility

The variation of the yield strength with the increase in the amount of bainite (ranging between 0.45 and 0.64 vol. %) is linear. It has been demonstrated [16] that as the ferrite volume fraction yield increases, the ultimate tensile strength decreases, while elongation increases (for $V_f < 0.34$). In this study, a different effect of V_f on ultimate tensile strength was noted. With increasing V_f in the considered range, yield strength decreases while elongation and UTS both increase.

The linear dependence of the yield strength on the volume fraction of the harder constituents in DP steels is often considered fortuitous, because the strength of bainite depends on the carbon content. The nonlinear dependence of strength of dual phase steel on the volume fraction of martensite in martensitic DP steels has also been indicated by some authors [25–28]. They reported that the non-linear increase of the strength with the volume fraction of martensite depends on the strength of martensite, which varies with its carbon content.

In addition, it is to be borne in mind that carbon partitioning between the constituents during processing of these steels would also affect the nature of the constituents, leading to alteration of their strength values. Thus, the overall strength of DP steel depends on: (i) the relative amount of the phases and (ii) their strength. Studies related to strength versus amount of ferrite in our earlier investigation [16] are limited to higher volume fractions of bainite. The observed variation of the ultimate tensile strength with the volume fraction of bainite in the investigated DP steel containing 45–63% of ferrite is dissimilar with high and low bainite DP steels. The ductility of the investigated steels (with 45–63 vol. % of ferrite) has been considered in terms of the elongation percentage, as shown in Fig. 3.

Elongation increases with the increase in the ferrite volume fraction. The variation of the ductility with the volume fraction of ferrite shows a maximum elongation (for ca. 65 vol. % of ferrite). It seems that above ca. 55 vol. % of ferrite the rate of UEL increasing has been reduced. In total, the variation of the strength and the ductility of DP steels are governed by three major factors: (a) the mean intercept lengths of the phases/constituents, (b) internal stresses in the phases/constituents and their influence on the composite structure, and (c) the strength and ductility of the individual phases/constituents governed by the compositional variation.

The magnitude of strain hardening stress, which is the difference between the UTS and YS, i.e.

$$\Delta\sigma = \sigma_{\text{uts}} - \sigma_{\text{ys}}$$

is plotted in dependence of the ferrite volume fraction (Fig. 4). It is seen that $\Delta\sigma$ increases as V_f increases.

For F-M DP steels, the dependence of the tensile strength on the hard phase content has been empirically modelled [29–31] and formulated based on the rule of mixtures

$$\sigma_t = \sigma_2 (1 - V_f) + \sigma_1 V_f \tag{1}$$

where σ_1 and σ_2 are the tensile strengths of the ferrite and the hard phases, respectively. If σ_1 and σ_2 are assumed to be invariant with respect to the amount, nature, and morphology

of the respective phases, Eq. (1) predicts a linear relation between σ_t and V_f. Experimental results obtained in the present work appear to agree with the suggested empirical expression of Byun and Kim, [30] up to $V_f = 45.3$ vol. %. However, the experimental results are inconsistent with the predicted trends for $V_f > 45.3$ vol. %. Beyond this level of V_f, the experimental results show that the tensile strength increases with the increase in the ferrite content, whereas the models predict the tensile strength to decrease.

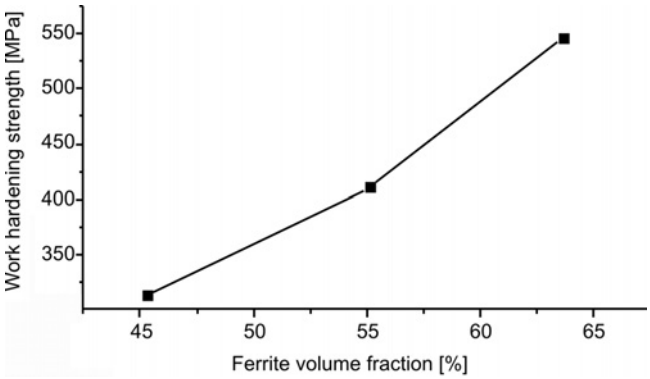

Fig. 4. Strain hardening stress vs. V_f

Furthermore, if σ_1 and σ_2 denote the YS of ferrite and bainite, respectively, and are assumed to be invariant with respect to the amount, nature, and morphology of the respective phases, the experimental results obtained in the present work appear to agree with the rules of mixtures (Eq. (1)). The YS decreases monotonically with the ferrite volume fraction in an approximately linear manner.

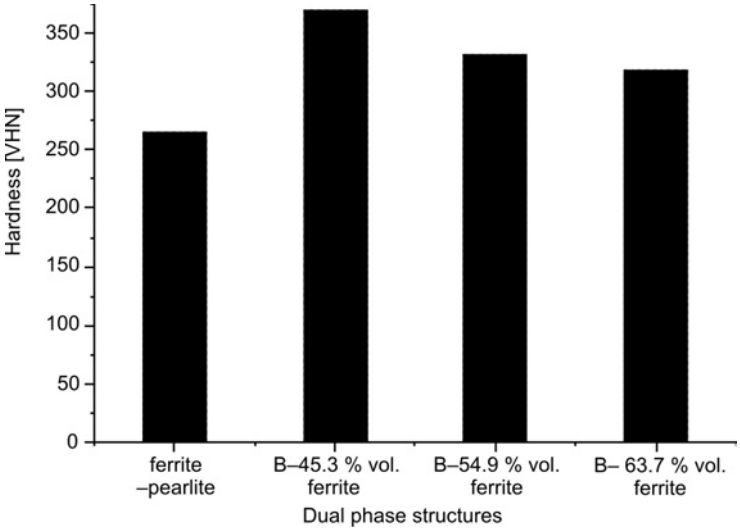

Fig. 5. Hardness [MPa] vs. YS for different dual phase structures

The Vickers hardness of different studied microstructures is shown in Fig. 5. According to the data in this figure, the variation in the hardness of dual phase steels is a good indication of the bainite content that existed in the microstructure. The Vickers hardness of the specimens (after intercritical annealing) bears extremely good polynomial correlation with the experimental yield strength as follows:

$$VHN = 0.0036YS^2 - 4.3896YS + 1667.5 \qquad VHN \text{ and } YS \text{ [MPa]}$$

3.3. Strain hardening behaviour. Hollomon analysis

Strain hardening exponents n of the investigated dual phase steels were determined using Hollomon's equation, as per ASTM standard E-646-98 [32]. These values are estimated from the slope of the lg–lg plots of the true stress σ vs. the true plastic strain ε data obtained from the tensile tests. Some typical representative plots of $\ln\sigma$–$\ln\varepsilon$ for the FBDP steels are shown in Fig. 6, which appear to deviate from linearity, though the linear regression coefficients (r^2) associated with the calculation of n are in the range of 0.965–0.997.

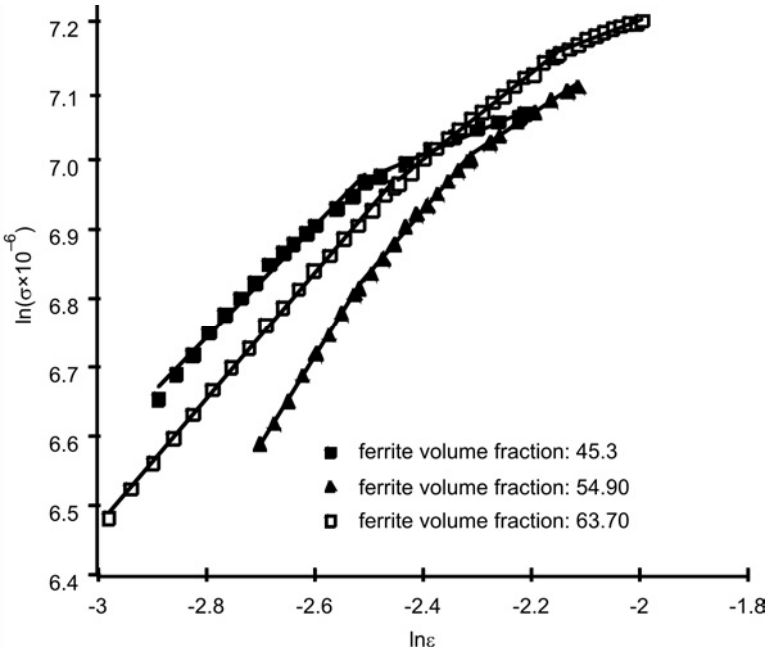

Fig. 6. $\ln\sigma$–$ln\varepsilon$ plots of investigated steel with various V_f

For these steels the dependence of $\ln\sigma$ on $\ln\varepsilon$ is nonlinear. This means that only one n value cannot describe the flow and work hardening behaviour of these materials. Some researchers explained that dual phase steels show two stage requiring two work hardening indices [16, 17, 28, 33–36]. Other authors showed three hardening stages

for some dual phase steels, such that each stage exhibits structural evolutions during deformation [2, 37–39]. The existence of different work hardening stages in various DP steels has been related to different activated deformation mechanisms at strain range corresponding to each stage. These mechanisms are a sequence of phase deformations (homogeneous or heterogeneous), minimum plastic incompatibility and possible phase transformation during deformation such as transformation of retained austenite to martensite and dynamic recovery [2, 16, 17, 28, 30, 33–38].

According to the results for the steel with V_f of ca. 45.3 %, two stages of work hardening were found [16, 17]. The first stage has a high strain hardening exponent and the second stage has a low one. These results are in agreement with the results of previous works on work hardening behaviour of ferrite–martensite dual phase steels [33–36]. According to these works, the first stage is associated with plastic deformation of the ferrite matrix and the second one with plastic deformation of both ferrite and martensite. However, Lian et al. [36] according to their theoretical and experimental results on work hardening behaviour of ferrite-martensite DP steels having different amounts of martensite concluded that the first stage of work hardening in steels with $V_m > 50\%$, martensite first deforms elastically and then deforms partly elastically and partly plastically. The second stage of work hardening is associated with plastic deformation of both ferrite and martensite.

In the present work, no TEM analysis was done on the deformation behaviour of bainite, but it seems that the model of Lian et al. is applicable to the present work, since the volume fraction of bainite is higher than 50 vol. %. The deformation of hard phase, martensite or bainite, depends on the strength difference between two phases. A higher strength difference corresponds to elastic deformation and a lower one corresponds to plastic deformation of the hard phase. The yield stress of the second phase (bainite) depends on its carbon content. The higher the carbon content, the higher the strength of the second phase is. The carbon content of the second phase decreases as the volume fraction of the second phase increases [39]. By applying the rule of mixtures, the carbon content of hard phase, bainite may be determined.

In the present work, for steel with $V_f > 54.9$ %, three-stage work hardening was found. The most probable explanation for the results is as follows:

Stage I is due to homogeneous deformation of ferrite. The rate of work hardening is high because undissolved carbide particles impede the glide of dislocations in the ferrite phase. The possibility of martensite deformation is not ruled out. Stage II is due to a condition of going through and minimum plastic incompatibility, resulting in lower internal stresses and, thus, enhancing the easy flow of dislocations. Stage III consists of simultaneous deformation of ferrite and martensite associated with dynamic recovery.

Specific evidence has not been obtained to support the above hypothesis; however, some experimental observations further support this view. First, the slope of the $\lg\sigma$–$\lg\varepsilon$ plots, for stage I, is lower for specimens containing higher amounts of ferrite. This observation implies a higher work hardening rate in stage I for samples contain-

ing more ferrite than for those containing less ferrite. The correspondence between lower work-hardening rates and higher V_b is attributed to an ease of the dislocation flow, owing to the absence of barriers, such as the undissolved carbide particles. Secondly, onset strains of stage III work hardening increase with the increase in the ferrite volume fraction. This corresponds to harder deformation of bainite which increasing ferrite volume fraction (i.e., carbon content of bainite) which need much strain to deform in the third stage. The occurrence of stage II may be due to dynamic changes of internal stresses during plastic deformation. However, no conclusive support could be obtained to satisfactorily explain this stage of deformation

3.4. Fractography

Figure 7 shows fracture surfaces of tensile tested specimens having a 45.3% and 63.70% volume fraction of ferrite. It was seen that the tensile fracture mechanism of

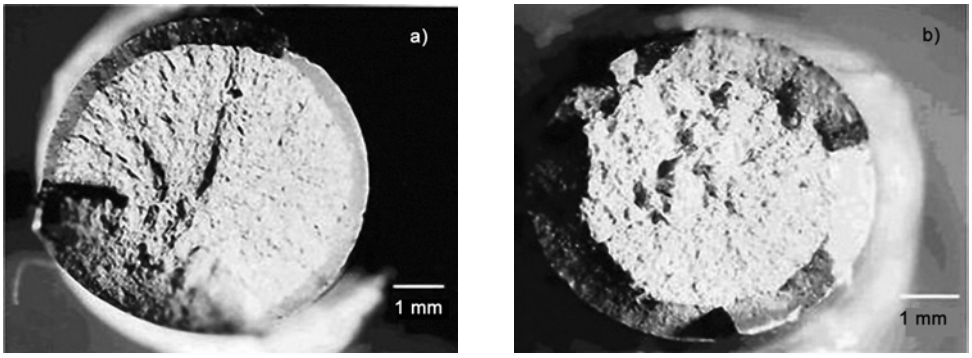

Fig. 7. Macrofracture surfaces of tensile tested specimens with:
a) 45.3% and b) 63.70% volume fractions of ferrite

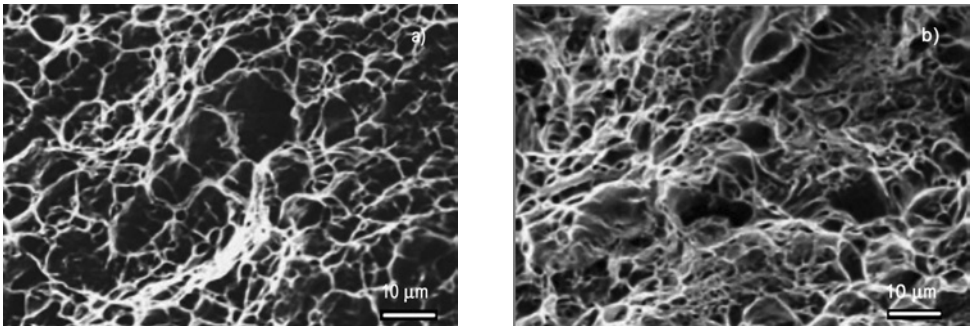

Fig. 8. SEM photographs of the central section of fracture surfaces
of tested specimens with: a) 45.3% and b) 63.70% volume fractions of ferrite

these steels is the classic “cup and cone” type fracture at room temperature. Also a scanning electron microscope photograph of the central section of the fracture sur-

faces are shown in Fig. 8. The fracture surfaces of the studied DP steels reveal the presence of dimples, indicating a typical ductile mode of fracture. According to Džupon et al. [40], the fracture surfaces of ferrite-martensite DP steel with different constituents volume fractions (20–88 vol. % of martensite) after uniaxial tension loading had ductile dimple morphology, with statistically distributed dimples of greater sizes and depths. As V_m grows, the occurrence of deeper and greater pits becomes more frequent. Similar to ferrite-martensite DP steels, samples having various bainite contents exhibited dimples of various sizes; as the volume fraction of ferrite increases, the dimple size decreases. The decrease in the dimple size is attributed to a larger number of void initiations in FBDP steels having higher ferrite content.

4. Conclusions

Ferrite-bainite dual phase steels with different ferrite volume fractions (from 45 vol. % to 65 vol. %), were produced using appropriate heat treatment, and were tensile tested at room temperature. The results are summarized as follows:

In ferrite-bainite DP steels, the yield strength (YS) increases monotonically with the ferrite volume fraction but the ultimate tensile strength (UTS) does not. UTS increases only when the ferrite volume fraction V_f increases above 55 vol. %.

The specimens intercritically annealed for 2.5 h and having 63.7 vol. % of ferrite exhibited the best combination of work hardening and ductility. Two or three Hollomon equations are sufficient to describe the flow behaviour of this DP steel adequately, and it was ascertained that as V_f increases, the work hardening takes place in three stages.

The Vickers hardness of DP steels decreased with the increase in the ferrite volume fraction. It is observed that the Vickers hardness of the specimens (after intercritical annealing) bears extremely good polynomial correlation with the experimental yield strength.

References

[1] KLAAR H.J., EL-SESY I.A., HUSSEIN A.A., Steel Res., 61 (1990).
[2] BAG A., RAY K.K., DWARAKADASA E.S., Metall. Trans., A 30 (1999), 1193.
[3] TAVARES S.S.M., PEDROZA P.D., TEODOSIO J.R., GUROVA T., Scr. Mater., 40 (1999), 887.
[4] SUN S., PUGH M., Mater. Sci. Eng. A, 335 (2002), 298.
[5] HILLIS D.J., LLEWELLYN D.T., EVANS P.J., J. Ironmaking Steelmaking, 25 (1998), 47.
[6] SUH D.W., KWON D.I., LEE S.H., KIN N.J., J. Metall. Mater. Trans. A, 28 (1997), 504.
[7] HANSEN S.S., PRADHAN R.R., *Fundamentals of dual phase steels*, [in:] *Proceedings of the Metallurgical Society of AIME*, Warrendale, USA, 1980, pp. 113–140.
[8] AHMAD E., MANZOOR T., ALI K.L., AKHTER J.I., J. Mater. Eng. Perf., 9 (2000), 306.
[9] ERDOGAN M., PRIESTNER R., J. Mater. Sci. Techn., 18 (2002), 369.
[10] SUDO M., IWAI T., ISIJ Int., 23 (1983), 294.
[11] SUDO M., HASHIMOTO S., KAMBE S., ISIJ Int., 23 (1983), 303.

[12] KIM I., RAIACHEL S., DAHL W., Steel Res., 58 (1987), 186.
[13] CHOI B.Y., KRAUSS G., MATLOCK D.K., Scr. Metall., 22 (1988), 1575.
[14] HELLER T., NUSS A., [in:] *Proceedings of the International Symposium on Transformation and Deformation Mechanisms in Advanced High Strength Steels*, M. Militzer, W.J. Poole, E. Essodiqui (Eds.), Vancouver, August 2003, 24–27.
[15] HASHIMOTO S., ISIJ Int., 43 (2003), 1658.
[16] AKBARPOUR M.R., EKRAMI A., Mater. Sci. Eng. A, 477 (2008), 306.
[17] AKBARPOUR M.R., EKRAMI A., Mater. Sci. Eng. A, 475 (2008), 293.
[18] KRAUSS G., *Steels, Heat Treatment and Processing Principles*, ASM, 1990.
[19] MATSUOKA T., YAMMORI K., Metall. Trans. A, 6 (1975), 1613.
[20] RIGSBEE J.M., ABRAHM J.K., DAVENPORT A.T., FRANKLIN J.E., PICKENS J.W., [in:] *Structure and Properties of Dual phase Steels*, R.A. Kot, J.W. Morris (Eds.), AIME, New York, 1979, pp. 304–329.
[21] BARBACKI A., J. Mater. Proc. Techn., 53 (1995), 57–63.
[22] BHADESHIA H.K.D.H., *Bainite in Steels*, 3rd Ed., IOM Communication Ltd., the Institute of Materials, London, 2001.
[23] DAVIS R.G., MAGEE C.L., *Dual phase and Cold Pressing Vanadium Steels in the Automobile Industry*, Vanitec, Berlin, 1978, p. 25.
[24] MEDIRATTA S.R., RAMASWAMY V., RAMA ROA P., Trans. Indian Inst. Met., 38 (1985), 350.
[25] THOMAS G., KOO J.Y., [in:] *Structure and Properties of Dual phase Steels*, R.A. Kot, J.W. Morris (Eds.), AIME, New York, 1979, pp. 183–201.
[26] SPEICH G.R., [in:] *Fundamental of Dual phase Steels*, R.A. Kot, B.L. Bramfitt (Eds.), AIME, New York, 1991, pp. 4–46.
[27] KOO J.Y., YOUNG M.J., THOMAS G., Metall. Trans. A, 11 (1980), 852.
[28] RAMOS L.F., MATLOCK D.K., KRAUSS G., Metall. Trans. A, 10 (1979), 259.
[29] DAVIES R.G., Metall. Trans. A, 9 (1978), 671.
[30] BYUN T.S., KIM I.S., J. Mater. Sci., 28 (1993), 2923.
[31] MARDER A.R., Metall. Trans. A, 13 (1982), 85.
[32] E-646-98, Annual Book of ASTM Standards vol. 03.01, Philadelphia, PA, 1999.
[33] JIANG Z., GUAN Z., LIAN J., J. Mater. Sci., 28 (1993), 1814.
[34] DAVIES R.G., Metall. Trans. A, 9 (1978), 671.
[35] ENDO T., HOPER S., ISHIKAWA N., OSAWA K., ISIJ Int., 39 (1999), 288.
[36] LIAN J., JIANG Z., LIU J., Mater. Sci. Eng. A, 147 (1991), 55.
[37] SAMUEL F.H., Mater. Sci. Eng., 92 (1987), L1.
[38] PARUZ H., EDMONDS D.V., Mater. Sci. Eng. A, 117 (1989), 67.
[39] DELINCE M., BRECHET Y., EMBURY J.D., GEERS M.G.D., JACQUES P.J., PARDEON T., Acta Materi., 55 (2007), 2337.
[40] DZUPON M., PARILAK L., KOLL AROVA M., SINAIOVA I., Metalurgija, 46 (2007), 15.

Received 5 November 2009
Revised 16 June 2009

Materials Science-Poland, *Vol. 28*, *No. 2*, *2010*

Synthesis of WC–20 wt. % Cu composite powders by co-precipitation and carburization processes

M. ARDESTANI*, H. ARABI, H. RAZAVIZADEH, H. R. REZAIE, H. MEHRJOO

Department of Materials and Metallurgical Engineering, Iran University of Science and Technology, Narmak, Tehran 16846-13114, Iran

WC/Cu composite powders were synthesized by co-precipitation and subsequent reduction-carburization process. The precipitates contained W-Cu compounds fabricated using a chemical procedure from a mixture of copper nitrate and ammonium paratungstate in distilled water. In order to synthesize the WC-Cu composite powders, dried precipitates were calcined at 823 K in air and then reduced and carburized by carbon monooxide (CO). The non-isothermal mechanism of reduction-carburization of the calcined powders in carbon monoxide was investigated by thermogravimetry, differential thermogravimetry and X-ray diffraction analyses. The optimum reduction-carburization temperature was determined as 1065 K. The microstructures of the powders were characterized by the scanning electron microscopy.

Keywords: *WC-Cu composites; reduction; carburization; thermogravimetry*

1. Introduction

Electrical contact materials should be characterized by a good combination of electrical conductivity, wearing qualities and resistance to erosion and welding [1]. WC-Cu contacts have high thermal conductivity as well as high electrical conductivity, because of their copper content. They also have high wear resistance, because of the hardness of tungsten carbide. WC-Cu contacts are therefore used in oil switches and wiping shoes in power transformers [2]. These kinds of materials, due to excellent wetting characteristics between tungsten carbide and copper as well as the limited solubility of tungsten in copper, are composites rather than solid solutions [3, 4].

A conventional method to synthesise these kinds of materials is infiltration of copper into a tungsten carbide skeleton, but infiltration does not result in a homogene-

*Corresponding author, e-mail: mohammadard@yahoo.com

ous microstructure and is not a net shape process, being unsuitable for mass production [5, 6]. Other than infiltration, WC-Cu metal matrix composites could be prepared by a powder metallurgy process, namely by blending and sintering WC and Cu powders [7]. However, it has been shown that by using composite powders instead of blending the constituents, the densification of the composite increases significantly. For these kinds of powders, the effectiveness of sintering can be enhanced by improving the homogeneity and decreasing the particle size of the starting powders. This is especially true for a liquid phase sintering system, such as for WC-Cu materials [8, 9].

In this study, in order to prepare WC-Cu composite powders, a new co-precipitation method, followed by calcination of the precipitates, was used to obtain a homogeneous mixture of W-Cu oxide powders. Subsequently, the oxide powders were reduced and then carburized by carbon monoxide. The mechanisms of reduction and carburization of oxide powders were investigated by TG, DTG and XRD analyses.

2. Experimental

Blue coloured copper nitrate ($Cu(NO_3)\cdot 3H_2O$), >99% purity, Merck, Germany) and white coloured ammonium paratungstate ($H_{42}N_{10}O_{42}W_{12}\cdot xH_2O$, >99% purity, Riedel-de Haen, Germany) were used as precursors.

In order to synthesise the initial precipitates with the desired weight proportion of copper and tungsten carbide (equal to 4), a predetermined mixture of ammonium paratungstate and copper nitrate in distilled water was heated to 358–368 K. In order to adjust pH to 3–4, ammonia solution was added to the mixture dropwise. The process was continued for 3 h. Then the precipitates were washed, dried and calcined at 823 K for 2 h in air. Thermogravimetry and differential thermogravimetry (Netzsch STA 409 PC/PG) analyses were carried out in carbon monoxide (CO) atmosphere with the heating rate of 7.5 $K\cdot min^{-1}$ and 50 $cm^3\cdot min^{-1}$ gas flow up to 1273 K. In order to characterize the weight loss stages revealed by thermogravimetry (TG) analyses, oxide powders reduced/carburized by carbon monoxide in a tube furnace were examined by the differential thermogravimetry method (DTG). The heights of the bed powders were 1 mm. The powders were characterized by X-ray diffraction (XRD-Jeol 8030, CuK_α) and scanning electron microscopy (SEM, Cambridge S360).

3. Results and discussion

3.1. Characterization of the initial and calcined precipitates

Figure 1 shows the XRD pattern of initial precipitates. According to this pattern, the precipitates consisted of APT and another chemical compound which cannot be

identified by XRD patterns. Based on the applied chemical process, the latter compounds should contain W, Cu, NH_3 and H_2O. It may be believed that due to the heating of the solution which contained $Cu(NH_3)_4(H_2O)^{2+}{}_2$ complex ions, NH_3 evaporated and was replaced by para A ($HW_6O_{21}^{5-}$) or para B ($H_{10}W_{12}O_{46}^{10-}$) ions which existed in the media because of a low solubility of APT in distilled water. The SEM micrograph of the initial precipitates is shown in Fig. 2. This figure shows the morphology of the dried precipitates: they have granular shapes and are of submicron size.

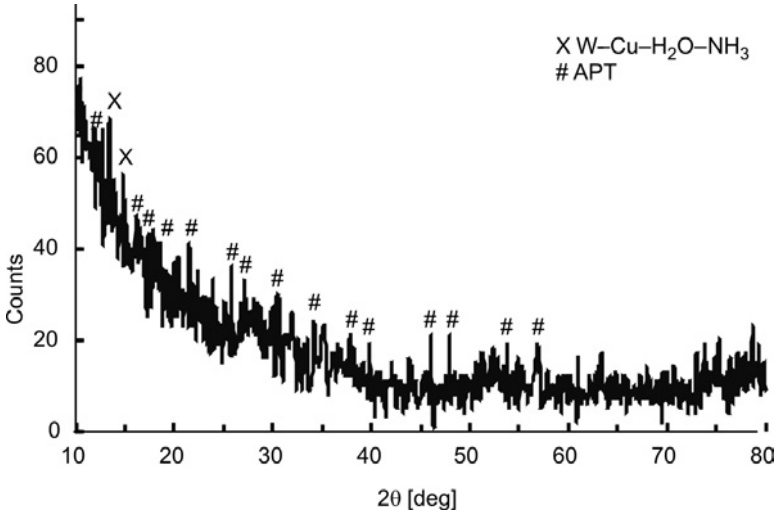

Fig. 1. XRD patterns of the initial precipitates

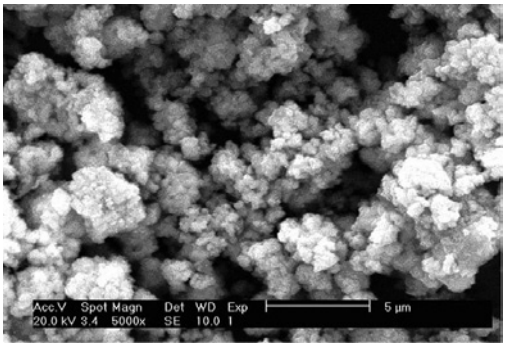

Fig. 2. SEM micrographs of the initial precipitates

The XRD pattern of the calcined powder is shown in Fig. 3. The calcined powders consisted of WO_3 and $CuWO_4$ phases. The SEM micrograph of the calcined powders is shown in Fig. 4. This figure shows that the particle sizes of the calcined powders have a wide distribution range and that the particles have spherical morphologies.

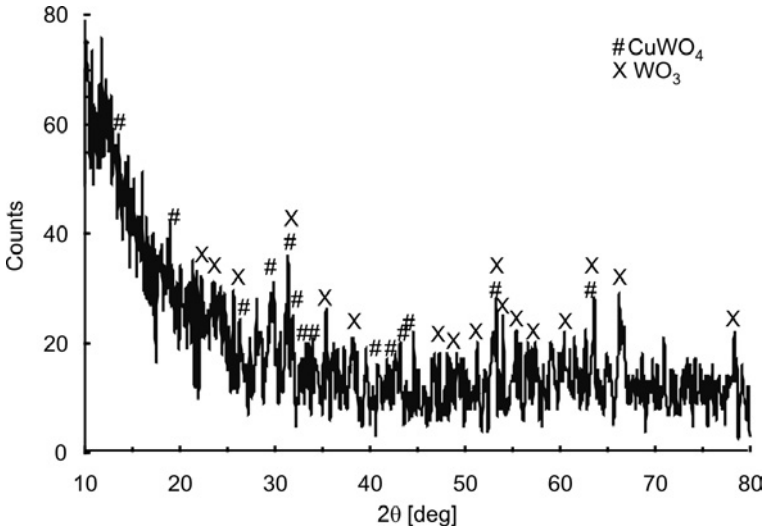

Fig. 3. XRD patterns of the calcined precipitates at 823 K

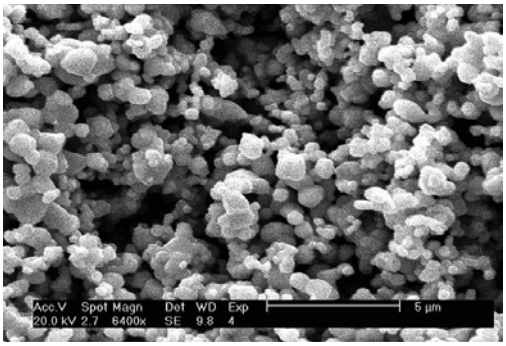

Fig. 4. SEM micrograph of the calcined powders at 823 K

3.2. Reduction-carburization of the oxide powders

3.2.1. TG/DTG analyses

Figures 5a (experimental curve) and 5b show TG and DTG curves of the oxide powders in carbon monoxide atmosphere. The TG curve shows two weight losses and one mass gain stages. These stages occur between 718 and 833 K, 928 and 1179 K and above 1179 K, respectively. The DTG curve exhibits two peaks at 756 K and 1065 K corresponding to the weight loss stages. The XRD pattern of the product of the first stage reaction is shown in Fig. 6. The first weight loss stage corresponds to reduction of $CuWO_4$. The reaction for the first weight loss stage is:

$$CuWO_4 + CO \rightarrow Cu + WO_3(WO_{2.9}) + CO_2 \quad (1)$$

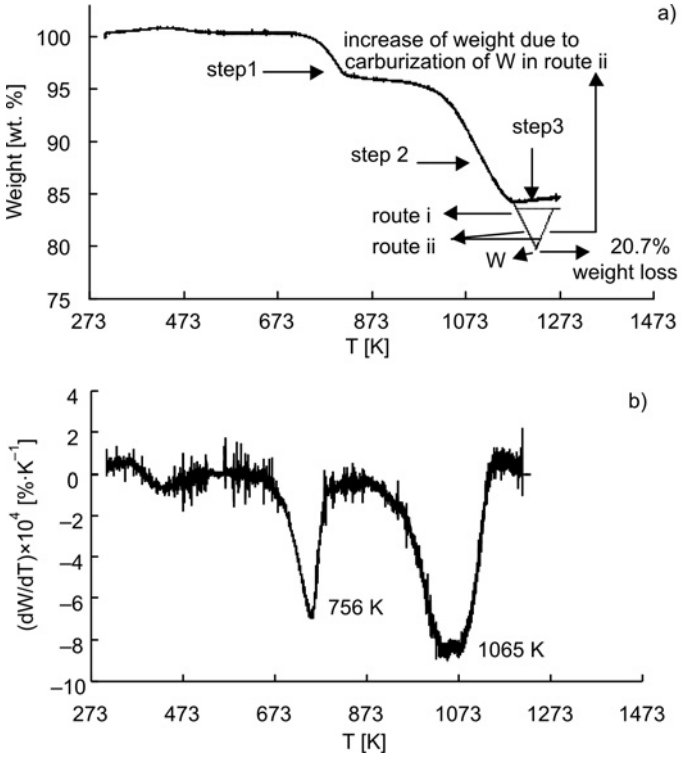

Fig. 5. TG (a) and DTG curves of oxide powder from room temperature to 1273 K in CO atmosphere

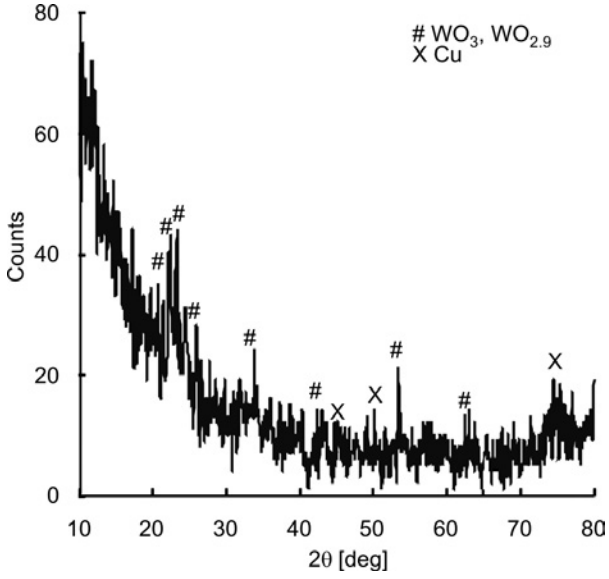

Fig. 6. XRD pattern of the reduced powder at 756 K for 1 h

It is worth noting that one or both of WO_3 ($WO_{2.9}$) oxide phases might have been formed, but according to the XRD observations the formation of WO_3 is the more probable. This result is due to the similar XRD pattern of these oxide phases. $WO_{2.9}$ is a simplified form of $W_{20}O_{58}$ oxide phase. According to the TG analysis, the corresponding weight loss of the first reaction is 3.85%. The theoretical weight loss for this step is 4% which is in agreement with experimental results.

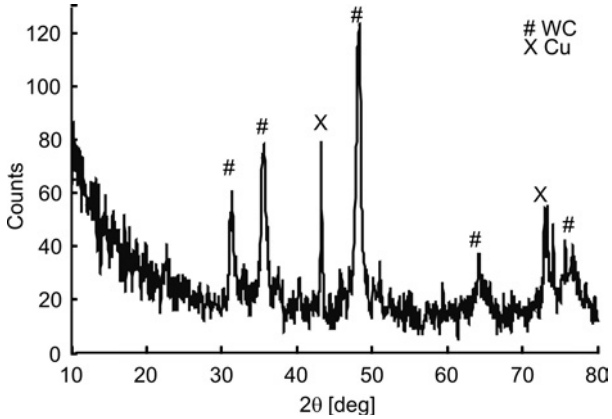

Fig. 7. XRD pattern of reduced and carburized powders at 1065 K for 6 h

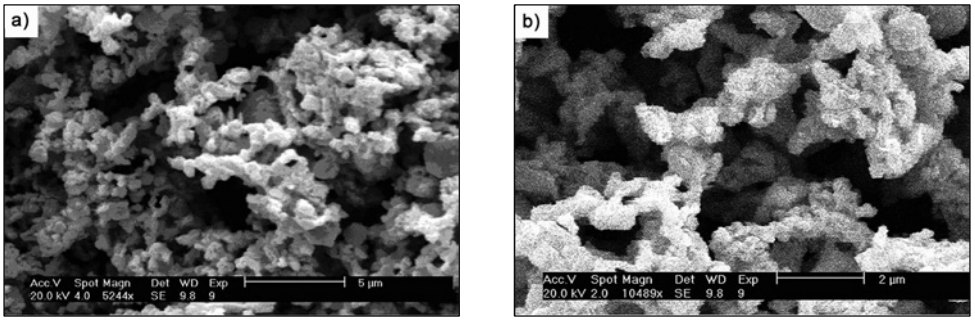

Fig. 8. SEM micrographs of reduced and carburized powders at 1065 K for 6 h in two magnifications (a, b)

The XRD pattern of the product of the second stage weight loss step is shown in Fig. 7. The product of the second reaction consisted of Cu and WC and. The SEM micrographs of the reduced and carburized powders at different magnifications are shown in Fig. 8. The images show that the agglomerates consist of several primary particles (~300–500 nm) having a worm-shape morphology.

The proposed reaction for this step is carburization of WO_3 ($WO_{2.9}$) to WC. The total weight loss of the reduction-carburization process is 15.9%. The theoretical

weight loss after the second weight loss step is 16.47%. According to the results, the theoretical value is about 0.57% higher than the weight loss which has been determined by TG analysis. The reason for this difference between the experimental and theoretical values might be due to deviation of the results and deposition of carbon according to the following reaction [9]:

$$2CO \rightarrow C + CO_2 \tag{2}$$

Also, the mass gain in the third stage of the TG analysis may be considered to be associated with carbon deposition, corresponding to reaction (2) [9]. According to the above results, the optimum temperature for the reduction-carburization process is 1065 K. At this temperature, the oxide phases (WO_3 and $CuWO_4$) could be completely reduced to Cu and WC.

3.2.2. Carburization of WO_3 to WC

Carburization of WO_3 to WC has been investigated by other authors [9, 11]. According to the results of Venables et al., the carburization can proceed by the following routes [9]:

$$WO_3 \rightarrow WO_{2.9} \rightarrow WO_{2.72} \rightarrow WO_2 \rightarrow WC \tag{i}$$

$$WO_3 \rightarrow WO_{2.9} \rightarrow WO_{2.72} \rightarrow WO_2 \rightarrow \alpha\text{-}W \rightarrow WC \tag{ii}$$

$$WO_3 \rightarrow WO_{2.9} \rightarrow WO_{2.72} \rightarrow \alpha\text{-}W \rightarrow WC$$

$WO_{2.72}$ is a simplified form of $W_{18}O_{49}$ oxide phase.

The difference of the two routes is that in the former one WO_2 directly converts to WC, and in the latter one WO_3 was reduced completely to W and then W carburized to WC. According to the TG curve in this study (Fig. 5a), the dominant mechanism of the non-isothermal carburization of WO_3 with CO is the first one. The reason for this conclusion is the formation of W in the reduction process of the second route. In other words it can be shown that although at the end of the two routes WC forms and the total weight losses of the both processes differ only by 0.57% from the experimental value, the curve of the weight versus temperature of route (ii) has a minimum peak because of the formation of W and then shows an increase in weight due to carburization of this agent. This profile is not in a good agreement with the experimental curve. However, the aforementioned minimum weight loss peak does not exist in route (i), and the reduction/carburization curve is similar to the experimental one (Fig. 5a).

4. Conclusion

WC-Cu composite powders were synthesized by the co-precipitation and a subsequent reduction-carburization method. The process consisted of precipitation of the

initial powder using ammonium para-tungstate and copper nitrate as raw materials, calcination the precipitates and reduction of the calcined powders by carbon monoxide. The reduction-carburization process of WO_3 and $CuWO_4$homogeneous mixture in CO atmosphere proceeded as:

$$CuWO_4, WO_3 \rightarrow Cu, WO_3(WO_{2.9}), WO_3 \rightarrow Cu, WC$$

The optimum reduction-carburization temperature of the mixture was 1065 K.

Acknowledgement

The authors acknowledge the Materials and Energy Research Centre (MERC) for its financial support.

References

[1] FINDIK F., UZUN H., Mater. Design, 24 (2003), 489.
[2] DAVIS JR, *Copper and Copper Alloys* (ASM Specialty Handbook), ASM International, 2001.
[3] DESHPANDE P.K., LIN R.Y., Mater. Sci. Eng., 418 A (2006), 137.
[4] DESHPANDE P.K., LI J.H., LIN R.Y., Mater. Sci. Eng., 429 A (2006), 58.
[5] LI Y., QU X., ZHEMG Z., LEI C., ZOU Z., YU S., Int. J. Ref. Met. Hard Mater., 21 (2003), 259.
[6] MOON I.H., KIM E.P., PETZOW G., Powder Metall., 41 (1998), 51.
[7] ZHAO N., LI J., YANG X., J. of Mater. Sci., 39 (2004), 4829.
[8] COSTA F.A., SILVA A.P., GOMES U.U., Powder Tech., 134 (2003), 123.
[9] VENABLES D.S., BROWN M.E., Thermochim. Acta, 291(1997), 131.
[10] CHENG J., SONG P., GONG Y., CAI Y., XIA Y., Mater. Sci. Eng., 488A (2008), 453.
[11] NAVA A.F.C., ZMBRANO M.M.L., URIBE S.A., BEDOLLA BECERRIL J.E., Int. J. Min. Proc., 20 (1987), 137.

Received 30 November 2008
Revised 20 April 2009

Materials Science-Poland, *Vol. 28*, *No. 2*, *2010*

Synthesis and characterization of nanocrystalline barium strontium titanate

M. GOLMOHAMMAD*, Z. A. NEMATI, M. A. FAGHIHI SANI

Ceramic Engineering Department School of Materials Science and Engineering,
Sharif University of Technology, Azadi Street, Tehran, Iran

Barium strontium titanate (BST) was prepared via the simple sol-gel method by using tetrabutyl titanate, ethanol, citric acid and ethylene glycol as starting materials. Thermogravimetry and differential thermal analysis were used to examine the behaviour of the xerogel. The particle size of BST was approximately 21 nm, as calculated by the X-ray diffraction and confirmed by transition electron microscopy for the calcination temperature of 750 °C. It was found that the particles of BST powders calcined at 750 °C were smaller and more homogeneous and uniform than those obtained at 800 °C.

Keywords: *(Ba,Sr)TiO3; sol-gel method; nanocrystalline material*

1. Introduction

Barium-strontium titanate (BST) is a useful electronic material due to its high electric permittivity and the Curie temperature depending upon the composition [1]. BST is applied in piezoelectric sensors, dynamic random access memories, microwave phase shifters and uncooled infrared detectors because of its good dielectric, ferroelectric, and pyroelectric properties [2–4].

High chemical purity and a uniform microstructure are the most important features for BST ceramics. Furthermore, the outstanding dielectric property observed on fine-grained BST ceramics has motivated the interest in the synthesis of nanocrystalline BST. To achieve a fine microstructure and high performance, it is necessary to fabricatea fine, stoichiometric and narrow size distribution powder. For this purpose, several wet chemical non-conventional methods, such as sol-gel, self-propagating high-temperature synthesis and hydrothermal techniques, were proposed as alternative approaches for the synthesis of dry mixed oxides, in order to improve the microstructural homogeneity and chemical reaction at low temperatures [5–9]. This paper presents a simple process for the synthesis of nanocrystalline BST powders.

*Corresponding author, e-mail: golmohamad@gmail.com

2. Experimental

Materials. BST powders were synthesized by the method shown schematically in Fig 1. For the preparation of the precursor solution, barium carbonate (99.0%), strontium carbonate (98.0%), tetrabutyl titanate (98%), citric acid (99.5%), and ethylene glycol (EG) were used as starting materials. First, 0.1 mol of $Ti(C_4H_9O)_4$ was dissolved into 2 moles of ethylene glycol. The mixture was stirred for about 3 min until it became transparent. Subsequently, 0.5 mol of citric acid powder and 0.1 mol water were directly added to this solution.

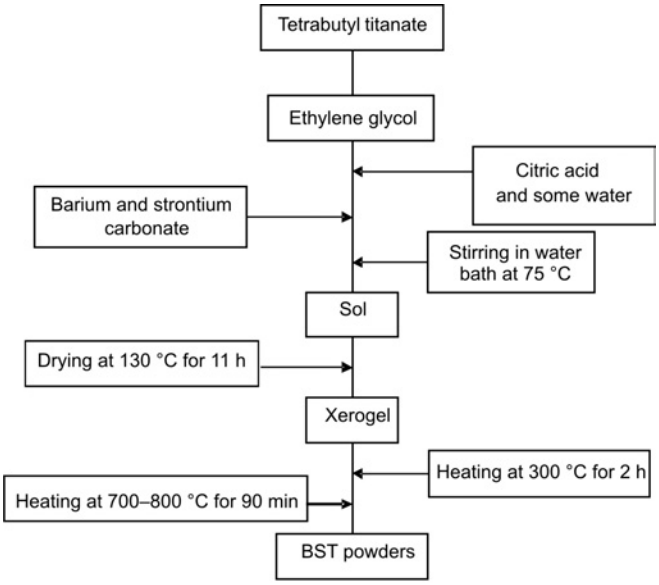

Fig. 1. Flow chart of synthesis BST nanoparticles

A small quantity of white precipitate was observed at first, but immediately dissolved after stirring for 20 min with a magnetic stirrer and the solution reverted back to clear appearance. Then, the stoichiometric amounts of $BaCO_3$ and $SrCO_3$ powders were added to this solution. Then, the mixed solution was put into a water bath and stirred at 75 °C, until it became pale brown and transparent. Then it was heated to 130 °C for 11 h to form xerogel. The xerogel was heated at 300 °C for 2 h and subsequently it was calcined at various temperatures for 90 min.

Characterization. IR spectra of the xerogel were recorded with a FT-IR spectrometer (Bruker Vektor33) in the range 400–4000 cm^{-1}. Thermogravimetric (TG) analysis and differential thermal analysis (DTA) of the precursor were carried out in static air under a heating rate of 10 °C/min, from room temperature to 1000 °C (Shimadzu 60AH). X-ray diffraction (XRD) with CuK_α radiation (Philips PW3710) was carried out to examine the phase composition of the obtained BST powders. The mi-

crostructure of the BST powders was investigated by transmission electron microscopy (Philips EM208).

3. Results and discussion

Figure 2 shows the IR spectrum of the precursor. Though it was very complex, the presence of broad bands centred at 3447 cm^{-1} (water stretching vibrations) [10], 2939 cm^{-1} (C–H stretching modes) [11], 1341 cm^{-1} (OH deformations of primary alcohols), 1065, 1955 cm^{-1} (C–O stretching vibration of primary alcohols) [11], 932 cm^{-1} (O–Ti–O stretching modes) [12] were evident. All the carbonates dissolved and thus no peaks corresponding to carbonates were found.

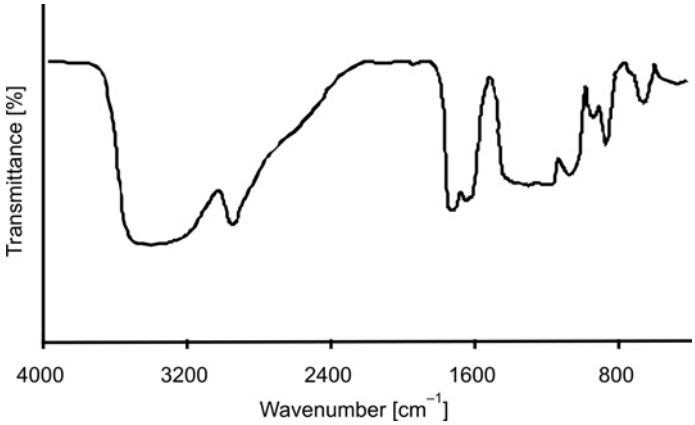

Fig. 2. FT-IR spectra of the xerogel

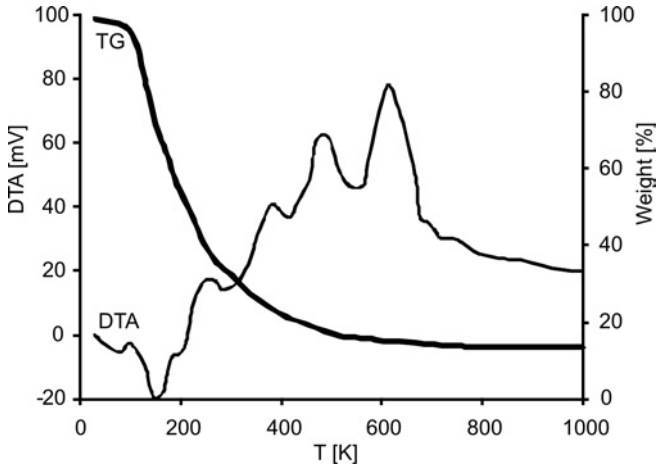

Fig. 3. TG and DTA curves of the xerogel
in static air from room temperature to 1000 °C

In order to determine the temperature of synthesis of BST powders, TG and DTA measurements of the xerogel were made and the results are shown in Fig 3. The TG trace indicates there were three minima in the sample weight. They occurred over the temperature ranges of 31–108,108–630 and 630–830 °C. During the first step, the weight loss was close to 3.9%, which can be attributed to the evaporation of trapped water. An endothermic peak near 98 °C was found in the DTA curve. The second step, with the weight loss of 83.5%, was recorded for the decomposition of the citrate precursor. This process consisted of two stages, as can be deduced from the position of the endothermic and exothermic peaks in the DTA curve. In the first stage, from 108 to 225 °C, the endothermic peak at 155 °C was attributed to the decomposition or removal of the organic parts which combined weakly with others in the precursor. On the other hand, there were three sharp exothermic peaks around 385, 475 and 623 °C during the second stage, which corresponded to drastic combustion of the organic species involved in the precursor.

There was a small mass loss of ca. 1.5% during the last step, accompanied with an endothermic peak at 673 °C which corresponded to the decomposition of residual carbonate and is confirmed by XRD.

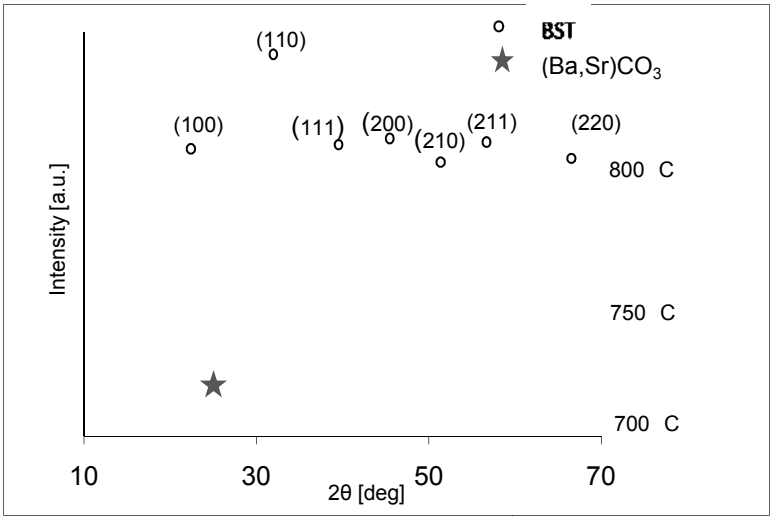

Fig. 4. XRD patterns of the BST powders synthesized at different temperatures

Figure 4 shows the XRD patterns of BST powders obtained at various temperatures. It can be seen that at 700 °C, weak lines occurred at 24.2°, corresponding to the residual carbonates phase such as $BaCO_3$, $SrCO_3$ and $(Ba,Sr)CO_3$ [13]. At higher temperatures, these peaks disappeared and a pure BST phase was identified at 750 °C and 800 °C. This indicates that as the temperature increased, residual carbonates decomposed.

Figure 5 shows the TEM image of the particles obtained at 750 °C. Most of the powders were rectangle in shape. The average particle diameter was found to be ap-

proximately 21 nm. This value was consistent with the result calculated by XRD (19 nm) using Scherrer's formula.

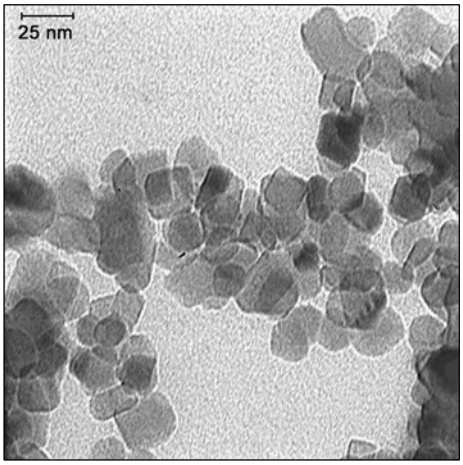

Fig. 5. TEM image of nanocrystalline BST powders obtained at 750 °C

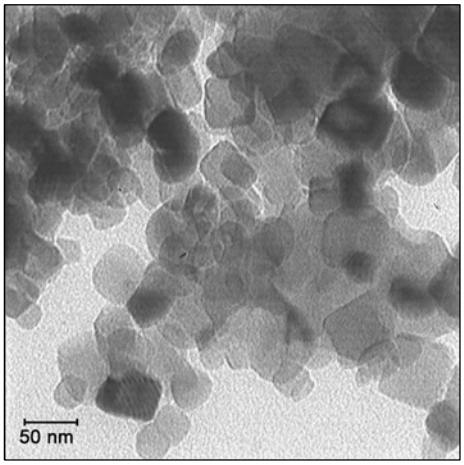

Fig. 6. TEM image of nanocrystalline BST powders obtained at 800 °C

Figure 6 shows the TEM image of the particles obtained at 800 °C. The average particle diameter was found to be approximately 44 nm. These powders were agglomerated and they were not as homogeneous and uniform as previous powders.

4. Conclusion

Fine BST nanoparticles, with the average particle size of 21 nm, were successfully synthesized by a repeatable simple sol-gel process. XRD and TG/DTA results revealed that pure phase BST can be obtained above 750 °C. It has been shown that nanoparticles obtained at 800 °C were more agglomerated and about twice the size as those obtained at 750 °C. This innovative, simple and time-saving method offers a new strategy for fabrication of nanoscaled powders in other electronic materials.

References

[1] BETHE K., WELZ F., Mater. Res. Bull., 6 (1971), 209.
[2] WANG J.Y., YAO X., ZHANG L.Y., Ceram. Int., 30 (2004), 1749.
[3] JANG H.M., JUN Y.H., Ferroelectrics., 193 (1997), 125.
[4] MAO C., DONG X., ZENG T., Matter. Lett., 61 (2007), 1633.
[5] SUASMORO S., PRATAPA S., HARTANTO D., SETYOKO D., DANI U.M., J. Eur. Ceram. Soc., 20 (2000), 309.
[6] KAO C.F., YANG W.D., Appl. Organometal. Chem., 13 (1999), 383.
[7] SHIIBASHI H., MATSUDA H., KUWABARA M., J. Sol-Gel Sci. Techn., 16 (1999), 129.
[8] KOMAROV A.V., PARKIN I.P., ODLYHA M., J. Mater. Sci., 31 (1996), 5033.

[9] ROEDER R.K., SLAMOVICH E.B., J. Am. Ceram. Soc., 82 (1999), 1665.
[10] TSAY J.D., FANG T.T., GUBIOTTI T.A., YING J.Y., J. Mater. Sci., 33 (1998), 3721.
[11] BELLAMY L.J., *The Infra-Red Spectra of Complex Molecules*, Methuen Co. Ltd., London, 1958.
[12] DURA N.P., CAPEL F., GUTIERREZ D., TARTAJ J., BANARES M.A., MOURE C., J. Mater. Chem., 11 (2001), 1828.
[13] TIAN H.Y., QI J.Q., WANG Y., WANG J., CHAN H.L.W., CHOY C.L., Nanotech., 16 (2005), 47.

Received 1 December 2008
Revised 4 August 2009

Materials Science-Poland, *Vol. 28*, *No. 2*, *2010*

Synthesis, characterization and properties of nanocrystalline perovskite cathode materials

S. GHOSH, S. DASGUPTA*

Ceramic Membrane Division, Central Glass and Ceramic Research Institute,
Council of Scientific and Industrial Research, Kolkata 700 032, India

A simple low temperature synthesis route has been presented of preparing nanosized, single phased $LaFeO_3$, $La_{(1-x)}Sr_xFeO_3$ (x = 0.3, 0.5) and $La_{(1-x)}Sr_xCo_{0.2}Fe_{0.8}O_3$ (x = 0.2, 0.4) for cathode applications in ITSOFC. A soft chemical method has been applied, using tartaric acid as a template material and nitric acid as an oxidizing agent. Phase pure materials were obtained at temperatures ranging from 550 °C to 700 °C. The synthesized powders were characterized by TGA, XRD, SEM and FTIR analysis. The crystallite size was 45–50 nm, with the surface area of 14–20 m^2/g. Electronic conductivity of the material was found to increase upon increasing Sr concentration and the sintering temperature. High electronic conductivities of 355 S/cm and 545 S/cm were obtained at 400 °C for $La_{0.5}Sr_{0.5}Fe_2O_3$ and $La_{0.6}Sr_{0.4}Co_{0.2}Fe_2O_3$, respectively. Activation energy decreases with the increase in Sr concentration. The values of thermal expansion coefficients (TEC) of the materials are compatible with the TEC of the ceria-gadolinium oxide CGO interlayer between cathode layer and electrolyte.

Keywords: *electronic materials; chemical synthesis; X-ray diffraction; electrical conductivity*

1. Introduction

Solid oxide fuel cells (SOFCs) are environmentally friendly potential energy sources for the future production of electrical power, due to their high efficiency, low emission, multifuel activity and modularity. The most widely used fuel cell consists of a cathode, typically an ABO_3 ($LaMnO_3$) perovskite, an electrolyte (yttria-stabilized zirconia, YSZ) and an anode (Ni-YSZ cermet). The problem with this system is that it operates at high temperatures. Reduction of operating temperature to 550–700 °C is now the primary hurdle for the commercialization of SOFC. However a decrease in the operating temperature will decrease the cell performances of the conventional fuel cell, due to cathode overpotential. Hence, for ITSOFC applications, one seeks perovskites having high conductivity at low temperature.

*Corresponding author, e-mail: sdasgupta@cgcri.res.in

Lanthanum–strontium–cobalt ferrite (LSCF) is the best known mixed ionic electronic conductor used in intermediate temperature SOFC (ITSOFC) applications [1–3] and oxygen permeating membranes [4, 5]. A high electronic and ionic conductivity of LSCF over lanthanum–strontium manganite (LSM), makes it an attractive cathode material. The properties of their defect states have been examined extensively [6, 7]. The lower operating temperature of LSCF makes it possible to use cheaper interconnect materials and a wide range of sealing materials [8], thereby improving the reliability and long term stability of the fuel cell. However, it is reported that the insulating $SrZrO_3$ or the $LaZr_2O_7$ phase between LSCF and the YSZ electrolyte is formed during the sintering of the fuel cell. Therefore, buffers of ceria–gadolinium oxide (CGO), GDC or SDC were used as interlayers between the LSCF and the YSZ, in order to prevent Sr and La percolation [9].

Various methods of preparation of lanthanum ferrite (LF), lanthanum strontium ferrite (LSF) and lanthanum strontium cobalt ferrite (LSCF) have been reported. Preparation conditions are mainly responsible for morphological differences and the disparity in their electrochemical properties. Various synthesis routes comprise such methods as spray pyrolysis [10], coprecipitation method [11], citrate gelling method [12], modified citrate pyrolysis method [13], citrate method under effect of various pH [14], oxalate precipitation method [15] glycine nitrate technique [16, 17], sol gel route [18], mechanochemical method [19] and solution combustion using tetraformyltrisazine and oxalyl dihydride [20].

The present work describes the synthesis of $LaFeO_3$, $La_{(1-x)}Sr_xFeO_3$, (x = 0.3, 0.5) $La_{(1-x)}Sr_xCo_{0.2}Fe_{0.8}O_3$, ($x$ = 0.2, 0.4) perovskite cathode materials by the tartarate template method, where phase pure perovskites were formed at temperature as low as 550–700 °C. Particle size, surface area studies, microstructure characterization, sintering behaviour, electrical properties and thermal expansion tests were carried out with the synthesized powder.

2. Experimental

Syntheses. Stoichiometric amounts of $La(NO_3)_3 \cdot 6H_20$ and $Fe(NO_3)_3 \cdot 9H_2O$ dissolved in 2M nitric acid were placed in a beaker. Tartaric acid in 1:2 molar ratio with respect to metal nitrates was added to the mixture. The mixture was heated under constant stirring on a hot plate until all the liquid had evaporated. The resultant mass was calcined at temperatures from 550 °C to 700 °C to obtain phase pure perovskite materials. The yield was 94%. The syntheses of $La_{(1-x)}Sr_xFeO_3$ and $La_{(1-x)}Sr_xCo_{0.2}Fe_{0.8}O_3$, ($x$ ranging from 0.2 to 0.5) was carried out by the same procedure, using nitrates of respective metals and tartaric acid as the chelating agent. All the chemicals were of analytical grade. Deionized water was used throughout the synthesis.

Characterization of the materials. Thermogravimetric studies of the uncalcined powders were carried out using a TG analyser (Model: Shimadzu TGA 50) in air, un-

der the heating rate of 20 °C/min in an alumina crucible. The temperature range was between room temperature and 800 °C.

X-ray diffractometry studies were carried out with an X-ray diffractometer (Philips, PW 1710) using a monochromatic CuK_α radiation from 10° to 70° (2θ), in order to identify the phase and the crystal system. Crystallite size was determined based on Scherer's formula from the line broadening of the peak at around 32°. FTIR spectra were obtained using a Nicolet Model 5PC FTIR. A Sorpty 1750 surface area analyzer, based on the BET principle, was used to measure the specific surface area. The morphologies of the calcined powders and the microstructure of the fracture surfaces of the sintered samples were studied with a scanning electron microscope (model No. Leo: 430i).

The phase pure powders were ground and mixed with 1 wt. % of binder (poly (vinyl) butaryl acetate) compacted at 2 t pressure in a motor driven uniaxial hydraulic press, using a mould 10 mm in diameter. Green pellets thus obtained were sintered at 1100 °C and 1200 °C for 6 h. The densities of the sintered pellets were determined geometrically, as well as by immersion in kerosene and applying Archimedes principle.

The electronic conductivities of the sintered samples were measured in air by the four probe method at various temperatures. The samples for measurement of electronic conductivity were of rectangular shapes having dimensions 20 mm × 8 mm × 1.8 mm, fabricated exactly the same way as for sintering studies. Electroding was done with platinum wire, adhered to the surface by a coating of platinum paste, cured at 900 °C for 30 min. Electronic conductivity measurements were carried out in air at temperatures ranging from room temperature to 700 °C, or up to the saturation limit of the sample in a temperature controlled furnace.

Relative thermal expansion was measured in air, from room temperature to 800 °C, on samples of dimensions 25 mm × 8mm × 5mm sintered at 1200 °C. A dilatometer Netzsch Dil 402C model was used with Al_2O_3 as reference at the heating rate of 5 °C/min.

3. Results and discussion

3.1. Thermal analysis and FTIR studies

Figure 1 shows the comparative TGA plots of the prepared uncalcined precursors, i.e., $LaFeO_3$, $La_{(1-x)}Sr_xFeO_3$ and $La_{(1-x)}Sr_xCo_{0.2}Fe_{0.8}O_3$, by the tartarate route. Considerable weight loss was observed up to 400 °C followed by a slight weight loss in the 400–600 °C range. A negligible weight loss occurred between 600–650 °C.

The TG curves can be interpreted well based on FTIR studies (Fig. 2). A broad peak around 3440 cm^{-1} in the green sample is due to the stretching mode of the hydroxyl group of bound water molecules, which gradually diminishes as the calcination temperature is raised to 700 °C. The peak at 2337 cm^{-1} is due to ambient CO_2. The

broad peaks at around 1630 cm^{-1} and at 1385 cm^{-1} are due to carboxylate and nitrate groups, respectively.

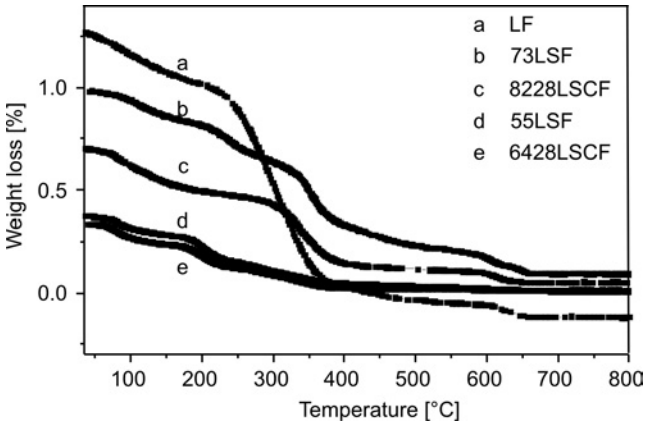

Fig. 1. TGA curves of $LaFeO_3$, $La_{(1-x)}Sr_xFeO_3$, and $La_{(1-x)}Sr_xCo_{0.2}Fe_{0.8}O_3$ precursors

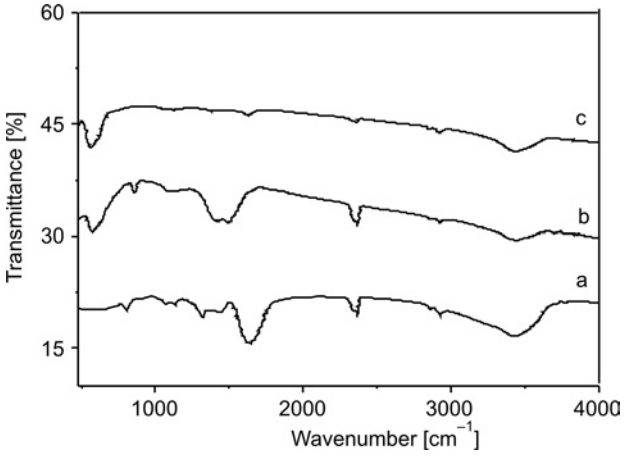

Fig. 2. FTIR spectra of $LaFeO_3$ uncalcined (a) and calcined at 550 °C (b) and 700 °C (c)

The carboxylate peak vanishes at 550 °C, whereas a broad band appears between 1400 cm^{-1} and 1500 cm^{-1} due to the bending vibration mode of bound water molecules and the υ_3 mode of CO_3^{2-} ions which disappears when calcination occurs at 700 °C. The peaks at around 1070 cm^{-1} and 860 cm^{-1} are attributed to the υ_1 and υ_2 modes of CO_3^{2-} ions, respectively. When the sample is calcined at 700 °C, all these peaks disappear, leaving phase pure perovskite, which is highly consistent with our TGA and XRD data.

3.2. X-ray analysis

Figure 3 shows the X-ray diffraction patterns of $LaFeO_3$, calcined at various temperatures. The XRD pattern reveals that phase pure material is formed at ca. 550 °C. Results of the TG and IR analyses show that there are, still some impurity phases, which are not detectable by XRD.

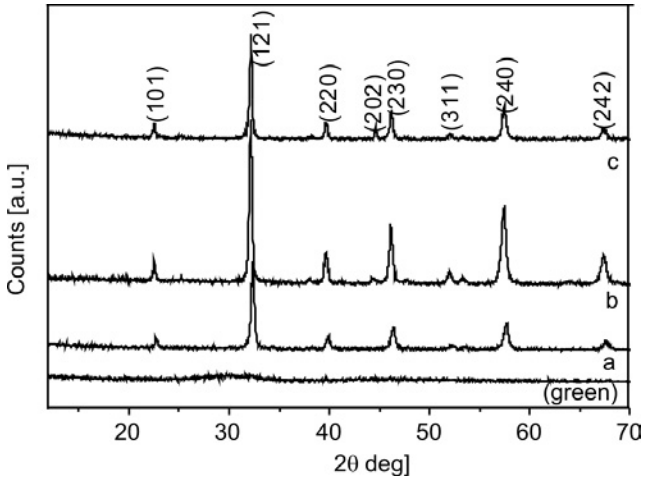

Fig. 3. XRD patterns of $LaFeO_3$ calcined at 550 °C (a), 600 °C (b) and 700 °C (c)

Since IR spectroscopy is a much more sensitive tool, it can only support the complete formation of phase pure material. Phase formation begins at 550 °C, and complete phase pure perovskite material was obtained on calcining the powder at 700 °C for 3 h. The line broadening decreased as the calcination temperature increased, as seen in the figure for the (121) plane of pure $LaFeO_3$. The primary particles were of nanosize dimensions, agglomerating during calcination. The average crystallite size calculated using Scherrer's formula was found to be ca. 45–50 nm.

Figure 4 shows the X-ray diffraction pattern of $La_{0.7}Sr_{0.3}FeO_3$ (73LSF) and $La_{0.8}Sr_{0.2}Co_{0.2}Fe_{0.8}O_3$ (8228LSCF) calcined at 700 °C. Traces of Co_3O_4 were found in $La_{0.8}Sr_{0.2}Co_{0.2}Fe_{0.8}O_3$, but they disappeared completely when calcining the sample at 800 °C [21].

The uniqueness of tartaric acid as a chelating agent in the synthesis of $BiFeO_3$ has been reported earlier. The formation of heteroatomic polynuclear complexes brings the metal atoms in close proximity with each other, which decays in the presence of nitric acid to give the product [22]. Our earlier work with oxalic acid [23] as a chelating agent in synthesizing $BiFeO_3$ reports the formation of transition metal ferrioxalate $Bi[Fe(ox)_3]$ intermediate which undergoes *in situ* decomposition by HNO_3, resulting in the formation of the product. The role of tartaric acid as a chelating agent in synthesis of $LaFeO_3$ probably consists in the formation of transition metal tartrato lanthanate(III) [24] precursor ($M[La(C_4H_4O_6)_3]\cdot xH_2O$).

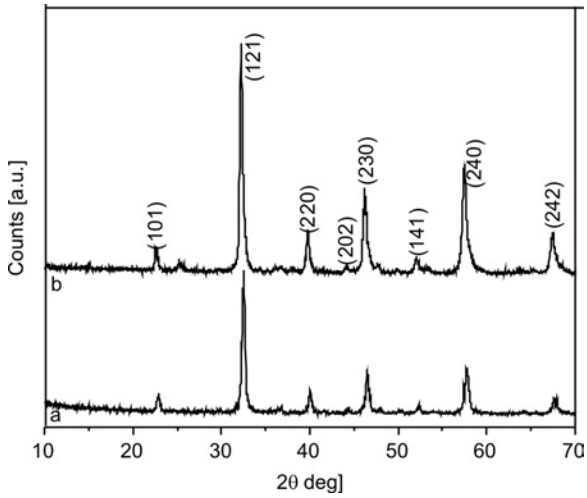

Fig. 4. XRD pattern of: a) $La_{0.7}Sr_{0.3}FeO_{3-x}$, b)$La_{0.8}Sr_{0.2}Co_{0.2}Fe_{0.8}O_3$ calcined at 700 °C

In this case $Fe[La(C_4H_4O_6)_3]\cdot 10H_2O$, like $La[La(C_4H_4O_6)_3]\cdot 10H_2O$ may be formed, as was observed by Deb [25] in the synthesis and thermolysis of lanthanum(III) tris tartrato lanthanate (III) decahydrate precursors. Here also, iron (III) tris tartrato lanthanate(III) decahydrate, $Fe[La(C_4H_4O_6)_3]\cdot 10H_2O$ formed by reaction with tartarate ligand, undergoes *in situ* decomposition, which occurs towards the end of the reaction, when the HNO_3 concentration is high enough to oxidize the precursor, resulting in the generation of NO_2, CO_2 and water vapour, along with the product.

3.3. Surface area analysis

The surface area of the phase pure powders was determined using the BET principle. The measured surface area of the synthesized powders was in the 14–20 m^2/g range (Table 1). $La_{0.5}Sr_{0.5}Fe_2O_3$ (55LSF) exhibits a maximum surface area of 19.10 m^2/g, which is much higher than the surface area of powder synthesized by the citrate method [26].

Table 1. Surface areas of various powders

Compound	Surface area [m^2/g]
73LSF	14.00
55LSF	19.10
8228LSCF	13.58
6428 LSCF	15.22

3.4. Morphology and microstructure analysis

Figure 5a shows the microstructure of $LaFeO_3$ powders calcined at 700 °C for 3 hs. The crystallite sizes are in good agreement with that obtained from XRD. Spherically shaped particles are seen to exhibit considerable agglomeration.

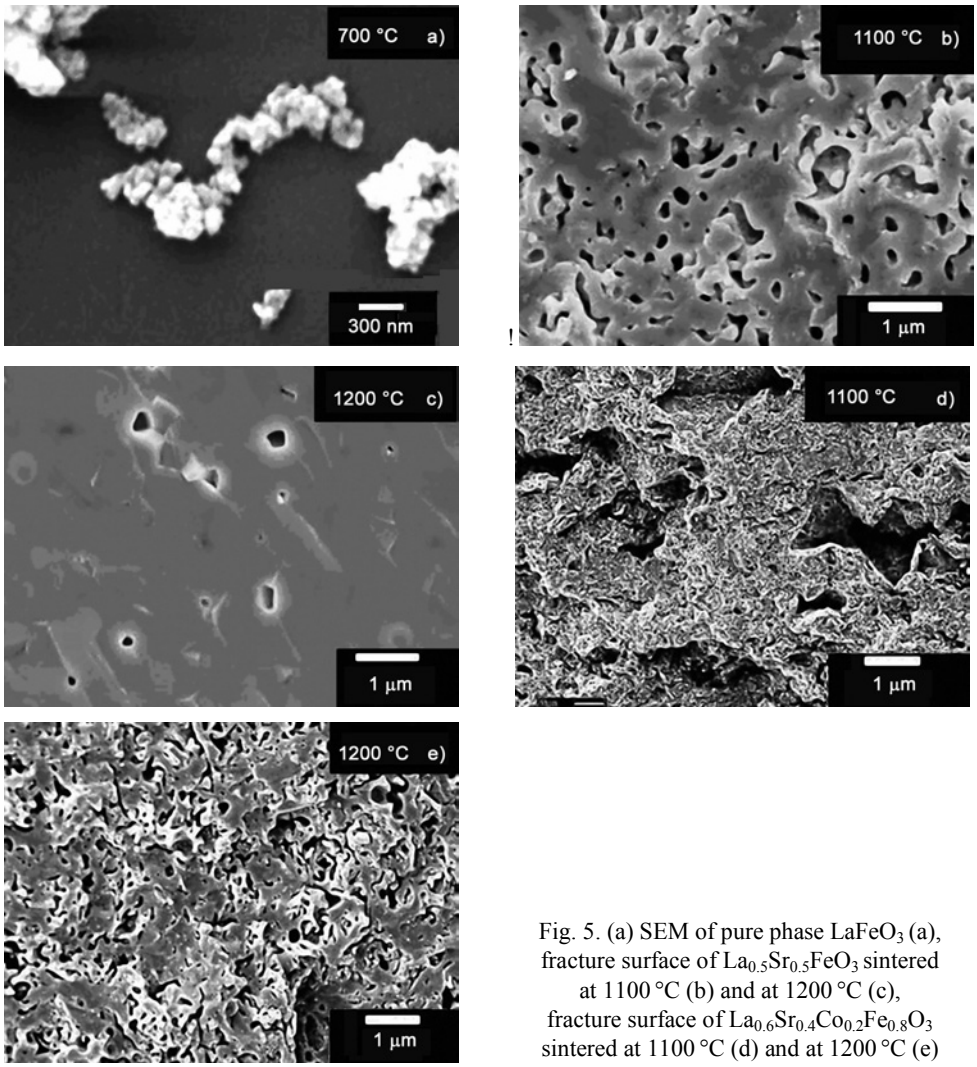

Fig. 5. (a) SEM of pure phase $LaFeO_3$ (a), fracture surface of $La_{0.5}Sr_{0.5}FeO_3$ sintered at 1100 °C (b) and at 1200 °C (c), fracture surface of $La_{0.6}Sr_{0.4}Co_{0.2}Fe_{0.8}O_3$ sintered at 1100 °C (d) and at 1200 °C (e)

Figures 5b–e show the microstructure of the fracture surface of $La_{0.5}Sr_{0.5}Fe_2O_3$ (55LSF) and $La_{0.6}Sr_{0.4}Co_{0.2}Fe_2O_3$ (6428LSCF) sintered at 1100 °C and 1200 °C. Porous and inhomogeneous structures are seen in samples sintered at 1100 °C, whereas a highly dense structure is seen in samples sintered at 1200 °C. Adjusting the sintering temperature improves the microstructure and thereby improves the electronic conductivity.

3.5. Conductivity studies

Electronic conductivities were measured by the four probe DC principle [27]. Figures 6 and 7 show the dependences of the logarithm of electrical conductivity on the reciprocal of temperature ($\lg\sigma(1/T)$) for the synthesized powders sintered at 1100 °C and 1200 °C.

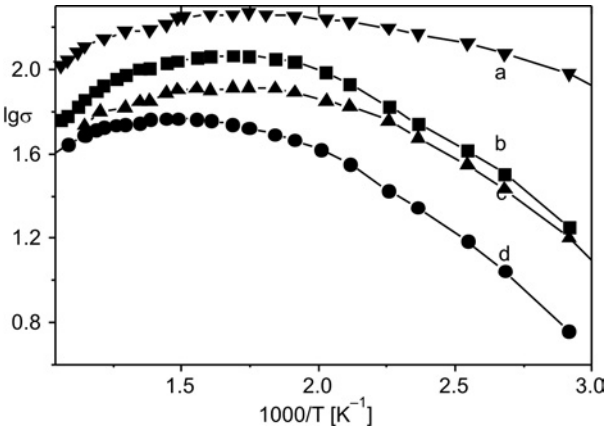

Fig. 6. Dependences of $\lg\sigma$ on the reciprocal temperature of:
a) $La_{0.6}Sr_{0.4}Co_{0.2}Fe_{0.8}O_3$ (6428LSCF), b) $La_{0.5}Sr_{0.}5Fe_2O_3$ (55LSF),
c) $La_{0.8}Sr_{0.2}Co_{0.2}Fe_{0.8}O_3$ (8228LSCF), d) $La_{0.7}Sr_{0.3}FeO_3$ (73LSF)
sintered at 1100 °C in air

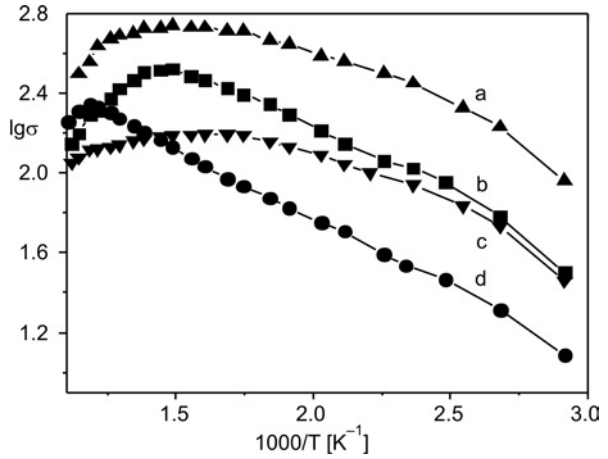

Fig. 7. Dependences of $\lg\sigma$ on the reciprocal temperature of:
a) $La_{0.6}Sr_{0.4}Co_{0.2}Fe_{0.8}O_3$ (6428LSCF), b) $La_{0.5}Sr_{0.}5Fe_2O_3$ (55LSF),
c) $La_{0.7}Sr_{0.3}FeO_3$ (73LSF), d) $La_{0.8}Sr_{0.2}Co_{0.2}Fe_{0.8}O_3$ (8228LSCF) sintered at 1200 °C in air

As expected, the figures show that the conductivity is highly dependent on the sintering temperature, i.e, the conductivity increases with the increase in the sintering

temperature. The conductivity of most of the powders is found to increase with temperature, up to 400 °C and in some cases up to 500 °C. A steep decline in conductivity is observed for the samples treated above these temperatures, suggesting that a semiconductor-to-insulator transition occurs. In all cases, the conductivity increased 2- or 3-fold with the increase in the sintering temperature, e.g. the conductivities at 500 °C of 8228LSCF sintered at 1100 °C and at 1200 °C are 65.74 S/cm and 187.08 S/cm, respectively. Increasing the sintering temperature significantly improves the conductivity, which is due to the better densification at higher temperatures. 55LSF shows a maximum conductivity at 420 °C of 355 S/cm and 263 S/cm at 500 °C. Bongio et al. [28] reported a maximum conductivity of 352 S/cm at 550 °C for the same composition. The authors have therefore achieved comparable conductivity at a much lower temperature, which may be due to reduced crystallite sizes and better sinterability.

3.6. Activation energy

The activation energies of the sintered samples were calculated from the slopes of $\log(\sigma T)$ vs. T^{-1} plots, according to the Arrhenius equation:

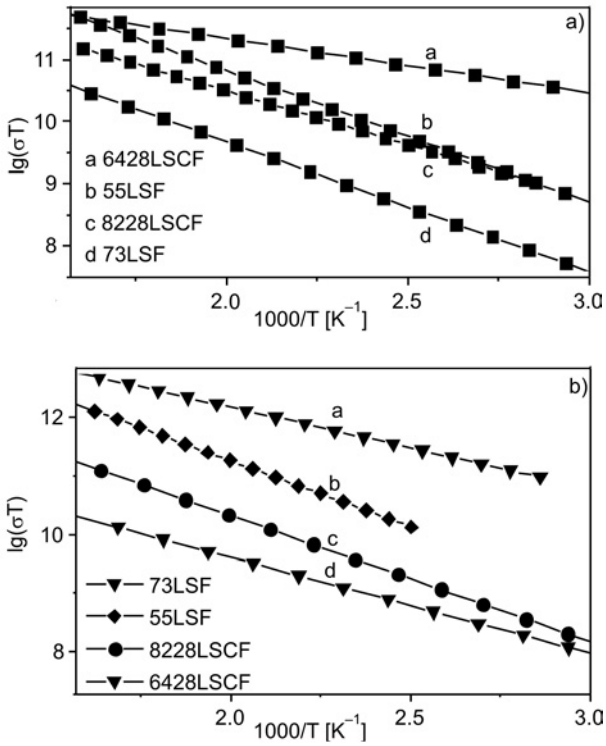

Fig. 8. Activation energy for samples sintered at 1100 °C (a) and at 1200 °C (b)

$$\sigma = \frac{A}{kT}\exp\left(-\frac{E_a}{kT}\right)$$

where A is a constant, E_a is the activation energy, k is the Boltzmann constant, T is the absolute temperature.

Figures 8a, b show the linear plots of $\log(\sigma T)$ vs $1000/T$ for the temperature ranges where the conductivity increased with temperature for the samples sintered at 1100 °C and 1200 °C, respectively [29]. The activation energies range from 0.025 eV to 0.194 eV in $La_{(1-x)}Sr_xFeO_3$, which is in close agreement with the value reported by Omata et al. [30]. As expected, the activation energy becomes lower if the strontium content is increased. In the case of $La_{(1-x)}Sr_xCo_{0.2}Fe_{0.8}O_3$, the E_a value ranges between 0.075 eV and 0.185 eV, which is in close agreement with the data reported by Tai et al. [31].

3.7. Measurement of the thermal expansion coefficients (TEC)

The cathode material should have matched TEC and sufficient stability with the electrolyte to avoid thermal mismatching and percolation. Figure 9 shows the TEC graphs of the materials (sintered at 1200 °C) for temperatures ranging between room temperature and 800 °C.

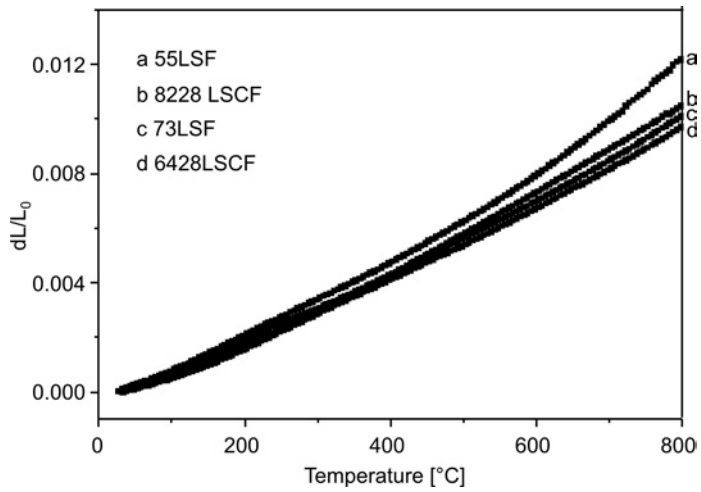

Fig. 9. Temperature dependences of the thermal expansion coefficients of Sr and Co doped samples

The TEC of the synthesized powders does not match with conventional 8% YSZ electrolyte (α_{YSZ} = 10.8×510^{-6} K^{-1} for 30–1000 °C) which is normally used in the SOFC. The TEC of 6428LSCF is found to be in well agreement with that for the CGO layer (α = 12.671×10^{-6} K^{-1}). Therefore a buffer layer of CGO has to be applied between LSCF and YSZ for matching TEC which will also prevent the percolation of Sr

and La to the YSZ layer hindering the formation of $SrZrO_3$ and $La_2Zr_2O_7$. 73LSF and 8228LSCF are also close matches for CGO interlayer as their TEC values are in accordance.

4. Conclusion

A low temperature method was used for the synthesis of nanosized lanthanum ferrite and doped lanthanum ferrite materials by simple solution evaporation technique. The synthesized materials were characterized and sintered at various temperatures, in order to study their suitability for ITSOFC applications. High conductivities of the synthesized materials at lower temperatures show that they are best suited as cathode materials for intermediate temperature SOFC applications. The activation energy can be reduced from 0.180 eV to 0.075 eV by appropriate increase of the strontium content. The TECs of the synthesized materials have a similar profile to the TEC of the CGO interlayer.

Acknowledgement

One of the authors (S. G.) is grateful to the CSIR for awarding SRF (No. 31/15(58)/06-EMR-I). Thanks are due to Dr R. N. Basu for providing the laboratory facilities. Thanks are also due to the Director CGCRI, for allowing us to publish this paper.

References

[1] KIM W.H., SONG H.S., MOON J., LEE H.W., Solid State Ionics, 177 (2006), 35.
[2] QIANG F., NING S.K., ZHANG N.Q, ZHU X.D., SHI X.D., LE R., ZHOU D.R., J. Power Sources, 168 (2007), 338.
[3] QIU L., ICHIKAWA T., HIRANO A., IMANISHI N., TAKEDA Y., Solid State Ionics, 158 (2003), 55.
[4] LEE S., LEE K.S., WOO S.K., KIM J.W., ISHIHARA T., KIM D.K., Solid State Ionics, 158 (2003), 287.
[5] TERAOKAY., HONBE Y., ISHII J., FURUKAWA H., MORIGUCHI I., Solid State Ionics, 152 (2002), 681.
[6] MISUZAKI J., SASAMOTO T., CANNON W.R., BOWEN H.K., J. Am. Ceram. Soc., 66 (1983), 247.
[7] BUCHER E., SITTE W., Solid State Ionics, 173 (2004), 23.
[8] JIANG S.P., ZHNAG J.P., ZHENG X.G., J. Eur. Ceram. Soc., 22 (2002), 361.
[9] MAI A., HANNAPPEL V.A.C., UHLENBRUCK S., TIETZ F., STOVER D., Solid State Ionics, 176 (2005), 1341.
[10] HOLTAPPELS P., VOGT U., SCHINDLER H., GUT B., 5th European Solid Oxide Fuel Cell Forum, J. Huijismans (Ed.), Lucerne, Switzeland (2002), pp. 103–107.
[11] ZENG Y., LIN Y.S., SWARTZ S.L., J. Membrane Sci., 150 (1998), 87.
[12] DUOY A., Int. J. Inorg. Mater., 3 (2001), 699.
[13] SFEIR J., VAUCHER S., HOLTAPPELS P., VOGT U., SCHINDLER H.J., HERLE J.V., SUVOROVA E., BUFFAT P., PERRET D., XANTHOPOLOUS N., BUCHELI O., J. Eur. Ceram. Soc., 25 (2005), 1991.
[14] LI S., XU N., J. Mater. Sci. Lett., 21 (2002), 245.
[15] WU Z., ZHOU W., JIN W., XU N., Materials, Interf. Elctrochem. Phen., 52 (2005), 769.
[16] RALPH J.M., ROSSIGNOL C., KUMAR R., J. Electrochem. Soc., 150 (2003), 1518.
[17] LEI Z., ZHU Q., ZHAO L., J. Power Sources, 161 (2006), 1169.
[18] GE L., ZHOU W., RAN R., SHAO Z., LIU S., J. Alloys Comp., 450 (2008), 338.

[19] YAKOVLEVA I.S., ISUPOVA L.A., TSYBULYA S.V., CHERNYSH A.V., BOLDYREVA N.N., ALIKINA G.M., SADIKOV V.A., J. Mater. Sci., 39 (2004), 5517.
[20] SURESH K., PANCHAPAGESAN T.S., PATIL K.C., Solid State Ionics,, 126 (1999), 299.
[21] TIETZ F., RAJ I.A., ZAHID M., STOVER D., Solid State Ionics, 177 (2006), 1753.
[22] GHOSH S., DASGUPTA S., SEN A., MAITI H.S., J. Am. Ceram. Soc., 88 (2005), 1349.
[23] GHOSH S., DASGUPTA S., SEN A., MAITI H.S., Mater. Res. Bull., 40 (2005), 2073.
[24] DEB N., J. Anal. App. Pyrolysis, online availability 27.03.2008.
[25] DEB N., J. Thermal An. Calorim., 78 (2004), 227.
[26] MURATA K., FUKUI T, ABE H., NAITO M., NOGI K., J. Power Sources, 145 (2005), 257.
[27] RIETVELD G., KOIJMANS C.V., HENDERSON L.C.A., HALL M.J., HARMON S., WARNECKE P., SCHUMACHER B., IEEE Trans. Inst. Meas., 52 (2003), 449.
[28] BONGIO E.V., BLACK H., RASZEWSKI F.C., EDWARDS D., MCCONVILLE C.J., AMARAKOON V.R.W., J. Electroceram., 14 (2005), 193.
[29] KOSTOGLOUDIS G.C., FTIKOS C., Solid State Ionics, 126 (1999), 143.
[30] OMATA T., IKAWA H., FIJITSU S., UEDA N., HOSONA H., KAWAZOE H., Solid State Com., 97 (1996), 411.
[31] TAI L.W., NASRSLLAH M.M., ANDERSON H.U., SPARLIN D.M., SEHLIN S.R., Solid State Ionics, 76 (1995), 259.

Received 2 December 2008
Revised 9 February 2009

Materials Science-Poland, *Vol. 28*, *No. 2*, *2010*

Electrochemical studies on metal-hexacyanocobaltate(III) thin solid films in aqueous electrolytes

KASEM K. KASEM*, D. HANNINGER, A. CROXFORD, F. PHETTEPLACE

Department of Nat. Info. Math. Sciences, Indiana University Kokomo, Kokomo, IN, 46904, USA

Electrochemical behaviour of thin films of potassium/metal hexacyanocobaltate(III) (KMHCCo or $KM_{x-1}[Co(CN)_6]_y$ where M = Co, Fe, or Ru, in terms of reduction of small oxoanions was investigated. Glassy carbon electrodes modified with electrochemically prepared KMHCCo were used as the solid phase in the heterogeneous solid–liquid charge transfer process. The redox behaviours of the counter central ions of KMHCCo have been investigated in aqueous electrolytes using dynamic voltammetric techniques, and electrochemical impedance spectroscopy. The effect of supporting electrolyte components on the electrochemical behaviour was also investigated. Evidences for electrocatalytic capabilities for oxidation of glucose and for the reduction of BrO_3^- and IO_3^- were recorded.

Keywords: *hexacyanocobaltate; electocatalysis; modified electrode; micropores; thin film*

1. Introduction

The attention of many researchers [1–14] has been focused on the special properties of polynuclear hexacyanometalates (HCM) such as the possibility of forming solid films of conductor phases or semiconductor phases; simplicity of manipulation of structures; occurrence of multi-redox centres; magnetic and electrochromic behaviours and their resemblance to zeolitic materials. In particular, in electrocatalysis, one can see how it is possible to make full use of these properties in applications [15–19], especially in electrochromic [20], and reversibility modelling [21]. The combination of more than one HCM, to form multilayered assemblies of these compounds, has been found to have applications in sensor fabrication [22], display technologies [23], solid state batteries [24], chemical precipitation of radioactive caesium from waste solutions [25], and hydrogen storage [26], to name but a few. Very limited studies have been done on metal hexacyanocobaltate polynuclear solid films. The paper reports on the electrochemical behaviour of KMHCCo thin solid films having microporous struc-

*Corresponding author, e-mail: kkasem@iuk.edu

ture prepared using an electrochemical technique. The redox behaviour of the counter cations and those of the central atoms in $[Co(CN)_6]^{3-}$ in various supporting electrolytes was also studied. The question of whether these assemblies improve catalytic activity on the electrode surface is also explored.

2. Experimental

Materials. Reagent grade $K_3[Co(CN)_6]$, $FeCl_3$, $RuCl_3$, KCl and $KClO_4$, were obtained from Aldrich Chemical Co. All other reagents were of at least reagent grade and were used without further purification.

Instruments and methods. An electrochemical cell of three conventional electrode types in a small vial container was used. The reference electrode was a Ag/AgCl (saturated KCl) with the half-cell potential of –45 mV vs. saturated calomel electrode (SCE), the counter (auxiliary) electrode was a platinum (Pt) wire, and the working electrode was glassy carbon (GC, 0.071 cm^2 surface area, Bioanalytical Systems). The working electrode was cleaned by polishing with 1 μm α-Alumna paste and rinsed with water and acetone prior to use. A BAS 100B electrochemical analyzer (Bioanalytical Co.) was used to perform the electrochemical studies.

Electrochemical impedance spectroscopy (EIS) studies were carried out using a BAS impedance module. Faradic impedance measurements were carried out within a frequency range of 0.1 mHz to 1 kHz. The current response was monitored by a current transducer whose sensitivity range was automatically adjusted for each frequency range examined. The data were analyzed with a Fourier transform algorithm.

Films of MHCCO (M = Co, Fe, Ru) were electrodeposited on glassy carbon electrode (GCE) surfaces by repetitive potential cycling of a glassy carbon (GC) disk electrode between –0.20 and 1.0 V vs. Ag/AgCl, in freshly prepared aqueous solutions containing equi 5 mM of $K_3[Co(CN)_6]2H_2O$, and $FeCl_3$, or $RuCl_3$, or $CoCl_2$ and 0.1 M KCl (pH 2). Unless otherwise stated, scans were carried out at a sweep rate of 0.2 $V{\cdot}s^{-1}$. The electrodes were then rinsed thoroughly and transferred to a redox free electrolyte where their electrochemical responses were examined.

3. Results and discussion

3.1. Redox behaviour of FEHCCO films. Background

In hexacyanometalates (HCM) of the general formula $M_A^X[M_B^Y(CN)_6]_Z$, M_B^Y is the central atom, while M_A^X is the fixed counter cation. Both M_A^X and M_B^Y are generally transition metals. The reduction of the fixed counter cation of these compounds can take place via electron/cation addition, according to the following equation:

$$M_A^X\left[M_B^Y(CN)_6\right]_Z + e + M^+ \longrightarrow MM_A^X\left[M_B^Y(CN)_6\right]_Z \quad (1)$$

Oxidation of the central atom can take place by electron loss followed by anion addition:

$$M_A^X\left[M_B^Y(CN)_6\right]_Z - e + X^- \longrightarrow M_A^X\left[M_B^{Y+1}(CN)_6\right]_Z \quad (2)$$

Reduction of the counter cation, according to Eq. (1), produces the reduced form, while oxidation of the central atom in the anion complex, according to Eq. (2), produces the oxidized form. The colour of the reduced or the oxidized forms depends on M_A^X and M_B^Y. The *CV* for HCM may show redox waves corresponding to the reduction of the counter ion and oxidation of the central atom. In some cases, the redox waves (if any) of the excess counter ions occupying interstitial sites of the octahedrally shaped metal cyanide complex may be detectable. Previous studies [8, 24] indicated that the redox wave at a lower positive potential corresponds to the reduction of the counter ion, while that at a higher positive potential it represents the oxidation of the central atom. Some of these studies [10] indicated that the counter ion affects the formal potential of the central atom.

3.2. Electrodeposition of $KCo_{x-1}[Co(CN)_6]_y$

Repetitive cycling of a glassy carbon (GC) disk electrode potential between –0.20 and 1.0 V vs. Ag/AgCl in aqueous solutions containing equi 5 mM of $K_3[Co(CN)_6]\cdot 2H_2O$, $CoCl_2$ and 0.1 M KCl (pH 2) is shown in Fig. 1a. The growth of the redox wave with successive scanning is an evidence for the buildup of the $KCo_{x-1}[Co(CN)_6]_y$ film. The redox behaviour of the deposited film was investigated by cycling the potential of the modified electrode in redox-free electrolytes. The results are shown in Fig. 1b. To understand the *CV* behaviour of the electrode we consider the effects of the electrolytes used in this study. The dissociation of the counter Co^{2+} ions from $KCo_{x-1}[Co(CN)_6]_y$ would result in formation of $[Co(H_2O)_6]^{2+}$ in neutral $KClO_4$ or $CoCl_4^{2-}$ in KCl solution. In Figure 1b, the *CV* characteristics of $KCo_{x-1}[Co(CN)_6]_y$ are shown in neutral KCl electrolyte, in KCl at pH = 2, and in $KClO_4$. The redox behaviour of either $CoCl_4^{2-}$ or $[Co(H_2O)_6]^{2+}$ cannot be identified under the adopted experimental conditions, or within the studied potential range. This suggests that the observed redox waves in Fig. 1b are due to the central Co atom in $[Co(CN)_6]^{3-}$. It can be noticed that increasing the acidity not only results in an upward shift in the formal potential by about 100 mV, but it also lowers both the cathodic and anodic redox currents. This can be attributed to the large ionic size of H_3O^+ (900 pm) in acidic electrolyte. On the other hand, in Fig. 1b a decrease of the redox wave formal potential in of $KCo_{x-1}[Co(CN)_6]_y$ in $KClO_4$ electrolyte approximately by 100 mV, with an increase of the cathodic and anodic currents. The lower reduction potential and larger current than that reported in KCl electrolytes suggests that the electron transfer process is thermodynamically and kinetically favoured in aqueous $KClO_4$.

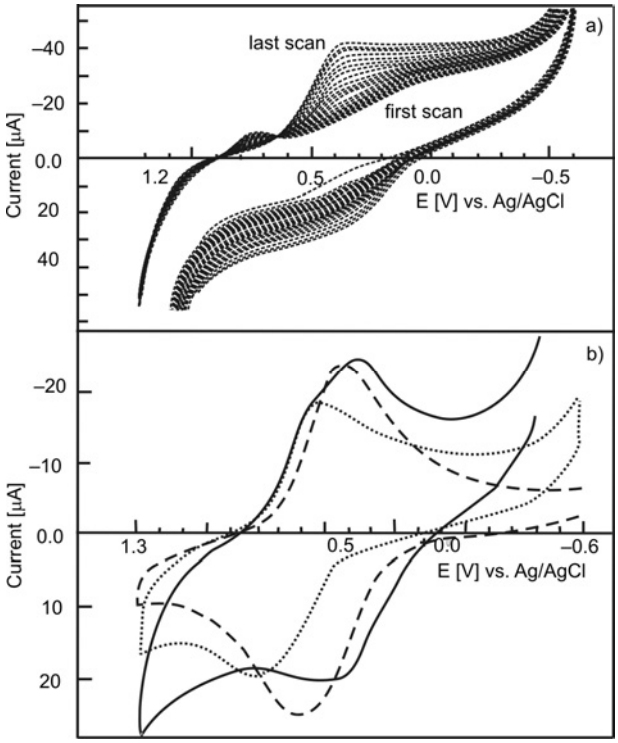

Fig. 1. Repetitive *CV* characteristics at 0.2 $V \cdot s^{-1}$ of GCE a) in equi 5 mM of $K_3[Co(CN)_6]$ and $CoCl_2$ in 0.1 M KCl/HCl (pH = 2), scan started at –0.20 V vs. Ag/AgCl, b) modified with $KCo_x[Co(CN)_6]_y$ in 0.1 M KCl (dashed line), 0.1 M KCl/HCl (pH = 2) (dotted line), and $KClO_4$ (solid line)

3.3. Electrodeposition of $KFe_{x-1}Ru[Co(CN)_6]_y$

Thin films of $KM[Co(CN)_6]_y$ where M = Fe or Ru were deposited, following the same procedure used in the electrodeposition of $KCo_{x-1}[Co(CN)_6]_y$. Figure 2 displays the *CV*s recorded for GCE in 0.1 M KCl/HCl (pH = 2) containing $K_3[Co(CN)_6]$, $FeCl_3$, (Fig. 2a), and $K_3[Co(CN)_6]$, $FeCl_3$, $RuCl_3$ (Fig. 2b). The film deposited with $FeCl_3$ gives poor stability and adherence to the surface of GCE. On the other hand, when both $FeCl_3$ and $RuCl_3$ are used (Fig. 2b), a steady growth of a robust film is observed, as indicated by the symmetric rise of both cathodic and anodic peak currents. This is not the case for the *CV* displayed in Fig. 2a. The obvious effect of $RuCl_3$ can be clearly identified from the *CV*s displayed in Fig. 3. This figure shows that the solid film of $KFe_{x-1}[Co(CN)_6]_y$ gives an ill defined *CV* in supporting electrolyte only (Fig. 3a) with a large capacitive current, while $KFe_xRu[Co(CN)_6]_y$ (Fig. 3b) shows three surface redox waves with formal potentials $E_f^{\circ\prime}$ at 0.2 V, 0.85 V and 1.230 V with a very low capacitive current. These well defined surface redox waves displayed in Fig. 3b along with the film stability support the reported studies [1, 12] that ruthenium provides a stability factor to the polynuclear hexacyano metal films.

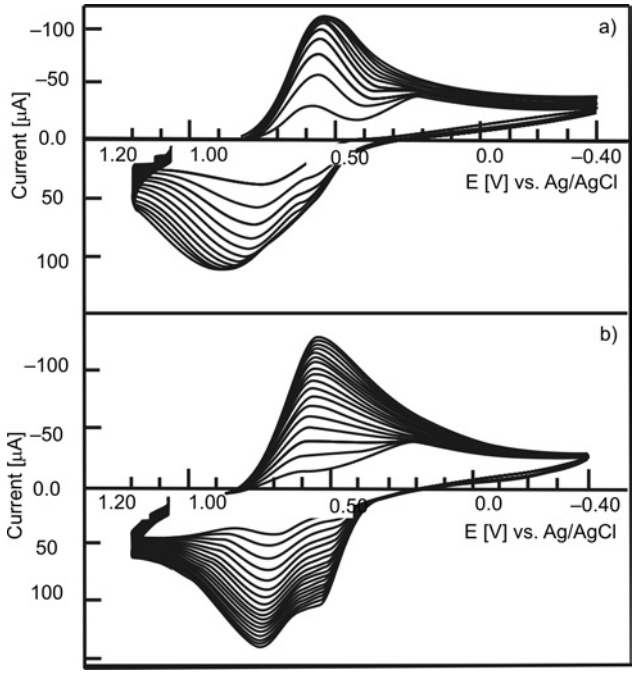

Fig. 2. Repetitive *CV* characteristics at 0.2 V·s^{-1} of GCE in equi 5mM of each of: a) $K_3[Co(CN)_6]$,$FeCl_3$, $RuCl_3$, b) $K_3[Co(CN)_6]$, $FeCl_3$, in 0.1 M KCl/HCl (pH = 2). Scan started at –0.20 V vs. Ag/AgCl

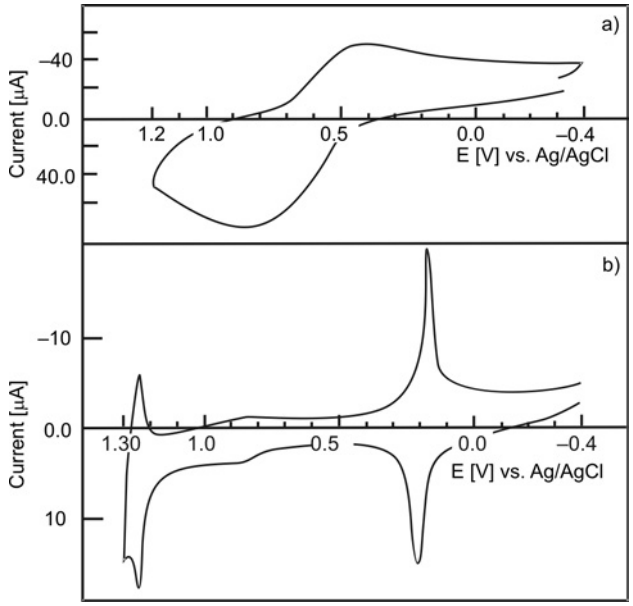

Fig. 3. *CV* characteristics in 0.1 M $KClO_4$/HCl (pH = 2) at 0.2 V·s^{-1} of GCE modified with: a) $KFe_x[Co(CN)_6]$, b) $KRu_xFe_y[Co(CN)_6]$

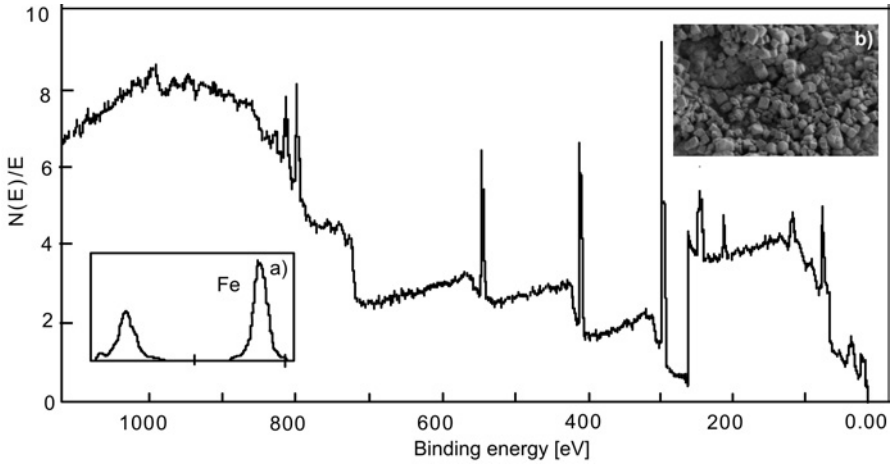

Fig. 4. XPS for the thin solid film of $KRu_xFe_y[Co(CN)_6]_z$.
Insets: a) Fe peaks, b) SEM of the deposited film

Figure 4 shows the **X**-ray photoelectron **s**pectrum (XPS) for $KFe_xRu[Co(CN)_6]_y$ film, the inset a) shows Fe peaks while Co peaks are clearly indentified, Ru 3d is being obscured by C 1s, and Ru 3p are covered by noise between 400 and 500 eV. Inset 4b is the scanning electron micrograph of the film $KFe_xRu[Co(CN)_6]_y$ deposited on GCE film. Although spectroscopic evidence of Ru with Fe in hexacyanocobaltate film is not as strong as the electrochemical evidence displayed in Fig. 3b, both are supporting evidences of deposition of $KFe_x Ru[Co(CN)_6]$. The redox wave with $E_f^{\circ\prime}$ at 1.235 V vs. Ag/AgCl is a strong indication of Ru existence in the film. The redox wave at 0.85 V, shown in Fig. 3, indicates that the formation of higher oxidation states of ruthenium (oxoruthenium) does not depend on the position of Ru atoms in the network of the polymer. Furthermore, studies show that the redox waves are independent of each other and are not affected by oxygen reduction (Fig. 2b).

3.4. Effect of the supporting electrolyte on the redox potentials of MHCCO

3.4.1. Cation effect

The influence of cations on the electrochemical behaviour of MHCCo was investigated by cycling the potential of GCE modified with $KFe_x Ru[Co(CN)_6]_y$ at 0.2 $V \cdot s^{-1}$ in 0.1 M $KClO_4$, 0.1 M $NaClO_4$, and 0.1 M $LiClO_4$. The results are shown in Fig. 5a. Similar studies were performed on CoHCCo film in 0.1 M KCl, 0.1 M $MgCl_2$**,** 0.1 M $BaCl_2$ or in 0.1 M $AlCl_3$ (Fig. 5b).

Reaction (1) indicates that the reduction process of the counter metal involves gaining electron/s and the addition of a supporting electrolyte cation. The change in the shape of the redox wave and potential can be used as an indicator for the cation effect. Recalling that the hydrated ionic sizes (in pm) are: $H_3O^+ - 900$, $Li^+ - 600$, Na^+

– 450, K^+ – 300, Mg^{2+} – 800, Ba^{2+} – 500, and Al^{3+} – 900. Replacing K^+ with a larger size cation leads to sluggish electron transfer and poor or ill defined redox peaks. This can be noticed in Fig. 5a, as the peak current of the redox waves with $E_f^{\circ\prime}$ at 0.180 V and that at 1.235 V decreases in the order $Li^+ > Na^+ > K^+$. On the other hand, the effects of multivalent cations such as Mg^{2+}, Ba^{2+}, and Al^{3+} on the redox wave of $[Co(CN)_6]^{3-}$ in $KCo_x[Co(CN)_6]_y$ were consistent with their ionic sizes, and were similar to that observed for monovalent cations.

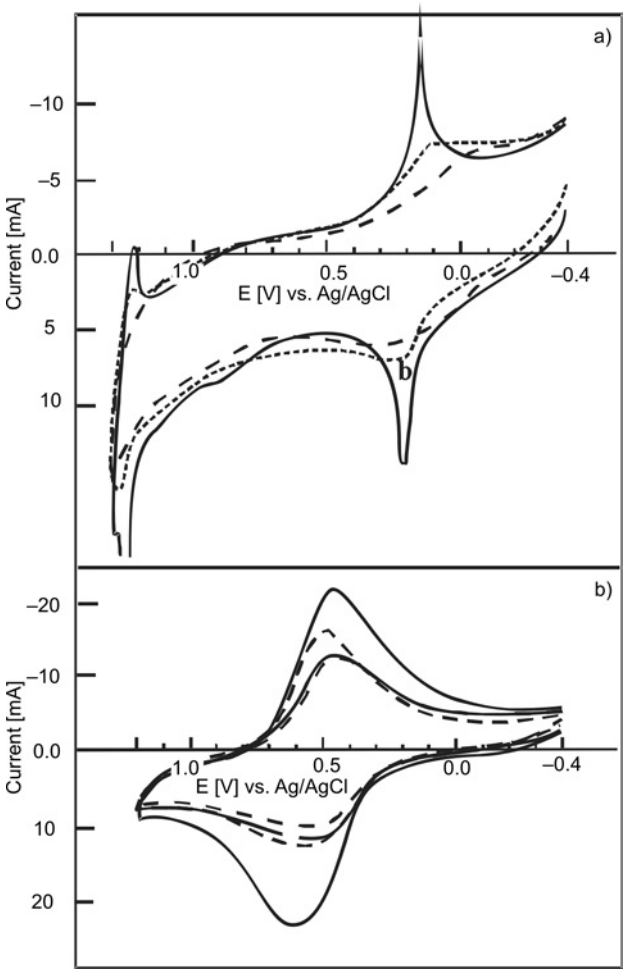

Fig. 5. *CV* characteristics at 0.2 $V \cdot s^{-1}$ of GCE modified with a) RuFeHCCo in: 0.1 M $KClO_4$ (solid line), 0.1 M $NaClO_4$ (dashed line), c) 0.1 M $LiClO_4$ (dotted line), b) $KCo_x[Co(CN)_6]_y$ in: 0.1 M KCl (thick solid line), 0.1 M $MgCl_2$ (thick dashed line), 0.1 M $BaCl_2$ solid line), 0.1 M $AlCl_3$ (dashed line)

The results displayed in Fig. 5b, illustrates such an effect. However, Ba^{2+} shows inconsistent effect with its ionic size. Such behaviour in the presence of barium can be

explained by the fact that Ba^{2+} can make a contact-pair with $[Co(CN)_6]^{3-}$ with the displacement of some of the water molecules from its hydrous complex. This contact-ion pair adopts an inner sphere mechanism during the charge transfer process. This phenomenon has been studied [27] with $[Fe(CN)_6]^{3-}$. Magnesium cations cannot form contact pairs but rather solvent separate pairs with hexacyanometalate unit without displacement any of any their hydrous complex water molecules. This keeps the outer sphere charge transfer mechanism unchanged. It is worthwhile mentioning that hexacyanocobaltate is very selective to some alkali metals ions such as Cs. This selectivity has its applications in chemical precipitation of radioactive caesium from waste solutions with iron(II) hexacyanocobaltate(III) and triphenylcyanoborate [25].

3.4.2. Anion effect

Reaction (2) involves the incorporation of supporting electrolyte anions. Studies show that changing the supporting electrolyte from KCl to $KClO_4$ does not cause a tangible difference in the formal redox potential (Fig. 1b). Such behaviour is anticipated, since there is no large difference in the hydrodynamic radii of Cl^- and ClO_4^- ions as they are 300 and 350 pm, respectively. Such results indicate that the anion size has little or no effect on reaction (2).

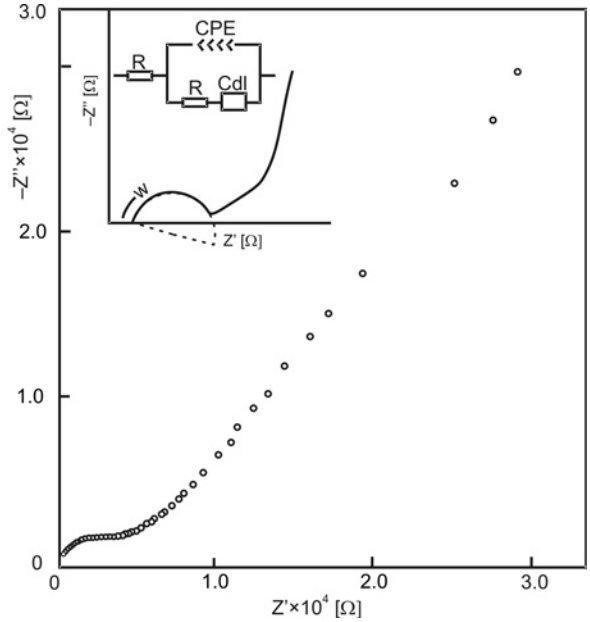

Fig. 6. Nyquest plot for GCE modified with $RuFe_x[Co(CN)_6]_3$ at 0.150 V vs. Ag/AgCl in 0.1 M $KClO_4$

In Figure 6, the Nyquest plot is shown for GCE modified with $RuFe_x[Co(CN)_6]_3$ at 0.150 V vs. Ag/AgCl in 0.1 M $KClO_4$. A case of overlapping kinetic/diffusional controlled regions of impedance behaviour can be noticed. At high frequencies, $\omega > 50$, an

ill-defined semicircular plot was obtained, while at very low frequencies, $1 < \omega < 0.01$, the impedance plot reflected a diffusional control. When measurements were extended to a very small ω (0.001 Hz), an indication of charge saturation behaviour was observed, however, Fig. 6 also can fit the modified Randles-type equivalent circuit with constant phase element (CPE), which acts as a capacitor. The permeability of the deposited film to aqueous K^+, which was confirmed by *CV* studies, indicates the porous nature of this film. This porosity is further confirmation for the equivalent circuit type of this electrochemical system.

3.5. Catalytic behaviour of K Fe_x Ru[Co(CN)$_6$]$_y$

Thin films of KFe_x Ru[Co(CN)$_6$]$_y$ on the surface of GCE exhibited some electrocatalytic activities towards the reduction of small oxoanions such as bromates and chlorates, and the oxidation of glucose.

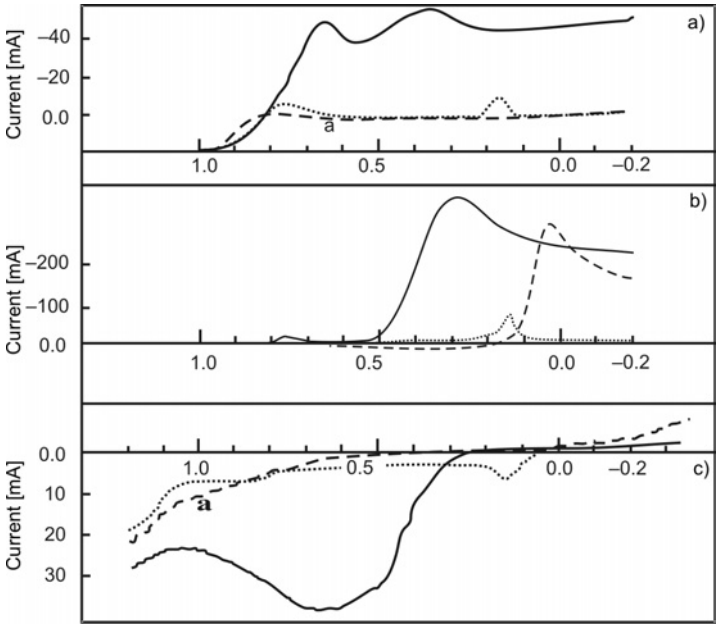

Fig. 7. Linear sweep voltammetry at 0.02 V·s^{-1} of: a) native GCE in KCl/HCl (pH = 2) containing 0.05M $KBrO_3$ (dashed line), GCE modified with RuFeHCCo in KCl/HCl (pH = 2) (dotted line) and GCE modified with RuFeHCCo in KCl/HCl (pH = 2) containing 0.05M $KBrO_3$ (solid line); b) native GCE in KCl/HCl (pH = 2) containing 0.05M $KClO_3$ (dashed line), GCE modified with RuFeHCCo in KCl/HCl (pH = 2) (dotted line) and c) GCE modified with RuFeHCCo in KCl/HCl (pH = 2) containing 0.05M $KClO_3$ (solid line); c) native GCE in KCl/HCl (pH = 2) containing 0.05 M glucose (dashed line), GCE modified with RuFeHCCo in KCl/HCl (pH = 2) (dotted line), GCE modified with RuFeHCCo in KCl/HCl (pH = 2) containing 0.05M glucose (solid line)

Evidence for such catalytic behaviour can be noticed in the linear scan voltammetry obtained in selected electrolytes. Figure 7a (solid line) shows a great increase in

the cathodic current starting at 0.815 V in the presence of BrO_3^-, thereby indicating the catalytic activities of the hexacyanometalate films. Similar results are shown in Fig. 7b (solid line) in the presence of ClO_3^-. The catalytic reduction of chlorates and bromates is evident by the rise of cathodic current at the reduction potential that is more positive than that recorded at native electrode. Figure 7 also shows that the reduction of bromates (Fig. 7a, solid line) took place at more positive potentials than those of chlorates (Fig. 7b, solid line). Such observations can be attributed to the electron configuration and hence the energy level diagram of the central chlorine and bromine atoms in the studied oxoanions. Reduction of Cl in ClO_3^- took place at 0.280 V while that for Br in BrO_3^- took place at 0.700 V. Br atom in bromate ion uses an expanded 4d orbital which occupies a larger volume with less orientation than that of 3d in the Cl atom of chlorate anions. Furthermore, the first of the two reduction peaks shown in Fig. 7a, solid line is due to the interaction between Br 4d and Ru 4d orbitals in the monooxoruthenium species incorporated in the film. The closer energy levels of these two atoms facilitate the charge transfer process. This is not the case with chlorates, due to the difference in Cl 3d and Ru 4d evident by oxoruthenium small cathodic peak shown in Fig. 7b at 0.780 V. The studies also show that hexacyanometalates catalyze the oxidation of glucose (Fig. 7c, solid line). This catalytic oxidation behaviour can be attributed to the inclusion of some oxoruthenium compound within the FEHCCO network structure [28] .

4. Conclusions

The electrochemical behaviour of KMHCCo thin solid films fabricated using electrochemical technique in aqueous electrolytes indicates only one redox wave for $KCo[Co(CN)_6]$, corresponding to the central Co atom in the $[Co(CN)_6]^{3-}$ anion . When Ru coexists among counter ions in the KMHCCo, the redox behaviour of the film shows multi one-electron *CV* waves. KMHCCo films show size-discrimination behaviour towards supporting electrolyte cations. Like other hexacyanometalates, KMHCCo posses catalytic activities towards both electro-oxidation of biologically active molecules such as glucose, and electro-reduction of some small oxoanions. Studies also demonstrated the possibility of seeding a variety of redox centres in hexacyanometalates inorganic polymers and manipulating these structures to perform a desired function now is possible.

Acknowledgements

Some authors (D. H., A. C., and F. P. are grateful for the support Undergraduate Research Summer Institute program at the Indiana University Kokomo.

References

[1] ROQUE J., REGUERA E., BALMASEDA J., RODRÍGUEZ-HERN J., REGUERA L., DEL CASTILLO L.F., Micropor. Mesopor. Mater., 103 (2007), 57.

[2] DOSTAL A., KAUSCHKE G., REDDY S.J., F.SCHOLTZ J., J. Electroanal. Chem., 406 (1996),155.
[3] GAO Z., WANG G., LI P., ZHAO Z., Electrochim. Acta., 36 (1991), 147.
[4] NEFF V.D., J. Electrochem. Soc., 125 (1978), 886.
[5] KULESZA P.I., J. Electroanal. Chem., 220 (1987), 295.
[6] DOSTAL A., HERMES M., SCHOLTZ A., J. Electroanal. Chem., 415 (1996), 133.
[7] KASEM K., STELDT F.R., MILLER T.J., ZIMMERMAN A.N., Micropor. Mesopor. Mater., 66 (2003), 133.
[8] SIPERKOL M., KUWANA T., J. Electrochem. Soc. 130 (1983), 396.
[9] TRANI Y., EUN H., UMERZAWA Y., Electrochim. Acta. 43 (1998), 3431.
[10] REDDY S.J., DOSTAL A., SCHOLTZ F., J. Electroanal. Chem., 403 (1996), 209.
[11] ABDOLKARIM A., AYATOLLAHI M.M., Anal. Chem., 76 (2004), 5690.
[12] COX J.A., KULESZA P.J., Anal. Chem., 5 (1998), 1021.
[13] CHEN S.-M., Electrochim. Acta, 43, (1998), 3359.
[14] EFTEKHARI A., J. Electroanal. Chem., 558 (2003), 75.
[15] KASEM K.K., J. Applied Electrochem., 29 (1999), 1471.
[16] CATALDI T.R., DE BENEDETTO G., BIANCHINI A., J. Electroanal. Chem., 471, (1999), 42.
[17] XUN Z., CAI C., LU T., Electroanal., 16, (2004), 674.
[18] COX J.A., J. Electroanal. Chem., 233 (1987) 87.
[19] KASEM K.K., Mater. Sci. Eng., B83 (2001), 97.
[20] CATLDI T.R., DE BENEDETTO C.E., CAMPA C., J. Electroanal. Chem., 437 (1997), 93.
[21] KASEM K., HAZEN R., SPAULDING R., Am. J. Undergr. Res., 2 (2003), 27.
[22] KARYAKIN A.A., GITELMACHER O.V., KARYAKINA E.E., Anal. Chem., 67 (1995), 2419.
[23] ITAYA K., SHIBAYAMA K., AKAHOUSHI H., TOSHIMA S., J. Appl. Phys., 53 (1982), 804.
[24] NEFF V.D., J. Electrochem. Soc., 132 (1985), 1382.
[25] BEHEIR S.G., BENYAMIN K., MEKHAILF M., J. Radioanal. Nucl. Chem., 232 (1998), 147.
[26] KAYE S.S., LONG J.R., J. Am. Chem. Soc., 127 (2005), 6506.
[27] ROBERTO A., Can. J. Chem., 60 (1987), 1828.
[28] LAI Y.K., WONG K.Y., Electrochim. Acta, 38 (1993),1015.

Received 15 January 2009

Materials Science-Poland, *Vol. 28*, *No. 2*, *2010*

The effect of plasma torch power on the microstructure and phase composition of alumina coatings

L. MARCINAUSKAS[1, 2*], P. VALATKEVIČIUS[2]

[1]Physics Department, Kaunas University of Technology,
Studentu 50, LT-51368, Kaunas, Lithuania

[2]Lithuanian Energy Institute, Breslaujos 3, LT-4440, Kaunas, Lithuania

Alumina coatings were obtained by the atmospheric plasma spraying using Al_2O_3 nanopowders. The powders were injected into the anode zone of the torch. The microstructures and phase compositions of the coatings were determined by the scanning electron microscopy and X-ray diffraction. The results indicated that the higher the plasma torch power, the lower the surface roughness is. The as-sprayed coatings are composed of γ-Al_2O_3 and α-Al_2O_3, while the original powders were composed of δ-Al_2O_3 and γ-Al_2O_3 phases. The amount of γ-Al_2O_3 in the coatings increases from 56.52% to 100% if the plasma torch power is increased from 3.2 kW to 4.5 kW

Keywords: *Al_2O_3; plasma sprayed coating; plasma torch*

1. Introduction

Aluminum oxide (Al_2O_3) films are widely used as insulating and wear resistant coatings [1–4] due to their high resistance to corrosion and erosion, their hardness, and dielectric strength. It is well known that alumina has stable (α) and metastable (γ, δ, η, θ, β) polymorphs. Corundum (α-Al_2O_3) is the most widely used and best known alumina. Metastable γ-Al_2O_3 is used as a catalyst in the formation of bulk and fine chemicals, and in hydrocarbon conversion for petroleum refining [5]. Atmospheric plasma spraying (APS) is the most versatile method of achieving Al_2O_3 coatings. APS technology is used, because the high plasma temperatures are high enough to melt refractory ceramic materials (Al_2O_3, TiO_2, ZrO_2) [6–11].

Over the past decade extensive research has been devoted to the synthesis of ceramic coatings from nanopowders. It was demonstrated that nanostructured thermal spray ceramic oxide coatings could have higher wear resistance, superior hardness,

*Corresponding author, e-mail: liutauras@mail.lei.lt

and lower porosity when compared with similar coatings deposited from conventional powders [12–19]. It is well known that the final properties of the deposited coatings depend on various process parameters. The melting point of a particle strongly depends on the injection place of powders [6]. Yugeswaran et al. [7] showed that the hardness, porosity, and adhesive strength of ceramic coatings are related to the power of the plasma torch. Gao [8] found that alumina coatings deposited at higher arc currents and voltages are correspondingly harder and denser. The particle size of the powders also affects the hardness, phase content, and porosity of Al_2O_3 coatings [4, 10, 15]. However, using nanosized powder to deposit the coatings creates new problems. The most important difficulty is injection of the nanoparticles into the plasma. The nanoparticles, due to their low mass, cannot be injected directly into the plasma. To solve this problem, the nanoparticles are agglomerated into micrometer size particles. It was demonstrated that the optimum size of these particles lies in the range 10–100 μm [12–16]. The second challenge is to select appropriate process parameters which will retain crystal grain size at the nanometer regime in sprayed coatings [12, 16].

This paper presents a study on the formation of Al_2O_3 coatings from nanopowders, using the APS technology. The effect of various plasma torch power on the surface microstructure and phase composition of the alumina coating was investigated.

2. Experimental

A direct current plasma torch was used to deposit Al_2O_3 coatings (Fig. 1) [20, 21]. It consisted of a copper cathode (1), a working gas injecting ring with two tangential

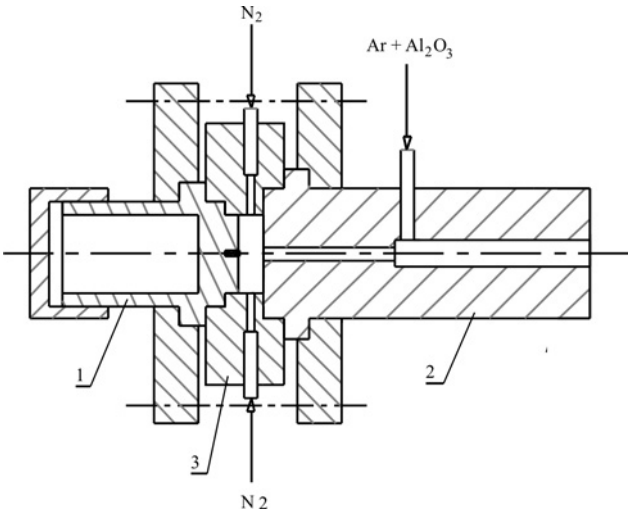

Fig. 1. Schematic diagram of the plasma torch:
1 – cathode, 2 – anode, 3 – gas injecting ring

blowholes (3), and an anode nozzle with a blowhole (2). Both electrodes were water cooled. The tangential injection of plasma forming gas stabilized the plasma. Nitrogen was used as the plasma forming gas (7.65 dm^3/min), while argon (1.20 dm^3/min) was used as the Al_2O_3 powder carrier gas. The powders were introduced through the anode nozzle, in order to improve the melting efficiency of the spray particles. The plasma torch was operated in an open atmosphere.

Ultra dispersion powder aluminium oxide (Sepros Corp. Int.), extracted by the gas dispersion synthesis method, was used as the starting material. The arithmetical mean of the Al_2O_3 nanoparticles was 87 nm, the apparent density – 3610 kg/m^3, the bulk density – 1890 kg/m^3, the melting temperature – 2320 K. The nanoparticles were composed of aluminum oxide (Al_2O_3) – 99.950%, magnesium oxide (MgO) – 0.011%, silicon oxide (SiO_2) – 0.007%, iron oxide (Fe_2O_3) – 0.002%, titanium oxide (TiO_2) – 0.001%, calcium oxide (CaO) – 0.017%, sodium oxide (Na_2O) – 0.009%. In order to make the nanosize oxide powders sprayable, the nanopowders were agglomerated into particles of 5–50 μm size and dried for 12 h at 473 K. The alumina ceramic coatings were sprayed on the stainless steel at various plasma torch powers. The deposition time for all coatings was 180 s. The detailed spray parameters are listed in Table 1.

Table 1. Deposition parameters and γ-Al_2O_3 phase fraction

Torch power [kW]	Spray distance [cm]	Mean plasma temperature (T_f) [K]	γ phase content (R) [%]
3.2	3.5	4665±20	56.52
3.75	3.5	5082±20	73.05
4.5	3.5	5603±20	100

In order to melt or partially melt the alumina, the temperature of the plasma should be higher than the melting point of Al_2O_3. According to the method presented in [20–22], it was found that the temperature of the nitrogen plasma at the exit of the anode nozzle may be estimated by the equation:

$$T_f = 36.8\left(\frac{I^2}{Gd_2}\right)^{0.225} \tag{1}$$

where I is the current (A), G – the nitrogen gas flow rate (kg/s), d_2 – the anode diameter (m), and T_f is the mean temperature of the plasma leaving the anode (K).

The surface morphology of the coatings was examined by the scanning electron microscopy (SEM), model JEOL JSM-5600. The coating structure was analyzed by X-ray diffraction (XRD) (DRON-UM1 with standard Bragg–Brentano focusing geometry) in a 10–70° range using CuK_α (λ = 0.154059 nm) radiation. Peak positions and full-width of peaks at half minimum intensity were obtained by fitting the data for the measured peaks with two Gaussian curves, in order to find the true peak position

and width corresponding to monochromatic $K\alpha_1$ radiation. The identification of phases was performed using the Crystallographica Search-Match program (Oxford Cryosystem Ltd, 1996-2003) for Powder Diffraction Data.

3. Results and discussion

3.1. Surface morphology

The agglomerated nanopowders observed with SEM are shown in Fig. 2a. The diameter of powder particles after agglomeration was 5–50 μm, and their shape was irregular.

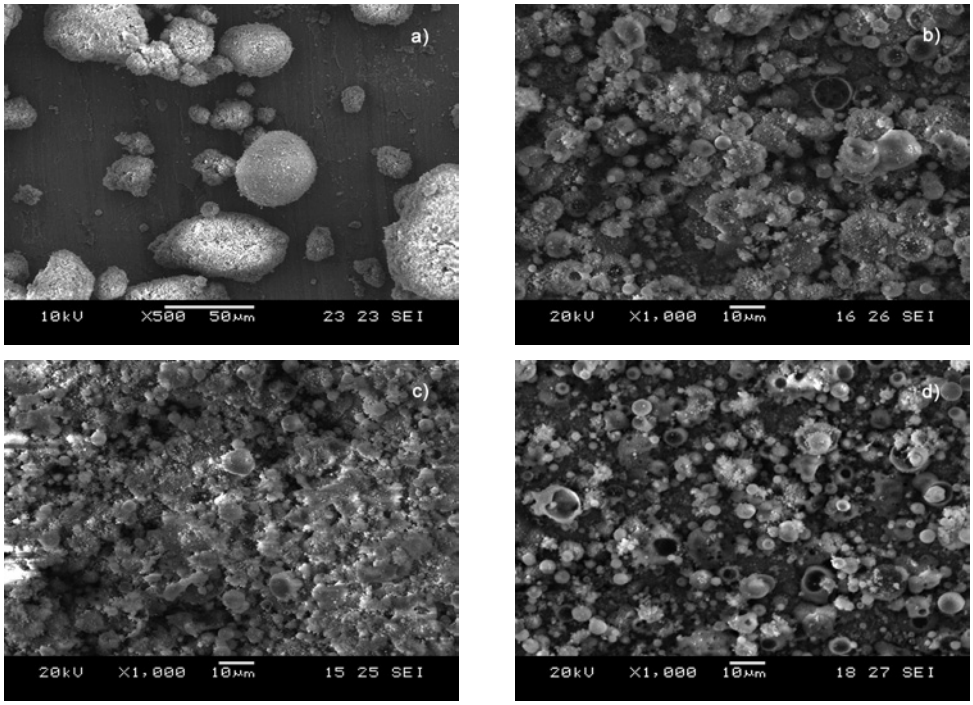

Fig. 2. SEM view of granulated aluminum oxide powders (a) and surface morphologies of the coatings deposited at various plasma torch powers: b) 3.2 kW, c) 3.75 kW, d) 4.5 kW

The surface morphologies of the as-sprayed Al_2O_3 coatings are presented in Fig. 2. The surface roughness decreases with the increase in the plasma torch power. The coatings consist mostly of splats and particles 0.5–10 μm wide. The surface of the coating deposited under 3.2 kW is composed of a relatively higher number of splats 5–10 μm wide. The coating produced at 3.75 kW mostly consists of ~5 μm splats (Fig. 2c). The coating obtained at the highest torch power beside discrete 5–10 μm

splats, have the highest number of splats and grains, whose size is lower than 1 μm (Fig. 2d). Beside the micrometer size splats, spherical nanosize (100–200 nm) particles were found on the surface of the coatings under larger magnification. It may be noted that all coatings have some pores, which is typical of the coatings produced by plasma spray.

The differences in the surface morphology depend on the input power. The feedstock granules were of various sizes (from 5 to 50 μm), and the momentum transferred from the plasma gas to the particles strongly depends on the mass of the injected granules. Large granules attain a lower velocity compared with the smaller ones. Usually, the larger particles tend to penetrate the core and travel around the periphery of the plasma jet, as a consequence of their larger inertia. Meanwhile, the smaller granules are near to the hottest core of the plasma jet [4]. Thus, the large total heat capacity will be higher for the larger size particles, and the larger particles need more time to be melted. The higher plasma torch power provides better heating and a higher melting degree of the particles. Eventually, the coatings will be composed of smaller size splats and particles, and the number of fully melted regions is also higher. Yugeswaran [7] indicated that the coatings deposited at higher plasma temperatures (input powers) exhibit a fine type structure, having lower surface roughness and fewer cracks formed in the solidification process. Song et al. [13] established that the coatings sprayed at higher heat input powers have a lower volume fraction of pores and fewer partially melted regions.

3.2. XRD characterization

The X-ray diffraction (XRD) patterns of the starting powders indicate that the powders are composed of two phases: δ-Al_2O_3 and γ-Al_2O_3 (Fig. 3). XRD studies revealed that dominant phases in the sprayed coatings are γ-Al_2O_3 and α-Al_2O_3 (Fig. 4). It may be noted that no δ-Al_2O_3 phase was obtained in the sprayed coatings. The coating deposited at the lowest power (3.2 kW) had peaks attributed to (113), (104), (012) alpha and (400), (440), (311) γ-Al_2O_3. The intensities of the γ-Al_2O_3 diffraction peaks increase with the increase in the plasma torch power (Fig. 4), whereas those of the α-Al_2O_3 peaks decrease. Thus the XRD patterns of the coating deposited at the highest power have the lowest intensity peaks, however only cubic γ-Al_2O_3 phase is obtained. These results indicate that the amount of γ-alumina increases and the amount of α-Al_2O_3 decreases as the power of the plasma torch increases.

The relative amount of the major phases was calculated from the XRD intensity data [23, 24]:

$$R = \frac{I_{(400)}^{\gamma\text{-}Al_2O_3}}{I_{(113)}^{\alpha\text{-}Al_2O_3} + I_{(400)}^{\gamma\text{-}Al_2O_3}} \times 100\% \tag{2}$$

where R is the γ-Al_2O_3 phase content, $I_{(hkl)}$ is the intensity of the peak diffraction for the corresponding plane of the α-Al_2O_3, and γ-Al_2O_3 phases.

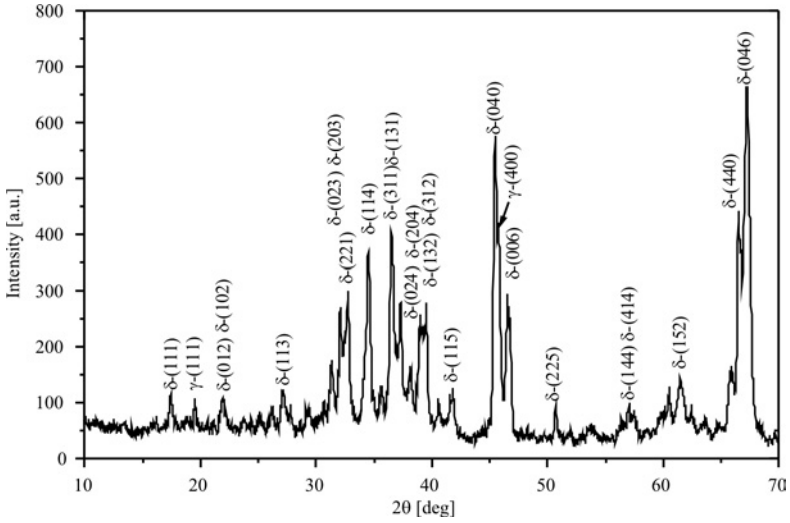

Fig. 3. X-ray diffraction patterns of the granulated Al_2O_3 nanopowders

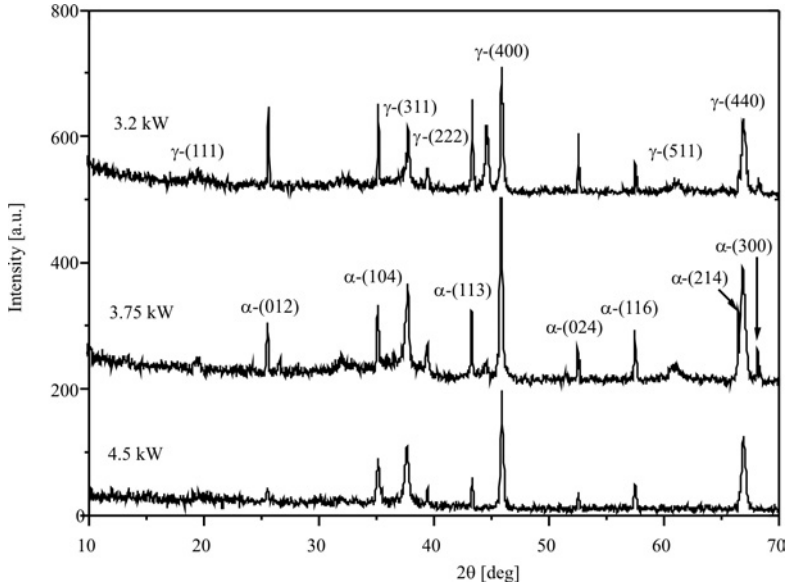

Fig. 4. XRD diffraction patterns of the sprayed Al_2O_3 coatings.

The results for phase compositions calculated from XRD data are presented in Table 1. The cubic γ-Al_2O_3 content was about 56.52%, at 3.2 kW. When the plasma torch power reached 3.75 kW, the γ-Al_2O_3 content increased to 73.05. The coating produced at 4.5 kW shows only peaks corresponding to γ-alumina phase. Gao et al. [8] also showed that the amount of γ-Al_2O_3 in the coatings increases and amount of α-Al_2O_3 decreases as the plasma power increases. Zeng [15] reported that the γ-Al_2O_3 content in the coatings will be higher when the particle size of the starting powder is smaller.

The residence time of Al_2O_3 powder inside the plasma jet is usually lower than 10^{-3} s. The melting points of the powders are higher for powders having smaller particle sizes. It is generally accepted that during solidification on impact, γ-Al_2O_3 is homogenously nucleated if the initial droplet is completely melted. Most authors [4, 7, 8, 15] suggest that the amount of γ-alumina in the coating represents the melting extent of the powders. The existence of α-Al_2O_3 in the sprayed coatings is attributed to both unmelted particles and to a solid-state γ-to-α phase transformation [25]. It is well known that the phase formation of the coatings is influenced by heat transferred from the plasma to the Al_2O_3 particles; the quenching rate of molten particles; the shape and size of the powder particles [4, 7]. The plasma flow temperature increases as the torch power increases (see Table 1). So, a higher fraction of the Al_2O_3 powder will melt, and consequently the coatings will consist of higher amounts of γ-Al_2O_3. The higher amount of gamma alumina produced is attributed to the high cooling rate (~10^6 K/s) of the molten granules during spraying. Furthermore, according to the laws of nucleation kinetics, γ alumina is more easily nucleated from the melt state than α-Al_2O_3 because of the lower interfacial energy between the γ alumina structure and the liquid [26]. The experimental results indicated that the granulated powders are completely melted at 4.5 kW torch power.

4. Conclusions

Al_2O_3 coatings were successfully deposited by the APS technique using nanopowders. The surface morphology and phase composition of the coatings were studied. SEM results indicated that the coatings produced at higher plasma torch power are composed of smaller sized splats and particles. XRD measurements revealed that the as-sprayed coatings were composed from γ-Al_2O_3 and α-Al_2O_3. The increase in the plasma torch power increases the melting degree of the powders, and consequently the amount of γ-Al_2O_3 phase in the coatings will be higher. The coating deposited at 4.5 kW is composed exclusively from γ-Al_2O_3 phase.

References

[1] MASALSKI J., GLUSZEKA J., ZABRZESKI J., NITSCH K., CLUSZEK P., Thin Solid Films, 349 (1999), 186.
[2] YOUNG E.J., MATEEVA E., MOORE J.J., MISHRA B., LOCH M., Thin Solid Films, 377–378 (2000), 788.
[3] IRISAWA T., MATSUMOTO H., Thin Solid Films, 509 (2006), 141.
[4] YIN Z., TAO S., ZHOU, X., DING C., J. Eur. Ceram. Soc., 28 (2008), 1143.
[5] FU L., JOHNSON D.L., ZHENG J.G., DRAVID V.P., Amer. Ceram. Soc., 86 (2003), 1635.
[6] FAUCHAIS P., VARDELLE A., DENOIRJEAN A., Surf. Coat. Technol., 97 (1997), 66.
[7] YUGESWARAN S., SELVARAJAN V., SEO D., OGAWA K., Surf. Coat. Technol., 203 (2008), 129.
[8] GAO Y., XU X., YAN Z., XIN G., Surf. Coat. Technol., 154 (2002), 189.
[9] CTIBOR P., BOHAC P., STRANYANEK M., CTVRTLIK R., J. Eur. Ceram. Soc., 26 (2006), 3509.
[10] WESTERGARD R., ERICKSON A., AXEN L.C.N., HAWTHORNE H.M., HOGMARK S., Tribol. Int., 31 (1998), 271.

[11] BRINKIENE K., KEZELIS R., J. Eur. Ceram. Soc., 25 (2005), 2181.
[12] SHAW L., GOBERMAN D., REN R., GELL M., JIANG S., WANG Y., XIAO T.D., SRRUTT P.R., Surf. Coat. Technol., 130 (2000), 1.
[13] SONG E.U., AHN J., LEE S., KIM N.K., Surf. Coat. Technol., 201 (2006), 1309.
[14] LIMA R.S., MARPLE B.R., Surf. Coat. Technol., 200 (2006), 3428.
[15] ZENG Y., LEE S.W., DING C.X., Matter. Lett., 57 (2002), 495.
[16] GADOW R., KERN F., KILLINGER A., Mater. Sci. Eng. B, 148 (2008), 58.
[17] CHEN H., ZENG Y., DING C., J. Eur. Ceram. Soc., 23 (2003), 491.
[18] ZENG Y., LEE S., GAO L., DING C. X., J. Eur. Ceram. Soc., 22 (2002), 347.
[19] HUI R., WANG Z., KESLER O., ROSE L., JANKOVIC J., YICK S., MARIC R., GHOSH D., J. Pow. Sourc., 170 (2007), 308.
[20] AKDOGAN E., COKELILER D., MARCINAUSKAS L., VALATKEVIČIUS P., VALINČIUS V., MUTLU M., Surf. Coat. Technol., 201 (2006), 2540.
[21] MARCINAUSKAS L., VALINČIUS V., VALATKEVIČIUS P., GRIGONIS A., Power Engineering, 1 (2006), 36. (in Lithuanian).
[22] VALINČIUS V., KRUŠINSKAITE V., VALATKEVIČIUS P., VALINČIŪTE V., MARCINAUSKAS L., Plasma Sources Sci. Technol., 13 (2004), 199.
[23] CAO L.H., KHOR K.A., FU L., BOEY F., Mater. Process. Technol., 89-90 (1999), 392.
[24] KHOR K.A., BOEY F.Y.C., ZHAO X.L., CAO L.H., Mater. Sci. Eng., A300 (2001), 203.
[25] YILMAZ S., IPEK M., CELEBI G.F., BINDAL C., Vacuum, 77 (2005), 315.
[26] MCPHERSON R., Thin Solid Films, 83 (1981), 297.

Received 16 March 2009
Revised 20 September 2009

Materials Science-Poland, *Vol. 28*, *No. 2*, *2010*

Fabrication of magnesium aluminum silicate glass ceramics by sintering route

S. K. DURRANI*, M. A. HUSSAIN, S. Z. HUSSAIN, J. AKHTAR, A. SAEED, N. HUSSAIN, N. AHMED

Materials Division, Directorate of Technology, PINSTECH, P.O. Nilore, Islamabad, Pakistan

Magnesium aluminum silicate (MAS) glass ceramic material was prepared by the sintering route. A three-stage heat treatment, consisting of calcination, nucleation and crystallization, was developed with MgF_2 as a nucleating agent. The effect of the percentage chemical composition and the sintering temperature on the density of the compacted material was also studied. The thermal stability of MAS was measured by thermogravimetry (TG), differential thermal analysis (DTA). TG/DTA studies revealed that the powder exists as $MgO–Al_2O_3–SiO_2–H_2O$ in solid state, and then transforms to $MgO–Al_2O_3–SiO_2$ via some metastable intermediates above 300 °C. The microstructure and phases were analyzed by X-ray diffractometry (XRD). XRD analysis revealed the formation of various phases such as magnesium silicate, fluorophlogopite, nobergite, siliminite etc. at various processing temperatures.

Keywords: *magnesium aluminum silicate; machinable glass; particle size distribution*

1. Introduction

Magnesium aluminum silicate (MAS) glass ceramic systems are of technological importance because of their usefulness in high voltage applications and in an ultra high vacuum. These materials not only posses peculiar machinability features but also have superior electrical insulation properties, ultra high vacuum compatibility, high thermal stability, low thermal conductivity and good mechanical strength [1]. MAS materials are also being used in nuclear technology [2, 3], in the production of prototype components, used in medicines for the axles of mechanisms providing energy for implanted cardiostimulators and are also used in the production of welding jets or as holders for welded components [4–7]. The properties of MAS glass ceramics such as hardness, machinability, and conductivity depend upon the composition and microstructure. Machining of these materials can be carried out to precise tolerances and

*Corresponding author, e-mail: durranisk@gmail.com

surface finish with conventional tools. The explanation underlying the good machinability of MAS lies in the unique microstructure of an interlocking array of plate-like mica crystals, dispersed uniformly throughout the glass matrix. MAS glass ceramic materials have been prepared by controlled crystallization in which a large number of tiny crystals rather than few bigger single crystals have been grown [2, 8]. Radonig ey al. [9] studied the effect of fluorine content and its source on the crystallization of MAS materials. The predominant crystalline phases identified in their study were fluorite, norbergite or fluorophlogopite, depending on the heat treatment, the fluorine concentration, etc. General preparation methods have been discussed in the literature [2, 4] but due to special nature and technological importance of the material, the crucial preparation process has either been too vaguely addressed or is missing entirely. Therefore, the preparation of these materials is of special importance. In the light of this fact, preparation of machinable MAS glass ceramic was undertaken using a sintering route.

2. Experimental

Materials. High purity chemicals, silica (Fluka), aluminum oxide (BDH), magnesium oxide (Merck), potassium carbonate (Riedel-de-Haen), boron oxide (BDH), magnesium fluoride (BDH), orthophosphoric acid (BDH) and acetone (BDH) were used as raw materials.

Preparation. Magnesium aluminum silicate (MAS) glass ceramic specimens were prepared by utilizing SiO_2, Al_2O_3, MgO, K_2CO_3, and B_2O_3 as given in Table 1.

Table 1. Magnesium aluminum silicate glass ceramic specimen's designation and composition

Specimen	Chemical composition (wt. %)					
	SiO_2	Al_2O_3	MgO	K_2CO_3	B_2O_3	MgF_2
MAS -1	36.62	12.73	16.87	13.93	1.91	17.91
MAS -2	37.57	13.19	16.49	14.26	1.97	16.49
MAS -3	37.72	13.23	16.05	13.98	2.48	16.54
MAS -4	38.51	13.51	16.38	14.27	2.53	14.78
MAS -5	36.34	24.82	13.23	11.32	3.53	10.76

Three-stage schedules, i.e. calcination, nucleation and crystallization processes were used. In the first stage, initial charge was mixed thoroughly and calcined at 950 °C for 24 h according to a pre-determined heating schedule. Approximately 4–7 wt. % MgF_2 was added to the calcined charge and milled in a planetary ball mill for 40 h. The fine ball milled charge was seasoned in 5% H_3PO_4 acid solution in an acetone medium for 72 h. Compacts of MAS ($61\times16\times5$ mm^3) were made using a hydraulic press of the load capacity of ca. 25 t/in^2 (1 t/in^2 = 15.44 M Pa).

Sintering. The compacts were sintered in a two-step heating program. In the former step, the compact was heated up to 600–630 °C for 2–4 h to ensure good nucleation and to initiate the crystal growth. In the latter step, heating was carried out at different heating rates, in the range of 15–60 °C/h, up to sintering temperatures of 950–1080 °C. The sample was kept at the sintering temperature for a sufficiently long time to achieve the desired crystal growth.

Characterization. The crystallinity of MAS specimens was determined by X-ray diffraction on a Rigaku Geiger flux instrument using CuKα radiation. For measurement of the weight loss, combined TG–DTA thermal analysis was performed using a Netzsch STA-409 thermoanalyzer. The particle size distribution of the powder specimens was measured by a laser particle size analyzer (SK-Laser Micron PRO-7000S). The density of MAS specimens was measured using an Ultra Pycnometer 1000 (Quantachrome). Porosity was measured by radiographic techniques, using a realtime radiography Instrument (Model Isvolt HS Panta SeiFert). Before making the measurements, the sample surface was polished with 3μ alumina powder to obtain a good reflective surface. The micro-structural features and porosity of the sintered specimen MAS-5 were observed using a scanning electron microscope (SEM, LEO 4401). The specimen was fully polished, placed on an aluminum stud, dried in air and then it was coated with thin gold film for the SEM observation.

Effect of acids and bases. The sintered specimens were treated with 5% hydrofluoric and hydrochloric acids for 24 hrs at 95 °C, in order to observe the effect of these acids. The effect of 5% sodium hydroxide and sodium carbonate was also studied, for 6 h at 95 °C. The samples were weighed, to check for any loss in weight, after washing off acids and bases.

3. Results and discussion

Thermal analysis (TG/DTA) was conducted and the representative thermograms of specimen MAS-5 are shown in Fig. 1. A total weight loss 9.14% was observed after heating up to 900 °C. Two peaks in the DTA data were observed. The former peak is an endothermal minimum, which is connected with glass transformation. The exothermal maxima (second peak) correspond to the separation of the crystalline phase. The position of the minimum on the DTA curve is basically determined by the chemical composition of the separated phase or by its transformation temperature. The exothermal crystallization peak, its position and shape are characterized by the crystallization process [10]. All the volatiles were completely removed at 900 °C. The particle size distribution curve of specimen MAS-5 powder is shown in Fig. 2. This curve revealed that the particle size distribution is <10μm with a median particle size of around 5.3 μm. Experimental results confirmed that a smaller particle size and the particle size distribution that has a narrow profile is essential for good sinterability. It was also found that specimen MAS-5 sintered at a temperature of 1040 °C yielded

a material of smaller and uniform particle distribution and the density of ca. 2.35 g/cm^3 (96% of the theoretical density).

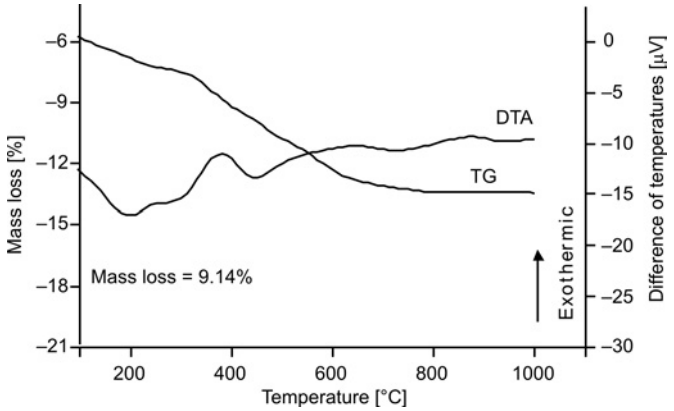

Fig. 1. TG/DTA curves for ceramic powder of magnesium aluminum silicate glass (specimen MAS-5)

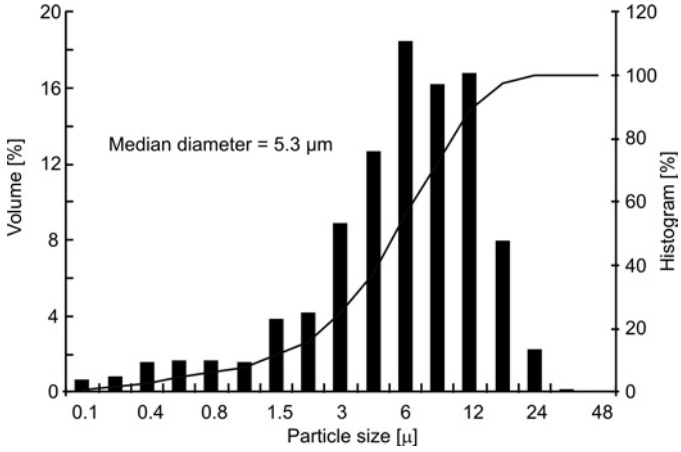

Fig. 2. Particle size distribution of ceramic powder of magnesium aluminum silicate glass (specimen MAS-5)

During pressing it was observed that if the initial charge was not pulverized for a sufficiently long time after calcination, the sintered briquette had a lot of open pores on the surface. Thus, in order to minimize the porosity in the sintered product, quite a long period was used for pulverization: finally 72 h duration was selected. The sintering parameters, along with the green and sintered densities of samples MAS-1 to MAS-5, are given in Table 2. The data for samples MAS-4 and MAS-5 sintered at other temperatures are also given in Table 2. A insignificant increase in density was observed in the sintering temperature range 1040–1060 °C, the duration being in the range 2–4 h. It was observed that as the sintering temperature was increased beyond

1060 °C, excessive thermal energy leads to some rearrangement among the grains as well as some isotropic crystal growth. In addition, decomposition of fluorophlogopite phase, formed at lower temperature, takes place, leading to the development of internal line cracks/voids [9] in the material. As a result of this, the material appears swelled and its density decreases at higher sintering temperatures.

Table 2. Sintering parameters, green and sintered densities

Specimen	Sintering conditions (Temperature [°C]/time [h])	Green density [g/cm^3]	Sintered density [g/cm^3]
MAS-1	1040/3	1.79	2.18
MAS-2	1040/3	1.74	2.12
MAS-3	1040/3	1.91	2.29
MAS-4	1040/3	1.68	2.15
MAS-4a	1040/2	1.65	2.12
MAS-4b	1050/2	1.72	2.14
MAS-4c	1060/2	1.64	2.14
MAS-5	1040/3	1.79	2.35
MAS-5a	1060/2	1.86	2.34
MAS-5b	1080/2	1.74	2.35

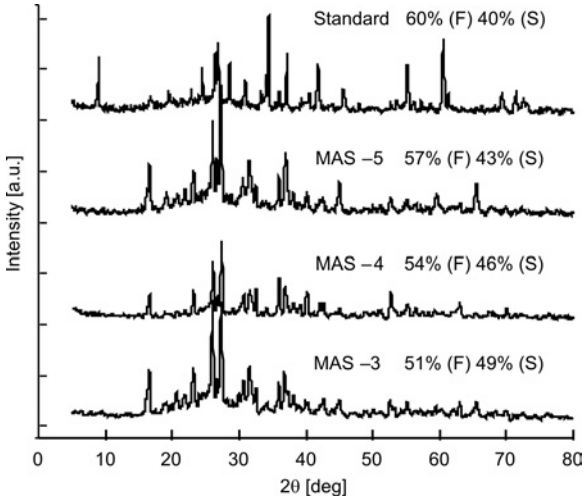

Fig. 3. XRD patterns of magnesium aluminum silicate glass ceramic, specimens MAS-3-5 (F – fluorophlogopite, S – sillimanite phase)

The XRD patterns of specimens MAS-1 to MAS-5, sintered at 1040 °C for 3 h, are presented in Fig. 3. The XRD peaks were indexed. The predominant phases in the synthesized MAS specimens were identified as fluorophlogopite (F), sillimanite (S) and lausite (L). The percentage of these phases in each specimen is given in Table 3. The specimen MAS-5 shows the predominant fluorophlogopite phase. Figure 4 shows

radiographic data for the estimation of porosity. The specimen MAS-5 after sintering is shown in Fig. 4a. Radiography of specimen MAS-5 was conducted in order to evaluate the porosity. The radiographic image, as indicated in Fig. 4b, does not show any sign of porosity.

Table 3. Percentage of phases in magnesium aluminum silicate glass ceramic observed by X-ray diffraction

Specimen	Fluorophlogopite (F) [%]	Lausite (L) or sillimanite (S) [%]
MAS-1	28	71
MAS-2	30	69
MAS-3	51	49
MAS-4	54	46
MAS-5	57	43

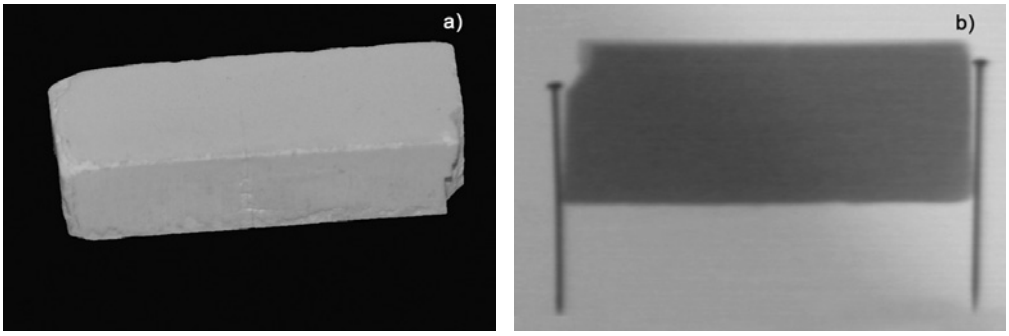

Fig. 4. Sintered specimen (MAS-5) of magnesium aluminum silicate glass ceramics (a) and a radiographic (RG) image of MAS-5 (b)

This means that the specimen MAS-5 has a through porosity. However, some surface porosity was observed in specimen MAS-5 by SEM. Figure 5 shows a SEM image of a sintered specimen of MAS-5.

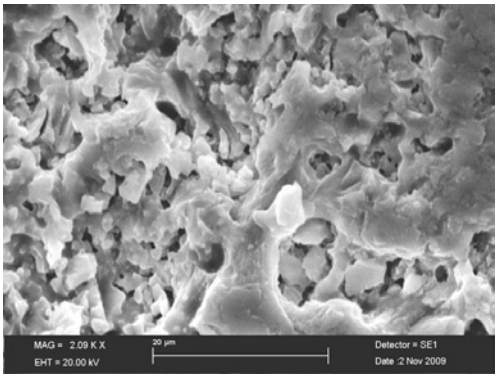

Fig. 5. SEM image of magnesium aluminum silicate glass ceramic (Specimen MAS-5)

Table 4. Effect of acids and bases on magnesium aluminum silicate glass ceramic

Specimen	Resistance to acid weight loss per unit area				Resistance to base weight loss per unit area			
	Temperature [°C]	Time [h]	HCl (5%) [mg/cm^2]	HF (5%) [mg/cm^2]	Temperature [°C]	Time [h]	NaOH (5%) [mg/cm^2]	Na_2CO_3 (5%) [mg/cm^2]
MAS-4	95	24	67	17.51	95	6	10.62	Nil
MAS-4a	95	24	87	156	95	6	9.52	2.13
MAS-5	95	24	48	6	95	6	11.82	1.35

The sintered specimens were tested for resistance to acids and bases when subjected to 5% hydrochloric acid, hydrofluoric acid at 95 °C for 24 h for acids and 6 h for sodium hydroxide and sodium carbonate bases (Table 4). The chemical resistance, i.e. weight loss per unit area (mg/cm^2) of MAS-4a either acids or base was found significant and the values were similar to those of Wawrziniak et al. [11].

4. Conclusions

Magnesium aluminum silicate glass (MAS) ceramic was prepared successfully by a sintering route. The chemical composition of specimen MAS-5 was found appropriate as compared to other four compositions, i.e. MAS-1-4. TG-DTA analysis showed that specimen MAS-5 was thermally stable at temperatures above 900 °C, and that it experienced a 9.14% weight loss after heating up to 900 °C.

MAS-5 sintered 1040 °C yielded a smaller and uniform particle size distribution, which was 96% of the theoretical density. Three various phases: fluorophlogopite (F), sillimanite (S) and lausite (L) were identified in the synthesized magnesium aluminum silicate glass ceramics, however the MAS-5 specimen predominantly consists of fluorophlogopite phase with a uniform particle size distribution. Radiographic tests show at least (3–4%) through porosity, whereas the SEM image indicates some surface porosity.

Acknowledgements

The authors wish to acknowledge the contributions of Dr. A. H. Qureshi for helpful discussions and for his assistance with the preparation of the manuscript. We are also grateful to Mr. M.M.R. Baig for assistance during the preparation of sintered specimens and the measurement of density using an ultra pycnometer 1000 (Quantachrome).

References

[1] STRAND Z., *Glass Ceramics*, Elsevier, Amsterdam, 1986.
[2] BEALL G.H., DOMAN R.C., Sci. Ceram., 10 (1980), 25.

[3] SKLAR A., Keramik, 28 (1978), 124.
[4] GROSSMAN D.G., US Patent 3839055 (1974).
[5] BAIK D.S., NO K.S., CHUN J.S., YOON Y.Y., CHO H.Y., J. Mater. Sci., 30 (1995), 1801.
[6] BOCCACCINI A.R., J. Mater. Process Technol., 65 (1997), 302.
[7] PANNHORST W., J. Non. Cryst. Solids, 219 (1997), 198.
[8] ZDAMIEWAKI W.J., J. Mater. Sci., 8 (1973), 192.
[9] RADOJIC L.J., NIKOLIC L.J., Eur. Ceram. Soc., 7 (1991), 11.
[10] SESTAK J., Phys. Chem. Glasses, 15 (1974), 137.
[11] WAWRZINIAK W., GRUNOV R., Silikattechnik, 31 (1980), 238.

Received 30 March 2009
Revised 13 November 2009

Materials Science-Poland, *Vol. 28*, *No. 2*, *2010*

Large-area self assembled monolayers of silica microspheres formed by dip coating

Y. WANG[1,2*], L. CHEN[1], H. YANG[1], Q. GUO[3], W. ZHOU[1], M. TAO[1,3]

[1]Department of Electrical Engineering, NanoFAB Center, University of Texas at Arlington, Arlington, TX 76019-0072, USA

[2]Department of Chemistry and Biology, University of Electronic Science and Technology of China, Zhongshan Institute, Zhongshan 528402, China

[3]ZT Solar, Inc., 1120 South Freeway, Fort Worth, TX 76104, USA

Formation by dip coating of highly ordered and closely packed, self assembled monolayers (SAMs) of microsized silica spheres has been reported. Under optimized coating conditions, SAMs were formed with 2 μm diameter silica spheres on record-breakingly large areas, measuring 3×10 mm^2 on silicon substrates and 1.5×11 mm^2 on glass substrates. The SAMs structure and their spatial extension were significantly influenced by the concentration of the solution, withdrawal speed, immersion time, relative humidity, types of solvent and substrate material. The SAMs of silica microspheres provide a glimpse into the wide range of photonic applications for dip coating such as surface texturing and anti-reflection coatings.

Keywords: *self assembled monolayer; silica microsphere; dip coating*

1. Introduction

Solution prepared omnidirectional antireflection (omni-AR) coatings were recently investigated both experimentally and theoretically, in order to improve the coupling of sunlight into solar cells [1, 2]. The basic structure of the omni-AR coating comprises an array of hemispherical microparticles of an optically transparent dielectric material. The hemispherical particles are formed by partially immersing spherical particles in a dielectric layer with a thickness lower than the diameter of the microspheres. The unique way the omni-AR coating is formed allows it to be prepared from solutions, which is inherently low cost. The hemispherical shape of the omni-AR coating makes sunlight collection less dependent on the incident angle of sunlight, from sunrise to sunset. The formation of the omni-AR coating on solar cells requires a simple assembly process for large area closely packed monolayers of microspheres.

*Corresponding author, e-mail: wangzsedu@126.com

Self-assembly is a spontaneous formation of ordered structures caused by interactions between the particles. Well ordered, self assembled monolayers (SAMs) of nanoparticles/microparticles attract increasing interest because of their significance for photonic crystals [3, 4], optoelectronic devices [5, 6], sensors [7, 8], coatings [9–12] and other applications [13–16]. Many practical devices require monolayers with ordered structures over large areas. Several self assembly processes have been proposed, including physical, chemical, layer-by-layer, molecular and evaporation induced self assemblies [17–23]. However, most self assembly research focuses on nanoparticles and modifications of their surface properties (e.g., organic ligands or surface charge). The introduction of organic compounds in the omni-AR coating for solar cell applications can lead to increased absorption and instability under constant ultraviolet radiation.

Dip coating is a popular self assembly process, in which a substrate is slowly withdrawn from a colloidal suspension and a uniform liquid film containing particles is formed on it. As the film thickness becomes lower than twice the particle diameter, due to solvent evaporation, the vertical component of the capillary forces drags the particles downwards to the substrate where they self assemble into ordered structures [19]. The mass transfer process simultaneously occurs over the entire substrate, ensuring a high process throughput. Recent experiments revealed the microscopic mechanism governing the formation of layered arrays of latex microparticles on glass substrates and silica/latex nanoparticles on glass/silicon substrates [9, 19–23]. However, the parameters that govern the self assembly process were not completely quantified, and no procedure has yet been proposed for obtaining monolayer arrays of microspheres over large areas and with few defects (e.g., voids and multilayers). On the other hand, bilayers start to form above a critical coverage of monolayer, whereas voids remain [24].

As summarized above, little has been published on the feasibility of dip coating for the formation of large area monolayers of microsized silica spheres, without the addition of organic compounds for surface modification. In the paper, the authors report on record breaking large areas of highly ordered and closely packed monolayers of silica microspheres, having dimensions of 3×10 mm^2 and 1.5×11 mm^2 on silicon (Si) and glass substrates, respectively. The spatial extension of these self assembled structures can be further increased, but depends on the volume of the solution. This process takes place at room temperature under ambient conditions without substrate pretreatment. The influence of the microsphere concentration, withdrawal speed, relative humidity and substrate immersion time, properties of solvent and substrate material on SAMs of silica microspheres is also revealed.

2. Experimental

Materials. Monodispersed plain silica mircospheres having the diameter of 2 μm were supplied by Microspheres-Nanospheres, the Corpuscular Company. The suspension was used without further purification. 1 mm thick glass slides from Fisher Scien-

tific and 500 μm thick silicon wafers from Nova Electronic Materials were used as substrates in the experiments. These substrates were cleaned by immersing them into a solution containing 30% H_2O_2 and 70% H_2SO_4 under ambient conditions for 24 h, then rinsing them with deionized water, and drying with dry N_2, before commencing the dipping coating process.

Formation of monolayers. SAMs of silica mircospheres were obtained by dipping silicon/glass substrates into a well dispersed silica mircosphere suspension. Before dipping, the suspension was dispersed in an ultrasonic bath and with a magnetic stirrer. During the coating process, the substrate was vertically dipped into the suspension for a few minutes and withdrawn at a programmed speed. The wet coating adhering to the substrate was subsequently air dried under ambient conditions. The coating parameters were: concentration of the suspension (5–27 wt. %), withdrawal speed (0.11 –5.35 mm/s), immersion time (1–6 min), relative ambient humidity (20–80%) and type of solvent (ethanol, water and ethanol/water 1:1 mixture). The temperature was fixed at 20 °C for all the experiments.

The formed SAMs of silica mircospheres were characterized with a Zeiss SUPRA 55VP scanning electron microscope (SEM), a Nikon LV100 optical microscope with a digital camera and optical diffraction pattern measurements. The surface coverage of the silica microsphere monolayers was calculated by directly counting the particle area using image analysis software. The criterion used to calculate the monolayer surface coverage was the ratio between the two dimensionally projected area of the silica microspheres and the substrate area.

3. Results and discussion

A series of SEM images taken at the same location but under various magnifications, as well as an optical microscope image, are shown in Fig. 1. The coating has a closely packed hexagonal structure and is sufficiently uniform, with a few voids in the monolayer (Figs. 1b–d). This can be illustrated by a two-dimensional fast Fourier transformation (FFT) and the well defined laser diffraction patterns in transmitted mode (Fig. 1f) [8]. Sharp peaks in the FFT confirm the presence of long range SAM order, and a set of regular, periodic hexagonal configuration of symmetrical spots, illuminated with a pinhole of diameter 0.50 mm in Fig. 2f confirms the microscopy observations that the sizes of the larger domains in the monolayer samples were about 500 μm.

It should be noted that the hexagonal closely packed structure is not formed everywhere over the substrate, in this case. A small area of multilayers and accumulation of microspheres and submonolayers with non-connected stripes and loosely packed islands can be observed at the bottom of the substrate (Fig. 2a) and sub-monolayers with short range ordering and loosely packed islands are visible at the top of the substrate (Fig. 2b). This is attributed to interactions of all the factors: evaporation, capillary forces, particle–particle interactions, particle–substrate interactions, concentration gradient in the suspension, etc.

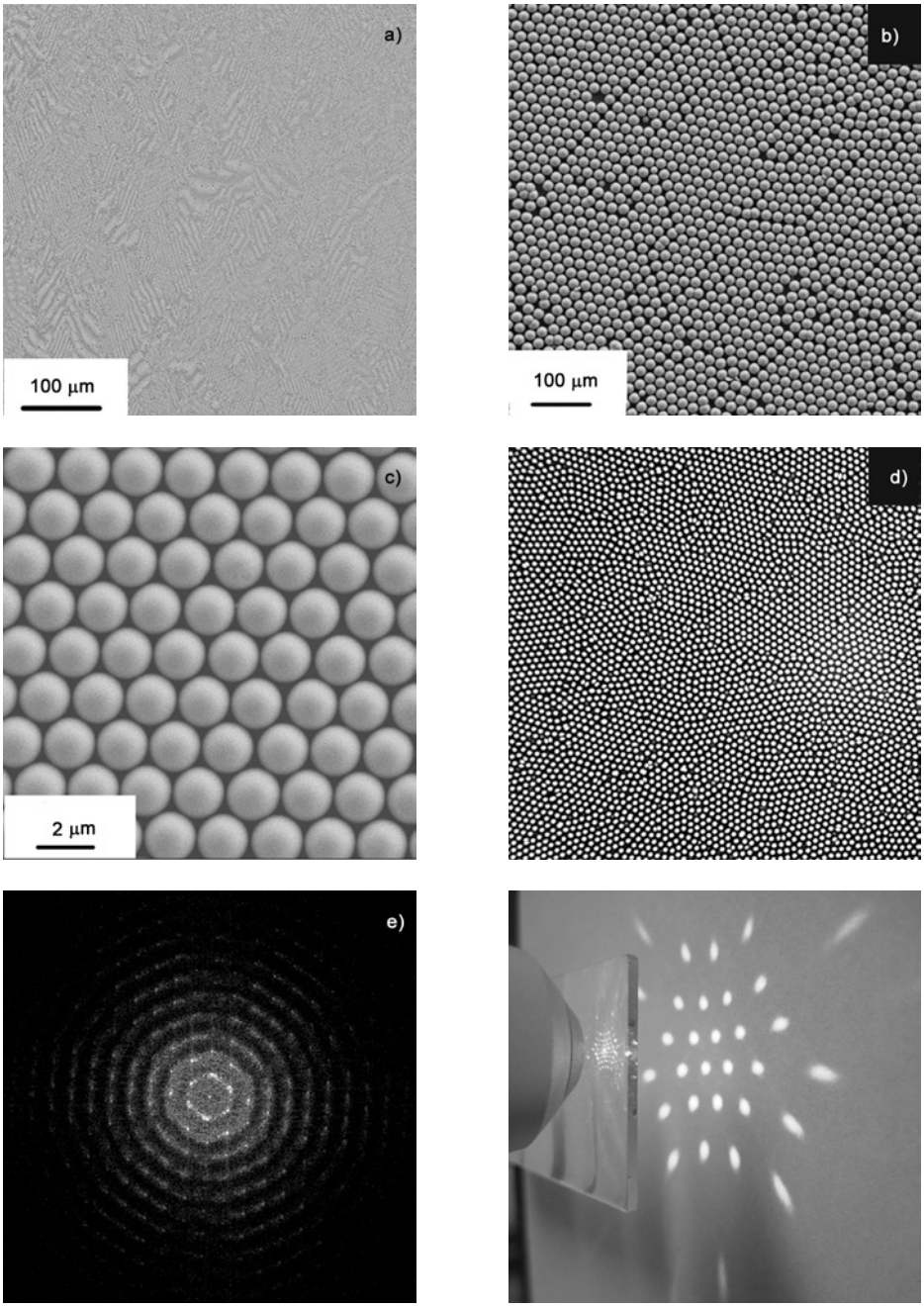

Fig. 1. Series of SEM images (a)–(c) with various magnifications, d) large area SAM on a silicon substrate under optical microscope showing a, e) two-dimensional Fourier transform pattern of a low-magnification SEM image, f) diffraction pattern of a green laser beam transmitted through a uniform hexagonally packed monolayer on a glass substrate

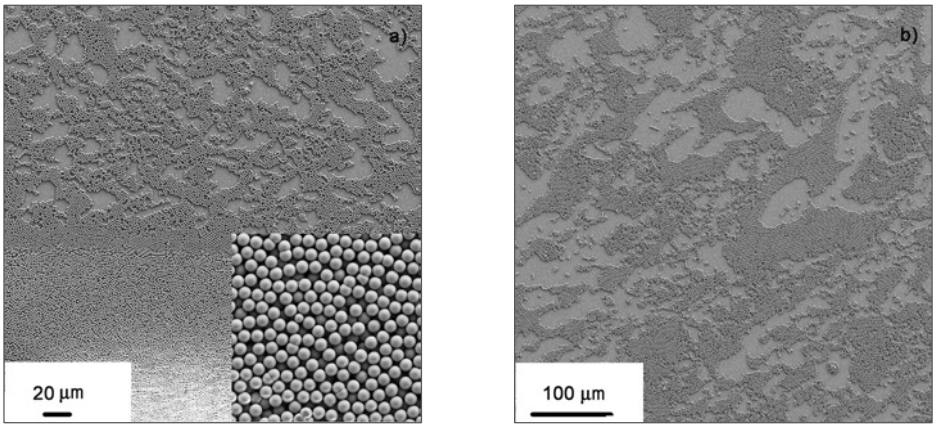

Fig. 2. SEM images at the bottom (a) and top (b) of the substrate and high-magnification SEM image of the same location (insert in (a))

Figure 3 illustrates the process of dip coating, driven by the convective flux generated by the evaporation of solvent in the meniscus region and the lateral capillary forces. The particle size and density influence the balance among various elements. Successive particle arrays are expected to form continuously as the particle flux fills up the meniscus [20, 21]. The attraction by the lateral capillary force leads to a dense hexagonal packing. At the same time, the upward flux of particles undergoes particle –particle interactions and particle–substrate interactions.

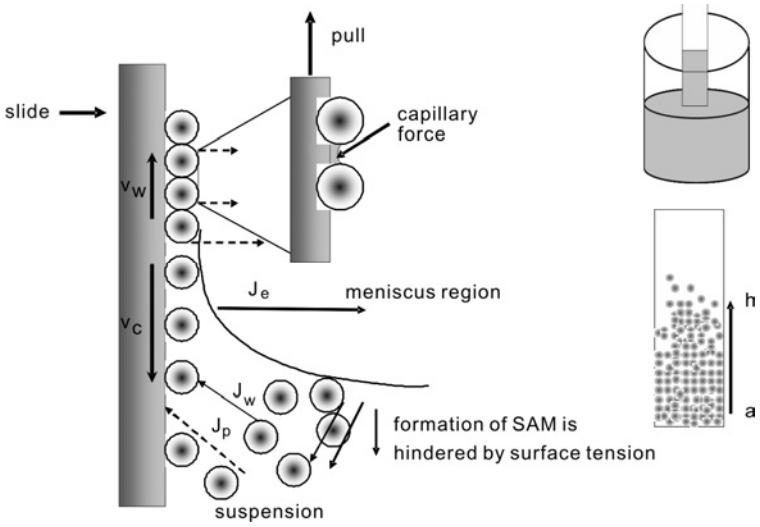

Fig. 3. Scheme of the dip coating mechanism, where various forces interact with each other to form self assembled coated structures: V_w – substrate withdrawal rate, V_c – monolayer growth rate, J_e – evaporation flux of solvent, J_w, J_p – entering fluxes of particles and solvent, respectively

In our experiments, the concentration gradient of silica microspheres in the suspension by gravity resulted in different upward fluxes of particles at different heights of the suspension, insufficient convective flux at the top of the suspension and superfluous convective flux at the bottom of the suspension, thus forming different structural characterizations on the substrate. Note that the coating area is limited by the volume of the solution. In our experiments, only 20 cm^3 of suspension is used, which corresponds to a maximum immersion depth of 16 mm for the substrate. Under optimum coating conditions, SAMs were formed with 2 μm diameter silica spheres at record-breaking large areas of 3×10 mm^2 on silicon substrates and 1.5×11 mm^2 on glass substrates.

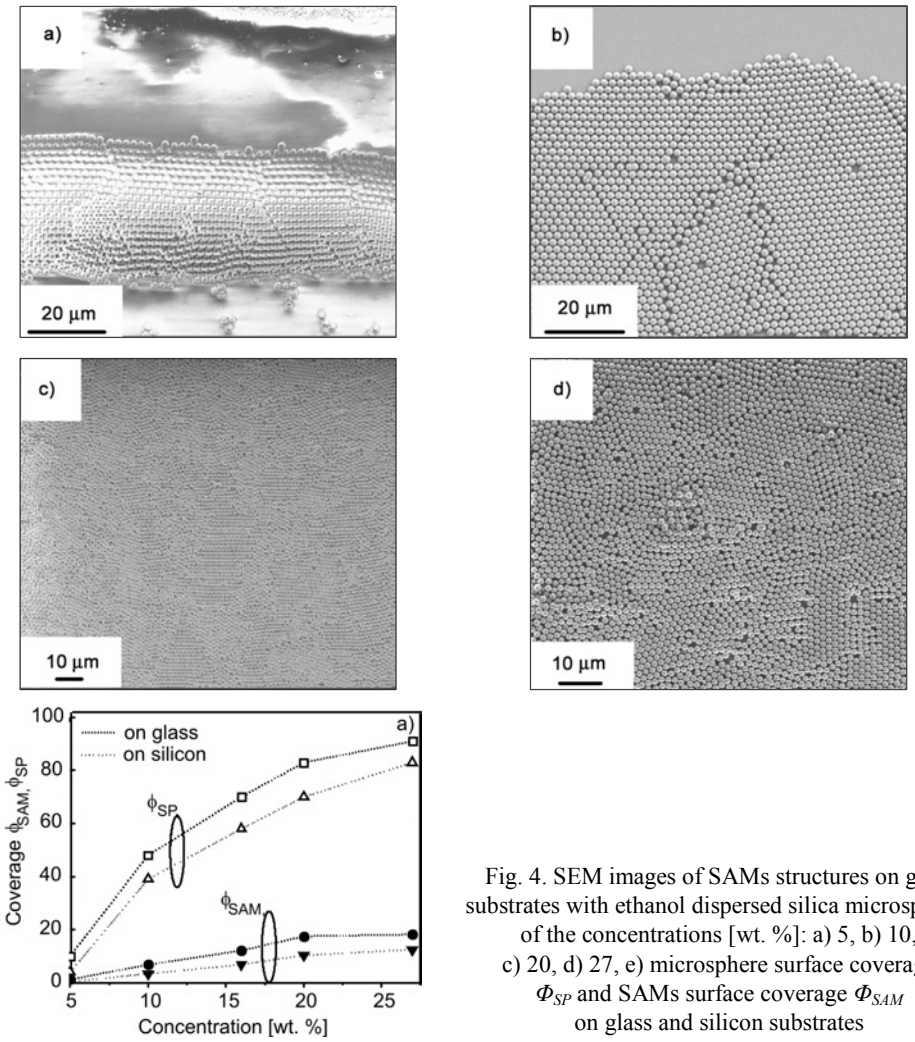

Fig. 4. SEM images of SAMs structures on glass substrates with ethanol dispersed silica microspheres of the concentrations [wt. %]: a) 5, b) 10, c) 20, d) 27, e) microsphere surface coverage Φ_{SP} and SAMs surface coverage Φ_{SAM} on glass and silicon substrates

The impact of the particle concentration in the coating solution was investigated first by varying it from 5 to 27 wt. %, with all other parameters kept constant. Fig-

ure 4e shows the results of the surface coverage of silica microspheres adhered onto the substrate surface, Φ_{SP}, and the surface coverage of the well ordered, closely packed SAMs of silica microspheres on the substrate surface, Φ_{SAM}, for various particle concentrations. With the increase in the particle concentration from 5 wt. % to 20 wt. %, both Φ_{SP} and Φ_{SAM} obviously increased. A further increase in the microsphere concentration, to 27 wt. %, clearly increased Φ_{SP}, but Φ_{SAM} increased only slightly. The structural characterization of self assembled silica microspheres was observed by SEM (Fig. 4a–d). Well ordered closely packed SAMs film is obtained with the 20 % concentration of silica microspheres (Fig. 4c). When the particle concentration is high, more particles adhere to the substrate and large area SAMs are easy to form (Fig. 4d). However, when the particle concentration is low, insufficiently many particles are supplied for a monolayer to form, resulting in scattered stripes (Fig. 4a, b). The conclusion from these experiments is that in dip coating, a proper concentration needs to be found for the fabrication of highly uniform closely packed SAMs of silica microspheres. This is because the concentration of particles in the suspension determines the upward flux of particles, for a given convective flux of liquid [20, 23].

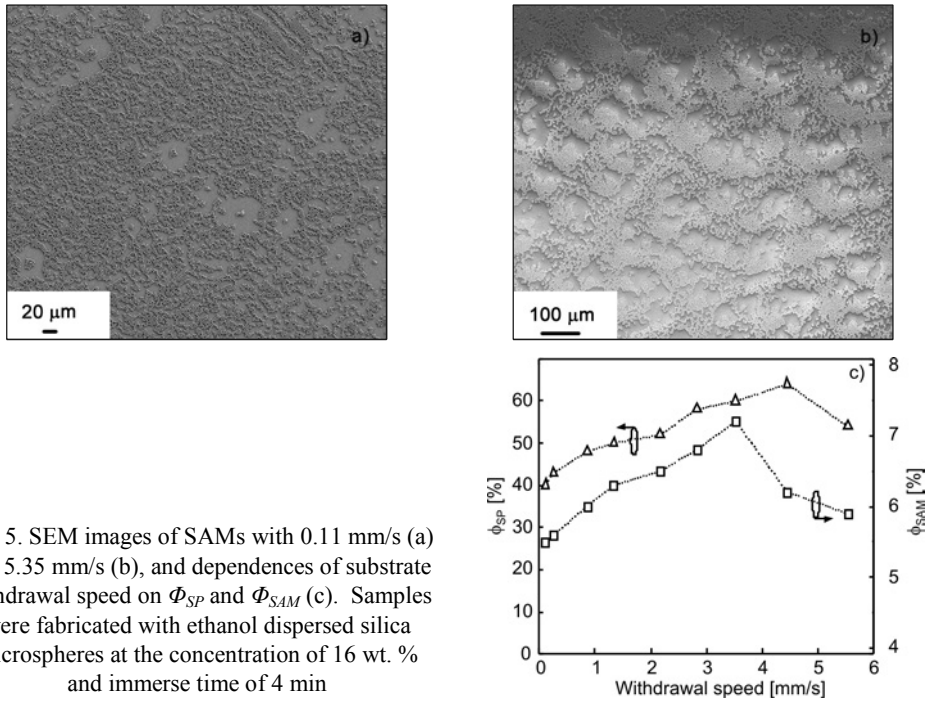

Fig. 5. SEM images of SAMs with 0.11 mm/s (a) and 5.35 mm/s (b), and dependences of substrate withdrawal speed on Φ_{SP} and Φ_{SAM} (c). Samples were fabricated with ethanol dispersed silica microspheres at the concentration of 16 wt. % and immerse time of 4 min

The substrate withdrawal speed, immersion time, relative humidity, type of solvent and substrate material were also investigated. Figure 5c shows the dependence of Φ_{SP} and Φ_{SAM} on the withdrawal speed. The samples were fabricated with ethanol dispersed silica microspheres at the concentration of 16 wt. % and 4 min immersion time. When the withdrawal speed increased from 0.11 to 3.53 mm/s, both Φ_{SP} and Φ_{SAM}

increased. A low withdrawal speed of 0.11 mm/s resulted in stripes of tens or hundreds of microspheres randomly scattered on the substrate (Fig. 5a). The microspheres in the stripes exhibited chaining and short range ordering. This structure was probably formed when the microspheres in the drying film were attracted to each other by capillary forces. Furthermore, narrow regions of multilayers were formed at the bottom of the substrate. Increasing the withdrawal speed resulted in better SAMs of silica microspheres with improved ordering and fewer voids. The stripes began to coalesce into a uniform ordered domain. With withdrawal speed exceeding 3.53 mm/s, Φ_{SAM} began to decrease but Φ_{SP} continued to increase up to a withdrawal speed of 4.45 mm/s. At the withdrawal speed of 5.35 mm/s, only a narrow region of well ordered SAMs was formed at the bottom of the substrate. Beyond that, long stripes and voids were observed, and were probably caused by the extremely rapid withdrawal speed (Fig. 5b). At a more suitable withdrawal speed, the upper region of the meniscus retreats below the height of the particles as the solvent evaporates, exposing the particles. At this moment, the microspheres experience an attractive lateral capillary force from the substrate, allowing the particles to be self assembled into an ordered monolayer array.

The consequences of selecting the optimum immersion time and the optimum relative humidity on the Φ_{SP} and Φ_{SAM} of silica microspheres are shown in Fig. 6. Both Φ_{SP} and Φ_{SAM} increased at first, and then decreased as both the optimum immersion time and the relative humidity were increased. The optimum immersion time of 4 min and relative humidity of 40% were found to yield a maximum for the Φ_{SP}. We observed in our experiments that gravity caused the silica microspheres to sink to the bottom of the suspension, resulting in a concentration gradient of silica microspheres in the suspension. Improved stability of the silica microsphere suspension is important to obtain large area well ordered and closely packed SAM of silica microspheres. For our applications, organic surfactants for the prevention of sedimentation were purposely avoided, since the coating should be fully inorganic in order to achieve the desired transparency and reliability [2].

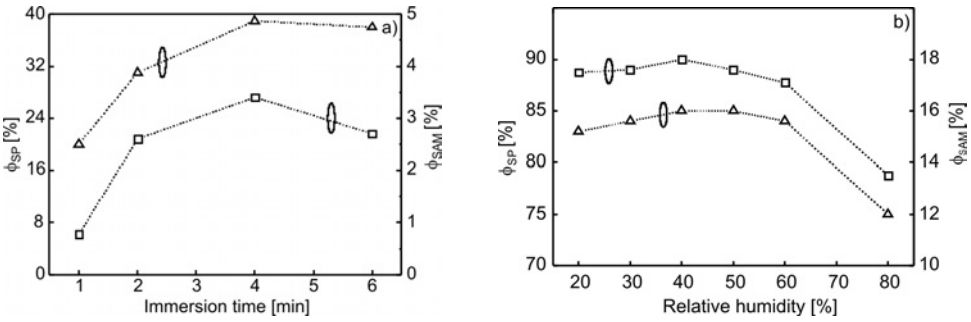

Fig. 6. The impact of the immersion time (a) and the relative humidity (b) on the coating coverage Φ_{SP} and Φ_{SAM}. Samples were fabricated with ethanol-dispersed silica microspheres with 16 wt. % (a) and 20 wt. % concentration (b), 4 min immersion time, and at ambient conditions on the glass substrate

The relative humidity controls the evaporation rate, which affects the motion of particles on the substrate. Figure 7 shows the scheme of impact of the evaporation rate

on the convective flux during dip coating. With low humidity, the evaporation rate is fast, and large convective flux accelerates particles to quickly stick to the substrate before an ordered structure can be achieved. At the same time, the particle flux into the meniscus increases, leading to faster array formation (Fig. 7a). For high humidity and low evaporation rate, the meniscus is thick and no sufficient convective flux exists to force particles upward (Fig. 7b). The particle concentration in the meniscus remains low and surface coverage by silica microspheres decreases.

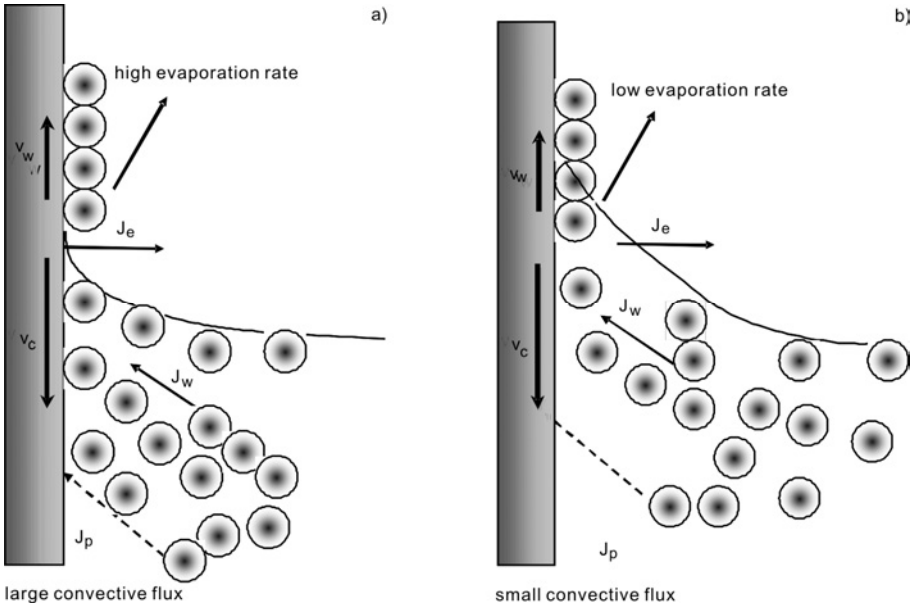

Fig. 7. Impact of the evaporation rate on the convective flux during dip coating

Figure 8 shows the impact of solvent type on SAMs structure. The samples were fabricated at the concentration of 10 wt. %, withdrawal speed 2.82 mm/s and immersion time 2 min on glass substrates. The solvent controls surface tension, evaporation rate and stability of the suspension. When the solvent was ethanol, multilayers were observed at the bottom of the substrate (bottom of Fig. 8a), in addition to well-ordered closely packed SAM structures in the centre. This may be due to fast solvent evaporation as well as high densities of microspheres towards the bottom of the substrate. On the other hand, a disordered loosely packed region was observed above the closely packed region (top of Fig. 8a). Φ_{SP} and Φ_{SAM} increased obviously in the aqueous solution (Fig. 8b), and a large area uniform closely packed SAMs region (centre in Fig. 8b) was sandwiched by loosely-packed monolayer regions, specifically between an upper monolayer and a lower one. The optimum condition for achieving large area well ordered and closely packed SAMs (Fig. 8c) was identified, namely a 1:1 mixture of ethanol and water. This is believed to an optimum balance between solvent evaporation and particle interactions. In the case of water, a solvent with high surface ten-

sion leads a thick meniscus to form, just as shown in Fig. 7a. No sufficient convective flux exists to force the particles upward, since the evaporation of solvent takes longer time. At the same time, the meniscus can still be maintained as the substrate is withdrawn. It is likely that the meniscus breaks into droplets due to its gravity, forming many stripes and islands. In the case of ethanol, a solvent with low surface tension results in a thin meniscus and quick evaporation, as shown in Fig. 7b. Although particles are supplied towards the meniscus, the capillary force between particles is insufficient for the formation of closely packed SAMs over large areas, because of the low surface tension [23].

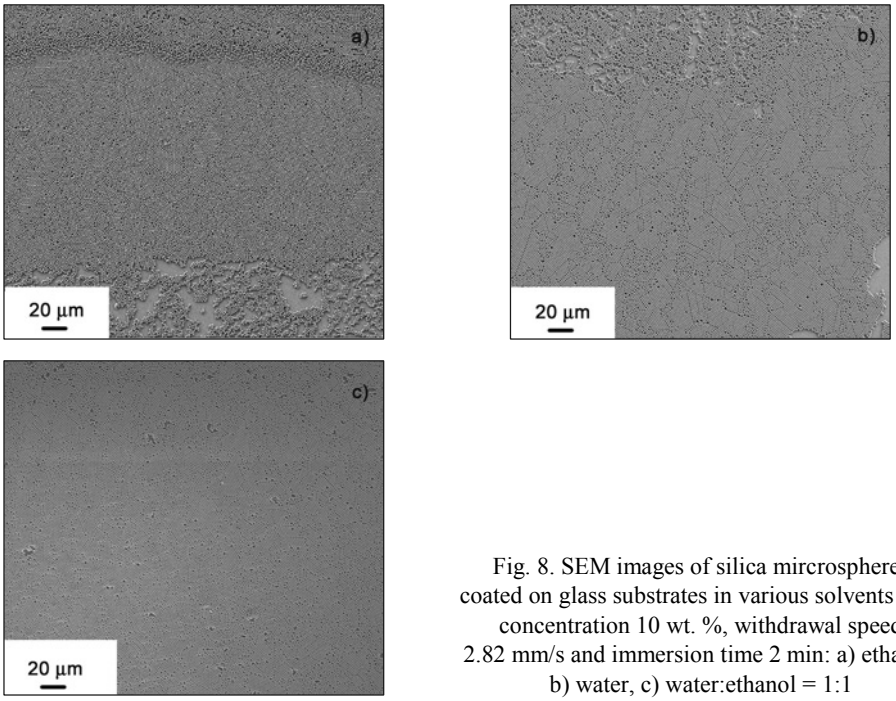

Fig. 8. SEM images of silica mircrospheres coated on glass substrates in various solvents with concentration 10 wt. %, withdrawal speed 2.82 mm/s and immersion time 2 min: a) ethanol, b) water, c) water:ethanol = 1:1

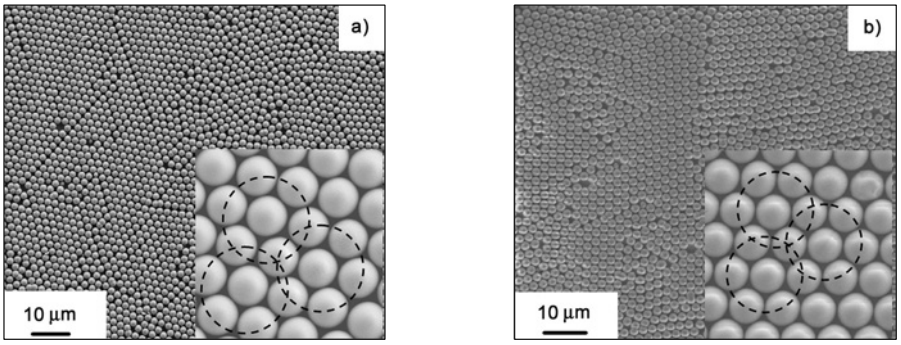

Fig. 9. SEM images of ethanol dispersed silica microspheres with concentration 20 wt. %, immersion time 4 min, relative humidity 40%, and withdrawal speed 2.82 mm/s on (a) silicon and (b) glass substrates

Seen from Fig. 4a, Φ_{SP} and Φ_{SAM} on glass substrates were higher than those on silicon substrates, indicating that the microspheres adhere better to glass than to silicon. Strong interactions between particles and glass probably resulted in more particles binding to the surface of glass, with each microsphere touching six neighbouring microspheres in the monolayer. The average separation of neighbouring microspheres was estimated, and found to be roughly 97 nm on glass substrates and 118 nm on silicon substrates (Fig. 9). This indicates that microspheres can be packed more closely together on glass substrates than on silicon substrates. However, the SAMs structures on glass and silicon substrates are very similar, as seen in Fig. 9.

4. Conclusions

We have demonstrated large area, self assembled monolayers of silica microspheres with the diameter of 2 μm by dip coating, forming uniform well ordered and closely packed SAM structures over areas of 3×0 mm^2 on silicon substrates and 1.5×11 mm^2 on glass substrates. The self assembled structure and its spatial extension are significantly influenced by the concentration of silica microspheres in the suspension, substrate withdrawal speed, substrate immersion time, relative humidity, solvent type and substrate material. A rapid formation of self assembled monolayers of silica microsphere provides a glimpse into a wide range of photonic applications of dip coating, such as large area surface texturing for antireflection coatings in solar cells.

Acknowledgements

We acknowledge financial support from the NSF under grants Nos. DMI-0625728 and IIP-0740147, and AFRL CONTACT Program under agreement No. FA8650-07-2-5061.

References

[1] TAO M., ZHOU W., YANG H., CHEN L., Appl. Phy. Lett., 91 (2007), 081118.
[2] ZHOU W., TAO M., YANG H.CHEN L., J. Appl. Phys., 102 (2007), 103105.
[3] VAN BLAASEREN A., RUEL R., WILTZIUS P., Nature, 385 (1997), 321.
[4] HAN S.E., STEIN A., NORRIS D., Phys. Rev. Lett., 99 (2007), 053906.
[5] NIGHT J.C., BROGENG J., BIRKS T.A., RUSSEL P.S.J., Science, 282 (1998), 1476.
[6] CHO A., Science, 299 (2003), 1685.
[7] HOLTZ J.H., ASHER S.A., Nature, 389 (1997), 829.
[8] PREVO B.G., VELEV O.D., Langmuir, 20 (2004), 2099.
[9] PREVO B.G., HON E.W., VELEV O.D., J. Mater. Chem., 17 (2007), 791.
[10] PREVO B.G., HWANG Y., VELEV O.D., Chem. Mater., 17 (2005), 3642.
[11] ARSENAULT A.C., MIGUEZ H., KITAEV V., OZIN G.A., MANNERS I., Adv. Mater. 15 (2003), 503.
[12] LIN S.Y., FLEMING J.G., EL-KADY I., BISWAS R., HO K.M., J. Opt. Soc. Am. B, 20 (2003), 1538.
[13] CASSAGNEAU T., CARUSO F., Adv. Mater. 14 (2002), 1629.
[14] GOPIDAS K.R., BOHORQUEX M., KAMAT P.V., J. Phys. Chem. 94 (1990), 6435.
[15] WANG D., MÖHWALD H., Adv. Mater. 16 (2004), 244.

[16] HULTEEN J.C., VAN DUYNE R.P., J. Vac. Sci. Technol. A, 13 (1995), 1553.
[17] SHERRINGTON D.C., TASKINEN K.A., Chem. Soc. Rev. 30 (2001), 83.
[18] PARK S.H., XIA Y., Chem. Mater. 10 (1998), 1745.
[19] MICHELETTO R., FUKUDA H., OHTSU M., Langmuir, 11 (1995), 33336.
[20] DIMITROV A.S., NAGAYAMA K., Langmuir, 12 (1996), 1303.
[21] DENKOV N.D., VELEV O.D., KRALCHEVAKY P.A., IVANOV I.B., YOSHIMURA H., NAGAYAMA K., Langmuir, 8 (1992), 3183.
[22] HU M., CHUJO S., NISHIKAWA H., YAMAUCHI Y., OKUBO T., J. Nanoparticle Res., 6 (2004), 479.
[23] KO H.-Y., LEE H.-W., MOON, J., Thin Solid Films, 447-448 (2004), 638.
[24] QIN Q., XIA Y., XU B., YANG H., ZHOU C., WHITESIDES M., Adv. Mater. 11 (1999), 1433.

Received 13 April 2009

Materials Science-Poland, *Vol. 28*, *No. 2*, *2010*

HRTEM nanostructural evolution of onion-like spheres in polyacrylonitrile fibres during stabilization and carbonization

Y. WEN[1, 2], H. LI[1], G. PENG[1, 2], Y. YANG[1*], L. LIU[1]

[1]Key Laboratory of Carbon Materials, Institute of Coal Chemistry, Chinese Academy of Sciences, Taiyuan 030001, China

[2] Graduate University of the Chinese Academy of Sciences, Beijing 100049, China

Ultrathin sections of polyacrylonitrile (PAN) fibre samples in the stabilization and carbonization stages were studied using high-resolution transmission electron microscopy. Supplementary analyses by the Fourier transform infrared, X-ray diffraction, thermogravimetry mass spectroscopy and elemental analysishave also been done. Results showed that the PAN fibres contained nanosized crystallites embedded in a continuous amorphous matrix. Amorphous onion-like spherical structures were also observed and their structural evolution was investigated. During the stabilization and carbonization process, the outer layers of the onion-like spheres gradually changed from an orderly layered structure into a disordered, dense structure due to cyclization and cross-linking reaction. During carbonization, the onion-like spheres became more dense and compact due to the merging of the ring structures. After carbonization, the onion-like spheres in the PAN fibres eventually turned into dense and amorphous domains of carbon fibres.

Keywords: *high resolution transmission electron microscopy; carbon fibre; onion-like sphere*

1. Introduction

Polyacrylonitrile (PAN) based carbon fibre is one of the most important fibre-reinforcing materials for composites, due to its high strength, high modulus and excellent chemical stability [1, 2]. During stabilization and carbonization, PAN fibres undergo major structural changes and transform from organic into inorganic phase [3]. The performance of carbon fibres is determined by their structure, which is usually investigated by XRD, scanning electron microscopy (SEM), atomic force microscope (AFM), field emission scanning electron microscopy (FESEM), transmission electron microscopy (TEM) and high-resolution transmission electron microscopy (HRTEM) [4–12].

Studies have been conducted on the structures of carbon fibres and their precursors. Mukesh et al. [13] have shown that, in the XRD spectra of carbon fibres during stabiliza-

*Corresponding author, e-mail: yangyg@sxicc.ac.cn

tion and carbonization, the diffraction peak at the angle $2\theta = 17°$ gradually decreased with the evolution of a broad peak at the angle $2\theta = 25.5°$, indicating that the structure of the PAN fibre was transformed from a crystalline to an amorphous state. Structural data such as the interplanar spacing and crystal parameters can also be obtained from the Bragg and Scherrer equations. Although XRD provides structural information averaged over a large region, it is not capable of giving insight into the precise nanostructure morphology, and thus cannot provide detailed information about the amorphous structure.

In contrast, HRTEM has become a powerful tool for investigating the microstructure of materials. Using HRTEM, Benneit et al. [10] directly obtained the interplanar spacing and stacking thickness of the crystalline structures in an ultrathin slice of high modulus carbon fibres. Bai et al. [11] also observed the coexistence of crystalline and amorphous regions in the PAN precursor using HRTEM which supported the structural model of the PAN nanostructure proposed by Warner et al. [14], and confirmed the appearance of amorphous onion-like spherical structures in PAN fibres. While XRD studies have shown that the microstructure of the PAN precursor was transformed from the crystalline to the amorphous state, we considered that it would be informative to probe into the evolution of the amorphous domains in PAN fibres, particularly the onion-like spherical structure, during stabilization and carbonization, in order to examine the mechanisms of such processes. Thus ultrathin sections of PAN fibre samples in stabilization and carbonization stages were studied using HRTEM, FTIR, XRD, TGMS and EA.

2. Experimental

PAN precursor fibres were prepared by a dry-jet wet spinning method. The spinning solution consisted of 20% copolymer of acrylonitrile and itaconic acid. The copolymer was prepared by free radical polymerization in dimethyl sulfoxide. 2,2-azobisbutyronitrile was used as the initiator. The copolymer consisted of 99% acrylonitrile and 1% itaconic acid. The average molecular weight of PAN was ca. 1.6×10^5. The solution was extruded through a spinneret and drew in a coagulation bath and water steam with a total drawing ratio of 1500%. Each single tow of PAN fibre had 1000 filaments, with each filament having the diameter of 11 μm. Stabilization was conducted at 230 °C, 250 °C, 270 °C, and 290° C in four stabilization furnaces with about one hundred meters at each stage in air. The subsequent carbonization used low and high temperatures of 300–900 °C and 1200–1400 °C, respectively, under nitrogen.

For the HRTEM experiments, fibre bundles were embedded in epoxy resin and cut with a Reichert–Jung instrument with transverse sections. The thickness of a slice was lower than 30 nm. The specimens, supported on copper microgrids, were examined using a Philips Tecnai 20U-Twin high resolution transmission electron microscope. The accelerating voltage was 200 kV.

For FTIR analysis, a Fourier transform infrared spectrometer, model EQUINOX55, Germany Bruker Inc., was used. For TG analysis, a thermogravimetric ana-

lyzer (SETARAM TGA92 model) and a mass spectrometer (MS OmniStar 200, Balzers Inc., Switzerland) were used. TG-MS was carried out under ultra high purity argon (99.999%) at a low pressure of 150 kPa. For XRD analysis, the samples were characterized using a Rigaku-D/max-RA rotating anode X-ray diffractometer from Japan (CuK_α radiation, voltage 40 kV, current 150 mA, graphite crystal monochromator, four slit collimation system with the scanning range 2θ from 10° to 40° and step size 2θ 0.05°. For EA analysis, an elemental analyzer (Vario EL III elemental Analysensysteme GmbH) was used.

3. Results and discussion

3.1. Characterization of PAN precursor fibres

HRTEM images of the ultrathin slices of PAN fibres are shown in Fig. 1. Fig. 1a shows a low magnification nanostructure of PAN precursor. A small piece of ultrathin

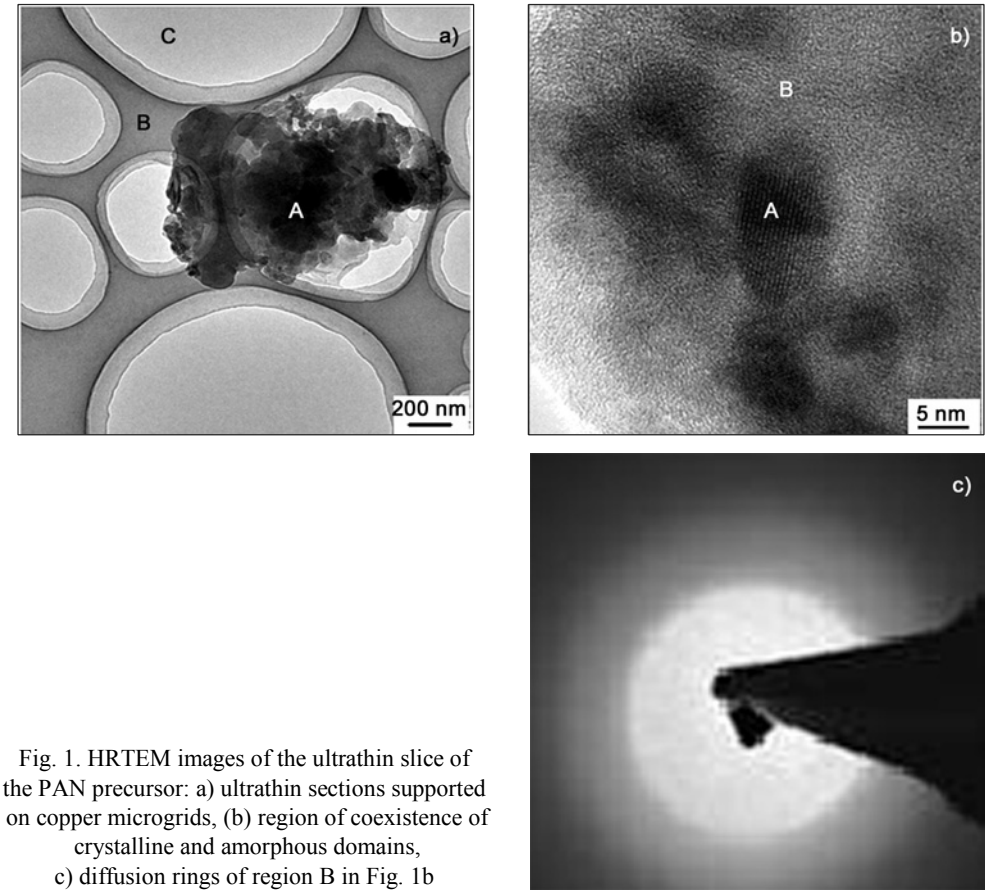

Fig. 1. HRTEM images of the ultrathin slice of the PAN precursor: a) ultrathin sections supported on copper microgrids, (b) region of coexistence of crystalline and amorphous domains, c) diffusion rings of region B in Fig. 1b

sections (region A in Fig. 1a), not a whole section of PAN fibre, is supported on the copper microgrids (region B in Fig. 1a). Region C in Fig. 1a is a hole of the copper microgrids. In a high magnification image, the coexistence of crystalline and amorphous regions was observed in the PAN precursor (Fig. 1b). Region A in Fig. 1b was a crystalline domain, as indicated by the crystal lattice, and interplanar spacing could be distinguished from the picture. The crystalline domain appeared to be a few nanometers in size. Region B in Fig. 1b had diffuse rings (Fig. 1c) in the electron diffraction pattern, indicating its non-crystalline organization. Fig. 1 also indicated that the amorphous domains in the nanostructures of the PAN fibres formed a continuous phase, whereas small crystalline particles were embedded in the amorphous matrix.

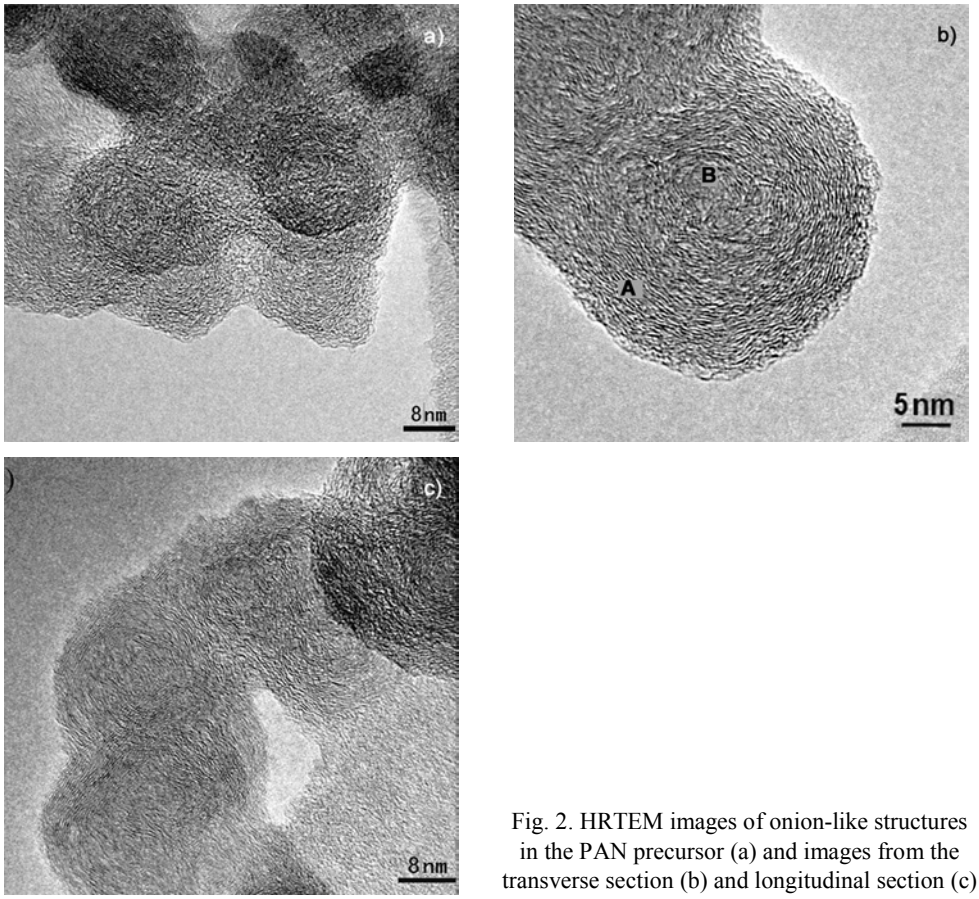

Fig. 2. HRTEM images of onion-like structures in the PAN precursor (a) and images from the transverse section (b) and longitudinal section (c)

More or less circular structures were also observed in the HRTEM images (Fig. 2). Electron diffraction patterns indicated that the structures were amorphous. To distinguish the detailed circular structure further, longitudinal sections of PAN fibre were also investigated (Fig. 2c), which showed similar circular structures. This indicated that the circular structures are spheres instead of cylinders, as also reported Bai

et al. [11]. The spheres actually have an onion-like structure, because the cores of the spheres (region B in Fig. 2b) were randomly organized, whereas in the outer layers, presumably, diametric sections (in region A in Fig. 2b) were more ordered. It is suggested that the onion-like spheres were transition phases between the crystalline structure and disordered amorphous structures.

Although the mechanism of the formation of the onion-like structures remains unknown, it is likely that the dipole–dipole interactions between nitrile groups in PAN are involved. In early stages of polymerization, intramolecular repulsion of nitrile groups results in the as-formed PAN molecules having a randomly arranged structure. As the polymerization proceeded, the attraction between the nitrile groups in the preformed and newly formed PAN molecules allowed the formation of circular layers surrounding the core [11].

3.2. Onion-like structures at various stages of stabilization

3.2.1. Onion-like structures after stabilization at 230 °C

The colour of PAN fibres changed from white to yellow after stabilization at 230 °C. Figure 3 shows FTIR spectra of PAN fibres at various stabilization stages.

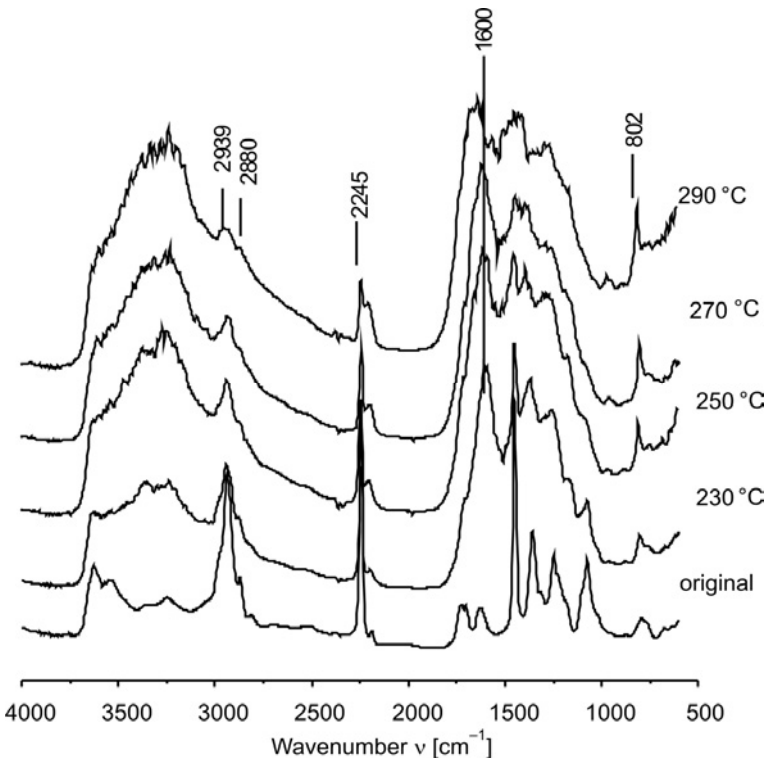

Fig. 3. FTIR spectra of PAN fibres at various stabilization stages

After stabilization at 230 °C, the intensity of the local peak at 2245cm^{-1}, assigned to –C≡N bond, decreased and new groups of vibrations around 1600 cm^{-1} (due to –C=N, –C=C, N–H mixed modes) appeared, and the intensity of the band at 810cm^{-1} (–C=CH) increased. All the above facts indicated that the cyclization had occurred. Cyclization reactions brought about the transformation of the microstructure of PAN from a linear structure to a ring one. The scheme of the cyclization of PAN fibres is as follows:

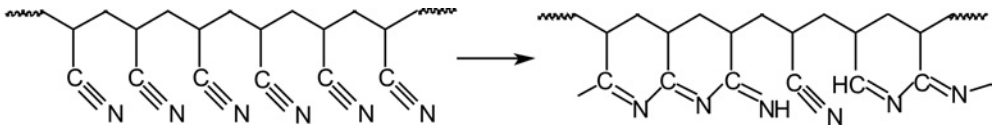

Previous XRD studies showed that in this stage, the cyclization occurred only in the amorphous regions of PAN fibres [15, 16]. However, no obvious changes in the onion-like structures were observed in the HRTEM images (Fig. 4). Regular organization of onion-like structures remained (the outer layer was ordered and the core was unordered). This suggested that the cyclization occurred only in completely disordered amorphous areas at 230 °C but not in the onion-like spheres.

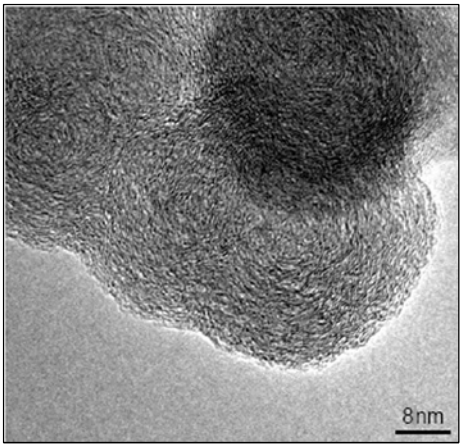

Fig. 4. HRTEM image of the onion-like structure after stabilization at 230 °C from the longitudinal section (close to the centre)

3.2.2. Onion-like structures after stabilization at 250 °C

A high magnification image of PAN fibres after stabilization at 250 °C (Fig. 5) showed a different onion-like sphere shape, compared with that at 230 °C. A relatively ordered region (B) between the disordered outer layer (A) and core region (C) is seen in Fig. 5. Presumably, during stabilization at 250 °C, cyclization began to occur from the completely disordered amorphous areas to onion-like spheres. Moreover, it mainly occurred at the outer layer of the onion structure, where the PAN molecules had more spatial flexibility. The microstructure of the PAN of the outer layer of the onion changed from a linear to a ring one, which resulted in the disappearance of the interchain dipole–dipole interaction between the nitrile groups, and changed the outer layer into a disordered, non-compact structure.

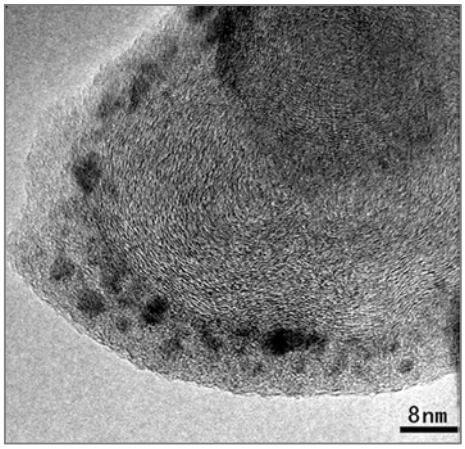

Fig. 5. HRTEM image of the onion-like structure after stabilization at 250 °C from the longitudinal section (close to the centre)

The scheme of the disappearance of dipole–dipole interactions between nitrile groups is as follows:

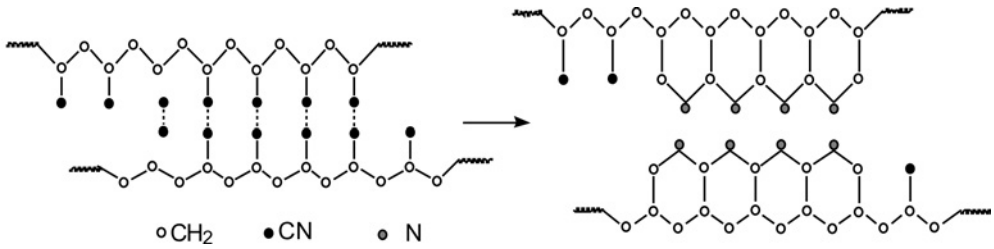

3.2.3. Onion-like structures after stabilization at 270 °C

After stabilization at 270°C (Fig. 6), both the entire outer layer and the core region of the onion-like structures appeared to be disordered, and the outer layer was very loose.

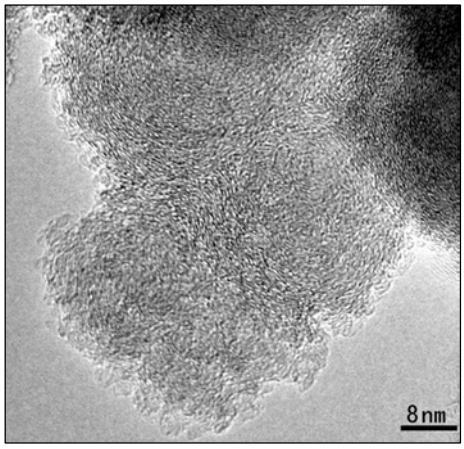

Fig. 6. HRTEM image of the onion-like structure after stabilization at 270 °C from the longitudinal section (close to the centre)

Figure 7 presents the XRD scans of PAN fibres in various stabilization stages. Precursor fibres gave two equatorial peaks at the Bragg angle $2\theta = 17°$ and $2\theta = 29°$.

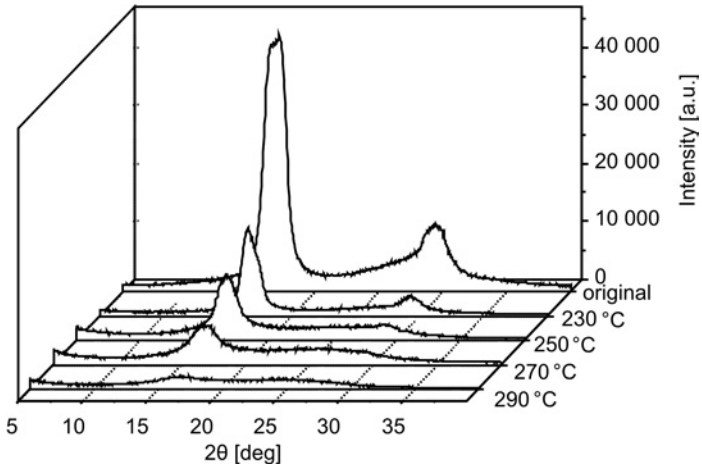

Fig. 7. XRD scans of PAN fibres at various stabilization stages

However, as the stabilization proceeded, the diffraction peak at $2\theta = 17°$ and $2\theta = 29°$ gradually decreased with the evolution of a broad peak at $2\theta = 25.5°$, and the diffraction peak almost disappeared at 270 °C, indicating that the structure of the PAN fibre was transformed into an amorphous one. It can be concluded from FTIR results (Fig. 3) that–C≡N groups had almost changed to –C=N groups. These suggested that the cyclization reaction was almost complete in the onion-like structures and that the attraction between the –C≡N groups had completely disappeared.

3.2.4. Onion-like structures after stabilization at 290 °C

After stabilization at 290 °C (Fig. 8), the core and outer layers of the onion-like spheres were more compact than those after stabilization at 270 °C (Fig. 6). It is most

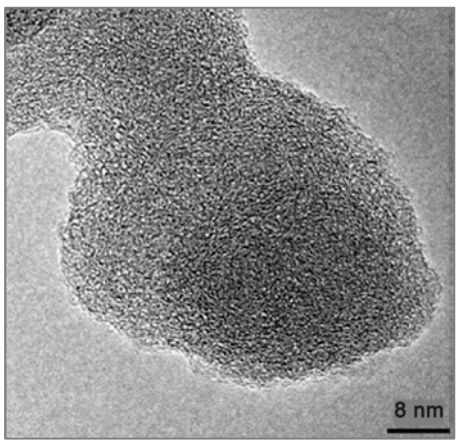

Fig. 8. HRTEM image of the onion-like structure after stabilization at 290 °C from the longitudinal section (close to the centre)

probable that at the end of the stabilization, chemical cross-linking occurred inside the onion-like structures, resulting in the shrinkage of the onion-like spheres from a loose, ring structure to a dense, cross-linked one. The FTIR and XRD spectra (Figs. 3, 7) have shown that some chemical processes occurred in the stabilization. For example, reaction of –C≡N resulted in conjugated –C=N bonds containing structures obtained by intermolecular cross-linking. The cross-linking reaction is very complex; one of its typical schemes is as follows:

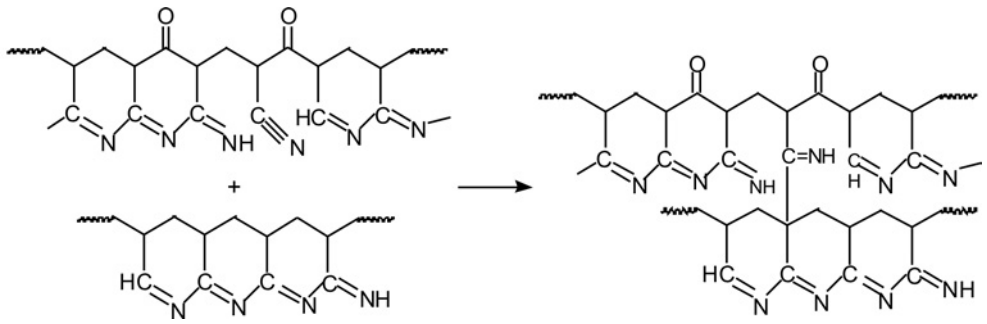

The investigation of the nanostructure evolution of PAN fibres at various stages of stabilization showed that at 230 °C, the cyclization occurred only in the complete disordered amorphous region. At 250 °C, this reaction extended into the amorphous region of the onion structures. The cyclization in the amorphous region was completed at 270 °C. When the stabilization was completed at 290 °C, the cross-linking reaction also occurred in the core of the onion-like structures, forming a densely organized structure.

3.3. Onion-like structures after carbonization

The stabilized PAN fibres were allowed to undergo further low temperature and high temperature carbonization. Table 1 presents the C, N and O contents after stabilization as well as after low- and high temperature carbonization. SF is a stabilized fibre, LTCF is a low temperature carbonized fibre and HTCF is a high temperature carbonized fibre.

Table 1. C, N and O contents [%] in the fibre after stabilization and low and high temperature carbonization

Fibre	C/	N/	O/
SF	63.41	23.20	7.78
LTCF	73.75	17.89	2.63
HTCF	94.26	4.84	<0.3*

*Below the detection limit of the instrument.

The content of C increased gradually, while the N and O contents decreased as the carbonization process progressed. The C content increased to 94.26% after high temperature carbonization at 1300 °C, which indicated that the PAN fibres had become completely carbon fibres. Onion-like structures were still observed in the carbon fibres (see Fig. 9), but they changed completely, compared with those in the original PAN precursor.

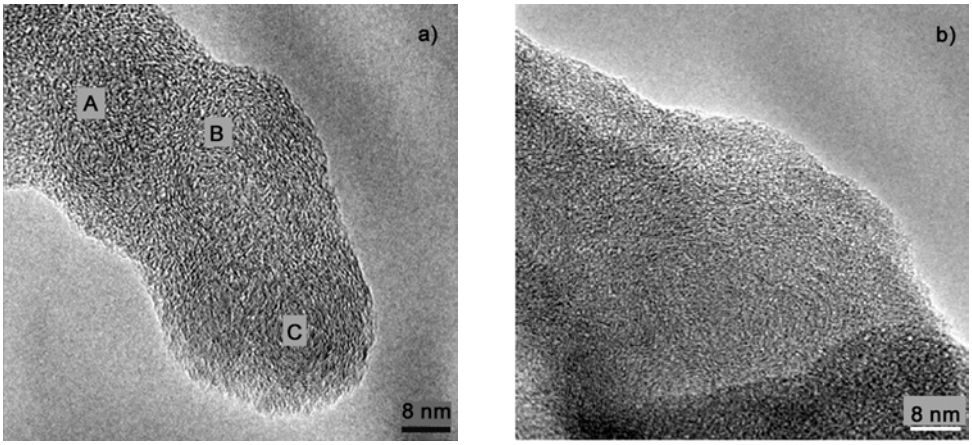

Fig. 9. HRTEM images of various onion-like structures after carbonization from longitudinal section (close to the centre, details in the text)

HRTEM images showed that the overlapping regions disappeared (Fig. 2a, c) and the onion-like structures merged, due to the further cross-linking reaction. As shown in Fig. 9a, three onion-like spheres (A, B, C) merged into an integrated structure. The interfaces of the onion structures were barely visible. Densely organized structures were also observed (Fig. 9b), probably due to the formation of a large flat carbon network from the combination of ring structures. The scheme of the formation of the cyclized and cross-linked structure is as follows:

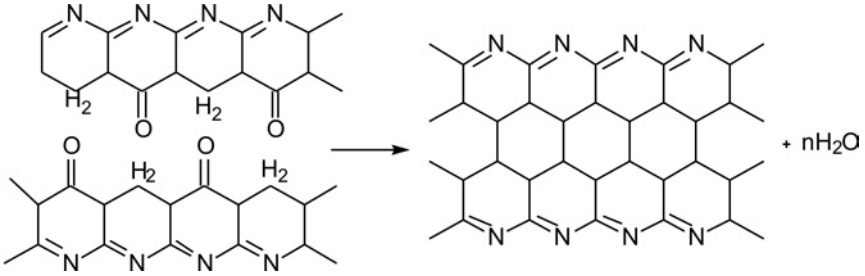

The hypothesis of the formation of large flat carbon network was confirmed by the result of TGMS analysis. The H_2O (*m*/*z* 18) MS signal in arbitrary units measured by TGMS during the carbonization of PAN fibres is shown in Fig. 10. As can be seen, the loss of H_2O occurred at two different stages. The first peak at 150 °C was attributed to

the loss of absorbed water. The second peak was formed due to the chemical loss of water, which testified, indirectly, to the formation of large flat carbon networks during the carbonization process of PAN fibres.

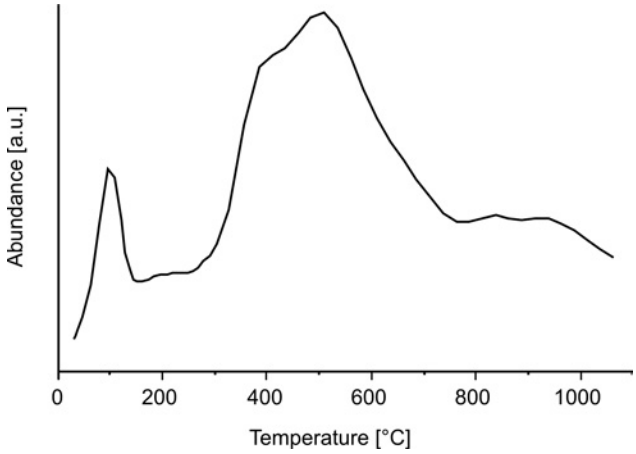

Fig. 10. MS response of H_2O of TG-MS analysis of PAN fibres after stabilization at 290°C

4. Conclusions

Ultrathin sections of PAN fibre samples at various stabilization and carbonization stages were studied by HRTEM and other methods of analysis. At the nanoscopic level, nanometer scale crystals embedded in a continuous amorphous phase were found in the PAN fibre. The investigation of the structural evolution of PAN fibres at various stages of stabilization showed that at 230 °C the cyclization only occurred in the complete disordered amorphous region. At 250 °C, this reaction extended into the onion-like structure, and the outer layer of that structure became disordered. The cyclization in the amorphous region was almost complete at 270 °C. In this stage, both the outer layer and the core region of the onion-like structures were disordered and loose. After the completion of stabilization at 290 °C, the cross-linking reaction also occurred in the core of the onion-like structures and a densely organized structure was formed, due to the shrinkage effect.

Although the borders were barely visible, due to the merger of the ring structures, onion-like spheres were still observed in the carbon fibres. Furthermore, the onion-like spheres became more dense and compact. The onion-like spheres in the PAN fibres eventually turned into dense and amorphous domains of the carbon fibres.

Acknowledgements

This work was financially supported by the National High Technology Research and Development Program of China (863 Program), and the National Basic Research Program of China (973 Program).

References

[1] CHEN J.C., HARRISON I.R., Carbon, 40 (2002), 25.
[2] TSAI J.S., J. Polym. Res., 4 (1994), 399.
[3] BAHL O.P., SHEN Z.M., LAVIN J.G., ROSS R.A., *Manufacture of Carbon Fibres*, Marcel Dekker, New York, 1998.
[4] GUPTA A., HARRISON I.R., Carbon, 34 (1996), 1427.
[5] DEURBERGUE A., OBERLIN A., Carbon, 30 (1992), 981.
[6] ZHANG W.X., WANG Y.Z., SUN C.F., J. Polym. Res., 14 (2007), 467.
[7] GE H.Y., LIU J.J., CHEN J., WANG C.G., J. Polym. Res., 14 (2007), 91.
[8] YU M.J., WANG C.G., BAI Y.J., JI M.X., XU Y., Polym. Bull., 58 (2007), 933.
[9] DILSIZ N., WIGHTMAN J.P., Carbon, 37 (1999), 1105.
[10] BENNEIT S.C., JOHNSON D.J., MURRAY R., Carbon, 14 (1976), 117.
[11] BAI Y.J., WANG C.G., LUN N., WANG Y. X., YU M.J., ZHU B., Carbon, 44 (2006), 1773.
[12] HE D.X., WANG C.G., BAI Y.J., LUN N., ZHU B., WANG C.G., J. Mater. Sci., 42 (2007), 7402.
[13] MUKESH K., JAIN A., ABHIRAMAN S., J. Mater. Sci., 22 (1987), 278.
[14] WARNER S.B., UHLMANN D.R., PEEBLES L.H., J. Mater. Sci., 14 (1979), 1893.
[15] WANG P.H., LIU J., YUE Z.R., LI R.Y., Carbon, 30 (1992), 1113.
[16] CHATTERJEE N., BASU S., PALIT S.K., MAITI M.M., J. Polym. Sci., Part B: Polym. Phys., 33(1995), 1705.

Received 8 May 2009
Revised 4 November 2009

Materials Science-Poland, *Vol. 28*, *No. 2*, *2010*

Humidity sensing properties of TiO_2–Sb_2O_5 nanocomposite

A. K. SRIVASTAVA, B. C. YADAV*

Nanomaterials and Sensors Research Laboratory, Department of Physics,
University of Lucknow, Lucknow-226007, India

The syntheses of TiO_2–Sb_2O_5 (AT) composites were investigated by the conventional precipitation method and their use as humidity sensors. 2–50 wt. % of Sb_2O_5 was added to TiO_2 and pellets were made under the pressure of 616 MPa a room temperature of 30ºC. The pellets were annealed at various temperatures (200, 500, 700 and 800 °C) for 3 h and the humidity sensing properties of each pellet were studied. A saturated aqueous solution of potassium sulphate was used as the humidifier and a saturated solution of potassium hydroxide was used as the dehumidifier. Upon increasing relative humidity (*RH*) inside the test chamber, the resistance of each pellet decreased for the *RH* range from 10% to 95%. Samples of the sensor material, differing in the percentage of the additive, were subject to SEM and XRD analysis. The minimum grain size, estimated from SEM, was 30 nm and the minimum crystallite size from XRD data was 20 nm. The material was found to have suitable properties to be applied as a resistive humidity sensor operating over the entire humidity range.

Keywords: *titania; humidity; nanocomposite; resistance; sensor; adsorption*

1. Introduction

TiO_2 is an important technological material used in electronic [1], electrical [2, 3], optical [4–6] and catalytic devices [7, 8] due to of its high electric permittivity, large birefringence, chemical stability and high photocatalytic activity. Physical properties of TiO_2 have been the subject of various investigations in terms of its suitability for various applications. TiO_2 occurs in three crystalline polymorphs: rutile, anatase and brookite, rutile being the most stable phase. Doping with impurities such as In, Cr, Cd, Fe and Co can change the magnetic and semiconducting properties of TiO_2. Among various oxide semiconductors, titania appears promising and important for the use in environmental purification, due to its strong oxidizing power, non-toxicity and long

*Corresponding author; e-mail: balchandra_yadav@rediffmail.com

term photostability. Many authors studied the synthesis, structure, and humidity sensitive electrical conduction of material containing TiO_2 [7–18].

We have already reported on the humidity sensing properties of pure TiO_2, but reproducibility was poor and the ageing effect was 91% during six months of observations. Therefore in order to improve the quality and sensing characteristics of humidity sensor, TiO_2–Sb_2O_5 (AT) composite has been investigated as the sensing material, fabricated by the conventional precipitation method. Sb_2O_5 was mixed with TiO_2 in various proportions and the dependence of the resistance on the humidity was measured.

2. Operating principles of the sensor

Ceramic humidity sensors exhibit chemical resistance [19]. The conductivity of such sensing materials depends on the amount of adsorbed water vapour. This principle is employed for the measurement of humidity in resistive type humidity sensors. This type of sensors can be subdivided into ionic-type and electronic-type humidity ones, depending on their conduction mechanism. The sensing mechanism generally accepted for porous oxides at room temperature is of the ionic type. Morimoto et al. [20] established that the changes in impedance of porous ceramics dependent on environmental humidity are related to the mechanism of water adsorption on the oxide surface. At low humidities, conduction is due to proton hopping between hydroxyl ions on the first layer of chemisorbed water, while at higher humidities, protons hop between physisorbed molecules according to the Grotthuss chain reaction mechanism. The morphology of the sensing element influences water vapour adsorption and desorption. The condensation of water vapour occurs as a result of capillary action. The behaviour of this condensation is a function of ceramic pore size and their distribution.

The sensitivity S of a humidity sensor has been defined as a change in resistance ΔR of a sensing element per unit change in relative humidity RH

$$S = \frac{\Delta R}{\Delta RH}$$

The porosity P of the material was determined from its density, according to the following expression:

$$P = \frac{\rho_{th} - \rho_m}{\rho_{th}} \times 100\%$$

where ρ_{th} ρ_m are the theoretical and measured densities, respectively. The theoretical densities of anatase and rutile TiO_2 are 3.84 and 4.24 g·cm^{-3}, respectively. Since the specimen is a circular pellet, the density was determined by measuring its volume and weight.

3. Experimental

Preparation of the sensing element. For fabrication of the sensing element, $SbCl_3$ was mixed with deionized water and stirred for 3 h. The precipitate was filtered and washed several times with deionized water in order to remove chloride ions. After drying, the powder was added to titania in the proportion 2, 5, 10, 20, 30, 40 and 50 wt. %. On vigorous grinding of the material, using a mortar and pestle, for 6 h, a very fine powder was produced. Pellets of this material were then subject to the pressure of 616 MPa at room temperature, using a hydraulic pressing machine. Each pellet was 9 mm in diameter, 5 mm thick. The pellets were annealed at various temperatures (200, 500, 700 and 800 °C) for 3 h inside an electric furnace. Each pellet was secured in an electrode holder and was exposed to various humidities in a humidity chamber. Resistances in function of humidity were measured using a digital multimeter (VC 9808, India). Relative humidity was measured using a standard hygrometer (Huger, Germany). The minimum hygrometer reading in our tests was $RH = 1$ %.

Surface morphology and crystal structure. Surface morphology was studied using a scanning electron microscope (SEM, LEO-0430, Cambridge). The micrographs shown in Figs. 1–5 reveal that molecules of TiO_2–Sb_2O_5 are agglomerated, of uniform size, equally distributed and highly porous, having the grain size of 30–120 nm and the average pore size of 80 nm. Higher porosity increases the surface-to-volume ratio of the material and, therefore, improves the sensitivity of the sensor material. Figure 1 shows SEM of 2% AT nanocomposite: clusters with small pores can be seen. In the SEM of 5% AT nanocomposite (Fig. 2) clusters with improved pores were identified. Figures 3 and 4 show SEM of 10% AT and 30% AT nanocomposites, respectively. Grains are less agglomerated and pore sizes increase. In the SEM of 50% AT nanocomposite (fig. 5), uniform flower-like morphology can be seen. Pores are largest in this photograph.

X-ray diffraction data, obtained with an X-Pert PRO XRD system (Netherland), having a CuK_α radiation source with the wavelength of 1.54 Å, shows the extent of crystallization of the TiO_2–Sb_2O_5 sensing element, annealed at 700 °C; the pattern is shown in Fig. 6. It reveals that the sensing material consists of titania and antimony oxide. Analysis shows that TiO_2 exists in an excess amount. Its peaks occur at 2θ values of 25.3, 37.0, 37.8, 38.6, 48.0, 53.9, 55.1, 62.2, 62.8, 70.4 and 74.1°. These peaks have d values of 3.513, 2.429, 2.378, 2.330, 1.890, 1.699, 1.664, 1.492, 1.480, 1.336 and 1.279 Å, with corresponding planes (101), (103), (004), (112), (200), (105), (211), (213), (204), (220) and (107), respectively. Peaks for Sb_2O_5 exist at 2θ values of 15.0, 24.6, 29.0, 30.3, 35.1, 46.1, 50.5, 53.0, 60.0 and 68.7°, with corresponding planes (111), (220), (311), (222), (400), (511), (440), (531), (622) and (642). The d values for these peaks are found to be 5.900, 3.613, 3.081, 2.950, 2.555, 1.967, 1.807, 1.728, 1.540 and 1.366 Å, respectively. Using the well known

Debye–Scherrer formula, the crystallite size was calculated (Table 1). The minimum size of the crystallite was found to be 20 nm, corresponding to the (531) plane, and maximum size was 112 nm, corresponding to the (112) plane.

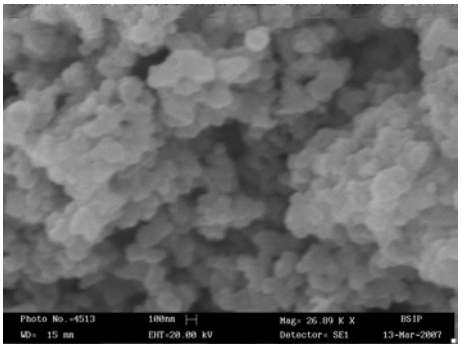

Fig. 1. Scanning electron micrograph of 2% AT nanocomposite

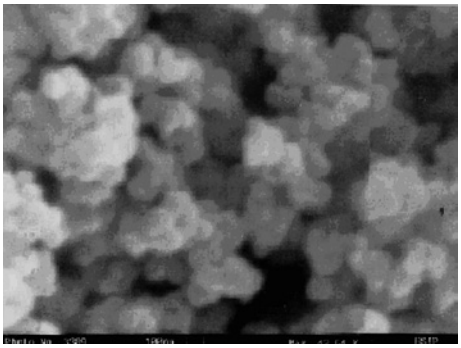

Fig. 2. Scanning electron micrograph of 5% AT nanocomposite

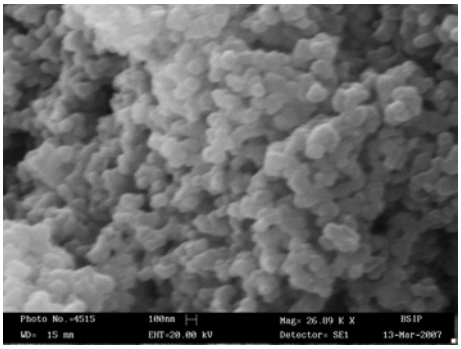

Fig. 3. Scanning electron micrograph of 10% AT nanocomposite

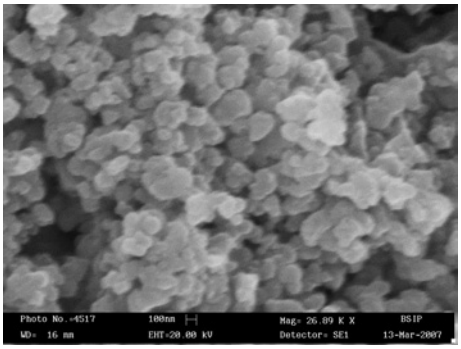

Fig. 4. Scanning electron micrograph of 30% AT nanocomposite

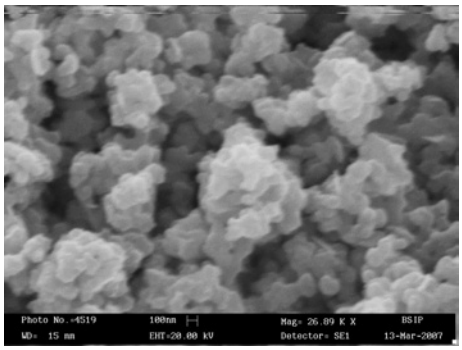

Fig. 5. Scanning electron micrograph of 50% AT nanocomposite

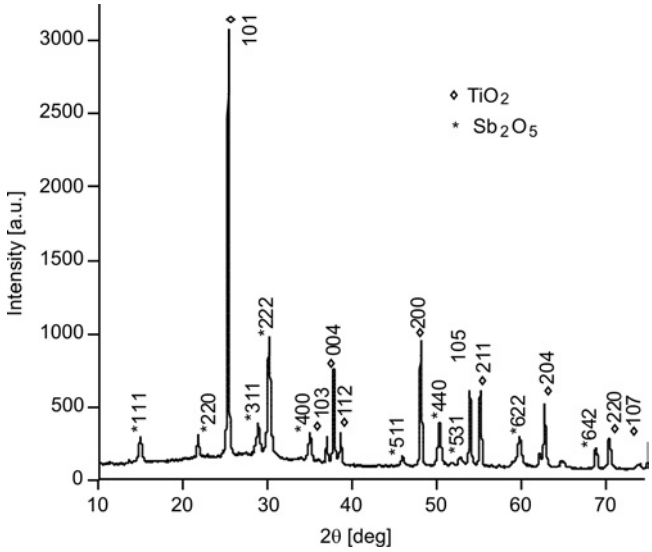

Fig. 6. X-ray diffraction pattern of 50% AT nanocomposite annealed at 700 °C

Table 1. Particles sizes calculated for various peaks with corresponding 2θ and FWHM values for 50% AT annealed at 700 °C

2θ [deg]	FWHM (β)	D [nm]
15.0	0.2204	38
24.6	0.0945	88
25.0	0.0945	90
29.0	0.1574	55
30.3	0.1417	61
35.1	0.2204	40
37.0	0.0787	111
37.8	0.0945	93
38.6	0.0787	112
46.1	0.3149	29
48.0	0.1152	79
50.5	0.2304	40
53.0	0.4608	20
54.0	0.1344	69
55.0	0.1152	81
60.0	0.3072	31
62.2	0.1152	84
62.8	0.1536	63
68.7	0.1920	52
70.4	0.1536	66

Device assembly. The device assembly is shown in Fig. 7a, and a schematic diagram of the pellet holder is shown in Figure 7b. The Cu–pellet–Cu electrode arrange-

ment is fixed on a non-conducting base inside the chamber such that the connecting wires remain outside the chamber. A saturated aqueous solution of potassium sulphate, increasing the humidity, is placed in a small container inside the steel chamber.

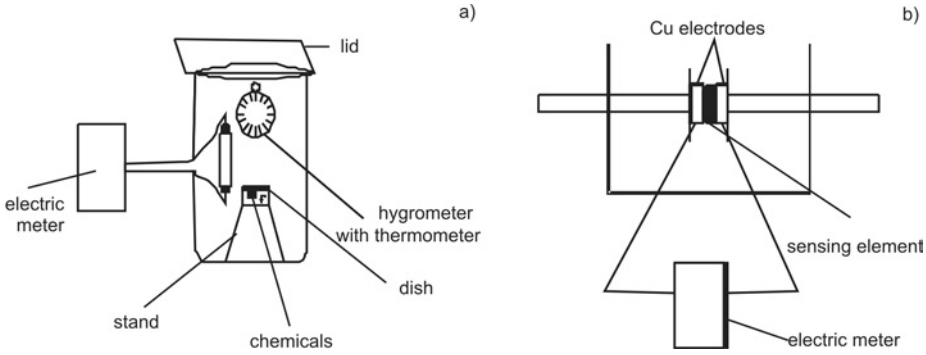

Fig. 7. Schematic diagrams of the device assembly (a) and of the Pellet holder (b)

The percentage relative humidity (*RH*) inside the chamber is increased from 10% to 95%. The resistance of TiO_2–Sb_2O_5 pellets in function of *RH* was recorded. The chamber was then dehumidified up to *RH* = 10%, by placing inside a dish of saturated salt solution of potassium hydroxide in deionized water. *RH* was measured with a standard hygrometer (Huger, Germany). A thermometer with the accuracy of ±1°C was hung in the chamber. Variations in the resistance were recorded using a sinometer of MΩ order (VC 9808).

4. Results and discussion

In Figure 8a, the dependences of the resistance on the relative humidity are shown for sensing elements of AT (2%, 5%, 10% and 20%) after annealing at 200 °C for 3 h. The curve for 2% AT shows that as the *RH* increases up to 25%, the resistance decreases drastically, whereas further increases in the *RH* yields a more gradual decrease in resistance, up to the point of saturation. The data for 5% AT shows that as the *RH* increases up to 30%, the resistance decreases rapidly, and then upon further increase in the *RH*, it decreases gradually up to *RH* of 95%. Data curves for 10% AT show that as *RH* increases up to 35%, the resistance decreases drastically and then it decreases gradually, up to the point of saturation. The data curve for 20% AT exhibits a similar profile to that for 5% AT, except that it has higher resistance at low humidity. Figure 8b shows the variation of resistance with respect to relative humidity for sensing elements of AT (30%, 40% and 50%) prepared under the same conditions as above. The data for 30% AT shows that as the *RH* increases up to 40%, the resistance decreases sharply, and then further increases, the *RH* yields a gradual decrease in the resistance up to the point of saturation. The data for 40% AT shows that as the *RH*

increases up to 45%, the resistance decreases rapidly, and then further increases in *RH* cause it to decrease gradually, up to an *RH* of 95%. Data for 50% AT shows that as the *RH* increases up to 55%, the resistance decreases drastically, and then it decreases gradually up to the point of saturation.

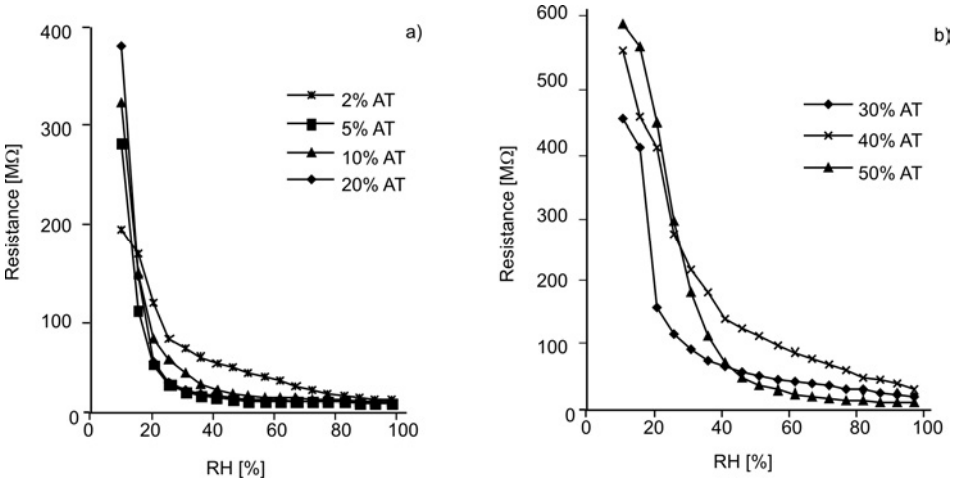

Fig. 8. Dependences of resistances of AT nanocomposites on the *RH* of sensing element of: a) 2%, 5%, 10% and 20%, b) 30%, 40% and 50%, all annealed at 200 °C

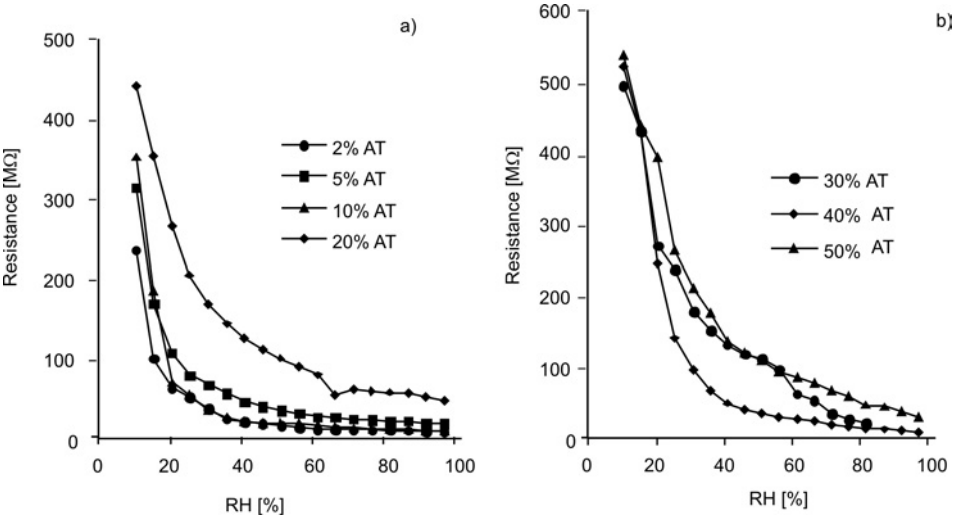

Fig. 9. Dependences of resistances of AT nanocomposites on the *RH* of sensing element of: a) 2%, 5%, 10% and 20%, b) 30%, 40% and 50%, all annealed at 500 °C

Figure 9a shows the dependences of the resistance on the relative humidity for AT sensing elements (2%, 5%, 10% and 20%) fabricated after annealing at 500 °C for 3 h. The data for 2% AT shows that as the *RH* increases, the resistance decreases drasti-

cally up to *RH* = 20%, and then it decreases gradually to the point of saturation. The data for 5% AT shows that as the *RH* increases up to 25%, the resistance decreases drastically, and then upon further increase in the *RH*, it decreases gradually over the rest of the *RH* range. The data for 10% AT exhibits a similar profile to that of 2% AT. The data for 20% AT shows that as the *RH* increases up to 65%, there is a rapid decrease in the resistance, and for higher *RH* values it decreases gradually up to an *RH* of 95%. Figure 9b shows the dependences of the resistance on the relative humidity for sensing elements of AT (30%, 40% and 50%) fabricated after annealing at 500 °C for 3 h. The data for 30% AT shows that as the *RH* increases up to 70%, the resistance decreases drastically and then, upon further increases in the *RH*, it corresponds to a gradual decrease in the resistance, up to the point of saturation. The data for 40% AT shows that as the *RH* increases up to 70%, the resistance decreases rapidly and, upon further increase in the *RH*, it decreases gradually, up to the *RH* of 95%. The data for 50% AT shows very similar behaviour demonstrating that the material is suitable for designing a sensor.

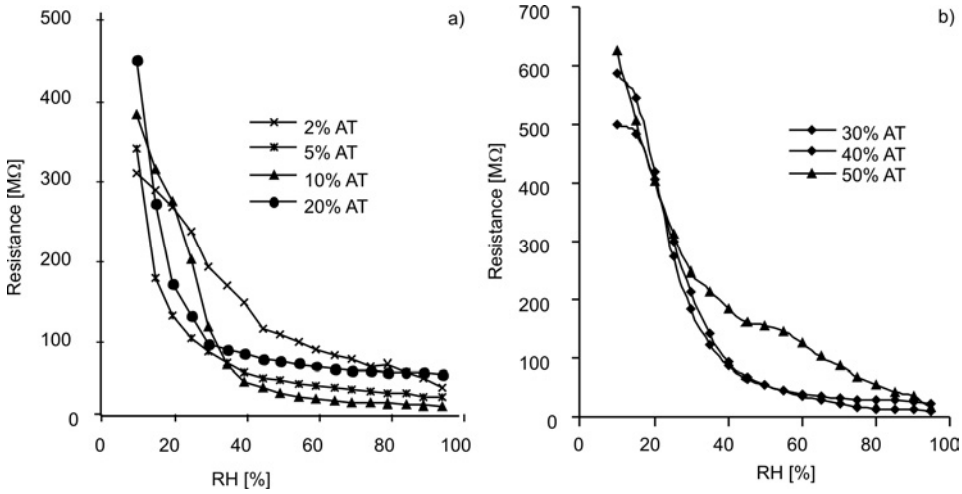

Fig. 10. Dependences of resistances of AT nanocomposites on the *RH* of sensing element of: a) 2%, 5%, 10% and 20%, b) 30%, 40% and 50%, all annealed at 700 °C

Figure 10 shows the dependences of electrical resistance on *RH* for 2%, 5%, 10%, 20% and 30%, 40%, 50% AT. The data for 2% AT (Fig. 10a), shows that as *RH* increases up to 65%, the resistance first decreases drastically, and further increase in *RH* leads to gradual decrease in the resistance up to the point of saturation. Curve for 5% AT shows that as the *RH* increases up to 30%, the resistance decreases rapidly and then, upon further increase in the *RH*, it decreases gradually up to an *RH* of 95%. Data for 10% and 20% AT give similar profile to that corresponding to 5% AT. Figure 10b shows the dependences of the resistance on the relative humidity for sensing elements of AT (30%, 40% and 50%). The data for 30% AT shows that as the *RH* increases up

to 40%, the resistance decreases drastically, and then, upon increasing the *RH*, it yields a gradual decrease in the resistance, up to an *RH* of 95%. The data for 40% AT exhibits a similar profile to that corresponding to 30% AT. The data for 50% AT shows that as the *RH* increases up to 80%, the resistance decreases linearly everywhere in the specified humidity range.

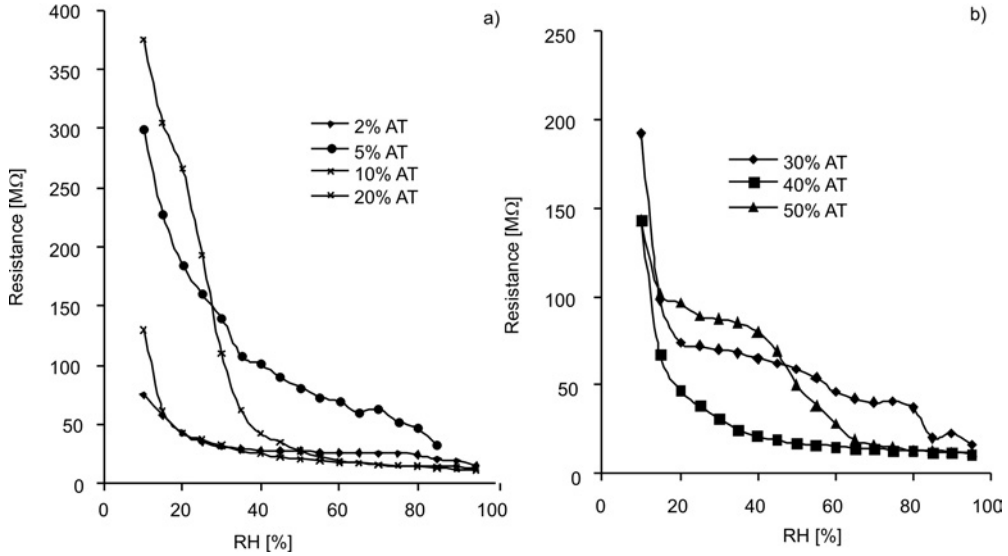

Fig. 11. Dependences of resistances of AT nanocomposites on the *RH* of sensing element of: a) 2%, 5%, 10% and 20%, b) 30%, 40% and 50%, all annealed at 800 °C

Figure 11a shows the dependence of the resistance on the relative humidity, for AT sensing elements prepared by adding 2%, 5%, 10% and 20% wt. % of antimony. The data for 2% AT shows a gradual change in the resistance, up to the point of saturation. The data for the 5% AT sensing element has a better slope, and there is a drastic decrease in the resistance, up to an *RH* of 45%; this decrease was observed to become more gradual, indeed it has a linear response, for higher *RH* values of up to 95%. The data for 10% and 20% AT exhibit a similar profile to that corresponding to 5% AT. Figure 11b shows the variation in the resistance with respect to relative humidity for the sensing elements of AT (30%, 40% and 50%) annealed at 800 °C. The data for 30% AT shows that as the *RH* increases up to 20%, the resistance decreases rapidly and then, upon further increase in the *RH*, it decreases gradually, up to the *RH* of 95%. The data for 40% AT shows that as the *RH* increases up to 15%, the resistance decreases drastically, and then, upon further increase in the *RH*, there is a gradual decrease in the resistance, up to the point of saturation. The data for 50% AT shows that as *RH* increases up to 40%, the resistance decreases rapidly and then, upon further increase in the *RH*, it decreases gradually, for the *RH* of up to 95%.

Figure 12 shows the dependences of the average sensitivity of the composite material annealed at 200, 500, 700 and 800 °C on the contents of Sb_2O_5. For annealing temperatures of 200, 500 and 700 °C, the average sensitivity increases as the percentage of Sb_2O_5 increases. The composite of 50% Sb_2O_5 with TiO_2 exhibits the highest average sensitivity, i.e. 7.5. The sensitivity of the sensing element annealed at 800 °C increases for the additive content up to 5%; for higher contents of the additive, the sensitivity decreases markedly. The sensing material probably becomes amorphous after annealing at 800 °C.

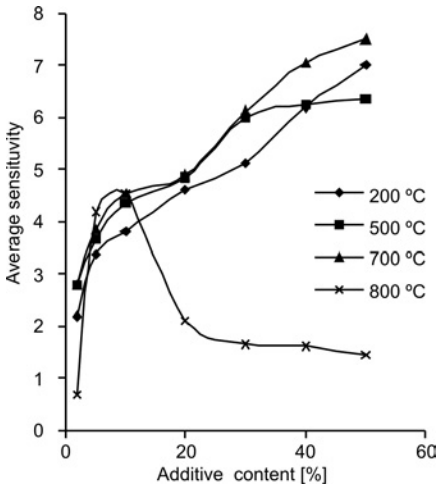

Fig. 12. Dependence of average sensitivity on additive content for the sensing elements annealed at various temperatures

As reported by the Moon et al. [8], the conduction behaviour of TiO_2–Sb_2O_5 in the presence of water vapour mainly depends on the presence of ions. The present study also proves that the conduction in TiO_2–Sb_2O_5 depends on ions, probably protons. In this sensing material, Sb^{3+} cations are assumed to be an highly active sites for adsorption, due to their highest charge density. These ions readily combine with the hydroxyl group of adsorbed water, thereby weakening the bonds between hydroxyl ions and protons: water molecule subsequently becomes dissociated. This provides free protons for electrical conduction. The hydroxyl ions thus remain chemically adsorbed at the cationic sites. Therefore, the first layer of adsorbed water molecule forms a chemisorbed layer, and this process is irreversible at room temperature. The subsequent layers are physically adsorbed on the first layer to form hydroxyl multilayers by hydrogen bonding. These free mobile protons, obtained from the first chemisorbed layer, react with physisorbed water layer and form hydronium ions.

When the physically adsorbed layer is abundant, the protons from one hydronium ion can hop to another hydronium ion; this proton transfer mechanism provides the means by which electrical conduction can occur. The physisorption of the water layer is reversible at room temperature and it exists in equilibrium in ambient humidity conditions. As the ambient humidity varies, the amount of water vapour physisorbed on the surface or condensed on the capillary pores also varies, subsequently changing the

concentration of the mobile protons, which in turn changes the conductivity of the ceramic.

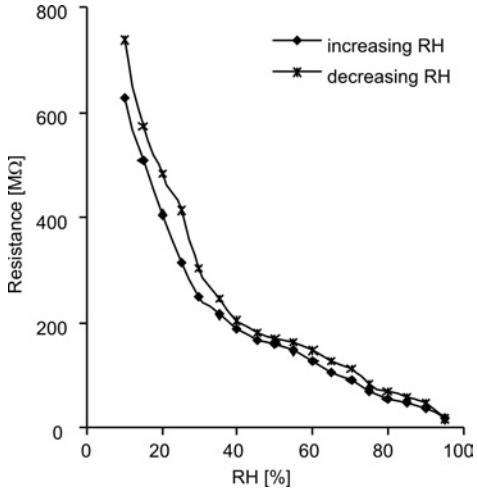

Fig. 13. Hysteresis curve for the sensing element 50% AT annealed at 700 °C

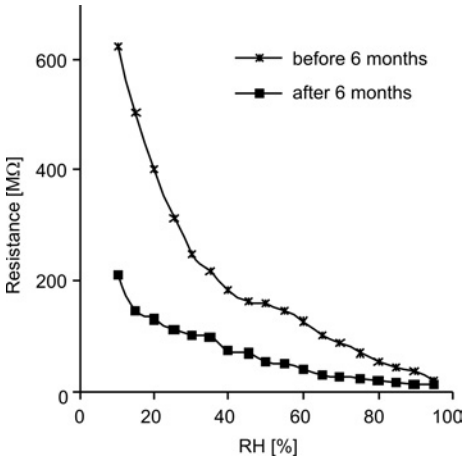

Fig. 14. Dependence of resistance of 50% AT nanocomposite annealed at 700°C on the *RH* of sensing element just after fabrication and after 6 months

The hysteresis curve for the TiO_2–Sb_2O_5 sensing element annealed at 700 °C in Fig. 13 shows 17.61% hysteresis. After humidity treatment, all the sensing elements were kept in a laboratory environment and their humidity sensing characteristics were regularly monitored. Figure 14 shows the dependences of the resistance of the TiO_2–Sb_2O_5 sensing element on the *RH*, both before annealing and 6 months after annealing at 700 °C. It was found that the sensor had become less sensitive to humidity and deteriorated by 67%.

5. Conclusion

TiO_2–Sb_2O_5 nanocomposite was investigated for its humidity sensing characteristics. The nanocrystals in the sensing material annealed at 700 °C had an average size of 20–112 nm, which meant that the material was highly sensitive to the presence of water vapour. Among the samples tested, this sensing element had the highest average sensitivity, namely a maximum sensitivity index of 7.5. Nearly all the sensing elements exhibited a similar profile, i.e. at the minimum *RH* their resistances were reached the maximum values and at the maximum *RH* their resistance were at the minimum. The humidity sensor reported in this paper is cheap and easy to fabricate, user-friendly and is sensitive to the entire *RH* range. This can be exploited in commercial production.

References

[1] FUYUKI T., MATSUNAMI H., Jpn. J. Appl. Phys., 25 (1986), 1288.
[2] YADAV B.C., SRIVASTAVA A.K., SHARMA P., Sen. Trans. J., 81 (2007), 1348.
[3] YADAV B.C., SHARMA P., SRIVASTAVA A.K., YADAV A.K., Sen. Trans. J., 92 (2008), 99.
[4] RAGHUPATHI P.S., GEORGE J., MENON C.S., Ind. J. Pure Appl. Phys., 43 (2005), 620.
[5] RAHMAN M.-U., YU G., KRISHNA K.M., SOGA T., JIMBO J.W.T., UMENO M., Appl. Opt., 37 (1998), 691.
[6] TANG H., PRASAD K., SANJINES R., SCHMID P.E., LEVY F., J. Appl. Phys., 75 (1994), 2042.
[7] NITTA T., TERADA Z., HAYABAWA S., J. Am. Ceram. Soc., 63 (1980), 295.
[8] MOON J., TSKAJI H., FUJISHIRO Y., AWANO M., J. Mater. Sci., 36 (2001), 949.
[9] CAROTTA M.C., FERRONI M., GNANI D., GUIDI V., MERLI M., MARTINELLI G., CASALE M.C., NOTARO M., Sens. Act. B, 58 (1999), 310.
[10] AKHTAR M.K., PRATSINIS S.E., MASTRANGELO S.V.R., J. Am. Ceram. Soc., 75 (1992), 3408.
[11] VEMURY S., PRATSINIS S.E., J. Am. Ceram. Soc., 78 (1995), 2984.
[12] BONINI N., CAROTTA M.C., CHIONINO A., GUIDI V., MALAGU C., MARTINELLI G., PAGLIALONGA L., SACERDOTI M., Sens. Act. B, 68 (2000), 274.
[13] ZHU B.L., XIE C.S., WANG W.Y., HUANG K.J., HU J.H., Mater. Lett., 58 (2004), 624.
[14] KALAYAMA K., HASEGAWA K., TAKAHASHI T., AKIBA T., YANAGIDA H., Sens. Act. A, 24 (1990), 55.
[15] KIM T.Y., LEE D.H., SHIM Y.C., BU J.U., KIM S.T., Sens. Act. B, 9 (1992), 221.
[16] MAKITA K., NOGAMI M., ABE Y., J. Ceram. Society Japan, 105 (1997), 595.
[17] YANG S.L., WU J.M., J. Mat. Sci., 26 (1991), 631.
[18] YOSHIMURA N., SATO S., ITOI M., TAGUCHI H., Sozai Busseigaku Zasshi, 3 (1990), 47.
[19] KULWICKI B.M., J. Amer. Ceram. Soc., 74.(1991), 697.
[20] MORIMOTO T., NAGAOAND M., TOKUDA F., J. Phys. Chem., 73 (1969), 243.

Received 7 June 2009
Revised 4 October 2009

Materials Science-Poland, *Vol. 28*, *No. 2*, *2010*

Preparation and photocatalytic activity of Cu_2O nanoparticles

X. F. LIN[1], R. M. ZHOU[1*], J. Q. ZHANG[1], X. H. SHENG[2]

[1]Shanghai Applied Radiation Institute, Shanghai University, Shanghai, 201800, China

[2]National Engineering Research Center for Nanotechnology, Shanghai, 200241, China

An electron beam irradiation route has been developed for the preparation of Cu_2O nanoparticles, with poly(ethylene glycol) (PEG, *Mw* = 10 000) as a template, and without using a further reducing reagent. Under various synthetic conditions, the composition of Cu_2O was changed by adjusting the PEG concentration and pH values of the starting solutions. Transmission electron microscopy data revealed that the morphology evolves from an irregular shape into a sphere and cube with increasing the concentration of PEG, and cube to irregular shape with increasing pH of starting solutions. UV-vis diffuse reflectance spectroscopy data indicated that the Cu_2O particles absorbed visible light. The photocatalytic activity of Cu_2O was evaluated by studying the decomposition of phenol and methyl orange in aqueous solution under irradiation with visible light.

Keywords: *Cu_2O; poly(ethylene glycol); electron beam irradiation; photodegradation*

1. Introduction

Tailoring the structure, size, and shape of inorganic materials is an important goal in syntheses of various materials due to possibility of obtaining unique shape and size-dependent properties. Cuprous oxide (Cu_2O), an important p-type semiconductor, is a relatively non-toxic material [1]. It has the band gap of 2.17 eV, and it has been shown to be useful for lithium ion batteries [2, 3], magnetic storage media [4], sensors [5] and catalysts [6]. The size and shape of Cu_2O particles are fundamentally important factors determining their properties [3, 7, 8]. Therefore, one of the challenges in syntheses of Cu_2O nanocrystals is to control not only the size but also shape of the crystal. In the past few years, numerous Cu_2O nanostructures such as hollow spheres [9], nanowires [10, 11], nanocages [12–14], octahedra [7, 15, 16], nanocubes [17], have been synthesized. Among these morphologies, nanocubes and octahedra may be the most interesting,

* Corresponding author, e-mail: zhourm47@staff.shu.edu.cn

owing to their tailor-made properties, and on the other hand, as they possess the highest symmetries, other more complex particle structures can be derived from these simple structural forms [18]. The selection of organic additives can be very important for controlling the morphology and size of Cu_2O nanoparticles. The organic additives often adsorb selectively onto different crystal faces and retard their growth rates, affecting the final morphology of the crystals [19]. For example, Cu_2O nanocubes can be formed in the presence of cetyltrimethylammonium (CTAB) [17], nanowires have been synthesized with poly(vinyl pyrrolidone) (PVP) as soft templates [10]. Recent reports revealed that the non-ionic surfactants PEG200, PEG400, PEG600, PEG8 000 or PEG20000 can be applied to adjust both the size and shape of Cu_2O nanoparticles [20–26].

A variety of techniques, including electrodeposition [27], γ-irradiation [28], oxidation of cppper [29], solution-phase synthesis [4] etc., have been employed to make Cu_2O form into various shapes. Here, in the present work, we utilize the electron beam irradiation method to fabricate Cu_2O nanoparticles. The effects of the PEG concentration and pH of the solution on the shape of the products are studied. X-ray powder diffraction (XRD), transmission electron microscopy (TEM) and UV-vis diffuse reflectance spectrometry were applied to study the structure, morphology, size and optical properties of the Cu_2O samples. The photodegradation of phenol and MO were employed to evaluate the photocatalytic activities of Cu_2O nanocrystals under visible light illumination.

2. Experimental

Syntheses of Cu_2O samples. All reagents were analytical grade and were used as received. Milli-Q purified water was used for all of the experiments. Typically, the Cu_2O nanoparticles were prepared by the following procedure. Varied amounts of PEG and 1.25 g of $CuSO_4 \cdot 5H_2O$ were dissolved in 96 cm^3 of water and ultrasonicated for 20 min. Next, 3.1 cm^3 isopropanol (as a scavenger of oxidative radicals such as ·OH produced during water-radiolysis) was added to the mixed solution. Then the solution was adjusted to advisable sensible pH values by ammonia solution, irradiated by the GJ-2-II accelerator (Dynamitron, 2 MV, 10 mA, manufactured from Shanghai Xianfeng electrical factory) at an absorbed dose of 280 kGy. Yellow orange precipitates were obtained after irradiation and were then collected by centrifugation, following by washing with water and absolute alcohol three times, respectively. Finally, they were dried in a vacuum oven at 60 °C for 4 h.

Characterization. XRD was performed with a Rigaku D\Max-2550 powder X-ray diffractometer (Cu Kα radiation, $\lambda = 1.54178$ Å). The TEM images were obtained on a JEOL JEM-200CX microscope operating at 160 kV. The DRS was measured with a Hitachi U-3010 spectrophotometer, in order to study the optical properties of the

products. Brunauer–Emmett–Teller (BET) surface areas of the samples were determined using a 3H-2000III nitrogen adsorption apparatus.

Photocatalytic properties of Cu_2O. A series of 0.05 g samples of Cu_2O were dispersed in 100 cm^3 phenol or MO solution (50 mg/dm^3) for 1 h in the dark, in order to obtain absorption equilibrium. Then the solution was irradiated with the radiation of a 500 W halogen-tungsten lamp, with air bubbles during the photocatalytic reaction. At certain intervals, 4 cm^3 of phenol or MO was centrifuged and analyzed.

3. Results and discussion

3.1. Effect of the PEG concentration on the morphology of Cu_2O

A common method used to adjust the size and shape of nanoparticles is to change the concentration of the capping surfactant or the capping group. Generally, upon increasing the concentration of the capping surfactant, the particle size decreases because the sites for further nucleation and growth are blocked by the addition of more capping agent.

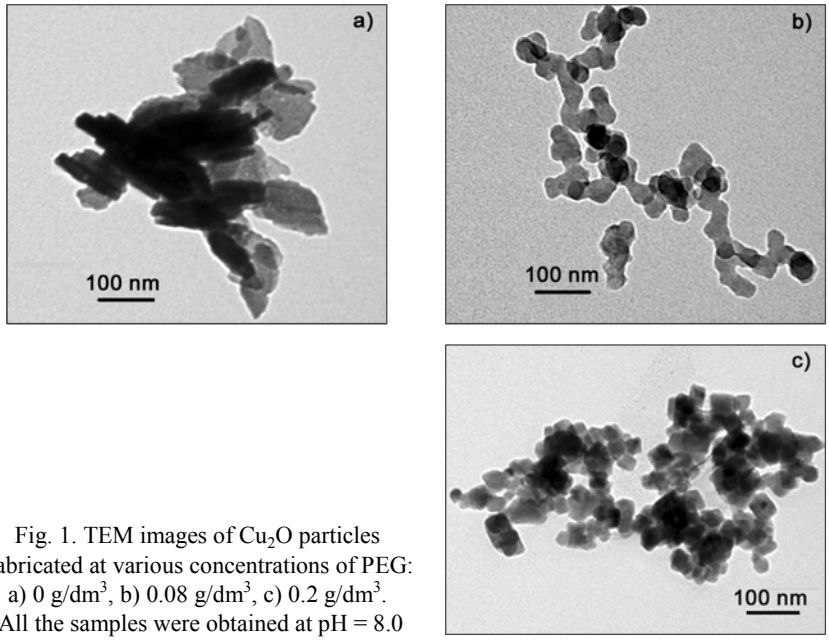

Fig. 1. TEM images of Cu_2O particles fabricated at various concentrations of PEG: a) 0 g/dm^3, b) 0.08 g/dm^3, c) 0.2 g/dm^3. All the samples were obtained at pH = 8.0

Figure 1 shows the TEM images of the Cu_2O particles synthesized at various concentrations of PEG ranging from 0 to 0.20 g/dm^3. As shown in Fig. 1a, Cu_2O particles with irregular morphology are obtained in the absence of PEG, and their sizes are

higher than 70 nm. With the addition of a small quantity of PEG (0.08 g/dm^3), the as-prepared Cu_2O particles are spherical or square-like, having an average size of 22 nm (Fig. 1b). Cubic Cu_2O nanoparticles with edge lengths higher than 20 nm are obtained at higher concentrations of PEG (0.20 g/dm^3, Fig. 1c). As one can see from Fig. 1, in this reaction system, it is obvious that Cu_2O nanoparticles fabricated at various amounts of PEG exhibit dramatically different morphologies.

The TEM observations lead us to believe that the concentration of PEG plays an important role in controlling the morphology of the Cu_2O. As a non-ionic surfactant, PEG has twisted polymeric segments, and the polymeric chain is alternately hydrophilic and hydrophobic [26]. The hydrophilic groups have oxygen atoms which can coordinate with Cu^{2+} to form Cu(II)–PEG complex. The non-combined PEG molecules may adsorb on the surface of the particles. They may adsorb onto a certain crystallographic plane, thereby influencing the surface energies and external growth environments of the crystal faces, thus, affecting the growth kinetics. Based on previous reports, Murphy [30] pointed out that preferential adsorption of molecules and ions in solution to different crystal faces causes the nanoparticles to grow into various shapes, by controlling the growth rates along different crystal axes. When PEG is absent or the quantity is small, the PEG molecules cannot effectively wrap the neonatal Cu_2O, thus the crystals exhibit irregular shapes. In the presence of excessive PEG, more and more PEG molecules adsorb on the <100> crystal faces, thus lowering the surface energies, and cubic shapes of Cu_2O are obtained. Consequently, a dramatic change in the morphology occurs.

3.2. Influence of pH of the starting solution on the products

Control experiments were carried out to investigate the influence of pH of starting solutions on the products. The morphology of the Cu_2O particles obtained at various

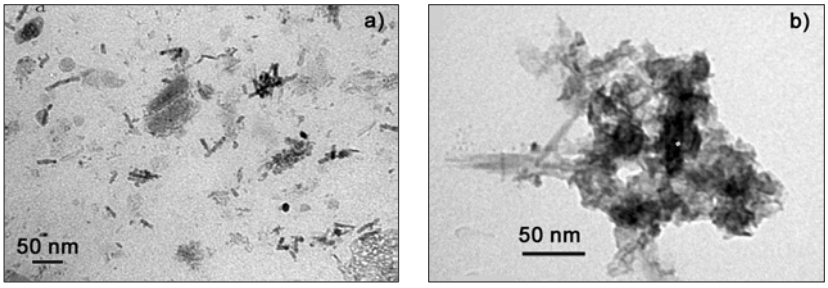

Fig. 2. TEM images of Cu_2O particles fabricated under various pH: a) 8.86, b) 9.40. Both samples were fabricated at 0.20 g/dm^3 PEG

pH values was characterized by TEM, as shown in Fig. 2. The TEM image of the Cu_2O synthesized at pH = 8.86 shows irregular shapes, some of them aggregated (Fig. 2a). When pH of the solution is adjusted to 9.40, the products also have irregular

morphologies, and they agglomerate strongly (Fig. 2b). With the increase in pH values of the solution from 8.00 to 9.40, the particles become smaller: at pH = 9.40, small particles aggregate very rapidly. The fact that the smaller particles are obtained at higher pH of the starting solution is also confirmed by the XRD pattern, which is presented in Fig. 3. It is obvious that the diffraction peaks of the Cu_2O sample prepared at 8.00 pH are narrower and have higher intensities than those of the samples prepared at pH between 8.86 and 9.40. This suggests that Cu_2O crystals formed at pH in the range 8.86–9.40 have smaller dimensions. The average particle sizes calculated from Scherrer's equation, based on the Cu_2O <111> diffraction peaks, are 18.8, 14.5, 12.0 nm, which are prepared at pH of 8.00, 8.86, 9.40, respectively. The results of the XRD analysis also confirmed that all diffraction peaks corresponded to Cu_2O phases. No obvious peaks of impurity were found.

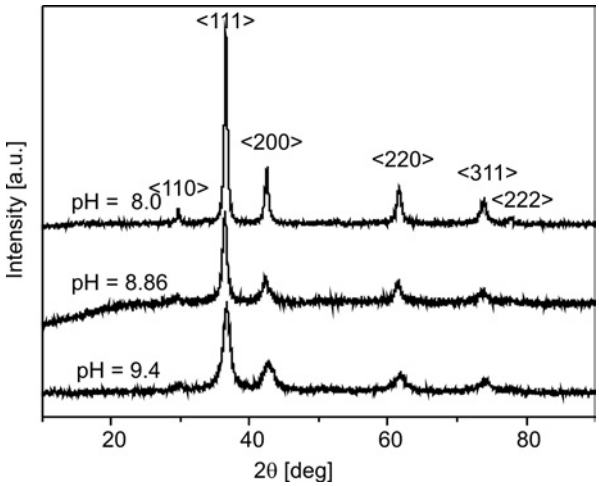

Fig. 3. XRD patterns of the products fabricated at various pH

It is well known that Cu_2O can be dissolved in ammonia solution to produce a complex $[Cu(NH_3)_2]^+$, which is unstable and easily oxidized to a blue complex $[Cu(NH_3)_4]^{2+}$. This dissolution resembles chemical etching [31]. The dissolution reactions of Cu_2O are as follows:

$$Cu_2O + 4NH_3 \cdot H_2O = 2[Cu(NH_3)_2]^+ + 2OH^- + 3H_2O \quad (1)$$

$$2[Cu(NH_3)_2]^+ + 4NH_3.H_2O + 0.5O_2 = 2[Cu(NH_3)_4]^{2+} + 2OH^- + H_2O \quad (2)$$

Since pH of the starting $CuSO_4$ solution is adjusted drop by drop with ammonia solution, a homogeneous $[Cu(NH_3)_n]^{2+}$ solution forms, when more and more ammonia solution is added to the solution, there is still some NH_3 remaining, so the freshly formed Cu_2O is etched by the excess ammonia solution. Upon increasing pH, there are more $NH_3 \cdot H_2O$ to dissolve Cu_2O in order to accelerate the etching reactions, the cubic Cu_2O will be dissolved into irregular and smaller particles. For this reason, the parti-

cles are easier to conglomerate (Fig. 2). If pH = 10.00, the yield of the precipitates decreases significantly after EB irradiation, the precipitates disappear within 10 min and the solution becomes blue.

Based on the above results, it is clear that the concentration of PEG and pH of the starting solution play a key role in determining the morphology of the final products.

3.3. Diffuse reflectance spectra (DRS)

The DRS of Cu_2O fabricated at pH = 8.00 and in the presence of 0.2 g/dm^3 PEG is shown in Fig. 4. The sample has an intense absorption in the visible range, which implies the possibility of high photocatalytic activity of Cu_2O under visible light irradiation. The steep gradient of the spectra indicates that the visible light absorption does not originate from a transition from the impurity level but is due to the band-gap transition.

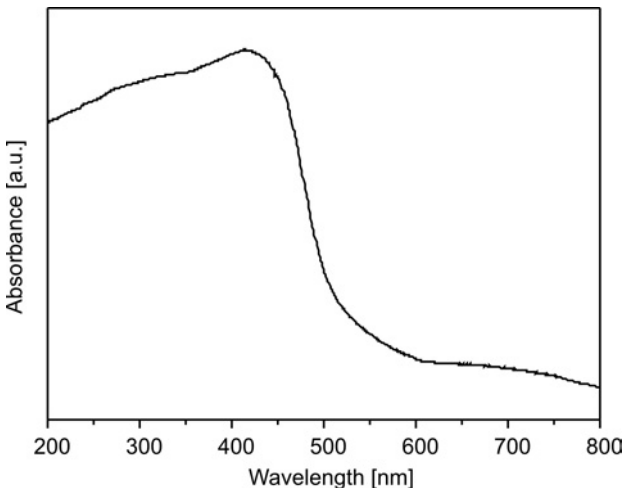

Fig. 4. Diffuse reflectance spectra of the as-prepared Cu_2O

3.4. Photocatalytic performance of Cu_2O samples

Successful synthesis of Cu_2O is a potential way of investigating the photocatalytic properties of Cu_2O nanoparticles. The degradation of phenol and MO by visible light was investigated. The photocatalytic reactivity of Cu_2O was quantified by the ratio, denoted $C/C_{0,}$ between the residual concentration and the initial concentration of phenol and MO. The ratio C/C_0, depends on the irradiation time. Blank tests (phenol and MO without any catalyst) under visible light exhibited little photolysis. The phenol and MO concentration only decreased by 1.9% and 4.3% after 150 and 70 min of irradiation, respectively, which demonstrated that the photodegradation of phenol and MO was extremely slow without a catalyst under visible light illumination. The degrada-

tion of phenol and MO with Cu_2O in the dark was similar to that of the blank test. Therefore, the degradation of phenol and MO after treatment with Cu_2O was most likely due to the photocatalysis of Cu_2O.

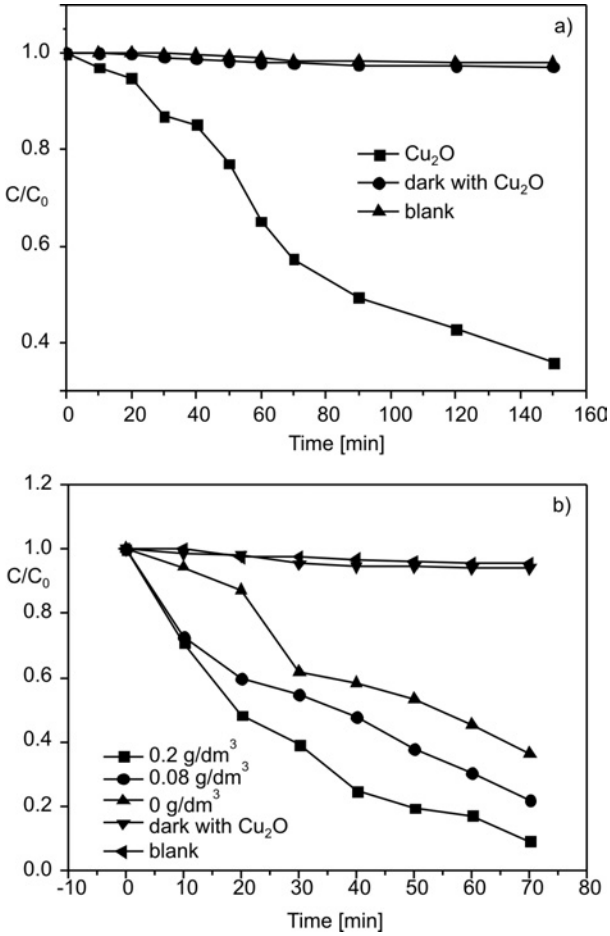

Fig. 5. Photodegradation of phenol (a) and MO (b) by Cu_2O samples

As is clearly shown in Fig. 5, Cu_2O nanoparticles were to a large extent responsible for the photodegradation reaction, both on phenol and MO after 150 and 70 min of irradiation, respectively. However, amongst all types of investigated Cu_2O crystals, cubic Cu_2O prepared with the starting solution at pH = 8.00 exhibited the highest photoefficiency for MO degradation. The photocatalytic activity is strongly dependent on the size, morphology, crystal structure, specific surface area or the efficiency of electron–hole (e^-/h^+) separation, etc., of a photocatalyst. The average diffusion time of randomly generated charge carriers from the bulk to the surface obeys the formula $\tau = r^2\pi^2 D$, where r and D are the grain radius and the diffusion coefficient of the carrier, respectively [32]. From this formula we know that if the grain radius decreases,

the migration rate of e^-/h^+ to the surface accelerates, thus the photogenerated electron –hole pairs could effectively move to the surface, where they may degrade the adsorbed phenol and MO molecules. In general, particles that are of smaller size and have higher surface area are better for the degradation of pollutants. A higher surface area of the adsorbent possibly leads to higher adsorption capacity, while adsorption is a prerequisite for the degradation reaction. The BET surface areas of the samples prepared at PEG concentrations of 0.20, 0.08, 0 g/dm^3 were ca. 22.6, 18.1, 11.4 m^2/g, respectively, and the adsorption of MO on Cu_2O is consistent with the fact that the adsorption efficiency increases when the BET surface area increases. However, an exact reason for a high photocatalytic activity of the cubic Cu_2O still needs to be explored further.

4. Conclusion

Cu_2O nanostructures were successfully prepared with PEG as a template by electron beam irradiation in aqueous copper(II) sulfate solution. Factors affecting the morphology and size of Cu_2O products were the concentration of PEG and pH of the starting solution. The photodegradation experiments demonstrated that cubic Cu_2O nanoparticles exhibited higher photocatalytic activity than those of their spherical and irregular counterparts under visible light irradiation.

Acknowledgement

This work was supported by the Shanghai Leading Academic Disciplines (No. S30109) and the Innovation Foundation of Shanghai University (No. SHUCX091033).

References

[1] GOLDEN T.D., SHUMSKY M.G., ZHOU Y., VANDERWERF R.A., VAN LEEUWEN R.A., SWITZER J.A., Chem. Mater., 8 (1996), 2499.
[2] GRUGEON S., LARUELLE S., URBINA R.H., DUPONT L., POIZOT P., TARASCONA J.M., J. Electrochem. Soc., A285 (2001), 148.
[3] POIZOT P., LARUELLE S., GRUGEON S., DUPONT L., TARASCON J.M., Nature, 407 (2000), 496.
[4] LI X., GAO H., MURPHY C.J., GOU L., Nano. Lett., 4 (2004), 1903.
[5] SHISHIYANU S.T., SHISHIYANU T.S., LUPAN O.I., Sensor Actuat B Chem., 113 (2006), 468.
[6] PETRA E.D.J., DANIEL V., JOHN J.K., Chem. Commun., (1999), 1069.
[7] XU H.L., WANG W.Z., ZHU W., J. Phys Chem. B., 110 (2006), 13829.
[8] ZHANG C.Q., TU J.P., HUANG X.H., YUAN Y.F., CHEN X.T., MAO F., J. Alloy. Compd., 441 (2007), 52.
[9] XU H.L., WANG W.Z., ZHU W., Micropor. Mesopor. Mat., 95 (2006), 321.
[10] HONG X., WANG G., ZHU W., SHEN X., WANG Y., J. Phys. Chem. C, 113 (2009), 14172.
[11] WANG W., WANG G., WANG X., ZHAN Y., LIU Y., ZHENG C., Adv. Mater. 14 (2002), 67.
[12] KUO C., HUANG M., J. Am. Chem. Soc., 130 (2008), 12815.
[13] TEO J.J., CHANG Y., ZENG H.C., Langmuir, 22 (2006), 7369.
[14] XU H., WANG W., Angew. Chem., Int. Ed., 46 (2007), 1489.
[15] WANG Z., WANG H., WANG L., PAN L., Cryst. Res. Technol., 44 (2009), 624.

[16] LIANG X., GAO L., YANG S., SUN J., Adv. Mater., 21(2009), 2068.
[17] GOU L., MURPHY C.J., Nano Lett., 3 (2003), 231.
[18] KUO C., HUANG M., J. Phys. Chem. C, 112 (2008), 18355.
[19] YU S., COLFEN H., J. Mater. Chem., 14 (2004), 2124.
[20] CHEN S.J., CHEN X.T., XUE Z.L., LI L.H., YOU X.Z., J. Cryst. Growth., 246 (2002), 169.
[21] GOU L.F., MURPHY C.J., J. Mater. Chem., 14 (2004), 735.
[22] KUMAR R.V., MASTAI Y., DIAMANT Y., GEDANKEN A., J. Mater. Chem., 11 (2001), 1209.
[23] QU Y.L., LI X.Y., CHEN G.H., ZHANG H.J., CHEN Y.Y., Mater. Lett., 62 (2008), 886.
[24] SHARMA P., BHATTI H.S., J. Phys. Chem. Solids., 69 (2008), 1718.
[25] WANG D.B., YU D.B., MO M.S., LIU X.M., QIAN Y.T., J. Colloid. Interf. Sci., 261 (2003), 565.
[26] XU Y.Y., CHEN D.R., JIAO X.L., XUE K.Y., J. Phys. Chem. C., 111 (2007), 16284.
[27] GUO S.J., FANG Y.X., DONG S.H., WANG E.K., Inorg. Chem., 46 (2007), 9537.
[28] CHEN Q.D., SHEN X.H., GAO H.C., J. Colloid. Interf. Sci., 312 (2007), 272.
[29] CHOON H.B.N., WAI Y.F., J. Phys. Chem. B., 110 (2006), 20801.
[30] MURPHY C.J., Science, 298 (2002), 2139.
[31] XIA Y.N., ZHAO X.M., KIM E., WHITESIDES G.M., Chem. Mater., 7 (1995), 2332.
[32] HAGFELDT A., GRATZEL M., Chem. Rev., 95 (1995), 49.

Received 10 June 2009
Revised 11 February 2010

Materials Science-Poland, *Vol. 28*, *No. 2*, *2010*

Chemical bath deposition and characterization of nanocrystalline ZnO thin films

A. KATHALINGAM[1], N. AMBIKA[2], M. R. KIM[1],
J. ELANCHEZHIYAN[3], Y. S. CHAE[1], J. K. RHEE[1*]

[1]Millimeter Wave Innovation Technology Research Center (MINT),
Dongguk University, Seoul 100-715, Korea

[2]Department of Physics, Periyar Maniammai University, Vallam,
Thanjavur-613403, Tamil Nadu, India

[3]Electronic Ceramics Center, Dong-Eui University, Busan, 614-714, Korea

The subject of this paper is the wet chemical synthesis and characterization of nanocrystalline ZnO thin films. ZnO thin film was deposited on a zinc plate using a chemical bath of zinc acetate ($Zn(O_2CCH_3)_2$) and ethylenediamine ($C_2N_2H_8$) at various temperatures. Different substrates were used and their effect on the chemical bath deposition of ZnO were investigated. The effect of pH levels and temperature on the crystalline quality and morphology of the ZnO film are also presented.

Keywords: *zinc oxide; chemical bath deposition; solution growth; nanocrystalline semiconductor*

1. Introduction

Nanocrystalline semiconducting materials have attracted a great deal of attention because of their size dependent properties and wide range of applications. ZnO is one of the most interesting semiconducting materials. It has the band gap energy of 3.37 eV and is considered a potential material for use in solid state emission, solar cells, chemical sensors, piezoelectric transducers, transparent electrodes, photo-catalysts, electroluminescent devices and ultraviolet laser diodes [1–4]. Numerous techniques have already been used to deposit ZnO thin films, including molecular beam epitaxy (MBE) [5], sputtering [6], ion implantation [7], metal-organic chemical vapour deposition (MOCVD) [8], sol-gel deposition [9], spray pyrolysis [10], pulsed laser deposition (PLD) [11], cathodic electrodeposition [12–14] and other solution

*Corresponding author, e-mail: jkrhee@dongguk.edu

phase methods. The latter are simple to implement in experimental setups and have good potential for scaling-up.

Chemical bath deposition (CBD) [15–19] is one of the solution phase methods useful for the preparation of compound semiconductors from aqueous solutions. It is widely used for the deposition of various metal chalcogenide thin films. It produces good deposits on suitable substrates by the controlled precipitation of the compounds from the solution. The method offers many advantages over other well-known vapour phase synthetic routes. It may allow us to easily control the growth factors such as film thickness, deposition rate and quality of crystallites by varying the solution pH, temperature and bath concentration [20]. It does not require high voltage equipment, works at room temperature, and hence it is inexpensive. The only requirement for this deposition route is an aqueous solution consisting of a few common chemicals and a substrate for the film to be deposited. It often suffers from a lack of reproducibility in comparison with other chemical processes; however, by the proper and careful optimization of the growth parameters, one can achieve reasonable reproducibility.

The major problem of the CBD method is the inefficiency of the process which converts the precursor materials into useful deposits. Two types of nucleation take place in solution: homogeneous nucleation and heterogeneous nucleation. Homogeneous nucleation leads to rapid formation of large particles throughout the solution, as precipitate. Conversely, heterogeneous nucleation occurs at the substrate surface and particles grow slowly to form a film. The heterogeneous growth of the film on the substrate is disrupted by the competing homogeneous reaction in solution and the subsequent deposition on the surface of the vessel containing the solution bath. This difficulty is avoided by using a pre-treated substrate for the formation of seed layers or by employing the successive ionic layer adsorption and reaction (SILAR) method. Growing of a ZnO thin film on a glass substrate from an alkaline solution requires a seed layer. However, the deposition of ZnO thin film on a zinc plate does not require a seed layer, unlike other substrates such as glass, ITO or FTO.

To the best of our knowledge, there is no report available on the use of a zinc plate as a substrate for the chemical bath deposition of ZnO thin films. Ku et al. used aqueous solutions of zinc acetate dehydrate (0.05 M) and hexamethylenetetramine for the deposition of ZnO film on ITO [21]. Peng et al. used an equimolar (0.03 M) aqueous solution of zinc nitrate ($Zn(NO_3)_2$) and hexamethyltetramine ($C_6H_{12}N_4$) to deposit ZnO thin films on an ITO substrate [22]. Drici et al. reported CBD growth of ZnO on bare soda glass and ITO coated glass using zinc acetate (0.0188 mol/dm^3) and ethylenediamine (0.03 mol/dm^3). Similarly, Tahir Saeed et al. have also used zinc acetate (0.0188 M) and ethylenediamine (0.03–0.0425 M) for the deposition of ZnO thin films on a glass slide [23].

In our experiment, the deposition bath consisted of equal volumes of zinc acetate ($Zn(O_2CCH_3)_2$), and ethylenediamine ($C_2N_2H_8$) solutions having concentrations varying between 0.25 and 1 M. Zinc plates were used as substrates to grow ZnO thin films from solutions. Subsequent characterization of the plates has been reported. The con-

sequences of using various substrates for the growth of ZnO thin films are also discussed.

2. Experimental

The chemicals such as zinc acetate ($Zn(O_2CCH_3)_2$), and ethylenediamine ($C_2N_2H_8$) were of analytical reagent grade. A hot plate with a magnetic stirrer was used to heat and stir the bath solution. Zinc plates were used as the substrate in this deposition and for further characterization. Bare soda lime glass and SnO_2 coated glass plates were also used as substrates, in order to study how the choice of substrate material affects the deposition of ZnO thin films. All the substrates were cleaned with acetone, and then washed with distilled water. The zinc plate was first scrubbed with emery paper before washing. The film deposition was performed at various temperatures, with and without stirring the bath solution. The bath solutions were prepared with zinc acetate and ethylenediamine, both their concentrations varying between 0.25 M and 1 M. A mixture of solution with the desired density of zinc acetate and ethylenediamine was placed in a 100 cm^3 beaker and the solution was kept in a constant temperature bath. One side of the surface of each substrate, in particular of the zinc plate, was covered with insulating tape before being dipped into the solution. The pH of the bath was varied between 8 and 11 with the use of NaOH solution. The reaction mixture was maintained as constant at a desired temperature for deposition with continuous stirring. The substrates were removed from the deposition solution at various time intervals, washed with distilled water and dried, and then these deposits were subject to various tests. The reflectance of each film was measured with an UV-Vis-NIR spectrophotometer (HR-2000, M/S Ocean Optics). X-ray diffraction patterns were recorded using an X-ray diffractometer (XPERT PRO PANalytical) with CuK_α radiation ($\lambda = 0.1540$ nm) and the analyses of the surface morphologies were performed with a scanning electron microscope (JEOL JSM 840).

3. Results and discussion

3.1. Physical properties of film growth

In the deposition, equal volumes of $Zn(O_2CCH_3)_2$ and $C_2N_2H_8$ solutions with various normality, as given in Table 1, were used for all the substrates. The temperature of the deposition bath was varied from 30 °C to 60 °C. The temperature needed to obtain thin film deposition was at least 50 °C. The deposition conditions, i.e. pH, temperature and the concentration of the bath were varied in order to achieve the deposition of good quality, adherent thin films. The thickness of the film was controlled by dipping the substrate into the solution for a specific time. The growth rate also depended both on temperature of the bath and the stirring conditions: for higher temperatures the

growth rate was also found to be high but the growth rates in depositions with stirring are higher than those in unstirred solutions at the same temperature.

Table 1. Effects of various concentrations of the solutions on film quality

Molarity [M]		pH	Substrate		
Zn	Eth		Glass plate	Zinc plate	SnO_2 plate
			Quality of coating		
1.00	0.25	8–11	–	–	–
0.75	0.50				
0.50	0.75	8–9			thin
		9–10			
		10–11	thin	thin	good
0.25	1.00	8–9	–	–	powdery
		9–10	powdery	powdery	thick precipitate
		10–11	thin	thin	black, thick

In the case of bare glass plates and SnO_2 coated substrates, only a very thin white layer of powdery coating was obtained. The pH of the bath was found to play a major role in this deposition, irrespective of the concentration of the bath. At low pH values (below 8), only poor quality films were produced, irrespective of the substrates used. In zinc plates, for pH < 9, a powder like coating was obtained. For pH ≈10, strongly adherent, smooth, dark gray deposits were obtained. For pH > 10.5, and if the concentration of $Zn(O_2CCH_3)_2$ in the bath is 0.25 M and $C_2N_2H_8$ 1 M, a thick black coating with cracks is produced.

When the concentration of $C_2N_2H_8$ increased, the solution turned milky and precipitate was formed, which may be due to ZnO particles. Initially the deposition solution turned milky due to the formation of ZnO particles by homogeneous nucleation. The particles soon settled on the bottom of the beaker, as a non-adherent powder, and on the top surface of the substrate. The influence of the concentration of solution and pH on the various substrates is summarized in Table 1.

The optimum CBD conditions for achieving smooth, strongly adherent ZnO thin films were found to be: pH around 10, temperature between 50 °C and 60 °C, and concentrations of $Zn(O_2CCH_3)_2$ ca. 0.5 M and of $C_2N_2H_8$ ca. 0.75 M.

3.2. Structural study

The structural properties of the as-deposited and annealed ZnO thin films were analyzed by recording their X-ray diffraction patterns. The XRD patterns were obtained for ZnO thin films deposited using a bath composition of 0.5 M zinc acetate and 0.75 M ethylenediamine, pH = 9.5 at various bath temperatures. Figure 1 shows X-ray diffraction (XRD) patterns of annealed (300 °C for 15 min) ZnO films fabricated at various temperatures. The diffraction peaks of ZnO exhibited a hexagonal plane with

preferred grain orientations along (100), (002), (101), (110) and (201). All of the peaks are well matched with the bulk ZnO, which could be indexed as the hexagonal wurtzite structure of ZnO [24]. All films obtained without annealing exhibited hydroxide peaks (the result not shown).

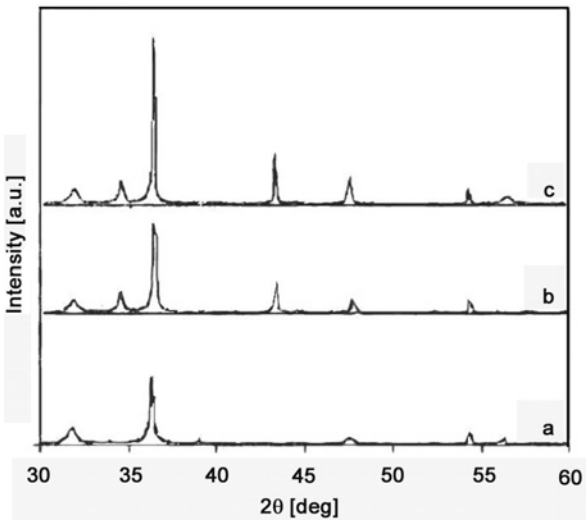

Fig. 1. XRD pattern of the annealed ZnO thin film grown at the bath temperature of: a) 30 °C, b) 40 °C, c) 50 °C

In Figure 1, pattern a corresponds to the film deposited with the bath temperature of 30 °C: it has only one prominent peak, other ones are very small. Patterns b and c show the XRD pattern of the films grown at 40 °C and 50 °C, respectively. They show that peak amplitudes are higher for the films grown with increased bath temperatures.

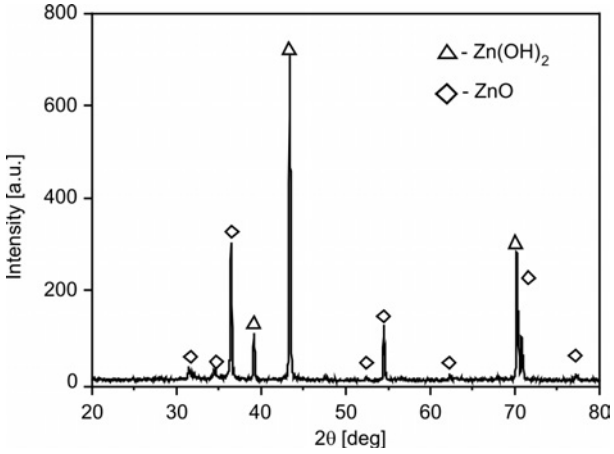

Fig. 2. XRD pattern of the ZnO thin film grown with a bath temperature of 60°

Figure 2 shows the XRD pattern of ZnO film with peaks originating from ZnO and $Zn(OH)_2$ before annealing of the films deposited at 60 °C. ZnO films deposited at considered temperatures also exhibited $Zn(OH)_2$ peaks and ZnO peaks but $Zn(OH)_2$ may be converted into ZnO by annealing in air [25]. Figure 3 shows the X-ray diffraction peaks of the annealed ZnO films deposited at the bath temperature of 60 °C. Annealing of the films at 300 °C for 1 h converted all $Zn(OH)_2$ into ZnO.

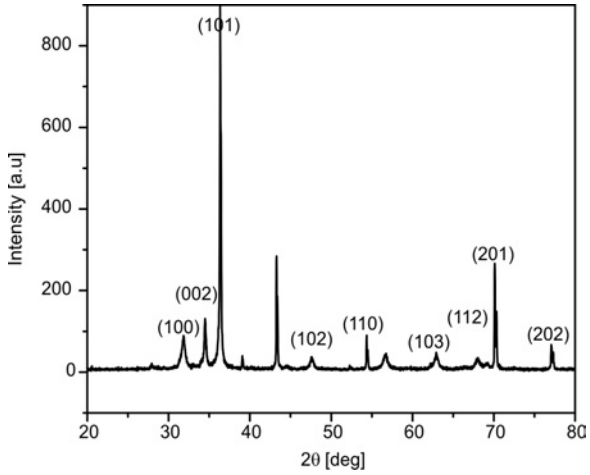

Fig. 3. XRD pattern of the ZnO thin film after annealing at 300 °C, grown at 60 °C

The annealed films crystallized in the hexagonal structure. The lattice parameters were calculated from:

$$\frac{1}{d_{hkl}^2} = \frac{4}{3}\left(\frac{h^2 + hk + k^2}{a^2}\right) + \frac{l^2}{c^2}$$

The mean values of the lattice parameters were found to be a = 3.251 Å, c = 5.213 Å, which are in good agreement with the literature data. A comparison of standard ASTMS data with the deposited ZnO thin films is also shown in Table 2.

Table 2. Comparison of calculated d values with JCPDS data

hkl	Calculated d_{hkl} [Å]	JCPDS d_{hkl} [Å]
100	2.808	2.816
002	2.598	2.602
101	2.471	2.476
102	1.907	1.913
110	1.632	1.626
103	1.469	1.478
112	1.381	1.379
201	1.358	1.360
202	1.232	1.239

In order to evaluate the mean crystallite size of the particles, the Debye–Scherrer formula was used

$$D = \frac{0.9\lambda}{\beta \cos\theta}$$

Table 3 shows the crystallite sizes and the band gap with the bath temperature. Greater crystallite sizes were obtained for the films grown at higher temperatures, whereas the band gap energy was observed to decrease as the bath temperature increased.

Table 3. Crystallite sizes and band gaps at various temperatures

Bath temperature [°C]	Crystallite size [nm]	Band gap [eV]
30	32	–
40	36	3.33
50	38	3.25
60	41	3.14

3.3. Study of the surface morphologies

The morphologies of the deposited materials were examined using scanning electron microscopy. The films deposited under the optimized conditions were smooth, dark gray in colour and uniformly covered the substrate with good adherence. Scanning electron micrographs of the ZnO films grown under various conditions are shown in Figs. 4–7.

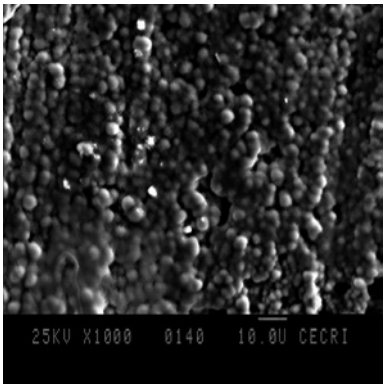

Fig. 4. SEM of the as-grown ZnO thin film deposited at 60 °C

Fig. 5. SEM of the ZnO thin film after annealing at 300 °C for 1 h, a magnified particle in the inset

Figure 4 shows the surface morphology of the as-grown ZnO film deposited at 60 °C. The morphology of the annealed film is shown in Fig. 5. It exhibits well defined grain edges, and the inset shows a magnified view of individual grains. The overall surface structure is seen to have grains of spherical shape, uniformly covering the substrate, without any cracks or pores.

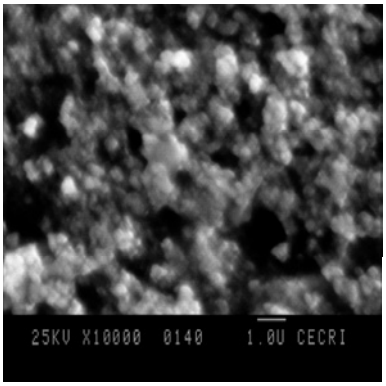

Fig. 6. SEM of the ZnO thin film deposited on a glass plate

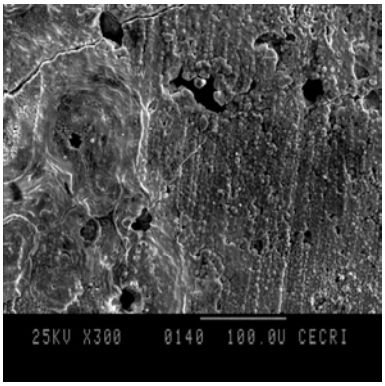

Fig. 7. SEM of the ZnO thin film deposited on a zinc plate for 15 h at 60 °C

Figure 6 presents the morphology of the ZnO film grown on the glass substrate. These films were non-uniform, powdery, and poorly adherent. The precipitated clusters are poorly adsorbed on the surface of the substrate. Figure 7 shows the film grown in a bath with pH = 11 pH for more than 15 h. Its surface is rough and has cracks. Some of these cracks are so severe that they even extend as far as the substrate itself.

3.4. Optical study

In order to study the optical properties of the ZnO thin films deposited by the chemical bath deposition technique, optical reflectance spectra were recorded in the 200–400 nm range, using a Varian Cary 500 instrument. The optical band gap energy of ZnO thin film was determined from the reflectance spectra [26].

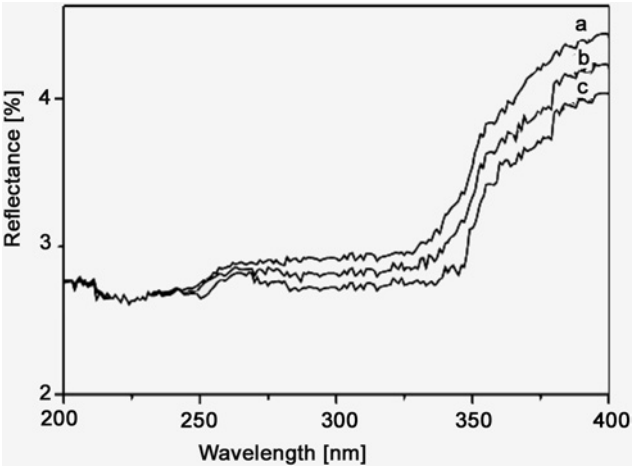

Fig. 8. Optical reflectance spectra of ZnO thin films deposited at: a) 40 °C, b) 50 °C, c) 60 °C

Figure 8 shows the reflectance spectra of the films deposited at 40 °C, 50 °C and 60 °C. The band gap energy (Table 3) of zinc oxide was found to be dependent on the bath temperature. It was found to be close agreement with the reported values [27].

4. Conclusion

The chemical bath deposition technique was successfully used to fabricate ZnO thin films on zinc plates. Structural, optical and morphological studies were carried out. The crystallite size and band gap energy were found to depend on the bath temperature. The band gap decreased as the crystallite size increased. The bath temperature was found to influence the growth of ZnO crystallites: at temperatures above 50 °C, good crystalline film was produced. The pH range 9.5–10.5 was found to be the most suitable for CBD growth of ZnO. The use of zinc as the substrate is conducive to smooth adsorption of zinc ions on the surface and it results in a high-quality coating. A decrease in the band gap was observed upon increasing the bath temperature and size of the crystallites.

Acknowledgements

This work has been supported by the Millimeter-Wave Innovation Technology Research Center (MINT), Dongguk University, Republic of Korea.

References

[1] JOHNSON J.C., YAN H., SCHALLER R.D., HABER L.H., SAYKALLY R.J., YANG P., J. Phys. Chem. B, 105 (2001), 11387.
[2] DURAN P., CAPEL F., TARTAJ J., MOURE C., Adv. Mater., 14 (2002), 137.
[3] HWANG D.-K., OH M.-S., LIM J.-H., PARK S.-J., J. Phys. D: Appl. Phys., 40 (2007), R387.
[4] IZYUMSKAYA N., AVRUTIN V., ÖZGÜR Ü., ALIVOV Y.I., MORKOÇ H., Phys. Stat. Sol. (b), 244 (2007), 1439.
[5] CHEN Y.F., BAGNALL D.M., KOH H.J., PARK K.T., HIRAGA K., ZHU Z.Q., YAO T.J., J. Appl. Phys., 84 (1998), 3912.
[6] MINAMI T., YAMAMOTO T., MIYATA T., Thin Solid Films, 366 (2000), 63.
[7] REN F., JIANG C.Z., XIAO X.H., Nanotechn., 18 (2007), 285609.
[8] MA Y., DU G., YIN J., YANG T., ZHANG Y., Semicond. Sci. Techn., 20 (2005), 1198.
[9] KOKUBUN Y., KIMURA H., NAKAGOMI S., Jpn. J. Appl. Phys., 42 (2003), L904.
[10] PARAGUAY F.D., ESTRADA W.L., ACASTA D.R.N., ANDRADE A., MIKI-YOSHIDA M., Thin Solid Films, 192 (1999), 350.
[11] KRISTOULAKIS S., SUCHEA M., KATHARAKIS M., KATSARAKIS N., KOUDOUMAS E., KIRIAKIDIS G., Rev. Adv. Mater. Sci., 10 (2005), 331.
[12] OSHIDA T.Y., KOMATSU D., SHIMOKAWA N., MINOURA H., Thin Solid Films, 451–452 (2004), 166.
[13] IZAKI M., SHINAGAWA T., TAKAHASHI H., J. Phys. D: Appl. Phys., 39 (2006), 1481.
[14] CAO B., CAI W., ZENG H., DUAN G., J. Appl. Phys., 99, (2006), 073516.
[15] DRICI A., DJETELI G., TCHANGBEDJI G., DEROUICHE H., JONDO K., NAPO K., BERNÈDE J.C., OURO-DJOBO S., GBAGBA M., Phys. Stat. Sol. (a), 201 (2004), 1528.

[16] OUERFELLI J., REGRAGUI M., MORSLI M., DJETELI G., JONDO K., AMORY C., TCHANGBEDJI G., NAPO K., BERNEDE J.C., J. Phys. D: Appl. Phys., 39 (2006), 1954.
[17] ENNAOUI A., WEBER M., SCHEER R., LEWERENZ H.J., Sol. Energy Mat. Solar Cells, 54 (1998), 286.
[18] NIESEN T.P., DE GUIRE M.R., J. Electroceram, 6 (2001), 169.
[19] GOVENDER K., BOYLE D.S., KENWAY P.B., O'BRIEN P.J., Mater. Chem., 14 (2004), 2575.
[20] SANKAPAL B.R., SARTALE S.D., LOKHANDE C.D., ENNAOUI A., Sol. Energy Mater. Solar Cells, 83 (2004), 447.
[21] KU C.-H., JENW J.U, Nanotechn., 18 (2007), 505706.
[22] PENG W., QU S., CONG G., WANG Z., Crystal Growth Design, 6 (2006), 1518.
[23] SAEED T., O'BRIEN P., Thin Solid Films, 271 (1995), 35.
[24] CAO H.L., QIAN X.F., GONG Q., DU W.M., MA X.D., ZHU Z.K., Nanotechn., 17 (2006), 3632.
[25] CHATTERJEE A.P., MITRA P., MUKHOPADHYAYA A.K., J. Mater. Sci., 34 (1999), 4225.
[26] XIE J., DENG H., XU Z.Q., LI Y., HUANG J., J. Crystal Growth, 292 (2006), 227.
[27] SINGH A.V., MEHRA R.M., BUTHRATH N., WAKAHARA A., YOSHIDA A., J. Appl. Phys., 90 (2001), 5661.

Received 15 June 2009
Revised 23 October 2009

Materials Science-Poland, *Vol. 28*, *No. 2*, *2010*

Activation energy of tribochemical and heterogeneous catalytic reactions

C. K. KAJDAS[1, 2*], A. KULCZYCKI[1], K. J. KURZYDŁOWSKI[2], G. J. MOLINA[3]

[1]Institute for Fuels and Renewable Energy, 55 Jagiellońska, 03-301 Warsaw, Poland

[2]Warsaw University of Technology, Institute of Chemistry in Płock, 17 Łukasiewicza, 09-400 Płock, Poland

[3]Warsaw University of Technology, Faculty of Materials Science and Engineering, ul. Wołoska 141, 02-507 Warsaw, Poland

[4]Department of Mechanical and Electrical Engineering Technology, Georgia Southern University, Statesboro, GA 30460-8045, USA

The relationship between the activation energy and enthalpy, either in the presence or absence of a catalyst, is of particular importance. If a catalyst is present, the energy required for a given chemical reaction to go into transition state decreases, thereby decreasing the energy required to initiate the reaction. The dynamics of heterogeneous catalysis is still under discussion. The same applies to tribochemistry and/or tribocatalysis. It has been assumed that heterogeneous solid catalysts decrease the activation energy, reflected as apparent activation energy. The model presented elsewhere has been theoretically evidenced for the first time by reviewing the existing literature data concerning anisotropy features of the angular distribution of exoelectrons emitted from perturbed surfaces. Metal–insulator–metal thin film sandwich structures are of particular interest in this paper. Other evidence supporting the model is also discussed such as the anisotropic desorption emission from a surface during catalytic processes. The conclusions of this work have been applied in practice to design specific measurement techniques and devices for estimating the angular distribution of electrons triboemitted from solid catalyst materials under sliding contact in a high-vacuum tribometer.

Keywords: *triboemission; tribochemical reaction; catalyst*

1. Introduction

A catalyst is a substance that increases the rate at which a chemical system approaches equilibrium, without itself being consumed in the process; catalysis is the action which occurs as a direct result of the presence of a catalyst. A catalyst lowers

*Corresponding author, e-mail: ckajdas@pw.plock.pl

the activation energy [1]. In chemical kinetics, E_a is the height of the potential barrier separating the products and reactants. It determines the temperature dependence of the reaction rate. When regular solid catalysts such as those applied in industry (for instance, nano-dispersed metals on amorphous aluminosilicates) are considered, the effect of this type of material might be compared with the action of mechanically activated solids such as in tribocatalysis [2]. Heterogeneous catalysis accelerates the movement of atoms on their passage through the transition state; it provides the link between reactants and products on a reaction pathway which involves simultaneous motion from several to numerous atoms [3]. Friction processes enhance the energy of the mating elements by, for instance, dislocation defects. The mechanism by which lubricants form a protective layer, in the space near solid materials, during a tribological process was recently analyzed by the so called α_i method [4]. The principle of the α_i model was presented by Kulczycki [5, 6]. Analysis of the model with regard to empirical data of tribological processes leads to conclusions regarding the mechanisms of catalytic processes. Assumptions of the model are as follows: (i) E_a is constant for a given type of reaction, and the initiation of the reaction depends not only on the energy (E_a) delivered to the substrates but also on the density of the energy stream introduced; (ii) a catalyst collects energy introduced into the system and emits it as impulses of a high density flux of energy, thereby triggering the reaction or increasing its rate, (iii) the catalyst emits impulses of energy flux of high density; at some angle γ, the energy emitted in a short time is equal to the activation energy E_a.

The model can be applied to tribological systems: the mechanical work done can be treated as the input, and the dissipated energy – predominantly heat – can be treated as the output. The functional input–output relationship may also be applied to tribochemical reactions which are known to proceed much faster than thermochemical ones. One further extension of the model, tribochemical reactions with heterogeneous catalytic reactions are compared [5, 7]. The energy accumulated in a solid increases the enthalpy of the system. Tkacova et al. [8] show that the dislocation concentrations with the specific energy of defect structures are of particular meaning for the energetic condition of the energy contributions. It relates to changes in both structure and enthalpy, and it is consistent with the statement that tribochemical reactions are mostly stimulated by triboelectrons emitted under friction conditions. This work proposes that both heterogeneous catalytic and tribochemical processes are controlled by triboelectrons [9]. A direct correlation between catalytic activity and the EEE intensity, for various deposited and promoted catalysts, was clearly shown by Sato and Seo [10]. Biernacki et al. [11] demonstrated the temperature dependence of the intensity of photostimulated EEE from Raney nickel, and cobalt alloys.

While theoretical friction dissipation models and computer simulations have significantly improved in sophistication over the past decade, their applicability is hampered by a lack of empirical data. Most of these models are either of a phenomenological nature only or they consider friction solely at the skin of rigid corrugated surface potentials.

The fact that friction also involves intrinsic activation modes, e.g., relaxation modes in organic solid materials, has only been recognized in a few isolated studies. Knorr et al. [12] provide direct insight into the basic material intrinsic mechanism for frictional dissipation at the submolecular scale of amorphous organic systems. They demonstrated that at low pressures and temperatures below the glass transition point, the phenyl pendant side groups of polystyrene, known for their preferential orientation at the free surface, were the primary channel by which the kinetic sliding-energy is dissipated. This process was found to be truly enthalpic, having an activation energy of 8 kcal/mol. The energy dissipation was shown to possess both enthalpic and cooperative entropic contributions above the loading capacity of the surface phenyl groups. They also found "apparent Arrhenius activation energies of frictional dissipation of 22 kcal/mol and 90 kcal/mol, respectively, and cooperative contributions up to 80% [12]." As such, the study highlighted issues critical to organic lubricant design, i.e., the intrinsic enthalpic activation barriers of mobile linker groups, the evaluation of cooperative mobility phenomena, and critical tribological parameters that permit or prevent coupling between shear disturbances and molecular actuators.

In the paper, activation energy types with respect to the EEE process have been analysed. The primary goal of the present work is to provide the first theoretical evidence for the model presented in [5] by exploiting relevant data in the existing literature about the anisotropy on angular distribution of exoelectrons (EE) emitted from perturbed surfaces, in particular from metal–insulator–metal thin film sandwich structures. The other goal of the paper is the design of specific measurement techniques and devices for use in a high vacuum tribometer [13] for estimating the angular distribution of triboelectrons emitted from solid catalyst materials under a sliding contact.

2. Direct background

Kajdas and Kulczycki [5] hypothesized that for standard and catalyzed heterogeneous reactions the same real activation energy E_a is needed to initiate reaction processes. It is proposed that energy introduced into a tribological system as a mechanical work, performed on a solid material, is accumulated in this material and then emitted as electrons and/or photons to the space in which reactions take place. The developed model includes the specific angle γ at which the stream of emitted energy e_γ, lying in the 3–5 eV range, is emitted and the reaction can be initiated [5].

The distribution of the energy emitted by the solid body (e.g., by the catalyst) is controlled by the angle of emission

$$e_\gamma = e_0 \cos\gamma$$

where γ is a function of loading P and depends on the stream of energy introduced into the tribological system, e_0 is the density of the energy flux in the direction perpendicular to the solid body surface [5]. Figure 1 shows the process by which the energy emitted from the surface as pulses can reach the value of E_a, and the heterogeneous catalytic process starts.

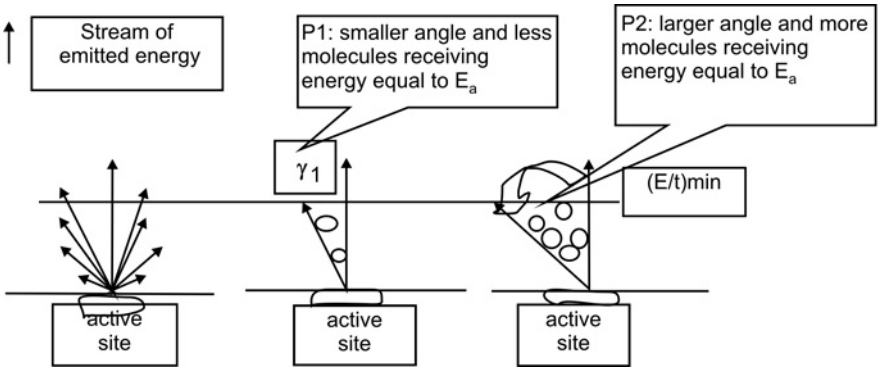

Fig. 1. Main concept of the model: the stream of energy emitted by the catalyst depends on the angle γ, hence the number of molecules receiving energy equal to E_a depends on γ

3. Electron and photon emission anisotropy

An exhaustive literature search did not reveal any available data on the angular distribution of triboemitted electrons but the published papers on electron emission from cathodes consistently report that the distributions are anisotropic [14–17]. Highly anisotropic distributions, having a maximum in the direction normal to the emitting surface, were measured.

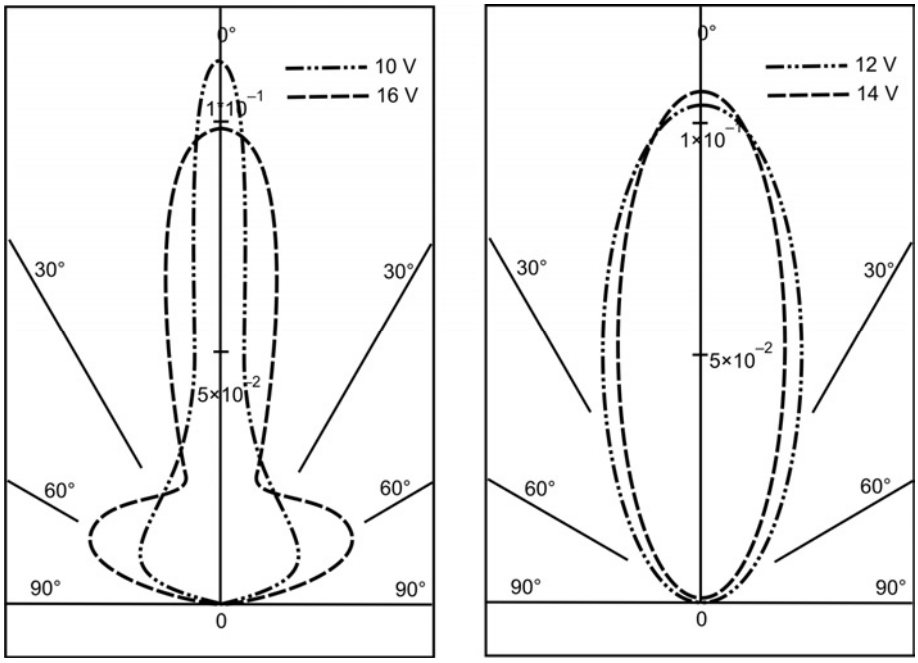

Fig. 2. Examples of EE from sandwich cathodes. The EE is highly anisotropic, and the maxima occur in the direction normal to the emitting surface [16, 17]

Figure 2 shows an example of anisotropic electron emission from sandwich cathodes, from the work of Hrach [16, 17]. At the emission temperature of 300 K, the measured electrons exhibit quasi-isotropic behaviour. But at a lower temperature of 80 K, the isotropic component vanishes. Furthermore, at room temperature approximately 1/3 of the total emission is located in a narrow region around the maximum [14, 15], oriented in the direction normal to the emitting surface. Hrach et al. [16, 17] recorded the energy characteristics of emitted electrons at various angles by means of a hemispherical collector and the retarding-grid technique. They found that at 300 K the anisotropic energy spectra of emitted electrons were in the 0–7 eV range but for emission angles closer to the normal to the surface the measured energy was between zero and 4 eV. In Figure 3, some of these findings are shown.

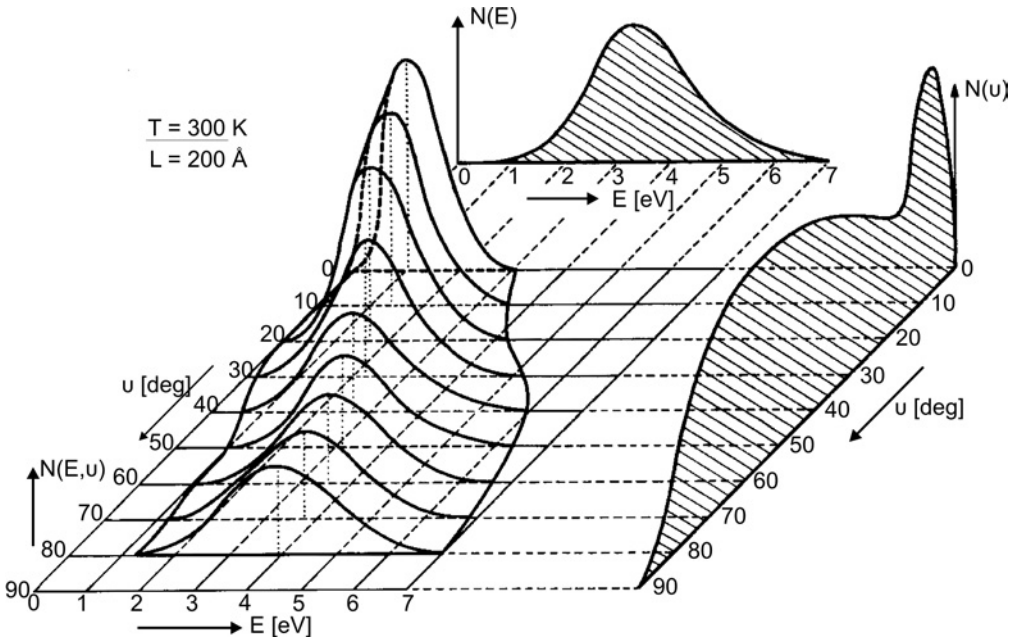

Fig. 3. Typical experimental angular and energy distributions of electrons emitted from Al–Al_2O_3–Au sandwich cathode structures. Applied voltage – 10 V [17]

A more recent study was presented by Fitting et al. [18] on the angular distribution of thermostimulated exoelectron emission (TSEE) from α-Al_2O_3. They found anisotropic angular distributions to be mainly oriented in the direction normal the surface; the energy of the emitted electrons was in the range 0–4 eV. Thus, the literature review provided strong evidence that low energy electrons are typically emitted according to highly anisotropic distributions, with maxima occurring in the direction normal to the surface. Interestingly, model calculations are consistent with the experimental data and the work of Kortov and Zolnikov [19], who predicted that the angular distri-

bution from an Auger type emission would not be influenced by roughness in homogeneous samples.

The available data on the measurement of the angular distribution of electron emissions is limited to cathode emission [14, 16, 17], TSEE [18] and backscattered emission [20] from electron bombardment of the emitting surfaces. The angular distributions of photoelectrons and emitted photons were also extensively studied; Jablonski and Zemek [21] found a highly anisotropic distribution, similar to the one of electron type, for photon emission from X-ray-irradiated thin polycrystalline aluminum foils. Hucek et al. [22] found similar anisotropy for irradiated Cu, Ag and Au foils, and that the isotropic component is attributable to elastic collisions that photoelectrons experience on their way out of the target. Anisotropy also occurs for other spectral lines.

4. Low energy electron triboemission

The emission of electrons, ions, neutral particles, photons, and acoustic emission under conditions of tribological contact and damage is called triboemission [23]. Triboemitted electrons, which make up the major part of the charged triboparticle emission stream associated with insulators and semiconductors are known to be related to exoemission (including chemical exoemission and fractoemission). Furthermore, it has been postulated that triboemitted electrons are key factors in the initiation and control of tribochemical reactions [24]. For examinations of triboemission of charged particles a high vacuum tribometer [25] was used, but there is evidence that triboemission occurs not only under high vacuum [26, 27]. Molina et al. characterized burst-type electron triboemission for diamond scratching under a constant load and constant scratch-speed. They tested insulators such as alumina, sapphire [23], silicon nitride [28], as well as semiconductors Si and Ge [29]. They also made tests on an alumina ball sliding on an alumina disk [30]. It is of note that positively charged emission from insulators was negligible, regardless of the specific choice of insulator material or the atmospheric conditions. Aluminum was found to produce much lower electron triboemission. Molina et al. [25] also found large fractions of low energy triboelectrons (e.g., 1–5 eV) arising from alumina and sapphire scratching, and spectra extending beyond the largest set potential (i.e., 48 eV). In Figure 4, a typical electron triboemission count (in the 100 msec acquisition window) is shown, obtained from diamond sliding on a silicon nitride disk. Low energy electron emission is clearly associated with, and initiated by, the process of sliding contact.

Some relevant electrical phenomena are well-known, such as triboelectrification on dielectric surfaces, even though their precise mechanisms have not yet been fully clarified. Electron triboemission is affected by surface charge and it may have an effect on the energy of emitted electrons. Figure 5 shows the results of measurement of negatively charged triboemission (CEM-count) when no grounded grid is placed between the emitting surface (a diamond scratching of an alumina disk) and the detector,

making apparent the higher rate of emission that can be attributed to the acceleration of electrons to higher energy levels caused by the surface charge.

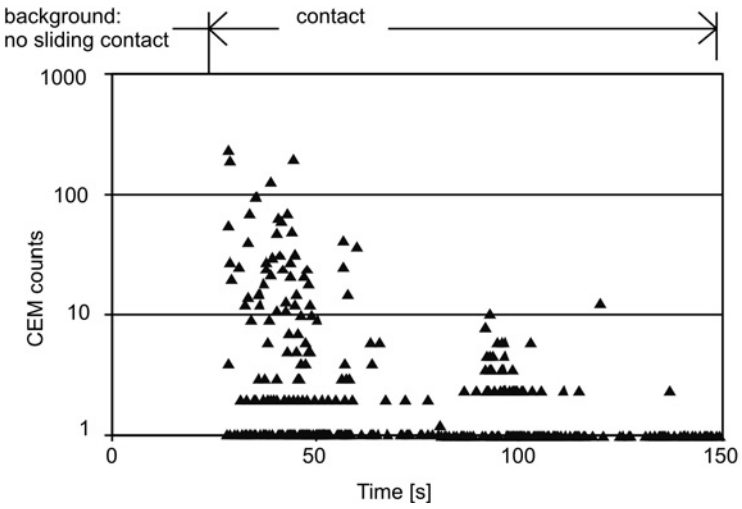

Fig. 4. Negatively charged triboemission (recorded with a channel electron multiplier (CEM) in the count mode) for diamond on Si_3N_4; acquisition window – 100 msec, load – 5 N, speed – 1.0 mm/s

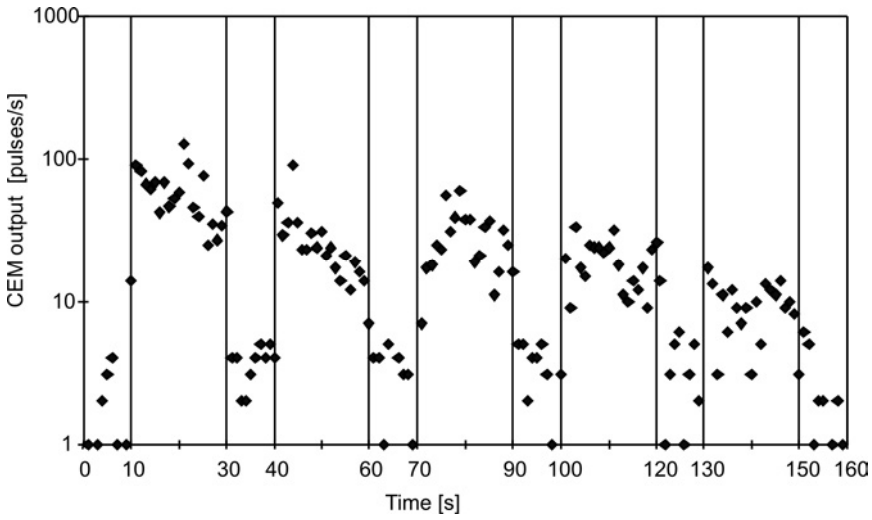

Fig. 5. Negatively-charged triboemission (CEM count for a non-grounded grid) for diamond on alumina sliding contact. 20s periods of sliding contact are followed by 10 s periods of no contact; load – 2N, speed – 0.14 cm/s, acquisition window – 10 ms

Figure 5 also shows that electron emission proceeds after the contact is arrested (e.g., during periods of no-sliding contact); it is attributed to the effect of activated sites on the surface, and has been experimentally shown to last for long periods after

tribological contact has stopped. Precise details of the mechanism by which triboelectron emission occurs still remain however unclear.

Molina et al. [24] have recently proposed that electron triboemission can be the result of non-adiabatic surface reactions according to the Kasemo model [31]. This model is based on the Auger decay process, in which an impingent gas particle provides an empty level that is filled by an electron from the solid, while energy is transferred to another emitted electron. The probability of such an event is very low, of ca. 10^{-4} per impingent molecule but is consistent with the observed exoemission processes.

Chemical reactions may dissipate part of their energy to electron–hole pairs in the surface region: part of the impingent molecule energy may be transferred to electronic states which are lower by several eV from the ground state potential of the surface. A low energy electron would then be emitted in a non-adiabatic process; this phenomenon of low energy "chemiemission" has been extensively observed. Although classical mathematical models of surface chemistry processes (i.e., quantum or first principle descriptions of the atomic interactions) assume that such deviations from adiabatic behaviour are small and of no practical importance, recent experimental works [32–34] have shown that exoelectron emission is just a fraction of the total electronic excitation on the surface. The majority of non-adiabatic excitations would not be typical exoemissions but they are detectable as "chemicurrents" which are due to chemically generated hot carriers, and stay in the solid. Nienhaus et al. [33] detected such chemicurrents by using thin film electronic devices that allow non-emitted excited electrons to traverse their Schottky barrier (of only about 0.7 eV) as "internal exoemissions". By this method they estimated that, for instance, for the oxidation of Mg surfaces approximately 10% of the chemical reaction energy is dissipated by non-adiabatic electronic excitation.

Bottcher et al. [35] identified the profile of the electron work function (WF) and the intensity of the exoemission that occurs when Cs is exposed to O_2. They found that no electron emission was detected during clean surface exposure to increasing quantities of O_2, until the pressure of ca. 10^{-6} Torr was reached, i.e., until partial oxidation would be needed for this chemiemission to occur. A decrease in the WF also was observed, but its minimum was reached for lower O_2 exposure than that of the electronic peak. This result suggests that the electronic excitation occurring through chemical reaction may govern exoemission, rather than the lowering of the WF being the dominant factor. The mechanism for this emission can be interpreted by the model of Kasemo et al. [31]. Bottcher et al. [35] also demonstrated that, according to this model, the probability of emission decreases monotonically as the formation of the oxide layer approaches completion.

Nonadiabatic reactions may facilitate explanation of some features of the surface catalytic processes where internal vibrational modes are highly excited and not in equilibrium with each other [36, 37] as in, for instance, the catalytic oxidation of CO on Pt. Interesting enough, product desorption from such catalytic reaction occurs in

a narrow angular cone. Becker et al. [38] established experimentally that the most probable CO_2 desorption energy is 3560 K, which occurs perpendicular to the Pt-emitting surface at 880 K. This is an important characteristic of desorption emissions that arise from surface catalytic processes. It provides further evidence supporting the predicted direction of anisotropy of the model [5] discussed in the paper.

5. Current research plans

Data on the angular distribution of triboemitted electrons are not available. Such measurements pose additional challenges when compared with cathode emission measurements, the two most important being: (i) the emitting surface is in motion (as either pin-on-disk or a reciprocating contact) and it will be a ring- or segment-wear-track; and (ii) the pin geometry would interfere with the path of triboelectrons emitted during and immediately after contact.

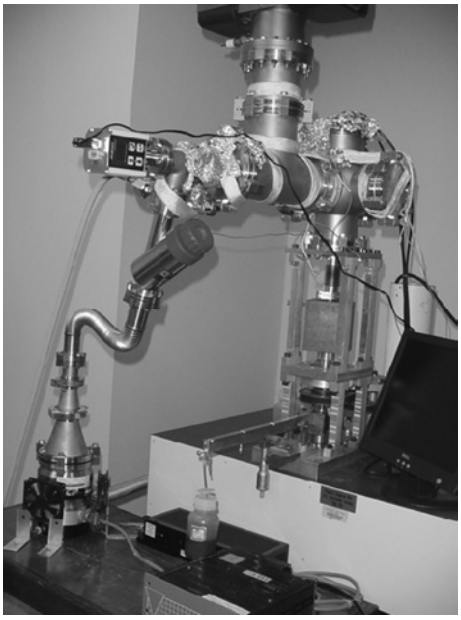

Fig. 6. High vacuum tribometer
(photograph by Molina et al. [2, 25])

Based on the conclusions of this work, the following experiments have been planned using high vacuum tribometer [13, 25] shown in Fig. 6:

- The design of a voltage-biased grid-filter with two openings at angles; one opening will maximize the collection of electrons in the direction normal to the emitting-surface, while the other will mostly collect emission for angles greater than about 30 degrees. The two grid-openings will be alternatively biased in a sequence (i.e., one for

negative potential while the other for zero one) that will be synchronized to the electron detection and counting.

• The use of an electron sensitive film (i.e., electron microscopy film), semispherical ring detector on top of a circular shield with a hole and the scratching pin.

• The use of cooled CCD camera for detection of electrons at various angles. However, this option may have a limitation with sensitivity for electrons of energy lower than 700 eV.

• The use of a hemispherical collector divided into concentric annular segments connected to a picoammeter which can be placed above a circular shield with a hole and the scratching pin as in the figure above.

• Alternatively, the measurement of triboemitted photons at various angles; the assumption could be made that photon angular distribution would be similar to that of triboelectrons. In this, the authors develop a setup for counting of triboemitted photons based on a solid state photon detector and a counter, and fibre optics to collect signals from the emitting surfaces.

6. Conclusions

This paper demonstrates that heterogeneous catalysis is controlled by low energy electrons, similarly to the way tribochemistry is controlled by triboelectrons. The data under review in this paper confirm the anisotropy of the angular distribution of exoelectrons emitted from perturbed surfaces, and thereby provide the first empirical evidence for the the α_i mathematical model [5]. The model discussed in this paper provides a new approach to investigate the activation energy and leads to better understanding of heterogeneous catalysis. Although the discussed anisotropic EE relates to metal–insulator–metal thin film sandwich structures, we consider this fact as a first evidence for the proposed model, which predicts such a distribution of triboelectrons. Devices and methods are designed for an updated high-vacuum tribometer [13], for the purpose of providing experimental evidence for the predicted angular distribution of electrons that are triboemitted from solid catalyst materials under sliding contact.

Acknowledgement

The authors gratefully acknowledge a Georgia Southern University faculty research grant and the support of the Institute for Fuels and Renewable Energy and Warsaw University of Technology.

References

[1] BOND G.C., *Heterogeneous Catalysis: Principles and Applications*, 2nd Ed., Clarendon Press, Oxford, 1987.
[2] HIRATSUKA K., KAJDAS C., *Tribology. Science and Application*, CUN PAN, Warsaw (2004), pp. 71–90.
[3] KLIER K., Topics Catal., 18 (2004), 141.
[4] KULCZYCKI A., KAJDAS C., Lubr. Sci., 6 (1994), 161.
[5] KAJDAS C.K., KULCZYCKI A., Mater. Sci.-Poland, 26 (2008), 787.

[6] KULCZYCKI A., Wear, 103 (1985), 67.
[7] KAJDAS C., Proc. 2nd World Tribology Congress, 2001, F. Franek, W.J. Bartz, A. Pauschitz (Eds.), The Austrian Tribology Society, Vienna 2001, pp. 39–41.
[8] TKACOVA K., HEEGN H., STEVULOVA N., Int. J. Mineral Proc., 40 (1993), 17.
[9] KAJDAS C.K., Tribology International, 38 (2005), 337.
[10] SATO N., SEO M., J. Catal., 24 (1972), 224.
[11] BIERNACKI L., GÓRECKI C., GÓRECKI T., Japan J. Appl. Phys., 24 (1985), 116.
[12] KNORR D.B. Jr., GRAY T.O., OVERNEY R.M., J. Chem. Phys., 129 (2008), 074504-1.
[13] MOLINA G.J., HIRATSUKA K., KAJDAS C., STLE Annual Meeting, CD, Cleveland (2008).
[14] HRACH H., MAY J., Phys. Stat. Sol. (a), 4 (1971), 637.
[15] GOULD R.D., HOGARTH C.A., Phys. Stat. Sol. (a), 41 (1977), 439.
[16] HRACH H., Czech. J. Phys., B23 (1973), 234.
[17] HRACH H., Thin Solid Films, 15 (1973), 65.
[18] FITTING H.-J., GLAEEFEKE H., WILD W., LANGE J., Phys. Stat. Sol. (a), 42 (1977), K75.
[19] KORTOV V.S., ZOLNIKOV P.P., Phys. Stat. Sol. (a), 31 (1975), 331.
[20] DARLINSKI A., Phys. Stat. Sol. (a), 63 (1981), 633.
[21] JABLONSKI A., ZEMEK J., Physical Review B, 48 (1993), 4799.
[22] HUCEK S., TILINION I.S., ZEMEK J., J. Electr. Spectry Rel. Phen., 85 (1997), 263.
[23] KAJDAS C., FUREY M.J., RITTER A.L., MOLINA G.J., Lubr. Sci., 14 (2002), 223.
[24] MOLINA G.J., KAJDAS C., FUREY M.J., Proc. Adhesion Society Meeting, Savannah, Georgia, USA, February 2009, pp. 327–329.
[25] MOLINA G.J., FUREY M.J., RITTER A.L., KAJDAS C., Wear, 249 (2001), 214.
[26] NAKAYAMA K., HASHIMOTO H., SUSUKI T., J. Phys. D, 25 (1992), 303.
[27] KIM M., LANGFORD S.C., DICKINSON J.T., Tribol. Lett., 1 (1995), 147.
[28] MOLINA G.J., FUREY M.J., KAJDAS C., Proc. 11th NORDTRIB, 2004, Oslo, Norway, CD Rom.
[29] MOLINA G.J., MAZILU D.A., FUREY M.J., KAJDAS C., Ann. Univ. "Dunarea De Jos" of Galați, Romania (2004), 8, pp. 22–29.
[30] MOLINA G.J., FUREY M.J., KAJDAS C., STEIKA N., Ann. Univ. "Dunarea De Jos" of Galați, Romania, (2005), 9, pp. 17–23.
[31] KASEMO B., TORNQVIST E., NORDSKOLD J.K., LUNDQVIST B.I., Surf.e Sci., 89 (1979), 554.
[32] NIENHAUS H., GLASS S., Surf. Sci., 600 (2006), 4285.
[33] GLASS S., NIENHAUS H., Phys. Rev. Lett., 93 (2004), 168302.
[34] GERGEN B., NIENHAUS H., WEIBERG W.H., MCFARLAND E.W., Science, 294 (2001), 2521.
[35] BOTTCHER A., IMBECK R., MORGAANTE A., ERTL G., Phys. Rev. Lett., 65 (1990), 2035.
[36] HASSELBRINK E., Surf. Sci., 603 (2009), 1564.
[37] MATSUSHIMA T., Progr. Surf. Sci., 82 (2007), 435.
[38] BECKER C.A., COWIN J.P., WHARTON L., AUERBACH D.J., J. Chem. Phys., 67 (1977), 3394.

Received 4 August 2009

Materials Science-Poland, *Vol. 28*, *No. 2*, *2010*

Synthesis and characterization of V_2O_3 microcrystal particles controlled by thermodynamic parameters

J. QI[1*], G. NING[2], Y. ZHAO[1], M. TIAN[1], Y. XU[1], H. HAI[1]

[1]Department of Chemical Engineering, Life Science College,
Dalian Nationalities University, 18 Laohe West Road, Dalian 116600, China

[2] Department of Chemical Engineering of Material, School of Chemical Engineering,
Dalian University of Technology, 158 Zhongshan Road, Dalian 116012, China

A facile process is developed for the synthesis of pure vanadium(III) oxide by thermal reduction of vanadium pentoxide (V_2O_5) in ammonia gas. The process of thermal reduction of V_2O_5 was optimized by experiments and by modeling of thermodynamic parameters. The obtained V_2O_3 was characterized by X-ray diffraction, X-ray photoelectron spectrometry, scanning electron microscopy and thermogravimetric analysis. The experimental results indicated that crystal particles of pure V_2O_3 were successfully synthesized within a short reaction period of 1 h and at a relatively low temperature of 903 K. The content of V_2O_3 in the product sample higher than 99 wt. %. The grain size of V_2O_3 ranged from several hundred nanometers to several micrometers. The morphologies of the V_2O_3 particles were micrometer layers in nanometer sheet structure.

Keywords: *vanadium oxides; chemical synthesis; thermodynamic parameters; X-ray diffraction; scanning electron microscopy*

1. Introduction

The V_2O_3 system has been the subject of many investigations because it exhibits at least one, if not several, spectacular metal–insulator transitions [1]. The most notable one is that pure vanadium(III) oxide displays a single metal–insulator transition (MIT) around 160 K, changing from a low-temperature antiferromagnetic insulator to a high-temperature paramagnetic phase [2]. Vanadium oxide V_2O_3 was chosen as the conductive ceramic oxide because of previous research on the properties of composite thermistors [3]. V_2O_3 is a potential material for many functional devices such as temperature sensors and current regulators [4]. V_2O_3 powder can also be used in conductive polymer composites [5], in catalysts [6], etc. V_2O_3 is the most unstable material among V_2O_5, VO_2 and V_2O_3. Fabrication of pure V_2O_3 is not straightforward because

*Corresponding author, e-mail: qiji@dlnu.edu.cn

it forms in conditions similar to those of formation of VO_2 [7]. In past years, many methods for preparing V_2O_3 powder have been studied. Spherical V_2O_3 particles were prepared by the O_2–H_2 flame of V_2O_3 at 2273 K [8]; spherical and necking V_2O_3 powder was synthesized by reducing V_2O_5 in a H_2 flow at 1123 K for 6 h [9]. V_2O_3 powder was also fabricated by pyrolyzing hydrazine containing vanadium salt and by reducing the sol-gel synthesized V_2O_5 in a H_2 stream [10]. Furthermore, V_2O_3 nanoparticles were synthesized by laser induced vapour phase reaction [11], by reductive pyrolysis of ammonium oxovanadium (IV) carbonate hydroxide, $(NH_4)_5[(VO)_6\ (CO_3)_4(OH)_9]\cdot 10H_2O$, under H_2 atmosphere [12], by thermal decomposition of vanadium oxalate [13], by reacting vanadium(V) oxoisopropoxide with benzyl alcohol at 473 K in a solvothermal process [14]. Sediri et al. synthesized V_2O_3 by the reduction of V_2O_5 with 1,6-diaminohexane under hydrothermal conditions [15]. In this paper, we report on a novel and efficient method of synthesizing pure V_2O_3 microcrystal particles by reducing V_2O_5 in ammonia gas. For the first time, the synthesis was optimized by thermodynamic modelling. The method has a short reaction period at a relatively low temperature of 903 K. Compared with previous reports, the synthesis process is more reasonable with respect to thermodynamic parameters, simpler to perform and easier to control, more suitable for large scale processing because it is less harmful to the environment. Furthermore, obtained V_2O_3 has a higher purity of 99.8 wt. %.

2. Experimental

Design of the technical process. The scheme of technical process of synthesizing V_2O_3 is shown in Fig. 1. In order to recycle ammonia gas, protect the environment and reduce material cost, the column for deoxygenation and dehydration was designed to remove the exhaust NH_3 gas from the tube furnace. The principle of the deoxy and drying column is that MnO (green) is oxidized by oxygen (O_2) to MnO_2 (brown) at room temperature. Water is adsorbed on dry microparticles of SiO_2 coated with MnO. The column was fabricated by the method described in the literature [16].

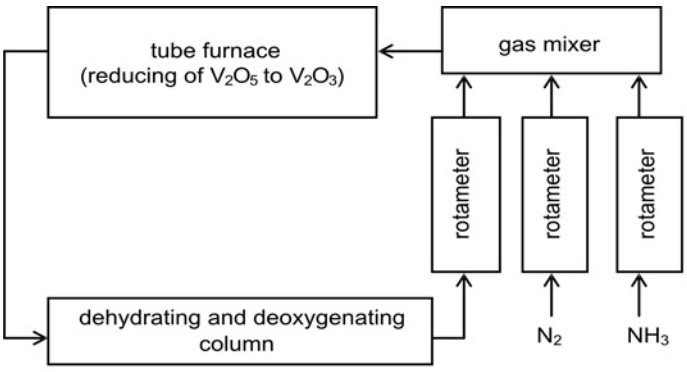

Fig. 1. Technical process of synthesis of V_2O_3 by thermal reduction of V_2O_5 in NH_3

Synthesis by thermal reduction. V_2O_3 particles were synthesized by thermal reduction of V_2O_5 in ammonia. 1 g of V_2O_5 (99.5%, Chinese Shanghai Chemical Limited Company, Analytical Reagent) was loaded into a ceramic container without a cover. The container loaded with V_2O_5 was placed into a tube furnace. After the temperature had reached 903 K, a mixture flow of NH_3 (5 cm^3/min) and N_2 (110 cm^3/min) was passed through the furnace. The furnace was naturally cooled to ambient temperature after 1 h and the sample was then ready for characterization.

Characterization of the sample. The phase composition and crystalline form of V_2O_3 were characterized by using a D/MAX-2400 X-ray diffractometer (Rigaku, Japan) in a reflection mode with Cu K_α (λ = 0.154 nm) radiation and a graphite monochromator. The 2θ scanning rate was 4 deg/min. Thermogravimetric (TG) data were acquired with a thermogravimetric analyzer, Mettler-Toledo TGA/SDTA 851e (Mettler-Toledo GmbH, Schwerzenbach, Switzerland) in the temperature range of 300–850 K at the heating rate of 5 K/min in an ambient atmosphere. X-ray photoelectron spectroscopy (XPS) was carried out using a Kratos Analytical Amicus XPS instrument (Perkin-Elmer Corporation, USA) with a MgK_α X-ray source operating at 160 W (8 kV, 20 mA). SEM images were obtained with a JSM-5600LV scanning electron microscope (JEOL, Japan) operating at 20 kV.

3. Results and discussions

3.1. Thermodynamic analysis of the synthesis of V_2O_3 by reducing V_2O_5 in NH_3

The thermodynamic properties of pure substances in their standard states, including standard enthalpies of formation $\Delta_f H_m^\circ$, standard Gibbs free energy of formation $\Delta_f G_m^\circ$ and absolute entropies S_m° at 298.15 K, were taken from the literature [17]. Enthalpies of formation allow us to calculate the enthalpies of any reaction, provided that we know $\Delta_f H_{m(T)}^\circ$ values for all the reactants and products [18]. The value of $\Delta_f H_{m(T)}^\circ$ for any reaction is the difference between the sum of the $\Delta_f H_{m(T)}^\circ$ values for all the products and the sum of the $\Delta_f H_{m(T)}^\circ$ values for all the reactants. The equations used are as follows:

$$\Delta_r H_{m\,(T)}^\circ = \sum \Delta_f H_{m\,(T)(\text{products})}^\circ - \sum \Delta_f H_{m\,(T)(\text{reactants})}^\circ \tag{1}$$

$$\Delta_r S_{m\,(T)}^\circ = \sum S_{m\,(T)(\text{products})}^\circ - \sum S_{m\,(T)(\text{reactants})}^\circ \tag{2}$$

$$\Delta_r H^\circ_{m\,(T)} = \Delta_r H^\circ_{m\,(298.15\ \mathrm{K})} + \int_{298.15\ \mathrm{K}}^{T} \sum v_B C^\circ_{P,\,m} dT \tag{3}$$

$$\Delta_r S^\circ_{m\,(T)} = \Delta_r S^\circ_{m\,(298.15\ \mathrm{K})} + \int_{298.15\ \mathrm{K}}^{T} \frac{\sum v_B C^\circ_{P,\,m}}{T} dT \tag{4}$$

$$\Delta_r G^\circ_{m\,(T)} = \Delta_r H^\circ_{m\,(T)} - T\Delta_r S^\circ_{m\,(T)} \tag{5}$$

$$C_{p,\,m} = a + bT + cT^2 + dT^3 + eT^4 \tag{6}$$

$$3V_2O_5 + 2NH_3 = 6VO_2 + N_2 + 3H_2O \tag{7}$$

$$6VO_2 + 2NH_3 = 3V_2O_3 + N_2 + 3H_2O \tag{8}$$

If absolute entropies of all reactants are known, it is a simple matter to calculate the change of entropy in the reaction (Eq. (2)). The thermodynamic parameters for the reactions at various temperatures except 298.15 K were calculated according to Eqs. (3)–(5), where v_B are the stoichiometric coefficients for the substances in the reactions, T denotes the reaction temperature, m is the molar value, the symbol ° indicates that the reactants and products are in their standard states, r denotes the reaction and f denotes the reactions of formation of the substances, $C^\circ_{p,\,m}$ is the heat capacity. The temperature dependence of the heat capacity $C^\circ_{p,\,m}$ is given in Eq. (6), where the coefficientsf a, b, c, d, e for pure reactants were taken from Ref. [17].

The reactions in the process of reduction of V_2O_5 under NH_3 are given in Eqs. (7) and (8). First we calculated $\Delta_r H^\circ_{m\,(298.15\ \mathrm{K})}$ and $\Delta_r S^\circ_{m\,(298.15\ \mathrm{K})}$ for the reactions (7) and (8), by applying Eqs. (1) and (2). Then we calculated $\Delta_r H^\circ_{m\,(T)}$ and $\Delta_r S^\circ_{m\,(T)}$ by substituting $C^\circ_{P,\,m}$ in Eqs. (3) and (4) for Eqs. (6). The integrations in Eqs. (3) and (4) included two parts: for liquid (l) and gaseous (g) water. The enthalpies and entropies of phase transitions for H_2O were included in the calculations for Eqs. (3) and (4), respectively. Finally the Gibbs free energy $\Delta_r G^\circ_{m(T)}$ for the reactions was calculated using Eq. (5). The results are shown in Table 1.

A negative value of $\Delta_r G^\circ_{m(T)}$ means that the reaction is spontaneous. The data in Table 1 shows that both the reactions (7) and (8) are spontaneous at the indicated temperatures. Actual reactions always take place in nonstandard state. The relationship between $\Delta_r G_{m(T)}$ and the pressure quotient (Q) for the reactions in a nonstandard state is given in Eq. (9). The pressure quotient Q for the reactions (7) and (8) is given by Eq. (10):

$$\Delta_r G_{m(T)} = \Delta_r G^{\circ}_{m(T)} + RT \ln Q \tag{9}$$

$$Q = \frac{P^3_{H_2O} P_{N_2}}{P^2_{NH_3}} \left(P^{\circ}\right)^{-2} \tag{10}$$

Here R is the universal gas constant, P_{H_2O}, P_{N_2}, P_{NH_3} are the partial pressures of H_2O, N_2, NH_3, respectively, and P° is the standard pressure (1.01×10^5 Pa).

Table 1. $\Delta_r G^{\circ}_{m(T)}$ [kJ·mol^{-1}] for reactions (7) and (8) at various temperatures

Temperature [K]	Reaction (7)	Reaction (8)
298.15	–398.72	–184.12
400	–417.50	–323.77
500	–448.13	–364.43
600	–476.51	–407.56
700	–501.65	–454.26
800	–522.43	–505.94
830	–527.62	–522.68
842	–529.55	–529.55
903	–537.88	–566.27
1000	–545.42	–631.63

Table 2. Ranges of he pressure quotient Q for synthesizing V_2O_3

Temperature [K]	$Q = \frac{P^3_{H_2O} P_{N_2}}{P^2_{NH_3}} (P^{\circ})^{-2}$
298.15	$<1.81\times10^{32}$
400	$<1.91\times10^{42}$
500	$<1.18\times10^{38}$
600	$<3.04\times10^{35}$
700	$<7.91\times10^{33}$
800	$<1.08\times10^{33}$
830	$<7.85\times10^{32}$
842	$<7.12\times10^{32}$
903	$<1.30\times10^{31}$
1000	$<3.10\times10^{28}$

Table 1 also shows that when the reaction temperature is lower than 842 K, $\Delta_r G^{\circ}_{m(T)}$ for reaction (7) has more negative values than that for reaction (8), whereas

according to Eq. (9) the values of $\Delta_r G_{m(T)}$ for reaction (8) seem to change first into positive ones upon increasing the pressure quotient Q. When the reaction temperature is higher than 842 K, the value of $\Delta_r G^{\circ}_{m(T)}$ in reaction (7) is less negative than its corresponding value in reaction (8), and $\Delta_r G_{m(T)}$ for reaction (7) upon increasing the pressure quotient Q will change first to a positive value. In non-standard state, the required pressure quotient Q for V_2O_3 formation leads to $\Delta_r G^{\circ}_{m(T)} < 0$, for both reactions (7) and (8). The required pressure quotient ranges, which are dependent on temperatures, were calculated and are shown in Table 2. The only requirement is that $\Delta_r G^{\circ}_{m(T)} < 0$ for reactions (7) and (8).

3.2. Structure and properties of V_2O_3

The XRD pattern of the product sample is shown in Fig. 2. By comparing the results with standard JCPDS card (PDF ID No. 34-0187) of XRD data documents, the sample was found to be a V_2O_3 pure phase. No impurity peaks were found in the diffraction pattern.

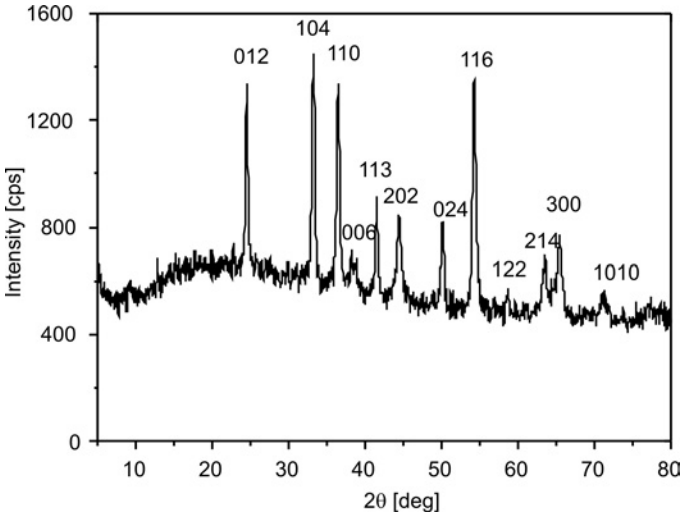

Fig. 2. X-ray diffraction pattern of the obtained V_2O_3

The results of thermogravimetric (TG) analysis (Fig. 3) showed that there was an initial weight loss below 363K, a slow weight increase above 423 K and a notable weight increase above 600 K. The weight loss between 300 K and 363 K was due to the elimination of water adsorbed on the particle surfaces, the weight increase between 423 K and 600 K indicated that V_2O_3 was oxidized to VO_2 above 423 K in ambient

atmosphere, and the rapid weight increase between 600 K and 723 K showed that further oxidation to V_2O_5 above 600 K was accelerated and complete at 723 K. This agrees with the result given in Ref. [16], stating that VO_2 is not stable above 600 K. The balance weight between 363 K and 423 K was 13.373 mg, and the balance weight from 723 K to 850 K was 16.225 mg. TG analysis confirmed that the following reactions took place:

$$2V_2O_3+O_2 = 4VO_2 \tag{11}$$

$$4VO_2+O_2 = 2V_2O_5 \tag{12}$$

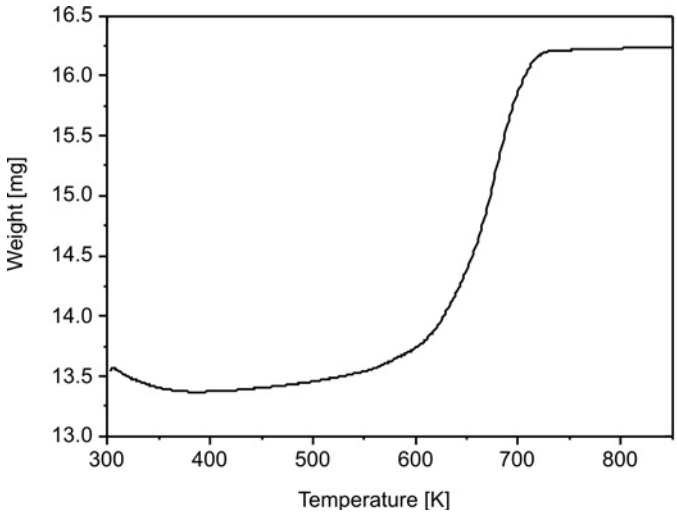

Fig. 3. Thermogravimetric curve of the product V_2O_3. The initial sample mass – 13.537 g, temperature range 300–850 K, the heating rate 5 K/min in an ambient atmosphere

It was calculated that 13.346 mg of V_2O_3 and 0.027 g of VO_2 were oxidized to 16.225 mg V_2O_5 on the assumption that only V_2O_3 and VO_2 were present in the sample. The TG data and the calculations of the V_2O_3 content in the sample are given in Table 3.

Table 3. Results of TG analysis and the calculated V_2O_3 contents in the sample

Parameter	Sample	V_2O_3	VO_2	H_2O	V_2O_5
Molar weight [g·mol^{-1}]	–	149.88	82. 94	18.01	181.88
Initial mass [mg]	13.537	13.346	0.027	0.164	
Mass change from 300 K to 363 K	–0.164				
Balance weight between 363 K and 423 K [mg]	13.373	13.346	0.027		
Balance weight between 723 K and 850 K [mg]	16.225				16.225
Mass change from 423 K to 723 K [mg]	2.852				
V_2O_3 content [wt. %] in the sample		99.8	0.2		

In Figure 4, the X-ray photoelectric energy spectrum is shown. It indicates that the binding energy of $V_{2P3/2}$ is 516.8 eV, that of $V_{2P1/2}$ is 524.2 eV and that of O_{1s} is 530.3 eV. This result is consistent with the literature data [19], and suggests that V ions exist in 3+ valence states. Multipeak data fitting was applied to the XPS in Fig. 4. No results suggested that V at any other valence state was present.

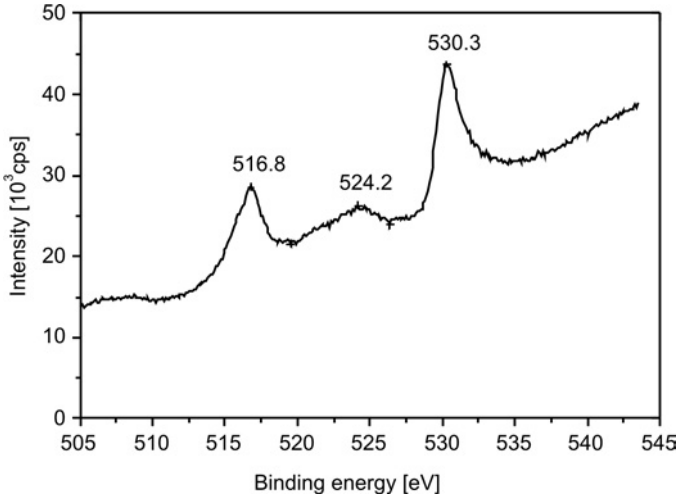

Fig. 4. XPS spectrum of the product V_2O_3

The scanning electron microscopy (SEM) results of V_2O_3 sample are shown in Fig. 5. The grain size distribution of the V_2O_3 microcrystal ranges from several micrometers to tens of micrometers. V_2O_3 particles consist of layers which are several micrometers thick. Each layer is made up of sheet structures, each sheet measuring several nanometers in thickness.

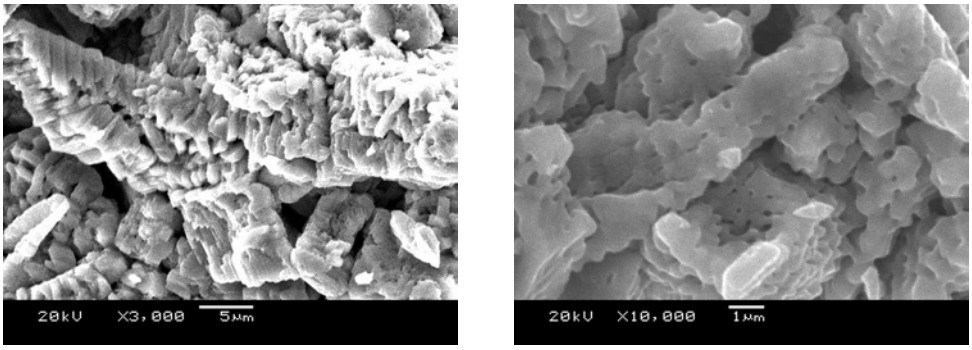

Fig. 5. SEM images of the product V_2O_3 with magnification 3000× (left) and 10 000× (right)

All the experimental results showed that high purity V_2O_3 microcrystal particles have been successfully synthesized.

4. Conclusions

A novel process was developed for synthesizing high purity V_2O_3 particles by thermal reduction of V_2O_5 under gaseous ammonia. The experimental results indicated that the process described in this paper is a convenient and efficient approach to synthesis of pure V_2O_3 crystal particles. The reduction parameters of V_2O_5 in ammonia were optimized by thermodynamic calculations for the relevant chemical reactions. Analysis of the reaction process suggested that the reaction temperature and pressure quotient are the key factors for producing pure vanadium(III) oxide. When the temperature of synthesis is 903 K, the required pressure quotient for vanadium formation is lower than 1.30×10^{31}, the reaction period is 1 h, the purity of the V_2O_3 product sample is higher than 99 wt. % and the grain size ranges from several hundred nanometers to several micrometers.

Acknowledgements

This work was supported by the Research Fund for the Doctoral Program of Dalian Nationalities University, People's Republic of China (Grant No. 20086105).

References

[1] KOKABI H.R., RAPEAUX M., AYMAMI J.A., DESGARDIN G., Mater. Sci. Eng. B, 38 (1996), 80.
[2] TOLEDANO D.S., METCALF P., HENRICH V.E., Surf. Sci., 449 (2000), 19.
[3] MOFFATT D.M., RUNT J.P., HALLIAYL A., NEWNHAM R.E., J. Mater. Sci., 24 (1989), 609.
[4] YANG Z., CAI P., CHEN L., GU Y., SHI L., ZHAO A., QIAN Y., J. Alloy Compd., 420 (2006), 229.
[5] PAN Y., WU G., YI X., J. Mater. Sci., 29 (1994), 5757.
[6] LEE G.V., SCHULLER B., POST H., FAVRE T.L.F., PONEC V., J. Catal., 98 (1986), 522.
[7] YI X., CHEN C., LIU Li, WANG Y., XIONG B., Infrared Phys. Technol., 44 (2003), 137.
[8] KITTAKA S., SASAKI S., MORIMOTO T., J. Mater. Sci., 22 (1987), 557.
[9] SULLIVAN J.R., SRINIVASAN T.T., NEWNHAM E.R., J. Am. Ceram. Soc., 73 (1990), 3715.
[10] PIAO J., TAKAHASHI S., KOHIKI S., Jpn. J. Appl. Phys. Part 1, 37 (1998), 6519.
[11] TOSHIYUKI O., YASUHIRO L., KENKYU K.R., J. Photopolym. Sci. Technol., 10 (1997), 211.
[12] ZHENG C., ZHANG X., HE S., FU Q., LEI D., J. Solid State Chem., 170 (2003), 221.
[13] ZHANG K., SUN X., LOU G., LIU X., LI H., SU Z., Mater. Lett., 59 (2005), 2729.
[14] PINNA N., ANTONIETTI M., NIEDERBERGER M., Colloids Surf. A, 250 (2004), 211.
[15] SEDIRI F., GHARBI N., Mater. Sci. Eng. B, 23 (2005), 136.
[16] QI J., NING G., LIN Y., Mater. Res. Bull., 43 (2008), 2300.
[17] DEAN J.A., *Lange's Handbook of Chemistry*, 15th Ed., McGraw-Hill, New York, 1999.
[18] LADLER K.J., MEISER J.H., *Physical Chemistry*, 3rd Ed., Houghton Mifflin, New York, 1999.
[19] MENDIALDUA J., CASANOVA R., BARBAUX Y., J. Electron Spectry., 71 (1995), 249.

Received 27 September 2009
Revised 4 November 2009

Materials Science-Poland, *Vol. 28*, *No. 2*, *2010*

New flame retardant and optically active poly(amide-imide)s based on N-trimellitylimido--L-amino acid and phosphine oxide moiety in the main chain: synthesis and characterization

KH. FAGHIHI*, M. HAJIBEYGI

Organic Polymer Chemistry Research Laboratory, Department of Chemistry,
Faculty of Science, Arak University, Arak, 38156, Iran

Six new flame retardant and optically active poly(amide-imide)s (PAIs) containing phosphine oxide moiety in the main chain were synthesized by direct polycondensation reactions of six chiral N-trimellitylimido-L-amino acids with bis(3-amino phenyl) phenyl phosphine oxide in a medium consisting of N-methyl-2-pyrrolidone (NMP), triphenyl phosphite (TPP), calcium chloride ($CaCl_2$) and pyridine (Py). The polymerization reactions produced a series of flame retardant and optically active PAIs with high yields and good inherent viscosities in the range of 0.43–0.71 $dm^3 \cdot g^{-1}$. The resulting polymers were fully characterized by means of FTIR and ^{1}H-NMR spectroscopy, elemental analyses, inherent viscosity, specific rotation and solubility tests. The thermal properties and flame retardant behaviour of the PAIs were investigated using thermal gravimetric analyses the limiting oxygen index (LOI) tests. Data obtained by the thermal analyses revealed that the polymers showed good thermal stability and also high char yields, in the TGA data, and good LOI values indicating that PAIs have good flame retardant properties.

Keywords: *poly(amide-imide); flame retardant; polycondensation*

1. Introduction

Aromatic polyamides such as e.g. Kevlar and Nomex, synthesized from aromatic diamines and aromatic dicarboxylic acids, possess excellent mechanical properties and outstanding thermal stability [1–6]. Aromatic polyimides are also recognised as high performance polymer materials, for their excellent mechanical strength and high thermal stability, as well as balanced mechanical and electric properties [7, 8]. However, most polyimides are difficult to process, due to their rigidity and poor solubility in organic solvents. To overcome this drawback, several copolymers have been devel-

*Corresponding author: e-mail: k-faghihi@araku.ac.ir

oped. Replacement of polyimides by copolyimides such as poly(amide-imide)s (PAIs), may be useful to tackle the intractability of polyimides [9, 10] and, among them, poly(amide-imide)s (PAIs) can improve solubility. PAIs are usually fabricated by low temperature polycondensation of an aromatic diamine with acyl chloride of trimellitic anhydride [11, 12] or with acyl chlorides of aromatic diacids containing preformed imide rings [13–16]. The former method requires high temperatures or chemical cyclodehydration step of the poly(amic acid) formed, while the latter method requires a two step synthesis of diacyl chloride monomers. Recently, we have synthesized thermally stable PAIs by various methods [17–21].

Polymers containing phosphorus are generally flame retardant. They are also characterized by good adhesion to substrates, metal ion binding properties and increased polarity [22, 23]. Major advantages have polymers with phosphine oxide moieties. Phosphine oxide groups possess have hydrolytically stable P–C and P–O–C bonds and oxidatively stable P=O bonds. Polymers containing phosphine oxide moieties typically display good flame resistance, high thermal oxidative stability, enhanced solubility and improved miscibility and adhesion [24–26].

Also, interesting applications have been found for optically active polymers because of their specific properties. For example, these polymers have the ability of molecular recognition which justifies their use as a stationary phase in chromatography methods for separations of enantiomers [27, 28]. They can also be used as chiral media for asymmetric synthesis and as chiral liquid crystals in ferroelectric and nonlinear optical devices [29].

In the paper, syntheses of a series of new flame retardant PAIs containing phosphine oxide moieties were synthesized by the reactions of direct polycondensation of six chiral N-trimellitylimido-L-amino acids with bis(3-amino phenyl) phenyl phosphine oxide in a medium consisting of N-methyl-2-pyrrolidone, triphenyl phosphite, calcium chloride and pyridine. The synthesis and application of optically active polymers are new topics, recently extensively studied [30].

2. Experimental

Materials. Trimellitic anhydride (**1**), L-alanine (**2a**), L-valine (**2b**), L-leucine (**2c**), L-isoleucine (**2d**), L-phenyl alanine (**2e**) and L-2-aminobutyric acid (**2f**) (from Merck) were used without previous purification; bis(3-amino phenyl) phenyl phosphine oxide ((**4**)) was prepared from bis(3-nitro phenyl) phenyl phosphine oxide [24, 25]. Solvents: N-methyl-2-pyrrolidone (NM, Fluka), pyridine (Acros), triphenyl phosphite (TPP, Merck) were used as received. Commercially available calcium chloride ($CaCl_2$, Merck) was dried under vacuum at 150 °C for 6 h.

Apparatus and techniques. ^{1}H-NMR and ^{13}C-NMR spectra were recorded using a Bruker 300 MHz instrument (Germany). Fourier transform infrared (FTIR) spectra were recorded with a Galaxy series FTIR 5000 spectrophotometer (UK). Spectra of

solids were recorded in KBr pellets. Band intensities were classified as weak (w), medium (m), shoulder (sh), strong (s) and broad (br). Inherent viscosities were measured by a standard procedure, using a Technico Regd Trad Mark Viscometer. Specific rotations were measured with an A-Kruss polarimeter. Limiting oxygen indexes (LOI) were measured with a Stanton Redcraft flame meter. Thermal gravimetric analysis (TGA and DTG curves) for polymers were taken on a Mettler TA4000 System under a N_2 atmosphere at rate of 10°C/min. Elemental analyses were performed with Vario EL equipment manufactured/provided by Arak University.

Syntheses of monomers. N-trimellitylimido-L-amino acids ((**3a–f**)) were synthesized as follows: 2 g (10 mmol) of trimellitic anhydride (**1**), 10 mmol of L-amino acid (**2a–f**), and 50 cm^3 of acetic acid were placed in a 250 cm^3 round-bottomed flask equipped with a stirring bar. The mixture was stirred at room temperature overnight and refluxed for 4 h. The solvent was removed under reduced pressure, and the residue was dissolved in 80 cm^3 of cold water, then the solution was decanted and 5 cm^3 of concentrated HCl was added. A white precipitate was filtered off, and dried to give N-trimellitylimido-L-amino acid ((**3a–f**)).

Bis(3-amino phenyl) phenyl phosphine oxide ((**4**)) was prepared according to the method described elsewhere [24, 25].

Syntheses of polymers. The PAIs (**5a–f**) were prepared by the following general procedure, taking polymer (**5a**) as an example: 0.10 g (0.38 mmol) of N-trimellitylimido-L-alanine (**3a**), 0.11 g (0.38 mmol) of bis(3-amino phenyl) phenyl phosphine oxide (**4**), 0.1 g (0.9 mmol) of calcium chloride, 0.84 cm^3 (3.00 mmol) of triphenyl phosphite, 0.18 cm^3 of pyridine and 2.00 cm^3 of N-methy-2-pyrrolidone were placed in a 25-cm^3 round-bottomed flask, which was equipped with a stirring bar. The reaction mixture was heated under reflux at 110 °C for 8 h. Then, the reaction mixture was poured into 50 cm^3 of methanol and the precipitated polymer was collected by filtration and washed thoroughly with hot methanol and dried at 60 °C for 12 h under vacuum to leave 0.2 g (98.5%) white solid polymer (**5a**).

Polymer (**5a**): FTIR (KBr): 3310 (m, br), 3061 (m, sh), 1778 (w), 1718 (s), 1670 (s), 1589 (m), 1541 (m), 1481 (m), 1381 (m), 1248 (m), 1168 (m), 1082 (w), 949 (w), 690 (w), 588 (w), 503 (w) cm^{-1}. ^{1}H-NMR (300 MHz, DMSO-d_6, δ, ppm): 10.81 (s, 1H), 10.14 (s, 1H), 7.09-8.36 (m, 16H), 4.93 (s, 1H), 1.55 (s, 3H).

Polymer (**5b**): FTIR (KBr): 3337 (m, br), 3059 (w), 2962 (m), 1776 (w), 1720 (s), 1670 (s), 1589 (m), 1543 (m), 1481 (m), 1415 (m), 1377 (m), 1307 (m), 1248 (m), 1170 (m), 1114 (w), 1082 (m), 941 (w), 690 (m) cm^{-1}. ^{1}H-NMR (300 MHz, DMSO-d_6, δ, ppm): 10.82 (s, 1H), 10.21 (s, 1H), 7.11-8.41 (m, 16H), 4.57 (s, 1H), 2.63-2.73 (m, 1H), 0.99 (d, 3H), 0.81 (d, 3H).

Polymer (**5c**): FTIR (KBr): 3330 (m, br), 3060 (w), 2960 (m), 1778 (w), 1722 (s), 1670 (s), 1589 (m), 1543 (m), 1485 (m), 1418 (m), 1383 (m), 1311 (m), 1248 (m), 1171 (m), 1117 (w), 1082 (m), 943 (w), 693 (m) cm^{-1}.

Polymer (**5d**): FTIR (KBr): 3294 (m, br), 3059 (w), 2962 (w), 1776 (w), 1720 (s), 1668 (s), 1589 (m), 1541 (m), 1479 (m), 1415 (m), 1375 (m), 1303 (m), 1246 (m), 1167 (m), 1082 (m), 939 (w), 790 (w), 690 (m), 499 (w) cm^{-1}.

Polymer (**5e**): FTIR (KBr): 3308 (m, br), 3061 (m), 2930 (w), 1178 (w), 1720 (s), 1670 (s), 1591 (m), 1541 (m), 1481 (m), 1415 (m), 1377 (m), 1307 (m), 1246 (m), 1170 (m), 1105 (m), 939 (w), 692 (m), 503 (w) cm^{-1}.

Polymer (**5f**): FTIR (KBr): 3308 (m, br), 3067 (w), 2974 (w), 1178 (w), 1718 (s), 1662 (s), 1670 (m), 1541 (m), 1477 (m), 1377 (m), 1303 (m), 1244 (m), 1165 (m), 688 (m), 499 (m) cm^{-1}.

3. Results and discussion

3.1. Syntheses of monomers

Asymmetric diacids (**3a–f**) were synthesized by the condensation of trimellitic anhydride (**1**) with equivalent quantities of L-amino acids [31] such as L-alanine (**2a**), L-valine (**2b**), L-leucine (**2c**), L-isoleucine (**2d**), L-phenyl alanine (**2e**) and L-2-aminobutyric acid (**2f**) in solution of acetic acid (Scheme 1). The yields and some physical properties of these compounds are given in Table 1.

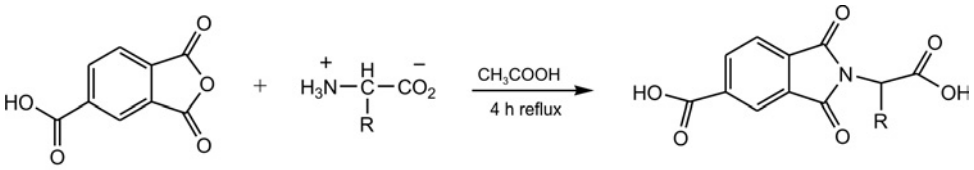

Scheme 1. Synthesis of N-trimellitylimido-L-amino acids (**3a–f**)

Table 1. Yields and some physical properties of diacids (**3a–f**)

Entry	Amino acid compound	R	Mp [°C]	Yield [%]	$[\alpha]_D^{25a}$
3a	L-Alanine	CH_3	272-275	92	+122.4
3b	L-Valine	$(CH_3)_2CH$	208-210	94	+128.9
3c	L-Leucine	$(CH_3)_2CHCH_2$	194-197	92	+117.3
3d	L-Isoleucine	$(C_2H_5)(CH_3)CH$	200-203	94	+131.5
3e	L-Phenyl alanine	$PhCH_2$	215-218	90	+128.7
3f	L-2-Aminobutyric acid	CH_3CH_2	234-237	95	+139.8

[a]Measured at the concentration of 0.5 g/dm^3 in DMF at 25 °C.

The chemical structure and purity of the optically active diacids (**3a–f**) were confirmed by elemental analyses, FTIR and ^{1}H-NMR spectroscopic techniques (Table 2).

Table 2. ^{1}H-NMR, FTIR spectra and elemental analyses data of diacid (**3a–f**)

Imide diacid	Spectral data
(**3a**)	^{1}H–NMR (300 MHz, DMSO–d_6, δ, ppm): 13.5 (s, br, 2H), 8.39–8.40 (d, 1H, *J* = 9 Hz), 8.26 (s, 1H), 8.04–8.07 (d, 1H, *J* = 9 Hz), 4.91 (q, 1H), 1.55 (d, 3H). FTIR (KBr): 2500–3400 (s, br), 1728 (s, sh), 1722 (s, br), 1604 (w, sh), 1487 (w, sh), 1423 (s, sh), 1384 (s), 1290 (s), 1095 (m), 927 (m), 731 (s), 655 (m), 532 (w) cm^{-1}. ELEM. ANAL. Calc. For $C_{12}H_9NO_6$ (263..04): C, 54.76; H, 3.45; N, 5.32. Found: C, 54.63; H, 3.40; N, 5.30.
(**3b**)	^{1}H–NMR (300 MHz, DMSO–d_6, δ, ppm): 13.64 (s, br, 2H), 8.51–8.54 (d, 1H, *J* = 9 Hz), 8.25 (s, 1H), 8.02–8.05 (d, 1H, *J* = 9 Hz), 5.02 (d, 1H), 2.32 (m, 1H), 1.06–1.08 (d, 3H), 0.83–0.85 (d, 3H). FTIR (KBr): 2500–3400 (m, br), 1782 (m, sh), 1722 (s, br), 1487 (w), 1384 (s), 1290 (s), 1095 (w), 929 (m), 733 (s), 609 (w), 532 (w) cm^{-1}. ELEM. ANAL. Calc. For $C_{14}H_{13}NO_6$ (291.07): C, 57.73; H, 4.50; N, 4.81. Found: C, 57.41; H, 4.50; N, 4.79.
(**3c**)	^{1}H–NMR (300 MHz, DMSO–d_6, δ, ppm): 13.07 (s, br, 2H), 8.51–8.54 (d, 1H, *J* = 9 Hz), 8.41 (s, 1H), 8.02–8.05 (d, 1H, *J* = 9 Hz), 4.78–4.83 (dd, 1H, *J* = 6, 3 Hz), 1.52 (m, 2H), 1.49 (s, 1H), 0.85–0.87 (d, 6H). FTIR (KBr): 2500–3400 (m, br), 1780 (m, sh), 1733 (s, br), 1485(w), 1380(s), 1295(s), 1095 (w), 920 (m), 743 (s), 609 (w), 533 (w) cm^{-1}. ELEM. ANAL. Calc. For $C_{15}H_{15}NO_6$ (305.09): C, 59.01; H, 4.95; N, 4.59. Found: C, 58.95; H, 4.95; N, 4.56.
(**3d**)	^{1}H–NMR (300 MHz, DMSO–d_6, δ, ppm): 13.39 (s, br, 2H), 8.38–8.41 (d, 1H, *J* = 9 Hz), 8.27 (s, 1H), 8.02–8.05 (d, 1H, *J* = 9 Hz), 4.53–4.56 (d, 1H), 2.36–2.38 (m, 1H), 1.46–1.52 (s, 2H), 1.00–1.06 (d, 3H), 0.77–0.82 (t, 3H). FTIR (KBr): 2400 –3500 (s, br), 1778 (s, sh), 1722 (s, br), 1379 (s), 1286 (s), 1093 (m), 929 (w), 733 (m), 538 (w) cm^{-1}. ELEM. ANAL. Calc. For $C_{15}H_{15}NO_6$ (305.09): C, 59.01; H, 4.95; N, 4.59. Found: C, 58.88; H, 4.96; N, 4.52.
(**3e**)	^{1}H–NMR (300 MHz, DMSO–d_6, δ, ppm): 13.57 (s, br, 2H), 8.33–8.53 (d, 1H, *J* = 6 Hz), 8.19 (s, 1H), 7.94–7.97 (d, 1H, *J* = 6 Hz), 7.15 (s, 5H), 5.12–5.17 (dd, 1H, *J* = 9, 3 Hz), 3.46–3.52 (dd, 1H, *J* = 9, 3 Hz), 3.29–3.35 (dd, 1H, *J* = 9, 3 Hz). FTIR (KBr): 2400–3500 (s, br), 1770 (s, sh), 1720 (s, br), 1383 (s), 1278 (s), 1091 (m), 925 (w), 731 (m), 539 (w) cm^{-1}. ELEM. ANAL. Calc. For $C_{18}H_{13}NO_6$ (339.07): C, 63.72; H, 3.86; N, 4.13. Found: C, 63.55; H, 3.78; N, 4.10.
(**3f**)	^{1}H–NMR (300 MHz, DMSO–d_6, δ, ppm): 13.45 (s, br, 2H), 8.37–8.40 (d, 1H, *J* = 9 Hz), 8.26 (s, 1H), 8.01–8.04 (d, 1H, *J* = 9 Hz), 4.66–4.71 (dd, 1H, *J* = 6, 3 Hz), 2.01–2.19 (m, 2H), 0.82–0.87 (t, 3H). FTIR (KBr): 2400–3500 (s, br), 1780 (s, sh), 1720 (s, br), 1604 (m), 1487 (m), 1383 (s), 1284 (s, sh), 1082 (s), 879 (s), 729 (s), 638 (m), 472 (w), 314 (w) cm^{-1}. ELEM. ANAL. Calc. For $C_{13}H_{11}NO_6$ (277.06): C, 56.32; H, 4.00; N, 5.05. Found: C, 56.11; H, 4.10; N, 5.15.

Exemplary FTIR spectrum of N-trimellitylimido-L-2-aminobutyric acid (**3f**) showed a broad peak between 2500 and 3400 cm^{-1}, assigned to COOH groups. Peaks appearing at 1780 cm^{-1} (asymmetric imide stretching), and a broad peak at 1710–1760 cm^{-1} (symmetric imide stretching and carbonyl group for carboxylic acids), 1383 and 729 cm^{-1} (imide characteristic ring vibration) confirmed the presence of an imide ring and carboxylic groups in the compound (Fig. 1).

The ^{1}H-NMR spectrum of diacid (**3f**) **is** shown in Fig 2. Carboxylic groups appeared at 13.45 ppm. Peaks in 4.66–4.71 ppm (*J* = 6, 3 Hz) were assigned to the CH(b)

proton, that is a chiral centre, peaks at 0.82–0.87 ppm were assigned to aliphatic CH_3(d), a multiplet at 2.01–2.19 ppm was assigned to H(c). Aromatic protons were detected at 8.01–8.4 ppm.

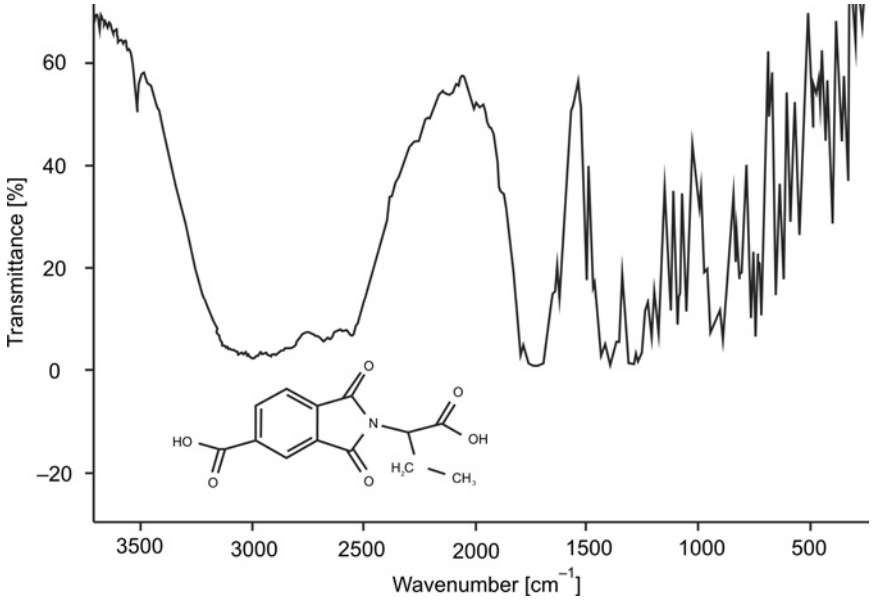

Fig. 1. FTIR spectrum of diacid (**3f**)

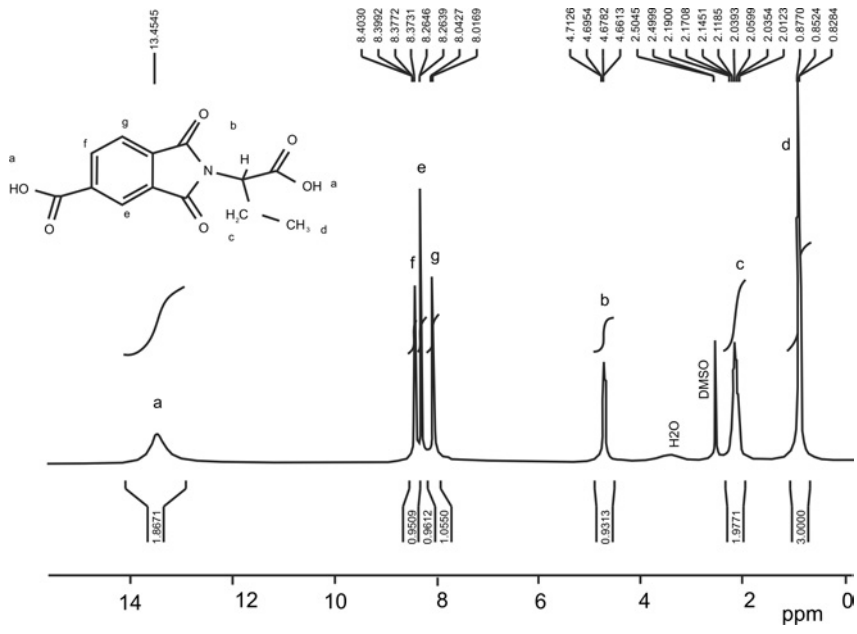

Fig. 2. ^{1}H-NMR spectrum of diacid (**3f**)

3.2. Syntheses of polymers

PAIs (**5a–f**) were synthesized by direct polycondensation of equimolar mixtures of diacids (**3a–f**) with bis(3-amino phenyl) phenyl phosphine oxide (**4**) in a medium consisting of N-methyl-2-pyrrolidone, triphenyl phosphite, calcium chloride and pyridine (Scheme 2).

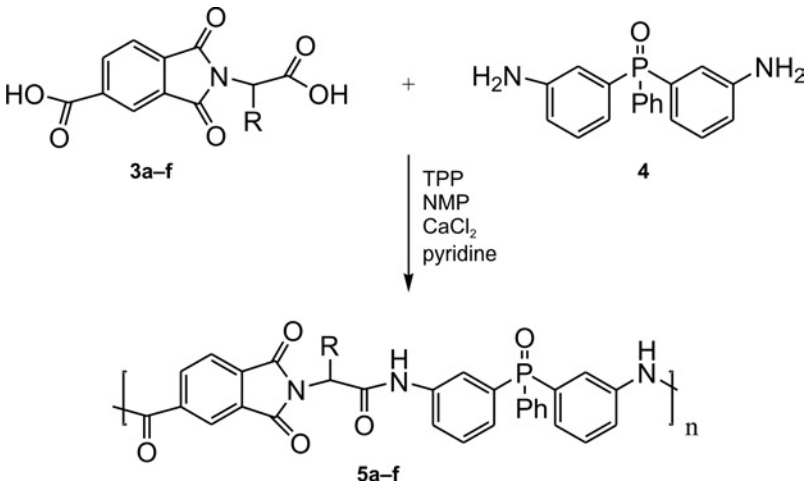

Scheme 2. Synthesis of PAIs (**5a–f**)

Table 3. Yields and some physical properties of PAIs (**5a–f**)

Diimide-diacid	Polymer	Yield [%]	η_{inh} [dm^3/g]	$[\alpha]_D^{25a}$	Colour[b]
3a	**5a**	98	0.58	+72.1	PY
3b	**5b**	95	0.71	+58.5	W
3c	**5c**	94	0.48	+124.3	W
3d	**5d**	96	0.43	+136.4	W
3e	**5e**	94	0.59	+94.8	PY
3f	**5f**	96	0.48	+114.4	PY

[a]Measured at the concentration of 0.5g/dm^3 in DMSO at 25 °C.
[b]W – white, PY – pale yellow.

The yields and some physical properties of the new PAIs (5a–f) are given in Table 3. The resulting polymers, due to the presence of chiral amino acid moieties (**2a–f**) in the main chain of polymer, are optically active, as shown by specific rotation measurements at the concentration of 0.5 g/dm^3 in DMSO at 25 °C. Also, the resulting polymers have a spectrum of colour between white and pale yellow. The entire polycondensation reaction readily proceeded in a homogeneous solution, tough and stringy precipitates formed when viscous PAIs solution was obtained in good yields.

3.3. Polymer characterization

The elemental analyses of the resulting PAIs (**5a–f**) were in good agreement with the calculated values for the proposed structure (Table 4).

Table 4. Results of elemental analyses of PAIs (**5a–f**)

Polymer	Formula		C [%]	H [%]	N [%]
(**5a**)	$C_{30}H_{22}N_3O_5P$	calculated	67.28	4.11	7.85
	$(535.04)_n$	found	66.15	4.66	7.34
(**5b**)	$C_{32}H_{26}N_3O_5P$	calculated	68.20	4.61	7.46
	$(563.21)_n$	found	67.78	4.23	7.65
(**5c**)	$C_{33}H_{28}N_3O_5P$	calculated	68.63	4.85	7.27
	$(577.11)_n$	found	67.14	4.21	7.13
(**5d**)	$C_{33}H_{28}N_3O_5P$	calculated	68.63	4.85	7.27
	$(577.11)_n$	found	67.04	4.35	7.33
(**5e**)	$C_{36}H_{26}N_3O_5P$	calculated	70.70	4.25	6.87
	$(611.15)_n$	found	69.98	4.46	6.17
(**5f**)	$C_{31}H_{24}N_3O_5P$	calculated	67.75	4.37	7.65
	$(549.17)_n$	found	66.23	4.01	7.01

To investigate the solubility of PAIs (**5a–f**), 0.01 g polymeric samples were dissolved in 2 cm^3 of various solvents. All PAIs are soluble in DMSO, DMAc and H_2SO_4, and partially soluble in organic solvents such as DMF, NMP, and insoluble in solvents such as chloroform, dichloromethane, methanol and ethanol. The results are given in Table 5; +means soluble at room temperature, ± partially soluble at room temperature and soluble after heating, – insoluble.

Table 5. Solubility of PAIs (**5a–f**)

Solvent	(**5a**)	(**5b**)	(**5c**)	(**5d**)	(**5e**)	**5f**
H_2SO_4	+	+	+	+	+	+
DMSO	+	+	+	+	+	+
DMF	±	±	+	+	±	±
NMP	±	±	+	+	±	±
DMAc	+	+	+	+	+	+
$CHCl_3$	–	–	–	–	–	–
CH_2Cl_2	–	–	–	–	–	–
MeOH	–	–	–	–	–	–
EtOH	–	–	–	–	–	–
Acetone	–	–	–	–	–	–

The structures of these polymers were confirmed by means of FTIR, ^{1}H-MNR spectroscopy and elemental analyses. An exemplary FTIR spectrum of PAI (**5a**) is shown in Fig 3. The polymer exhibited characteristic absorption bands at 1778 and

1718 cm^{-1} for the imide ring (asymmetric and symmetric C=O stretching vibration), 1718 cm^{-1} (C= O stretching vibration for amide group) and 1381 cm^{-1} (C–N stretching vibration). The absorption bands of amide groups appeared at 3310 cm^{-1} (N–H stretching).

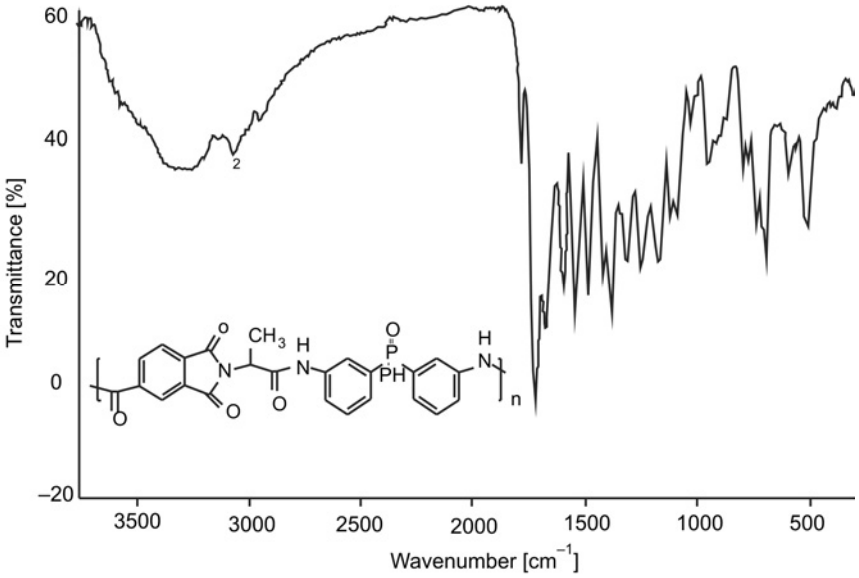

Fig. 3. FTIR spectrum of PAI (**5a**)

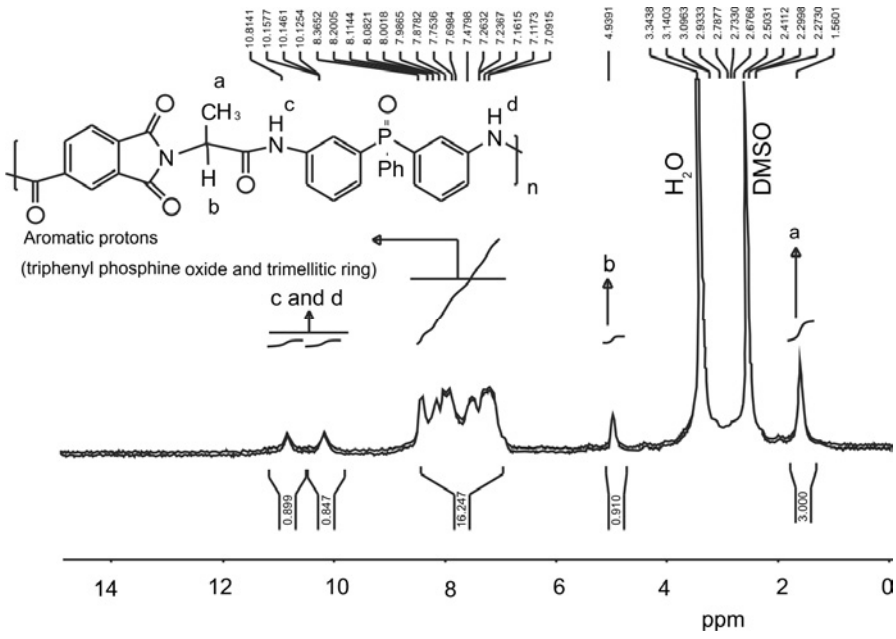

Fig. 4. ^{1}H-NMR spectrum of PAI (**5a**)

The ^{1}H-NMR spectrum of PAI (**5a**) is shown in Fig. 4. Thirteen protons related to triphenyl phosphine oxide and three protons related to trimellitic ring in the region of 7.09–8.36 ppm, and peaks in the regions of 10.14 and 10.81 ppm corresponded to N–H of various amide groups in the main chain. Decaying peak related to protons of carboxylic acid and peaks related to amide groups and triphenyl phosphine oxide protons in the polymer chain confirmed the proposed structures of PAIs (**5a**).

3.4. Thermal properties

Thermal properties of PAIs (**5a**), (**5b**) and (**5e**) in nitrogen atmosphere were investigated by TGA (with the heating rate of 10 °C/min). All the polymers showed approximately similar decomposition behaviour (Fig. 5).

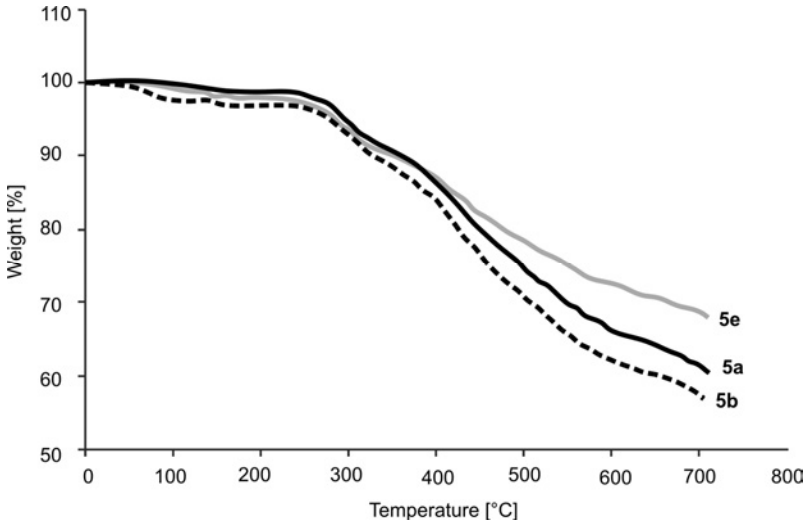

Fig. 5. TGA curves of PAIs (**5a**), (**5b**) and (**5e**)

The temperatures of initial decomposition, and of the 5% and 10% weight losses (T_5, T_{10}), and the char yields are given in Table 6.

Table 6. Thermal behaviour of PAIs (**5a**), (**5b**) and (**5e**)

Polymer	T_5 [°C][a]	T_{10} [°C][a]	Char yield[b]	LOI[c]
(**5a**)	290–295	350–355	66.17	35
(**5b**)	270–275	320–325	61.94	33
(**5e**)	275–280	345–350	72.47	30

[a]Temperature at which 5% or 10% weight loss was recorded by TGA at the heating rate of 10 °C/min under N_2.

[b]Weight percentage of material left after TGA analysis at the maximum temperature of 600 °C under N_2.

[c]LOI, Limited oxygen index.

The polymers exhibited good resistance to thermal decomposition up to 270–290 °C in nitrogen, and began to decompose gradually above that temperature. The temperature of 5% weight loss, for all the polymers, ranged from 270 to 290 °C, and the residual weight at 600 °C ranged from 61.94 to 72.47% in nitrogen. The high char yields of the PAIs in the high temperature region show that these polymers have good thermal stability. According to the TGA thermogram of PAIs (**5a**), (**5b**) and (**5e**), PAI (**5e**) has the highest thermal resistance. It is due to the presence of aromatic rings related to phenyl alanine in the polymer. The flame retardation of the polymers was evaluated by measuring their limiting oxygen index (LOI) values: the higher the LOI value, the more effective the flame-retardation. The (LOI) data of these polymers ranged between 30 and 35. Generally, materials exhibiting (LOI) values greater than 26 would show self-extinguishing behaviour [26], and were considered to be flame retardant. Therefore, a high char yield, alongside with good (LOI) values indicated that these polymers have good flame retardant properties.

4. Conclusions

A new series of PAIs (**5a–f**) containing phosphine oxide moiety were synthesized by a direct polycondensation reaction of six asymmetric diacids (**3a–f**) with bis (3-aminophenyl)phenyl phosphine oxide (**4**) by using triphenyl phosphite, NMP, calcium chloride and pyridine as condensing agents. The high char yields and good LOI data of these polymers showed that the introduction of phosphine oxide moiety into the backbone improved their flame retardation. Also, due to the presence of chiral amino acid moieties in the main chain, the synthesized polymers are optically active. Optically active flame retardant polymers with good thermal stability have the potential to be used as a chiral stationary phase in chromatographic techniques for the separation of racemic mixtures [32, 33]. These properties can make these polymers attractive for processable, high-performance engineering plastics.

References

[1] CASSIDY P.E., *Thermally Stable Polymers*, Dekker, New York, 1980.
[2] SEYMOUR R.B., CARRAHER C.E., *Polymer Chemistry. An Introduction*, Dekker, New York, 1981.
[3] SAXENA A., RAO V.L., PRABHAKARAN P.V., NINAN K.N., Eur. Polym. J., 39 (2003), 401.
[4] GE Z., YANG S., TAO Z., LIU J., FAN L., Polymer., 45 (2004), 3627.
[5] TAMAMI B., YEGANEH H., Polymer., 42 (2001), 415.
[6] FAGHIHI KH., HAGIBEYGI M., Eur. Polym. J., 39 (2003), 2307.
[7] QIU Z., WANG J., ZHANG Q., ZHANG S., DING M., GAO L., Polymer., 47 (2006), 8444.
[8] HAN S.S., IM S.S., WON J.C., LEE J.H., CHOI K.Y., KIM Y.S., Eur. Polym. J., 43 (2007), 1541.
[9] CHANG Y.T., SHU C.F., *Macromolecules*, 36 (2003), 661.
[10] LIAW D.J., CHEN W.H., Polym. Degrad. Stab., 91 (2006), 1731.
[11] MALLAKPOUR S.E., HAJIPOUR A.R., VAHABI R., J. Appl. Polym. Sci., 84 (2002), 35.
[12] GHOSH M., Angew. Macromol. Chem., 172 (1989), 165.
[13] MALLAKPOUR S., SHAHMOHAMMADI M.H., Iran. Polym. J., 14(5) (2005), 473.

[14] RAY A., DAS S., MAITI S., Macromol. Chem. Rapid. Commun., 2 (1981), 333.
[15] FAGHIHI KH., ZAMANI KH., MIRSAMIE A., SANGI M.R., Eur. Polym. J., 39 (2003), 247.
[16] MAITI S., RAY A., Macromol. Chem. Rapid. Commun., 2 (1981), 649.
[17] FAGHIHI KH., NAGHAVI H., J. Appl. Polym. Sci., 96 (2005), 1776.
[18] FAGHIHI KH., HAJIBEYGI M., J. Appl. Polym. Sci., 92 (2004), 3447.
[19] FAGHIHI KH., ZAMANI KH., MIRSAMIE A., MALLAKPOUR S., J. Appl. Polym. Sci., 91 (2004), 516.
[20] FAGHIHI KH., J. Appl. Polym. Sci., 109 (2008), 74.
[21] FAGHIHI KH., HAGIBEYGI M., Macromol. Res., 13 (2005), 14.
[22] GEFTER E.L., *Organophosphorus Monomers and Polymers*, Assoc. Technical Services. Inc. GLEN RIDGE. N.J. 1969.
[23] JENG R.J., SHAU S.M., LIN J.J., SU W.C., CHIU Y.S., Eur. Polym. J., 38 (2002), 683.
[24] FAGHIHI KH., J. Appl. Polym. Sci., 102 (2006), 5062.
[25] FAGHIHI KH., ZAMANI KH., J. Appl. Polym. Sci., 101 (2006), 4263.
[26] YING-LING L., YIE-CHAN C., TSUNG-YU C., Polym. Int., 52 (2003), 1256.
[27] CIANGA L., Eur. Polym. J., 39 (2003), 2271.
[28] LIAW D.J., CHANG F.C., LIU J.H., WANG K.L., FAGHIHI KH., HUANG S.H., LEE K.R., LAI J.Y., Polym. Degrad. Stab., 92 (2007), 323.
[29] ANGIOLINI L., BENELLI T., GIORGINI L., SALATELLI E., Polymer., 46 (2005), 2424.
[30] OKAMURA A., HIRAI T., TANIHARA M., YAMAOKA T., Polymer., 43 (2002), 3549.
[31] HSIAO S.H., YANG C.P., WU F.Y., Macromol. Chem. Phys., 195 (1994), 2531.
[32] MALLAKPOUR S., TAGHAVI M., React. Funct. Polym., 69 (2009), 206.
[33] MALLAKPOUR S.E., HAJIPOUR A.R., MAHDAVIAN A.R., KHOEE S., J. Appl. Polym. Sci., 76 (2000), 240.

Received 2 July 2009
Revised 27 August 2009

Materials Science-Poland, *Vol. 28*, *No. 2*, *2010*

Synthesis of nanocrystalline metal molybdates using cyclic microwave radiation

A. PHURUANGRAT[1], T. THONGTEM[2*], S. THONGTEM[1]

[1]Department of Physics and Materials Science, Faculty of Science, Chiang Mai University, Chiang Mai 50200, Thailand

[2]Department of Chemistry, Faculty of Science, Chiang Mai University, Chiang Mai 50200, Thailand

Nanocrystalline compounds $MMoO_4$ (M = Ca, Sr and Ba) were synthesized in propylene glycol using cyclic microwave radiation. XRD, TEM, SAED and EDX analyses revealed the presence of nanocrystallites of the phases containing the corresponding alkaline earth metals, Mo and O. The calculated lattice parameters and the crystallite sizes both increased with the increase in the atomic masses and the ionic radii of the divalent metals. Six different vibrations were detected using Raman spectroscopy, and very strong Mo–O stretching mode of $[MoO_4]^{2-}$ tetrahedrons was observed using FTIR.

Keywords: *alkaline earth metal molybdate; cyclic microwave-assisted synthesis; scheelite structure*

1. Introduction

Nanomaterials have very unusual physical and chemical properties, different from their bulks [1, 2]. Metal molybdates $MMoO_4$ (M = Ca, Sr and Ba, ionic radii of divalent metals > 0.1 nm) with scheelite structure [3] are very suitable for use as luminescent materials, optical fibres, scintillators and catalysts [4, 5].

A variety of methods are used to synthesize nanosized metal molybdates such as hydrothermal processing [5], reverse microemulsion [6], reverse micelles with solvothermal method [7], the molten salt method [8] and solid state reactions [9]. Recently, the microwave-assisted route has been applied as a novel way to synthesize nanomaterials. The process requires a short reaction time. The products have a narrow particle size distribution and high purity compared with those synthesized by the conventional method [2]. Previously, metal molybdates were synthesized via a citrate complex route assisted by microwave radiation, followed by high temperature calcination [4]. For the present research, purified nanocrystalline $MMoO_4$ (M = Ca, Sr and Ba) were synthesized using cyclic microwave radiation without any further calcination at high temperatures.

*Corresponding author, e-mail: ttpthongtem@yahoo.com

2. Experimental

0.005 mol of each $M(NO_3)_2$ (M = Ca, Sr and Ba) and Na_2MoO_4 was separately dissolved in 15 cm^3 propylene glycol (PG). The corresponding solutions were mixed and stirred for 30 min. The mixtures were heated at 600 W cyclic microwave radiation. Every 100 s, the microwave was switched on for 15 s and switched off for 85 s. The cyclic process was terminated after 30 min had elapsed. Finally, white precipitates were produced. They were washed with distilled water and absolute ethanol, and dried in air at 80 °C for 24 h.

The final products were characterized using an X-ray diffractometer (D-500 Siemens) with CuK_α radiation, a graphite monochrome and Ni filter with 2θ scanning angle ranging from 15° to 60°, Fourier transform infrared spectrometer (Bruker Tensor 27) with the spectral resolution of 4 cm^{-1} with KBr as a diluting agent, Raman spectrometer (Horiba Jobin Yvon T64000) using 50 mW Ar laser (λ = 514.5 nm) with the spectral resolution of 5 cm^{-1}, and a transmission electron microscope (Jeol, Jem-2010) operating at 200 kV with an energy dispersive X-ray analyzer (Oxford Instruments, INCA).

3. Results and discussion

XRD spectra of $MMoO_4$ (M = Ca, Sr and Ba) are shown in Fig 1. The phases were identified by comparing their spectra with those of the JCPDS standard, PDF numbers: 85-0585 ($CaMoO_4$), 86-0586 ($SrMoO_4$) and 29-0193 ($BaMoO_4$) [10].

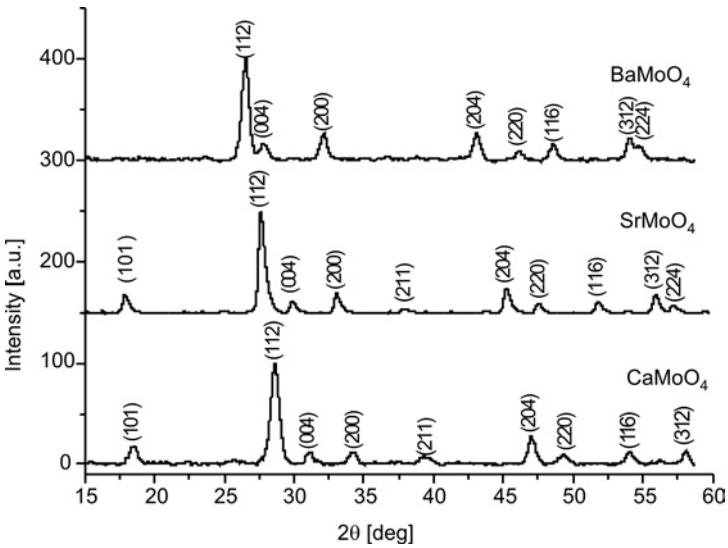

Fig. 1. XRD spectra of $CaMoO_4$, $SrMoO_4$ and $BaMoO_4$

No characteristic peaks of impurities were detected. The molybdates have tetragonal scheelite structure ($a = b \neq c$ and $\alpha = \beta = \gamma = 90°$) with $I4_1/a$ space group [6, 10]. Their lattice parameters were calculated from the equation of plane spacing for the tetragonal structure and Bragg's law for diffraction [11]. They are a = 0.5221 nm, c = 1.1417 nm for $CaMoO_4$, a = 0.5417 nm, c = 1.2004 nm for $SrMoO_4$, and a = 0.5610 nm, c = 1.2766 nm for $BaMoO_4$. The calculated parameters are very close to those of the JCPDS standard [10]. Increase in the lattice parameters was related to the atomic masses and ionic radii of alkaline earth metals (Ca^{2+} – 0.112 nm, Sr^{2+} – 0.125 nm, Ba^{2+} – 0.142 nm) [3], which imply the difference of charge densities in MO_8 polyhedral environment of the scheelite structure [12].

The crystallite sizes of $MMoO_4$ (M = Ca, Sr and Ba) were calculated from the (112) peaks of XRD spectra and by applying Scherrer's formula, $B = \lambda k/L\cos\theta$, where λ, θ, L, k and B are the wavelength of CuK_α radiation, the Bragg angle, the average crystallite size, a constant (0.89), and the full width at half maximum of (112) peak in radians, respectively [11]. The calculated crystallite sizes of $CaMoO_4$, $SrMoO_4$ and $BaMoO_4$ are 14.48, 15.83 and 18.00 nm, respectively. They all increased with the increase in the ionic radii and the atomic masses of the alkaline earth metals.

It is proposed that the most likely reaction occurring in the synthesis of the nanocrystalline molybdates via the cyclic microwave radiation process is:

$$M(NO_3)_2 + Na_2MoO_4 \rightarrow MMoO_4 + 2NaNO_3$$

PG and microwave radiation influence the fabrication of uniform nanosized particles, which can be explained as follows. PG has a high boiling point (187 °C) [13], thus the problem of overheating by microwave radiation can be overcome. At 25 °C, PG has a high permanent dipole moment (2.50 D) and a high electric permittivity (30.2) [14] which enables coupling with the electric field leading to the molecular vibration of PG. The solution may be rapidly heated to a high temperature and due to the microwave vibration (2.45 GHz) [15], nucleation and growth proceed in uniform environment. Finally, nanosized particles are synthesized.

Alkaline earth metal molybdates contain $[MoO_4]^{2-}$ tetrahedrons. 26 various vibrations in the lattice space ($3A_g + 5A_u + 5B_g + 3B_u + 5E_g + 5E_u$) were determined by the group theory calculations [3,16]. $3A_g$, $5B_g$ and $5E_g$ vibrations are Raman active. Only $4A_u$ and $4E_u$ of the $5A_u$ and $5E_u$ vibrations are infrared active, and the remaining ones ($1A_u$ and $1E_u$) are acoustic vibrations. $3B_u$ vibrations are silent modes [3, 17]. Raman spectra (Fig. 2) show six vibrations at 875, 845, 792, 392, 322 and 204 cm^{-1} for $CaMoO_4$, 883, 842, 794, 368, 327 and 181 cm^{-1} for $SrMoO_4$, and 887, 834, 788, 359, 327 and 192 cm^{-1} for $BaMoO_4$. They correspond to $\nu_1(A_g)$, $\nu_3(B_g)$, $\nu_3(E_g)$, $\nu_4(B_g)$, $\nu_2(A_g)$ and $\nu_{\text{free rotation}}(A_g)$ modes, respectively [18].

FTIR spectra of the molybdates are shown in Fig 3. For T_d symmetry, $\nu_3(F_2)$ and $\nu_4(F_2)$ modes are infrared active. They correspond to stretching and bending modes, respectively [19, 20]. Very strong Mo–O stretching vibration in $[MoO_4]^{2-}$ tetrahedrons was detected at 783–955 cm^{-1} and weak Mo–O bending vibration was evident at 422 cm^{-1}.

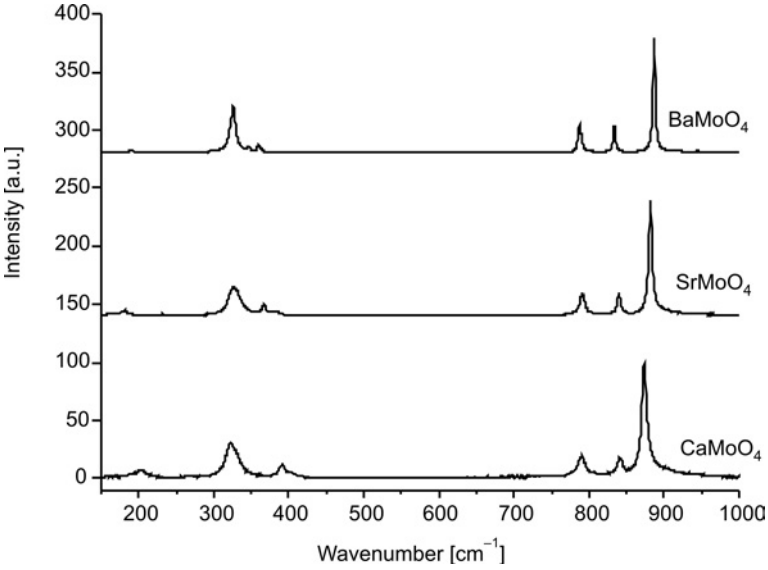

Fig. 2. Raman spectra of $CaMoO_4$, $SrMoO_4$ and $BaMoO_4$

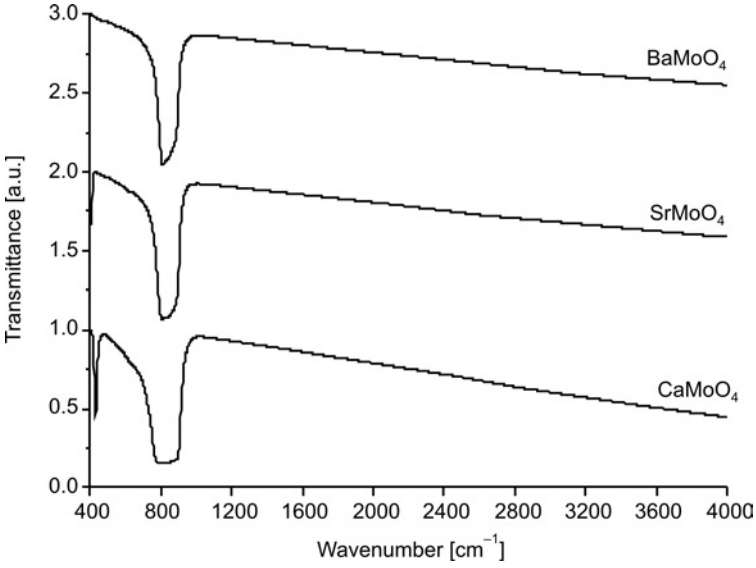

Fig. 3. FTIR spectra of $CaMoO_4$, $SrMoO_4$ and $BaMoO_4$

TEM images and SAED patterns of metal molybdates are shown in Fig 4. The products were composed of a number of round nanosized particles. Their average sizes were estimated from 500 particles seen on TEM images. Their distribution curves (Fig. 5) are narrow. The particle sizes are 20 ± 5 nm for $CaMoO_4$, 21 ± 5 nm for $SrMoO_4$, and 22 ± 5 nm for $BaMoO_4$.

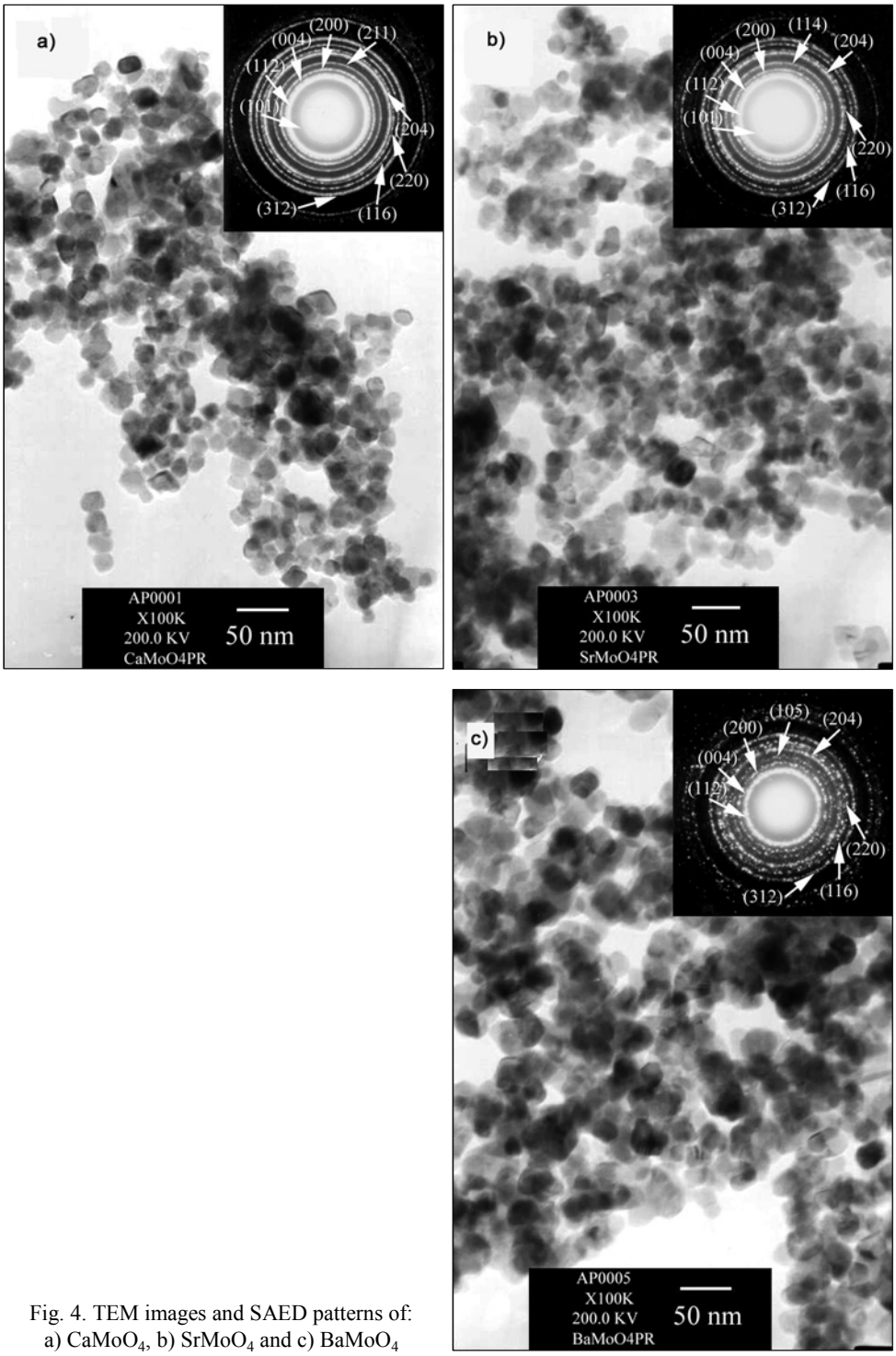

Fig. 4. TEM images and SAED patterns of: a) $CaMoO_4$, b) $SrMoO_4$ and c) $BaMoO_4$

Narrow particle size distributions and homogeneous particles favour good luminescent properties [21]. The products contain less contaminations, or fewer dead layers on the phosphor surface [21]. SAED patterns show a number of bright spots: the brightness of some of them is continuous, whereas for others they are at random. The spots are so close that they form fully concentric rings. These indicate that the molybdates consist of nanosized polycrystals with different orientations. Interplanar spaces were calculated from the diameters of the rings [22, 23], and compared with those of the JCPDS standard [10]. Crystallographic planes were indexed on the patterns. The products are specified as $MMoO_4$ (M = Ca, Sr and Ba).

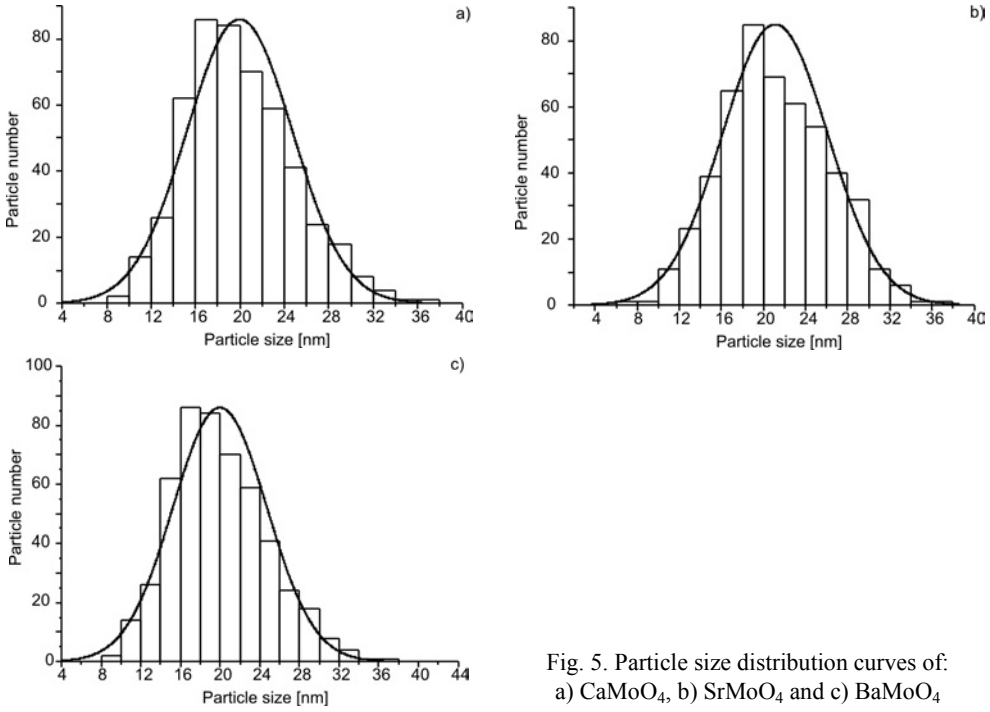

Fig. 5. Particle size distribution curves of: a) $CaMoO_4$, b) $SrMoO_4$ and c) $BaMoO_4$

EDX analyses of $CaMoO_4$, $SrMoO_4$ and $BaMoO_4$ (results not shown) revealed Ca peaks at 3.69 keV (K_α) and 4.01 keV (K_β), Sr peaks at 1.81 keV (L_α), 14.14 keV (K_α) and 15.84 keV (K_β), and Ba peaks at 4.47 keV (L_α), 4.83 keV ($L_{\beta1}$), and 5.16 keV ($L_{\beta2}$). O peaks of the three molybdates were detected at 0.53 keV (K_α), and Mo peaks were detected at 2.29 keV (L_α), 17.45 keV (K_α) and 19.61 keV (K_β) [24]. Elemental analysis shows that the M:Mo:O atomic ratios are very close to those of the corresponding stoichiometric molybdates. Cu of copper grids and C layers were also detected.

4. Conclusions

Nanocrystalline compounds $MMoO_4$ (M = Ca, Sr and Ba) were successfully synthesized from $M(NO_3)_2$ and Na_2MoO_4 in propylene glycol, by applying cyclic micro-

wave radiation. XRD, SAED and EDX analyses revealed the presence of nanocrystalline $MMoO_4$ containing the corresponding alkaline earth metals, Mo and O. The products were composed of a number of round nanosized particles, according to TEM analysis. Their size distributions are very narrow. Six vibrations were detected using Raman spectroscopy. FTIR data revealed very strong Mo–O stretching vibrations in $[MoO_4]^{2-}$ tetrahedrons, which were detected in the 783–955 cm^{-1} range. FTIR data also confirmed weak Mo–O bending at 422 cm^{-1}.

Acknowledgements

The authors are extremely grateful to the Thailand Research Fund and the National Research Council of Thailand for supporting the research, and the Graduate School of Chiang Mai University for general funding.

References

[1] ZHAO Y., LIAO X.H., HONG J.M., ZHU J.J., Mater. Chem. Phys., 87 (2004), 149.
[2] LIAO X.H., CHEN N.Y., XU S., YANG S.B., ZHU J.J., J. Cryst. Growth, 252 (2003), 593.
[3] BASIEV T.T., SOBOL A.A., VORONKO Y.K., ZVEREV P.G., Opt. Mater., 15 (2000), 205.
[4] RYU J.H., YOON J.W., SHIM K.B., J. Alloy. Comp., 413 (2006), 144.
[5] ZHANG Y., YANG F., YANG J., TANG Y., YUAN P., Solid State Commun., 133 (2005), 759.
[6] LI Z., DU J., ZHANG J., MU T., GAO Y., HAN B., CHEN J., CHEN J., Mater. Lett., 59 (2005), 64.
[7] ZHANG C., SHEN E., WANG E., KANG Z., GAO L., HU C., XU L., Mater. Chem. Phys., 96 (2006), 240.
[8] WANG Y., MA J., TAO J., ZHU X., ZHOU J., ZHAO Z., XIE L., TIAN H., Ceram. Int., 33 (2007), 693.
[9] PARHI P., SINGH S.S., RAY A.R., RAMANAN A., Bull. Mater. Sci., 29 (2006), 115.
[10] Powder Diffract. File, JCPDS Int. Centre Diffr. Data, U.S.A. (2001).
[11] SURYANARAYANA C., NORTON M.G., *X-ray Diffraction. A Practical Approach*, Plenum Press, New York, (1998).
[12] ERRANDONEA D., PELLICER-PORRES J., MANJON F.J., SEGURA A., FERRER-ROCA CH., KUMAR R.S., TSCHAUNER O., RODRÍGUEZ-HERNÁNDEZ P., LÓPEZ-SOLANO J., RADESCU S., MUJICA A., MUÑOZ A., AQUILANTI G., Phys. Rev. B, 72 (2005), 174106.
[13] ANDREESCU D., MATIJEVIĆ E., GOIA D.V., Colloid. Surf. A, 291 (2006), 93.
[14] SENGWA R.J., J. Mol. Liq., 108 (2003), 47.
[15] CHEN D., TANG K., SHEN G., SHENG J., FANG Z., LIU X., ZHENG H., QIAN Y., Mater. Chem. Phys., 82 (2003), 206.
[16] PORTO S.P.S., SCOTT J.F., Phys. Rev. 157 (1967), 716.
[17] GOLUBOVIĆ A., GAJIĆ R., DOHČEVIĆ-MITROVIĆ Z., NIKOLIĆ S., J. Alloys Comp., 415 (2006), 16.
[18] CHEN D., TANG K., LI F., ZHENG H., Cryst. Growth Design, 6 (2006), 247.
[19] DE AZEVEDO MARQUES A.P., DE MELO D.M.A., PASKOCIMAS C.A., PIZANI P.S., JOYA M.R., LEITE E.R., LONGO E., J. Solid State Chem., 179 (2006), 671.
[20] CLARK G.M., DOYLE W.P., Spectrochim. Acta, 22 (1966), 1441.
[21] RYU J.H., YOON J.W., LIM C.S., OH W.C., SHIM K.B., J. Alloy. Comp., 390 (2005), 245.
[22] THONGTEM T., PHURUANGRAT A., THONGTEM S., J. Mater. Sci., 42 (2007), 9316.
[23] THONGTEM T., KAOWPHONG S.AND THONGTEM S., J. Mater. Sci., 42 (2007), 3923.
[24] *X-ray Absorption and Emission Energy*, Oxford Instrum. Analyt., Halifax Rd., High Wycombe Bucks HP12 3SE, U.K.

Received 7 October 2007
Revised 2 December 2007

Materials Science-Poland, *Vol. 28*, *No. 2*, *2010*

A novel highly acidic sulfonic functionalized SBA-1 cubic mesoporous catalyst and its application in the esterification of palmitic acid

A. ABBASI[1], A. REZA MAHJOUB[1*], A. R. BADIEI[2]

[1]Department of Chemistry, School of Basic Sciences,
Tarbiat Modares University,Tehran, 14115-175, Iran

[2]School of Chemistry, University College of Science, University of Tehran, Tehran, Iran

Propylsulfonic acid functionalized cubic mesoporous silica was fabricated through in situ oxidization of mercaptopropyl groups with H_2O_2 during co-condensation of tetraethyl orthosilicate and 3-mercaptopropyl trimethoxysilane under strong acidic conditions. The materials obtained with 5–20 mol % loadings of sulfonic acid groups had surface areas of up to 1300 m^2/g and pore sizes of ca. 2.5 nm. The catalytic activity of this material was investigated: tests were performed on the esterification of palmitic acid being a model compound in the process of biodiesel production. Methyl ester yield on this new nanoporous catalyst is very remarkable during a mild liquid phase reaction.

Keywords: *cubic mesoporous silica; SBA-1; esterification; biodiesel; palmitic acid*

1. Introduction

The discovery of an ordered M41S family of mesoporous materials has stimulated extensive research in the field of their potential use as catalysts, adsorbents, and templates for the syntheses of nanostructures [1, 2]. To further explore possible applications of these materials, much effort was devoted to syntheses of organically hybrid well defined pore structures, highly accessible functional groups, and controlled surface reactivity [3, 4]. Grafting of functional organosilanes by using surface hydroxyl groups as anchor points has been widely used [5, 6].

It is generally accepted that a cubic mesostructure is more advantageous for catalytic applications than a hexagonal one, since three dimensional pore arrangements of cubic mesostructures are more resistant to pore blocking and allow faster diffusion of reactants. Therefore, organo-functionalized mesoporous silicas with cubic mesostruc-

*Corresponding author, e-mail: mahjouba@modares.ac.ir

tures would be more desirable than those with hexagonal mesostructures such as MCM-41. For the first time, Huo et al. [7–9] reported a successful synthesis of SBA-1 (cubic *Pm*3*n*) through the S+XI route, where S, X, and I correspond to surfactant, halide, and inorganic species, respectively. In this approach, acidic conditions were imposed, and a surfactant having a large head group, namely cetyltriethylammonium bromide (CTEABr) was used. However, so far only a few functionalized SBA-1 mesoporous materials have been reported. Indeed, it has a direct relation to poor structural stability of SBA-1 under hydrothermal conditions. On the other hand, the addition of organosilanes during the direct synthesis of organo-functionalized SBA-1 mesoporous materials in strongly acidic conditions is much more favourable [10].

Sulfonic-functionalized mesoporous materials received exceptional attention because of their numerous practical applications in heterogeneous acid catalysis, toxic mercury ion trapping, biomolecule immobilization, and as a support material for metallic nanoparticles [11]. Acid catalysts increase reaction rates of esterification and trans-esterification processes. Fatty acid methyl esters are products of trans-esterification of vegetable oils and fats with methanol in the presence of acid or basic catalysts. These products are so-called biodiesels. A worldwide interest in biofuels being an alternative to diesel fuel is growing, especially in environmentally conscious countries.

Many researchers made attempts to synthesize vegetable oil based derivatives with properties and performance similar to those of petroleum based diesel fuel. Biodiesel (monoalkyl esters) is one such alternative fuel, which is obtained by the trans-esterification of triglyceride oil with monohydric alcohols. It has been reported that biodiesel obtained from canola and soybean oil is a very good substitute for diesel fuel [12]. Despite its environmental benefits, the high cost of biodiesel production is the major obstacle to its commercialization. Trans-esterification of waste cooking oil is an effective way to reduce the cost of raw materials and to solve the problem of waste oil disposal. Unlike virgin oils, waste oils contain high quantities of free fatty acids (FFA) and water. Free fatty acid and water can limit the effectiveness of alkali-catalyzed processes. Also free fatty acids react with alkali catalysts and produce soaps and water. Therefore, saponification not only consumes the catalyst, but the resulting soaps can also cause the formation of emulsions. Both the aforementioned problems make the production of biodiesel more expensive. For this reason, acid catalysts, especially heterogeneous catalysts, attracted much more attention in regard to esterification reactions and biodiesel production.

This joint study is focused on synthesizing a novel organoacid functionalized mesoporous catalyst with remarkable hydrothermal stability, in order to catalyze the esterification of palmitic acid.

2. Experimental

Template preparation. The surfactant cetyltriethylammonium bromide (CTEAB) was fabricated by mixing of 1-bromohexadecane (98%, Merck) and triethylamine

(99%, Merck) in absolute ethanol under reflux conditions for 24 h. The ethanol was then removed with a rotary evaporator until a white, viscous paste was obtained. The resulting gel is recrystallised by a minimum addition of chloroform, and then ethyl acetate, until the whole solid precipitates [13].

Sulfonic acid-functionalized SBA-1 preparation. Sulfonic acid-functionalized mesoporous silica materials were fabricated by one-pot co-condensation of tetraethoxysilane (TEOS) and MPTMS in the presence of CTEAB under acidic conditions, along with a direct reaction with H_2O_2 at room temperature. The final molar composition of the initial gel was as follows: TEOS: *y* MPTMS: 0.2 CTEAB: (30–40) HCl: 700 H_2O:(0–2) H_2O_2.

In a typical procedure, 8 g of TEOS was first placed in an opening beaker with 12.5 cm^3 of 12 M HCl and 100 cm^3 of water, and was subsequently hydrolyzed at room temperature under stirring for an appropriate duration. Then, 1.5 g of CTEAB was added to a prehydrolyzed mixture and the stirring was continued. The mixture became a slightly viscous solution; appropriate quantities of MPTMS and aqueous solution of H_2O_2 (30 wt. %) were slowly added to the solution. Stirring of the mixture was maintained at a constant temperature for 3 h. The solution was then transferred to a Teflon lined autoclave for about 1 h at 100 °C, and finally the solid was filtered, washed and dried at 100 °C overnight. The MPTMS/H_2O_2 molar ratio was 1/10, and the MPTMS/(TEOS + MPTMS) ratio varied from 0 to 0.20. The resultant samples are referred to as SBA-1-SO_3H-*x*-*T*, where *T* stands for the "prehydrolysis time of TEOS in minutes" and *x* is the MPTMS/(TEOS + MPTMS) molar percentage.

For example, SBA-1-SO_3H-10-30 represents the sample prepared with TEOS prehydrolysis for 30 min and such that MPTMS/(TEOS + MPTMS) = 10 mol %. For comparison, samples were also prepared without TEOS prehydrolysis. They are labelled as SBA-1-SO_3H-*x*-0. Another sample containing 10 mol % of MPTMS was prepared with TEOS prehydrolysis in the absence of H_2O_2 and is denoted SBA-1-SH-10-*T*. The thiol groups in SBA-1-SH-10-*T* were post-oxidized to sulfonic acid groups with a 15-fold excess of aqueous solution of H_2O_2 (30 wt. %) at room temperature for 4 h. The solids were then acidified with aqueous solution of 2M HCl, followed by filtration, washing with water and ethanol, and finally drying at 100 °C. The post-oxidized sample was defined as SBA-1-SO_3H-10-*P*. A hexagonal MCM-41 sample was synthesized as described in literature [2]. It was functionalized and post-oxidized in the same way, and was named as MCM-41-SO_3H-10-P.

Template extraction. Resultant samples were extracted in a soxhlet extraction apparatus, with ethanol as the extraction solvent, in order to remove templates. FTIR was used to monitor the removal of templates. All characterizations and catalytic tests confirmed the samples were template-free.

Catalyst characterization. N_2 sorption isotherms were recorded using a Belsorp-18 (Bel Japan Inc.,) at liquid nitrogen temperature. Before taking the measurements, the samples were degassed at 150 °C for 4 h. The specific surface areas were evaluated

using the Brunauer–Emmett–Teller (BET) method in the p/p_0 range of 0.05–0.3. Pore size distribution curves were calculated from the adsorption branch of the isotherms and by the Barrett–Joyner–Halenda (BJH) method. The pore volume was taken at the p/p_0= 0.990 point. X-ray powder diffraction (XRD) patterns were obtained on a Philips X'Pert diffractometer using CuK_α radiation (1.5418 Å).

Thermogravimetric (TG) analyses were carried out on a Shimadzu DTG 60 thermogravimetric analyzer with the heating rate of 10 °C/min in the air flow of 50 cm^3/min. Fourier transform infrared (FTIR) spectra were taken on a Bruker Equinox 55 spectrometer, with the resolution of 2 cm^{-1}, using the KBr method. The content of sulfonic acid centres in the materials was determined by ion-exchange with sodium cations followed by acid titration [11]. Aqueous solutions of sodium chloride (NaCl, 2M), were used as the exchange agents. In a typical experiment, 0.20 g of solid, treated at 150 °C for 5 h, was added to 20 cm^3 of aqueous solution containing the corresponding salt. The resultant suspension was equilibrated for 4 h, then filtered and washed with a small amount of water. Finally, the filtrate was titrated potentiometrically by dropwise addition of aqueous solution of 0.01 M NaOH.

Catalytic reactions. The catalysts were heat treated at 200 °C for 6 h in order to remove adsorbed water in the materials. Then, esterification of palmitic acid with methanol was carried out in a two-necked flask of 50 cm^3 with a reflux condenser placed in a hot plate with a magnetic stirrer. In a typical experiment, 0.02 mol of palmitic acid and 0.2 mol of methanol were mixed under vigorous stirring and heated to 50 °C. Then 0.1 g of the treated catalyst was added into the reaction mixture. Reaction rates were determined during the reaction intervals. Quantitative analysis was based on the methyl ester products and the corresponding standard methyl palmitate (from Supelco).

In all cases, the liquid products were extracted from the reaction mixture at appropriate reaction intervals with a filtering syringe, and analyzed using an Agilent 5890 gas chromatograph (GC) equipped with a 30 m × 0.53 mm HP-5 capillary column and an FID detector.

3. Results and discussion

Powder X-ray diffraction analyses were performed on all the MPTMS-functionalized materials. The X-ray diffraction patterns of functionalized SBA-1 samples contain (200), (210), and (211) reflections belonging to the space group *pm*3*n*. Such patterns are characteristic of materials having ordered cubic arrays of a cage-like channel structure (Fig. 1).

The N_2 adsorption–desorption isotherms of the sulfonic acid-functionalized materials are illustrated in Fig. 2. The samples prepared with prehydrolysis of TEOS exhibit characteristic isotherms of type IV with apparent hysteresis loops, which are typical of mesoporous materials, according to the IUPAC classification. Pore diameter increases with the prehydrolysis time in the initial gel.

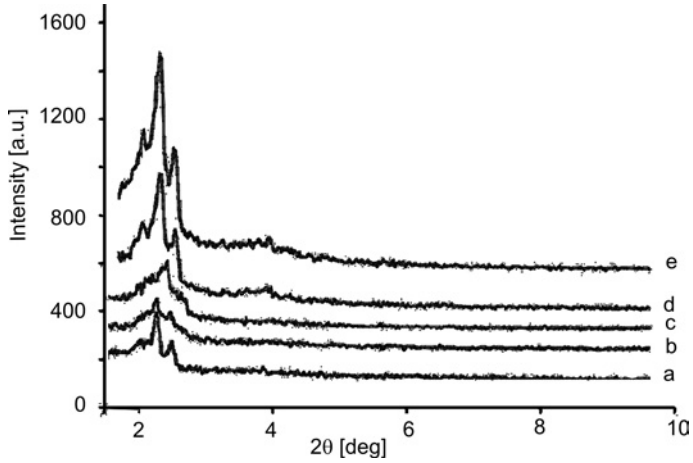

Fig. 1. XRD patterns of template extracted of: a) SBA-1-SO_3H-10-0, b) SBA-1-SO_3H-15-0, c) SBA-1-SO_3H-20-0, d) SBA-1-SO_3H-10-30, e) SBA-1-SO_3H-10-60

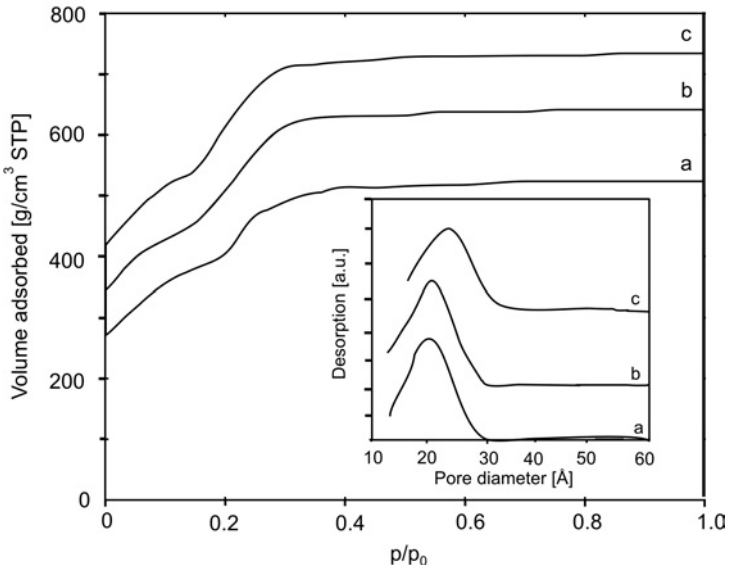

Fig. 2. N_2 adsorption isotherms of: a) SBA-1-SO_3H-10-0, b) SBA-1-SO_3H-10-30 and c) SBA-1-SO_3H-10-60

Basic physicochemical and textural data on the functionalized materials are shown in Table 1. All the samples prepared by co-condensation of TEOS and MPTMS show high surface areas and the BJH pore sizes (Dp) are around 2.1–2.5 nm. The surface area and the pore volume decrease as the MPTMS content is increased from 5 to 20 mol % in the synthesis mixture. Conversely, the samples prepared without TEOS pre-hydrolysis exhibit lower surface areas, smaller pore volumes, and smaller average pore sizes than their counterparts synthesized with TEOS prehydrolysis.

Table 1. Textural properties of silica materials

Sample	$(A_{BET})^a$ [m^2/g]	$(V_p)^b$ [cm^3/g]	$(D_p)^c$ [nm]
SBA-1-SO_3H-10-30	1140	1.06	2.2
SBA-1-SO_3H-10-60	1170	0.97	2.3
SBA-1-SO_3H-10-180	1290	1.14	2.5
SBA-1-SO_3H-10-0	1050	0.95	2.1
SBA-1-SO_3H-10-PO	1018	0.98	2.1
SBA-1-SO_3H-5-0	1103	0.99	2.1
SBA-1-SO_3H-15-0	1037	0.85	2.1

[a] BET surface area.
[b]Total pore volume.
[c]BJH pore size.

The sulfur contents in the MPTMS-functionalized materials was analyzed by TG and elemental analyses (EA), and the results are given in Table 2. It can be seen that MPTMS in the initial mixture was mostly incorporated into the silica materials. The acid capacities of the materials fabricated in the presence of H_2O_2 increased with the MPTMS content in the initial mixture. The numerical values for the acid capacity are very close to those obtained from EA or TG analyses, and constitute further confirmation that complete oxidation of the thiol groups had occurred. By contrast, the SBA-1 -SO_3H-10-P sample obtained by post-oxidation shows lower values for acid capacity than those obtained from EA or TG analyses: this is attributed to the incomplete oxidation of thiol groups.

Table 2. Sulfur contents and acid capacities of functionalized SBA-1 materials with MPTMS

Sample	Sulphur content [mmol/g]			Acid capacity [mmol/g]
	Calculated by EA by TG			NaCl
SBA-1-SO_3H-10-30	1.4	1.28	1.30	1.2
SBA-1-SO_3H-10-60	1.4	1.32	1.30	1.21
SBA-1-SO_3H-10-180	1.4	1.32	1.33	1.25
SBA-1-SO_3H-10-0	1.4	1.20	1.13	1.10
SBA-1-SO_3H-10-PO	1.4	1.10	1.11	0.91
SBA-1-SO_3H-5-0	0.75	0.77	0.58	0.68
SBA-1-SO_3H-15-0	1.9	1.5	1.45	1.3

Esterification of palmitic acid with methanol was used to test the catalytic activities of a propylsulfonic acid functionalized catalyst in liquid phase reactions. The activities in the reactions were expressed by ester production.

The catalytic performance of the SBA-1-SO_3H-10-60 catalyst in esterification at 50 °C, expressed as a function of the reaction time, is shown in Fig. 3. The methyl ester content increases very rapidly and almost linearly with the reaction time in the first 150 min. Then, the reaction rate slows down as the reaction time prolongs. After 4 h, a conversion of around 85% had been obtained.

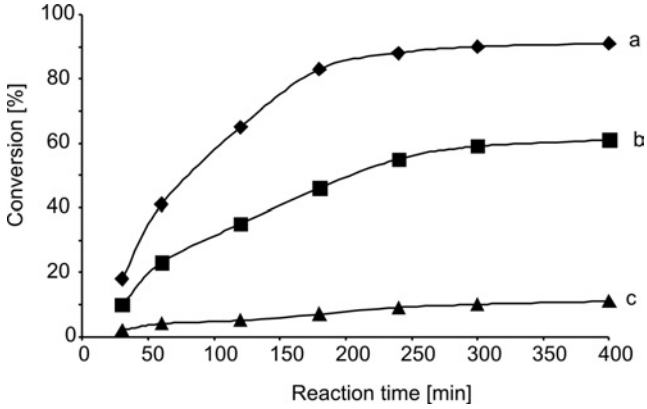

Fig. 3. Time dependence of degree of conversion of palmitic acid at 50 °C over sulfonic acid functionalized silica SBA-1 (a), MCM-41-SO_3H-10-P (b) and pure silica (c)

Esterification in a homogeneous system without solid catalysts or over pure silica was inefficient. Even after 4 h, the conversion did not exceed 10%. The catalytic activity of hexagonal MCM-41-SO_3H-10-P catalyst is lower than that of the acidified cubic SBA-1 (Fig. 3).

4. Conclusions

Novel functionalized cubic SBA-1 silica materials with different loadings of propylsulfonic acid groups were prepared by a simple co-condensation of TEOS and MPTMS under acidic conditions at room temperature. Samples prepared with TEOS prehydrolysis showed higher surface areas and larger pore volumes than those prepared without TEOS prehydrolysis. Thiol groups could be completely in situ oxidized into sulfonic acid groups in the procedure of synthesis, when H_2O_2 was also added to the mixture.

Esterification of palmitic acid with methanol was used to investigate the catalytic activity. This reaction opens up a new synthesis route which facilitates the use of inexpensive waste oils, having high free fatty acid contents, for the production of biofuels in mild conditions. Furthermore, the yield is high in comparison with conventional base catalysts.

Acknowledgement

Thanks are expressed to the Tarbiat Modarres University for providing financial support for the research.

References

[1] KRESGE C.T., LEONOWICZ M.E., ROTH W.J., VARTULI J.C., BECK J.S., Nature, 359 (1992), 710.
[2] BECK J.S., VARTULI J.C., ROTH W.J., LEONOWICZ M.E., KRESGE C.T., SCHMITT K.D., CHU C.T., OLSON D.H., SHEPPARD E.W., MCCULLEN S.B., HIGGINS J.B., SHLENKER J.L., J. Am. Chem. Soc., 114 (1992), 10834.
[3] SHIN H.J., RYOO R., LIU Z., TERASAKI O., J. Am. Chem. Soc., 123 (2001), 1246.
[4] YANG C.M., LIU P.H., HO Y.FO., CHIU C.Y., CHAO K.J., Chem. Mater., 15 (2003), 275.
[5] STEIN A., MELDE B.J., SCHRODEN R.C., Adv. Mater., 12 (2000), 1403 and references therein.
[6] WRIGHT A.P., DAVIS M.E., Chem. Rev., 102 (2002), 3589.
[7] HUO Q., MARGOLESE D.I., CIESLA U., DEMUTH D.G., FENG P., GIER T.E., SIEGER P., FIROUZI A., CHMELKA B.F., SCHUTH F., STUCKY G.D., Chem. Mater., 6 (1994), 1176.
[8] HUO Q., LEON R., PETROFF P.M., STUCKY G.D., Science, 268 (1995), 1324.
[9] HUO Q., MARGOLESE D.I., STUCKY G.D., Chem. Mater., 8 (1996), 1147.
[10] KAO M., WU J.D., CHENG C.C., CHIANG A.S.T., Micropor. Mesopor. Mater., 88 (2006), 319.
[11] MARGOLESE D., MELERO J.A., CHRISTIANSEN S.C., CHMELKA B.F., STUCKY G.D., Chem. Mater., 12 (2000), 2448.
[12] FREEDMAN B., BUTTERFIELD R.O., PRYDE E.H., J. Am. Oil Chem. Soc., 63 (1986), 1375.
[13] KIM M.J., RYOO R., Chem. Mater., 11 (1999), 487.

Received 27 January 2008
Revised 19 March 2008

Materials Science-Poland, *Vol. 28*, *No. 2*, *2010*

Crystal structure and spectroscopic properties of [Zn(2-qmpe)Cl_2] containing diethyl (quinolin-2-ylmethyl)phosphonate ligand (2-qmpe)

B. ŻUROWSKA[1*], A. BIAŁOŃSKA[1], A. KOTYŃSKI[2], J. OCHOCKI[2]

[1]Faculty of Chemistry, University of Wrocław, F. Joliot- Curie 14, 50-383 Wroclaw, Poland

[2]Department of Bioinorganic Chemistry, Faculty of Pharmacy,
Muszyńskiego 1, Medical University, 90-151 Łódź, Poland

The crystal structure of [Zn(2-qmpe)Cl_2] (2-qmpe, diethyl (quinolin-2-ylmethyl) phosphonate) ligand) was determined by X-ray-diffraction. The compound was also characterized by IR, far-IR, ^{1}H and ^{31}P NMR spectroscopy. In the molecule, 2-qmpe acts as a bidentate N,O-chelate ligand. Tetrahedral ZnNOCl2 environment of Zn(II) atom is slightly distorted. The structure is stabilized by intermolecular H bond and π···π interactions. The spectral features are in agreement with the structural data.

Keywords: *Zn(II); phosphonic acid ester N,O-donor ligand; crystal structure*

1. Introduction

Zinc is one of the most important trace elements, playing a versatile role in biological systems due to its structural properties and catalytic role in enzymes [1–7]. On the other hand, various phosphonate derivatives are of interest because of their broad spectrum of biological properties [8–15]. In a previous study we demonstrated the reactivity of the N,O-donor (quinolin-2-ylmethyl)phosphonate ligand (2-qmpe) to various transition metal salts [16, 17]. The crystal structures of the compounds [M(2-qmpe)$_4$(H_2O)$_2$](ClO_4)$_2$ (with O bonded ligand), where M = Ni, Mn [16], and [Pd(2-qmpe)$_2$$Cl_2$] (with N bonded ligand) [18] were determined. For the Cu(II), the dimeric compound with a di-μ-hydroxo bridge having the formula [Cu(2-qmpe)$_2$(OH)(H_2O)$_2$]$_2$(ClO_4)$_2$ (with O-bonded ligand) was identified [16]. In solution, under atmospheric oxygen, this compound undergoes oxidative decomposition to [Cu(2-qca)$_2$·H_2O] (2-qca – quinoline-2-carboxylate) [19]. The biological relevance of the phosphonate derivatives to the heterocyclic system, and their reactivity to transition metal ions, was the motivation behind our investiga-

*Corresponding author, e-mail: zurowska@wchuwr.pl

tions into its zinc complexes. It is worth mentioning that in the interaction of the Zn(II) with (pyridyn-3-ylmethyl)phosphonate (3-pmpe), three interesting crystal forms were isolated [20].

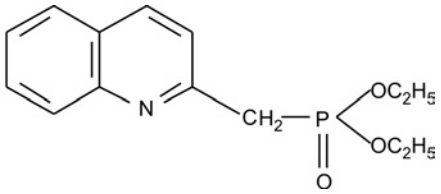

Fig. 1. A molecule of diethyl(quinolin-2-ylmethyl)phosphonate

In the paper, the synthesis, infrared spectra and crystal structure of the compound of the formula $[Zn(2\text{-qmpe})Cl_2]$ have been presented.

2. Experimental

Reagents and physical measurements: Starting materials and solvents were obtained commercially and used as-received. Elemental analyses were carried out using a Perkin-Elmer elemental analyzer 2400CHN. Infrared spectra (100–4000 cm^{-1}) were recorded using a Bruker IFS 113v spectrophotometer in KBr wafers. ^1H and ^{31}P NMR spectra were recorded on a Varian Mercury-300 spectrometer operating at the frequency of 300 MHz. Chemical shifts were reported using the standard (δ) notation in ppm with respect to TMS (1%) as an internal standard and H_3PO_4 (85%) as the external standard.

Determination of the crystal structure of [Zn(2-qmpe)Cl$_2$]: X-Ray data were collected on a Kuma KM4CCD diffractometer (MoK_α radiation, $\lambda = 0.71073$ Å). X-Ray data were collected at 100 K using an Oxford Cryosystem device. Data reduction and analysis were carried out with the CrysAlice 'RED' program [21].

Analytical numeric absorption correction using a multifaceted crystal model based on expressions derived by Clark and Reid was applied [22]. The space group was determined using the XPREP program. The structure was determined by direct methods, using the XS program, and refined using all the F^2 data, as implemented by the XL program [23]. Non-hydrogen atoms were refined with anisotropic displacement parameters. All H atoms were placed at the calculated positions. Before the last cycle of refinement, all H atoms were fixed and were allowed to ride on their parent atoms.

Synthesis of the diethyl (quinolin-2-ylmethyl)phosphonate ligand (2-qmpe). The ligand was prepared by phosphorylation of 2-chloromethylquinoline with diethyl phosphine according to the procedure described in detail elsewhere [16], and was checked for purity by spectroscopic and analytical methods.

^1H–NMR (300 MHz, $CDCl_3$): $\delta = 1.21$ (t, 6H, $^3J_{HH} = 6.8$, 2 CH_3), 3.57 (d, 2H, $^2J_{HP} = 22.02$; q–CH_2P), 4.05 (dq, 4H, $^3J_{HH} = 6.8$; 2 $POCH_2$), 7.12 (d, 1H, (q) H–C3), 7.46

(t, 1H, (q) H–C6), 7.64 (t, 1H, (q) H–C7), 7.73 (d, 1H, (q) H–C5), 8.01 (d, 1H, (q) H–C4), 8.05 (d, 1H, (q) H–C8); ^{31}P–NMR (121 MHz, $CDCl_3$): δ = 24.53; IR (film) ν_{max}(cm^{-1}): (py–ring) 1600(s), 1560(m), (P=O) 1254 (vs), (P–O–C) 1050–1030 (vs), (vs – very strong, s – strong, m – medium).

Synthesis of the Zn(2–qmpe)Cl$_2$ complex. The complex was prepared by dissolving the appropriate hydrated zinc nitrate (1 mmol) in ethanol (10 cm^3) and adding it to a solution of the ligand (1 mmol) in ethanol (15 cm^3). The resulting solution was filtered and left to evaporate slowly at room temperature. Pale yellow monocrystals of the Zn(II) compound, suitable for X-ray determination, were obtained after two weeks.

Anal. Calc. for $C1_4H_{18}C_{l2}NO_3PZn$: C, 40.46; H, 4.37; N, 3.37; Found: C, 40.05; H, 4.52; N, 3.17 ^{1}H–NMR (300 MHz, $CDCl_3$): δ = 1.34 (t, 6H, $^3J_{HH}$ = 6.8, 2 CH_3), 4.07 (d, 2H, $^2J_{HP}$ = 22.81; q–CH_2P), 4.35 (dq, 4H,$^3J_{HH}$ = 6.8; 2 POCH_2), 7.49 (d, 1H, (q) H–C3), 7.73 (t, 1H, (q) H–C6), 7.96 (m, 2H, (q) H–C7, H–C5), 8.49 (d, 1H, (q) H–C4), 9.14 (d, 1H, (q) H–C8); ^{31}P–NMR (121 MHz, $CDCl_3$): δ = 24.53.

3. Results and discussion

3.1. Description of the structure of [Zn(2-qmpe)Cl$_2$]

The crystallographic parameters of [Zn(2-qmpe)Cl_2] are summarized in Table 1. The selected bond lengths and angles are listed in Table 2. Figure 2 shows the structure and labelling scheme for the zinc(II) complex.

Table 1. Crystal data and structure refinement for [Zn(2-qmpe)Cl_2]

Empirical formula	$C_{14}H_{18}Cl_2NO_3PZn$	D_c [Mg·m^{-3}]	1.618
Formula weight	415.53	Absorption coefficient [mm^{-1}]	1.856
Temperature [K]	100(2)	F(000)	424
Wavelength [Å]	0.71073	Crystal size [mm]	0.15×0.13×0.12
Crystal system	triclinic	θ range for data collection [deg]	3.02–26.99
Space group	$\bar{P}1$	Ranges of h,k,l	–9÷9, –11÷11, –17÷17
a [Å]	7.505(3)	Reflections collected	8340
b [Å]	8.821(4)	Independent reflections (R_{int})	3700 (0.0315)
c [Å]	14.008(4)	Completeness to 2θ = 28.00	99.2%
α [°]	98.06(3)	Data/parameters	3700/199
β [°]	100.21(2)	Goodness-of-fit (F^2)	1.075
γ [°]	107.26(3)	Final R/wR indices ($I > 2\sigma I$)	0.0362/0.0685
Volume [Å^3]	853.0(6)	Largest diff. peak/hole [Å^{-3}]	0.346/–0.295
Z	2		

The 2-qmpe ligand chelates to the zinc ion, forming a six-membered ring. Zn(II) ion is surrounded by the nitrogen atom of pyridine, oxygen atom of the phosphoryl group of the 2-qmpe ligand, and two chloride atoms. A distorted tetrahedral environ-

ment ($ZnONCl2$) reveals around the metal cation, with angles deviate from 109.5°. The Zn–O(1), Zn–N(1) bond lengths are equal to 2.0114(19) and 2.087(2) Å, respectively. However, the Zn–Cl(1) and Zn-Cl(2) distances are equal to 2.2270(11) and 2.2249(13) Å, respectively (Table 2), being similar to those described previously in the literature [20].

Table 2. Bond lengths [Å] and angles [deg] for $[Zn(2\text{-qmpe})Cl_2]$

Zn–O(1) 2.0114(19)	C(14)–C(15) 1.490(4)
Zn–N(1) 2.087(2)	N(1)–C(2) 1.336(3)
Zn–Cl(2) 2.2249(13)	N(1)–C(10) 1.383(3)
Zn–Cl(1) 2.2270(11)	O(1)–Zn–N(1) 97.34(8)
P–O(1) 1.4902(19)	O(1)–Zn–Cl(2) 101.56(6)
P–O(2) 1.5523(19)	N(1)–Zn–Cl(2) 120.43(7)
P–O(3) 1.5631(18)	O(1)–Zn–Cl(1) 112.14(6)
P–C(11) 1.794(2)	N(1)–Zn–Cl(1) 103.45(6)
O(2)–C(12) 1.485(3)	Cl(2)–Zn–Cl(1) 119.71(4)
O(3)–C(14) 1.475(3)	O(1)–Zn–Cl(2) 101.56(6)
C(12)–C(13) 1.479(4)	

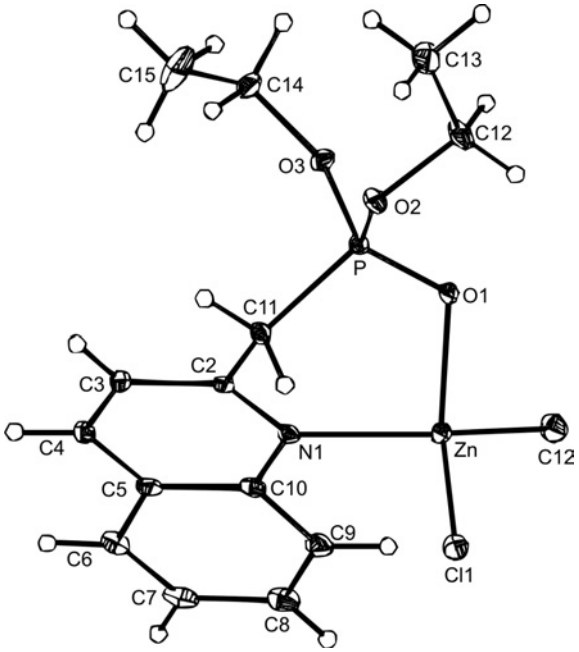

Fig. 2. Diagram of a molecule of $[Zn(2\text{-qmpe})Cl_2]$ showing the atomic numbering

The structure reveals the ligand to have a short P=O distance for the phosphoryl group (P–O(1) of 1.4902(19) Å), and longer distances between the P–O atoms of the phosphonate groups (P–O(2) and P–O(3) of 1.5523(19) and 1.5631(18) Å, respective-

ly). The geometry of the phosphonate groups deviates significantly from an ideal tetrahedron (Table 2), as is observed for phosphonate diesters [16, 18, 24]. The structure of the monomer (Table 3) is stabilized by the intramolecular hydrogen interaction, in which the quinolil group is involved: C(9)–H(9)···Cl(2).

Table 3. Hydrogen bonds [Å] and contacts [deg] for [Zn(2-qmpe)Cl$_2$]

D–H...A	*d*(D–H)	*d*(H...A)	*d*(D...A)	Angle (DHA)
C(4)–H(4)...Cl(1)^{i}	0.95	2.96	3.758(3)	143
C(8)–H(8)...Cl(1)^{ii}	0.95	2.94	3.824(3)	155
C(13)–H(13A)...Cl(1)^{iii}	0.98	2.91	3.669(3)	136
C(3)–H(3)...Cl(2)^{iv}	0.95	2.80	3.698(3)	158
C(9)–H(9)...Cl(2)	0.95	2.77	3.576(3)	144
C(11)–H(11B)...Cl(2)^{iv}	0.99	2.91	3.862(3)	161
C(14)–H(14B)...Cl(2)^{iv}	0.99	2.96	3.773(3)	140
C(14)–H(14A)...O(1)^{v}	0.99	2.66	3.299(3)	122
C(12)–H(12B)...O(3)^{v}	0.99	2.52	3.470(4)	162

S*y*mmetr*y* transformations used to generate equivalent atoms are: (i) $-x + 2$, $-y + 1$, $-z + 1$; (ii) $-x + 2$, $-y + 2$, $-z + 1$; (iii) $-x + 1$, $-y + 1$, $-z$; (iv) x, $y-1$, z; (v) $-x + 2$, $-y + 1$, $-z$.

The crystal structure of the compound is additionally stabilized by intermolecular C–H···Cl hydrogen interactions, in which the C(4), C(8), C(3) quinolil, C(11) methylene and the C(13), C(14) etoxy atoms are involved. Additionally, the structure is stabilized by the C–H···O interactions between the C(12) atom of the etoxy group and the phosphoryl oxygen atom O(3)^{v} of the ester group OC_2H_5. With regard to the observed weak C-H···O hydrogen bonds, the D···A bond distance and the D-H···A angle are well within the accepted range reported for similar C-H···O hydrogen bonds [25].

Table 4. π–π interactions in [Zn(2-qmpe)Cl$_2$]

Interaction	C1G...C1G	Interplanar angle	C1g(perp)	Slippage
C1G...C1G^{a}	3.588	0.00(13)	3.440(2)	1.02

S*y*mmetr*y* transformations used to generate equivalent atoms: (i) $-x + 2$, $-y + 1$, $-z + 1$. C1g represents the centroid of the ring N(1) C(2) C(3) C(4) C(5) C(10). C1g(perp) is the perpendicular distance of the C1g^{i} centroid from the ring N(1) C(2) C(3) C(4) C(5) C(10).

The C–H···O, C–H···Cl hydrogen bonds and π-π interactions (symmetry codes are given in Tables 3 and 4) stabilize the structure and lead to a three-dimensional (3D) network. The crystal packing is shown in Figs. 3 and 4.

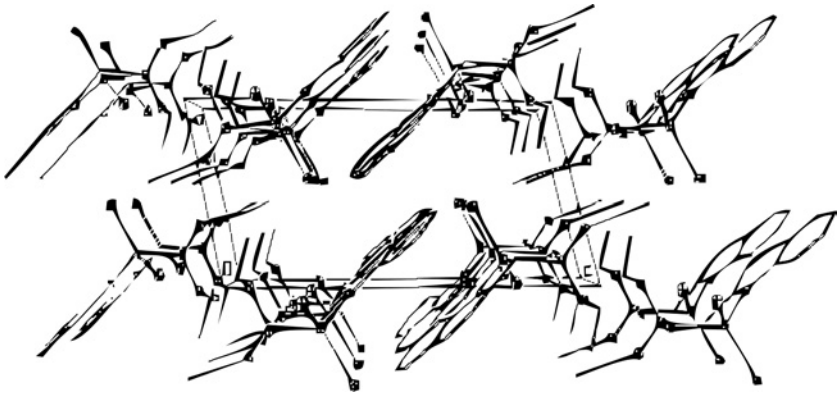

Fig. 3. Crystal packing of [Zn(2-qmpe)Cl_2] along the *b* axis

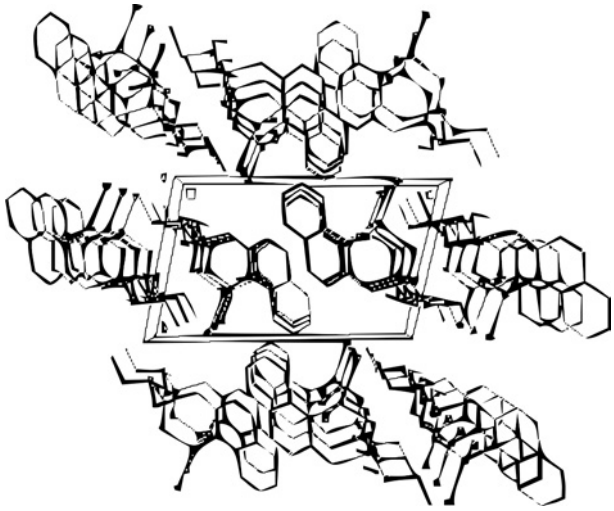

Fig. 4. Crystal packing of [Zn(2-qmpe)Cl_2] along the *a* axis

3.2. ^{1}H and ^{31}P NMR spectroscopy

The ^{1}H-NMR spectrum of 2-qmpe shows that the two ester groups, $POCH_2CH_3$, are equivalent. Only one triplet at 1.21 ppm is found for the methyl protons, and only one double quartet at 4.05 ppm is found for methylene protons. The two methylene protons of the CH_2P group give rise to a doublet at δ = 3.57 ppm and $^2J_{HP}$ = 22.02 Hz. The multiplets above 7 ppm are attributed to the quinoline ring, i.e. δ = 7.12 ppm (d) is attributed to the C-3 proton, δ = 7.46 ppm (t) to the C-6 proton, δ = 7.64 ppm (t) to the C-7 proton, δ = 7.73 ppm (d) to the C-5 proton, δ = 8.01 ppm (d) to the C-4 proton, and δ = 8.05 ppm (d) to the C-8 proton.

In the spectra of the complex a shift to lower fields exists for the protons adjacent to the coordination site with respect to the free ligand. The greatest shifts are observed

for the protons of the q-CH_2-P group ($\Delta\delta$ = 0.50 ppm) and H(8) of the quinoline ring ($\Delta\delta$ = 1.09 ppm) which indicates that the nitrogen atom is coordinated to the zinc. These shifts may be explained by the lowering of the electron density in the quinoline ring caused by the coordination to the zinc ion.

3.3. Infrared spectrum

In the IR spectrum of the compound under investigation, the band corresponding to the C=C and C=N stretching modes of the pyridine molecule in the range 1600–1500 cm^{-1} are not shifted appreciably, whereas the characteristic out-of-plane and in-plane deformation bands of the 2-substituted pyridine ring (at 396 and 620 cm^{-1} in free ligand, respectively) are shifted to higher frequencies (406 and 635 cm^{-1}, respectively), suggesting coordination of the quinolil nitrogen donor atom. The band at 967 cm^{-1} is associated with a pyridine ring breathing mode, and is characteristically shifted to higher energy on coordination. Thus, the band observed at 974 cm^{-1} indicates the coordination of pyridine residues. A very strong band at 1254 cm^{-1} corresponding to P=O stretching frequencies of the free ligand in the spectrum of the compound, is shifted towards lower frequencies (1192 cm^{-1}), indicating the coordination of the phosphoryl oxygen to the metal ion. Other ligand bands characteristic of the phosphonate moiety, namely δ(PO–C) at 1130–1170 cm^{-1} and ν(P–OC) at 1030–1050 cm^{-1}, do not display any significant shifts upon the formation of the Zn(II) complex. In the far IR region one band attributed to the ν(Zn–N) stretching vibration was found. The ν(Zn–Cl) symmetric and asymmetric frequencies (302 and 328 cm^{-1-}, respectively) are consistent with a pseudotetrahedral environment [26].

4. Conclusions

Zn(II) compound with diethyl quinolin-2-ylmethyl)phosphonate ester (2-qmpe) has been successfully synthesized. The presented results demonstrate that $ZnCl_2$ reacts with 2-qmpe ligand in a 1:1 molar metal/ligand ratio, forming the compound of the empirical formula [Zn(2-qmpe)Cl_2]. X-ray analysis of the crystal structure indicates that the Zn(II) displays tetrahedral coordination (most common for zinc), which is in agreement with the spectroscopic data. The earlier works [16, 17] and the results presented in this paper indicate that 2-qmpe ligand in reaction with metal salts can act as a monodentate ligand coordinated through the nitrogen or oxygen atoms.

Thereby, the 2-qmpe ligand engagement into monodentate coordination favours coordination by O donor atom (perchlorate metal compounds [16], chloride cobalt [17] and copper compounds [16,19]) in contrast to a compound with $PdCl_2$ [18]. In this compound Pd(II) is bound in a N-monodentate fashion to the nitrogen pyridine atom according to the known strong preference of the pallad ion as a soft metal toward nitrogen atom. 2-qmpe ligand coordinated in bidentate chelate manner via the quinoline nitrogen and the phosphoryl oxygen donor atoms [17] with nitrate and chloride metal

salts. The non-coordinating behaviour of the pyridine nitrogen atom in perchlorate compounds is probably due to poor donor properties in combination with possible steric constraints and/or crystal packing effects.

In summary, Zn(II) ions are recognized to be essential for life, being present in several naturally occurring metalloenzymes. On the other hand, it is well known that some organophosphorous compounds, in particular various derivatives of phosphonic acid and esters, can exhibit antibiotic, antibacterial, and antiviral and cytostatic activity [27–32]. However, some of their palladium and platinum halide complexes have been found to be cytostatic to various animal and human tumor cells [18, 24–35]. Similar behaviour may be expected in Zn(II) complexes having been synthesised and studied also for this purpose; then its metal complexes should be investigated as potential cytotoxic agents. It is expected that Zn(II) complexes will exhibit similar behaviour. In particular, the question of whether the metal complexes of Zn(II) can potentially be used as cytotoxic agents is one which deserves further investigation*.

Acknowledgement

This work was supported by the Polish Ministry of Science and Higher Education (Grant No. N405 303236 (JO).

References

[1] VALLE B.L. AULD D.S., Biochem., 29 (1990), 5647.
[2] LIPSCOMB W.N., STRAETER N., Chem. Rev., 96 (1996), 2375.
[3] COLEMAN J.E., Ann. Rev. Biochem., 61 (1997), 897.
[4] BERG J.M., GODWIN H.A., Annu. Rev. Biophys. Biomol., Struct. 26 (1997), 357.
[5] CHRISTIANSON D.W., COX J.D., Annu. Rev. Biochem., 68 (1999), 33.
[6] SORENSON J.R., J. Curr. Med. Chem., 9 (2002), 1867.
[7] PARKI G., Chem. Rev., 104 (2004), 699.
[8] OCHOCKI J., ERXLEBEN A., LIPPERT B., J. Heterocycl. Chem., 34 (1997), 1179.
[9] SANCHEZ-MORENO M.J., GOMEZ-COCA R.B., BOTELLO A.F., OCHOCKi J., KOTYNSKI A., GRIESSER R., SIGEL H., Org. Biomol. Chem., 1 (2003), 1819.
[10] OCHOCKI J., GRACZYK J., Pharmazie, 53 (1998), 884.
[11] OCHOCKI J., ERXLEBEN A., LIPPERT B., J. Heterocycl. Chem., 34 (1997), 1179.
[12] MORENO-LUQUE C.F., FREISINGER E., COSTISELLA B., GRIESSER R., OCHOCKI J., LIPPERT B., SIGEL H., J. Chem. Soc. Perkin. Trans., 2 (2001), 1882.
[13] MORENO-LUQUE C.F., GRIESSER R., OCHOCKI J., SIGEL H., Z. Anorg. Allg. Chem., 627 (2001), 1882.
[14] ARANOWSKA K., GRACZYK J., CHIŃSKA L., PAKULSKA W., OCHOCKI J., Pharm., 61 (2006), 457.
[15] KOSTKA B., SIKORA J., ARANOWSKI K., PARA J., OCHOCKI J., Acta Tox., 1 (2005), 113.
[16] OCHOCKI J., ŻUROWSKA B., MROZIŃSKI J., KOOIJMAN H., SPEK A.L., REEDIJK J., Eur. J. Inorg. Chem., (1998), 169.
[17] ŻUROWSKA B., MROZINSKI J., OCHOCKI J., Mater. Sci.-Poland, 25 (2007), 1063.

*Crystallographic data for the structure have been sent to the Cambridge Crystallographic Data Centre, CCDC-672232. Copies of the data can be obtained free of charge on application to The Director, CCDC, 12 Union Road, Cambridge CB2 1EZ, UK (Fax: int.code+(1223)336-033; e-mail for inquiry: fileserv@ccdc.cam.ac.uk).

[18] TUŠEK-BOŽIĆ L., MATIJASIĆ I., BOCELLI G., CALESTANI G., FURLANI A., STARCIA V., PAPAIOANNOU A., J. Chem. Soc. Dalton Trans., (1991), 195.
[19] ŻUROWSKA B., OCHOCKI J., MROZIŃSKI J., CIUNIK Z., REEDIJK J., Inorg. Chim. Acta, 357 (2004), 755.
[20] ŻUROWSKA B., ŚLEPOKURA K., LIS T., OCHOCKI J., Inorg. Chim. Acta, 362 (2008), 733.
[21] CrysAlis 'RED', Oxford Diffraction (Poland), Wroclaw, 2001, 2003.
[22] CLARK, R.C., REID, J. S. Acta Cryst. A51, (1995), 887.
[23] SHELXTL-NT [version 5.1], Bruker AXS Inc., Madison, WI, 1999.
[24] TUŠEK-BOŽIĆ L., MATIJASIĆ I., BOCELLI G., SGARABOTTO P., FURLANI A., SCARCIA V., PAPAIOANNOU A., Inorg. Chim. Acta, 185 (1991), 229.
[25] DESIRAJU G.R., ACC. Chem Res., 29 (1966), 441.
[26] NAKAMOTO K., in: Infrared and Raman Spectra of Inorganic and Coordination Compounds, Wiley Interscience, New York, 1986, p. 191.
[27] SCHLAPFER C.W., SAITO Y., NAKAMOTO K., Inorg. Chim. Acta, 129 (1972), 284.
[28] SHELDRICK W.S., Z. Naturforsch., Teil B 37 (1982), 653.
[29] STEFFEN W.L., PALENIK G.L., Inorg. Chem., 17 (1978), 1338.
[30] SIEWEK J., KRYSINSKI J., KUCHARSKI S., Pharm., 96 (1981), 782.
[31] SCHÖLLKOPF U., HOPPE J., THIELE A., Liebigs Ann. Chem., (1985) 555.
[32] ARANOWSKA K., GRACZYK J., CHĘCIŃSKA L., PAKULSKA W., OCHOCKI J., Pharm., 61 (2006), 5.
[33] NAJMAN-BRONŻEWSKA L., OCHOCKI J., Pharmazie, 52 (1997), 19.
[34] KALINOWSKA U., MATŁAWSKA K., CHĘCIŃSKA L., DOMAGAŁA M., KONTEK R., OSIECKA R., OCHOCKI J., J. Inorg. Biochem., 99 (2005), 2024.
[35] TUŠEK-BOŽIĆ L., FURLANI A., STARCIA V., DE CLERCQ E., BALZARINI J., J. Inorg. Biochem., 72 (1998) 201.

Received 27 January 2010

Materials Science-Poland, *Vol. 28*, *No. 2*, *2010*

Structural, morphological and electrochemical characterization of electron beam deposited $Li_{1+x}Mn_2O_4$ (x = 0, 0.05) thin films

S. BALAJI[1*], S. SHANMUGAN[1], D. MUTHARASU[2], K. RAMANATHAN[1]

[1]Materials Laboratory, Thiagarajar Advanced Research Centre,
Thiagarajar College of Engineering, Madurai-625 015, Tamil Nadu, India

[2]School of Physics, University Sains Malaysia, 11800, Penang, Malaysia

$Li_{1+x}Mn_2O_4$ (x = 0, 0.05) powders were synthesized using the microwave assisted co-precipitation method. Materials were evaporated using an electron beam gun. Structural analyses of thin films coated over platinum substrates revealed their cubic structure. The lattice constant of $Li_{1.05}Mn_2O_4$ thin film was found to be around 8.2475 Å. The lattice constant of $Li_{1.05}Mn_2O_4$ Powder was found to be 8.2488 Å. Morphological properties of the coated films were studied by SEM and the obtained micrographs were analyzed using the Image-j software. The roughness and the porosity were observed to be higher for the samples containing an excess of Li. The thin films were subjected to electrochemical characterization in aqueous $LiNO_3$ solution; cyclic voltammograms obtained for the samples revealed two sets of well defined redox peaks around 0.07 and 0.1 V in $LiNO_3$ solution. The redox peaks in $Li_{1.05}Mn_2O_4$ thin film samples had lower intensities than those of the stochiometric compound.

Keywords: *$LiMn_2O_4$; microwave synthesis; electron beam evaporation*

1. Introduction

Miniaturization of electronic devices has resulted in very low current and power requirements for many applications. Microenergy sources such as thin film battery devices have been developed to power these microelectronic devices. Lithium manganese oxide has been studied as a promising cathode material for lithium ion batteries, owing to its low cost, ease of preparation, and environmental harmlessness when compared with conventional $LiCoO_2$ [1]. In order to obtain efficient performance, thin film electrodes are expected to possess correct stoichiometry, good crystallinity and excellent adherence to the substrate. Much effort has been made for the fabrication of

*Corresponding author, e-mail: sbalaji@tce.edu

thin film electrodes using various deposition techniques such as electron beam evaporation, RF magnetron sputtering, pulsed laser deposition, chemical vapour deposition, etc. [2–4]. Even though the RF sputtering method has attracted a great deal of attention, due to the reproducibility of thin films that have good adherence, it requires high vacuum conditions, inert gases and high purity or high density targets. As a result, electron beam deposition has emerged as an alternative to RF sputtering, since it does not require highly voluminous electrode materials and sophisticated vacuum equipment. Moreover, the main advantage of this method is that doping cations can be added during deposition, which occludes the capacity fading of $LiMn_2O_4$ [5].

The conventional solid state reaction of mixing oxides or carbonates is widely adopted for the synthesis of $LiMn_2O_4$. Since the method has various limitations like high temperature processing, longer processing time, chemical inhomogeneity of the product and coarser particle size, several methods have been developed by many authors to obtain phase pure and smaller grain size products. Recently, a novel method, known as the microwave synthesis method, has been developed to prepare cathode materials for lithium ion batteries [6, 7]. In the microwave irradiation field, since the microwave energy is absorbed directly by the heated object, uniform and rapid heating can be achieved within several minutes. Such rapid synthesis may deliver fine powder, due to the suppressed diffusion process of growing crystal particles.

Conventionally, the electrochemical performances of the cathode materials are studied in the non-aqueous electrolytes, owing to their stability in the electrolyte and their reversibility during cycling. But the development of alternative Li ion cells has paved the way to identify new electrolytes including aqueous electrolytes. Recently Dahn et al. reported the charge and discharge properties of $LiMn_2O_4$ in aqueous solutions of LiOH and $LiNO_3$ [8], showing that aqueous electrolytes can be used to replace non-aqueous ones for the preliminary study of cathode materials for lithium battery applications.

In the present paper, the microwave synthesis of $Li_{1+x}Mn_2O_4$ (x = 0, 0.05) has been presented as well as evaporation of materials through an electron beam gun on a polycrystalline platinum substrate and the relevant structural properties.

2. Experimental

$LiMn_2O_4$ (sample A) and $Li_{1.05}Mn_2O_4$ (sample B) have been fabricated by the microwave assisted co-precipitation method. Manganese acetate was dissolved with desired stochiometric quantity in double distilled water and the solution has been pumped into reaction vessel with continuous stirring. At the same time, 2 M NaOH aqueous solution has been separately fed into the reaction vessel. The pH of the solution has been maintained at 10.0, stirring speed has been fixed at 60 r.p.m. and the temperature has been controlled at 60 °C. The precipitated $Mn(OH)_2$ was filtered and washed. The obtained powders were dried at 110 °C to remove adsorbed water and mixed thoroughly with $LiOH{\cdot}H_2O$ powder of required quantity.

The grounded powder was calcined in a microwave furnace in two steps. Initially, small pellets of 1 cm in diameter were heated to 500 °C for 10 min, and then calcined at 800 °C for about 20 min. In practice, many materials could not couple with microwave directly in the room temperature and hence it would be necessary to preheat them. Since the dielectric loss of the material increases with temperature, low dielectric loss materials could be made absorptive by raising their temperature [9]. Most commonly, the specimen would be enshrouded by room temperature susceptor material to supply thermal energy by heat transfer and hence the specimen would be subjected simultaneously to thermal and electromagnetic energy. In this case, SiC granules have been used as susceptors which could readily combine with microwave and boost the temperature so as to enable the sample to couple directly with the field [10]. The samples were digested in concentrated HCl and subjected to ICP-AES compositional analyses.

The electron beam evaporation of the samples synthesized via the microwave synthesis was carried out under the vacuum range of 7×0^{-6} mBar, the potential applied between the electrodes was kept constant at 6 kV, the emission current was maintained at 50 mA and the distance between the source and substrate was 7 cm. In order to achieve uniform and homogeneous deposition, the substrate holder rotation was carried out at 40 r.p.m. using a rotary drive. The films were coated over polycrystalline platinum substrate and the thicknesses of the films have been maintained around 4 μ and controlled during the deposition using an in-built quartz crystal monitor. After annealing at 600 °C in the ambient atmosphere, the coated films were subjected to structural and electrochemical characterization.

The structural characterization of the samples was carried by the X-Ray powder diffraction method, using a Philips PW 1710 diffractometer with automatic data acquisition. All scans were recorded for 2θ ranging from 10° to 80°. The indexation was carried out based on the JCPDS standards. The lattice parameters were calculated using the 'Powder-X' software. The scanning electron microscopy was performed using JEOL, JSM-6460 equipment. Three representative areas were randomly selected and scanned in vertical direction and a series of sequential images was recorded for each selected area. The micrographs were subjected to image processing using the Image-J software.

The electrochemical characterizations have been performed using Micro auto lab with FRA III model potentiostat/galvanostat equipment. The Ag/AgCl with 3M KCl (E = 0.208 V versus SHE) and platinum was used as a reference electrode and a counter electrode, respectively. Thin film electrodes on platinum substrate were used as working electrodes and 9 M aqueous solution of $LiNO_3$ was used as the electrolyte. The electrodes were stable throughout the experimentation in the electrolyte. Initially the lithiated electrodes were believed to react with water in aqueous solutions but the work of Dahn et al. has proved their stability [11]. Upon increasing concentration of Li^+ ions in the electrolyte, the chemical potential of the Li^+ ions would also increase; thereby the reaction with water could be eliminated. The detailed reaction has been

presented in Sect. 3.3. The cyclic voltammetry of the samples was recorded after de-aerating the cell with N_2 for more than 10 min.

3. Results and discussion

3.1. Structural characterization

Figure 1 shows the X-ray diffraction pattern of powder sample A calcined in a microwave furnace at 800 °C for 20 min and the respective thin film, evaporated using electron beam gun. The observed diffraction patterns for both powder and thin film samples could be indexed to a cubic unit cell with *Fd*3*m* space group and good agreement has been obtained with the JCPDS standard (file No. 35-0782) for $LiMn_2O_4$ powder.

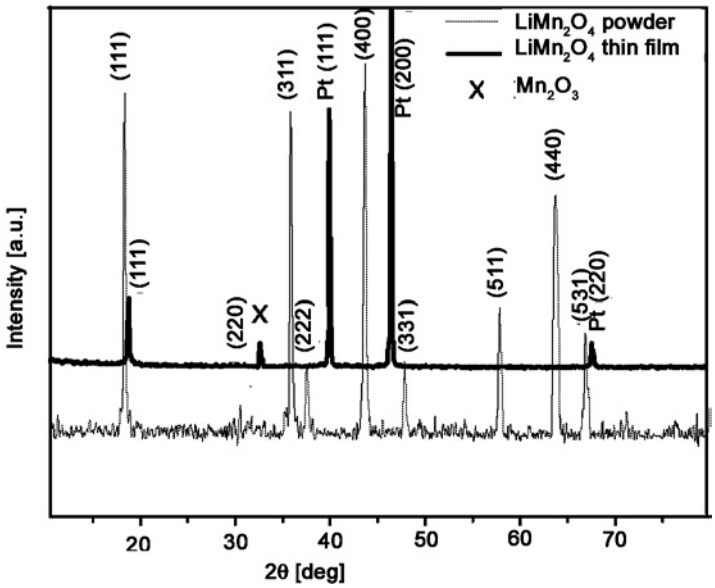

Fig. 1. XRD patterns of $LiMn_2O_4$ powder sintered at 800 °C in a microwave furnace and of $LiMn_2O_4$ thin film annealed at 600 °C

The lattice parameter of sample A was around 8.248 Å, which is comparable with the lattice parameter as per the JCPDS standard around 8.2476 Å. For the powder samples, the peaks corresponding to 2θ – 18.35, 35.814, 43.6, 57.85 and 63.546 were assigned to the planes (111), (311), (400), (511) and (440), respectively. The existence of the above peaks confirms the formation of the spinel phase of $LiMn_2O_4$; lithium ions occupy there tetrahedral sites (8a), Mn^{3+}, Mn^{4+} ions occupy octahedral sites and O^{2-} ions are located at 32e sites [12]. In general, the impurity peaks corresponding to MnO_2 and Mn_2O_3 have usually been observed in microwave synthesis by many au-

thors due to the lithium loss during evaporation and thereby lead to formation of compounds with lower concentrations of lithium. But the observed result for powder samples reveals the formation of single phase $LiMn_2O_4$ without any impurity phases, if microwave heating is set at 800 °C for 20 min. This may be due to the rapidity of microwave processing, resulting in a thermodynamically more favourable structure in a much shorter time, and thereby possible phase transitions might be avoided. The results were cross-checked with the ICP-AES measurements. ICP-AES analyses showed the Li/Mn molar ratios for the powder specimens of sample A and sample B were around 1.013/1.9877 and 1.0506/2.0062, respectively.

The XRD pattern corresponding to a thin film of $LiMn_2O_4$ material is shown in the same figure. It was observed to possess a preferred orientation of (111). However, the lattice parameters of the powder (8.2488 Å) and thin film (8.1305 Å) samples exhibit a marked difference. A small impurity peak corresponding to Mn_2O_3 is visible in the thin film sample, and this may be due to the lithium loss during the evaporation. Hence the compensation of the Li loss during evaporation has been observed to be necessary. Quantitative analyses of thin films by ICP-AES testing further clarify the above observation. Thin films, after being dissolved in concentrated HCl were subjected to ICP-AES analysis. The Li/Mn ratio in thin film of sample A was observed to be around 0.63/2.23.

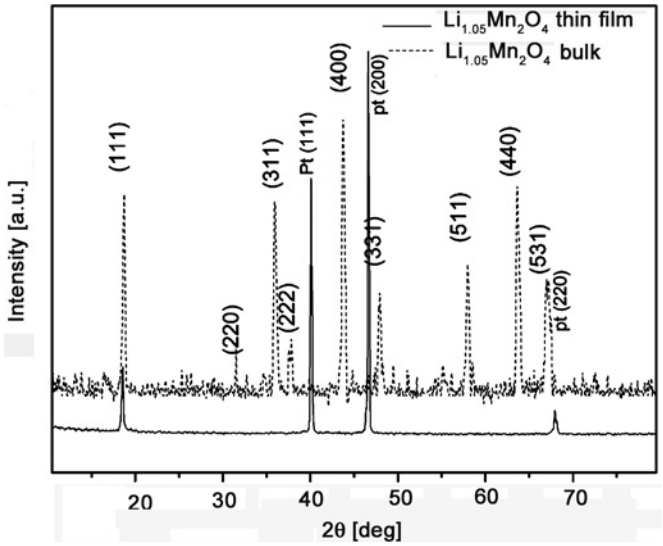

Fig. 2. XRD patterns of $Li_{1.05}Mn_2O_4$ powder sintered at 800 °C in microwave furnace and of $Li_{1.05}Mn_2O_4$ thin film annealed at 600 °C

To compensate for Li loss, a sample with 5% lithium excess was fabricated. The XRD patterns of the powder and thin film of such samples are shown in Fig. 2. The powder sample showed very good conformity with the JCPDS standard (file No. 35-0782). The lattice constant, however, has been found to be much higher than that of

$LiMn_2O_4$. This observation is in close agreement with the report made by Ohzuku et al. on changes in the lattice constant in spinel-related manganese dioxide $Li_xMn_2O_4$ ($0 \le x \le 2$) [13]. Due to the increase in the lithium concentration, the unit cell volume expansion may occur, which is evident from the increase in the lattice parameter for $Li_{1.05}Mn_2O_4$. However the formation of impure phases has been occluded during the evaporation of materials into thin films and this is evident from the diffraction pattern of the $Li_{1+x}Mn_2O_4$ thin film sample. The diffraction pattern of the thin film sample corresponded to a single $LiMn_2O_4$ phase with a preferred orientation in the [111] plane. Furthermore, differences between the lattice constants of $LiMn_2O_4$ powder (8.2488 Å), $Li_{1+x}Mn_2O_4$ powder (8.2533Å) and $Li_{1+x}Mn_2O_4$ thin film sample (8.2475Å) were observed to be negligible. Moreover, the unit cell dimensions of the $Li_{1+x}Mn_2O_4$ thin film sample and the $LiMn_2O_4$ bulk sample are very similar . Hence it is logical to conclude that the addition of extra lithium in the compound compensates for the lithium loss which occurs during thin film vapour deposition. The above conclusion is confirmed by ICP-AES analysis of the thin film sample. Quantitative analysis of thin film of sample B showed the Li/Mn ratio to be around 0.932/2.045.

The structural parameters are shown in Table 1.

Table 1. Structural parameters of powders and thin films

Sample	FWHM	Lattice constant [Å]	Crystallite size [nm]	Strain [$lines^{-2\cdot0}\cdot m^{-4}$]	Dislocation density [$\times10^{-18}$ $lines\cdot m^{-2}$]
$LiMn_2O_4$ (powder)	0.2606	8.248	32.2	0.0643	0.00096
$Li_{1.05}Mn_2O_4$ (powder)	0.2997	8.253	28.0	0.0739	0.00127
$LiMn_2O_4$ (thin film)	0.2717	8.131	30.9	0.0669	0.00104
$Li_{1.05}Mn_2O_4$ (thin film)	0.2647	8.247	31.6	0.0670	0.00100

The strain and dislocation density of the films were calculated using the equations [14]

$$\text{strain}(\varepsilon) = \frac{\beta \cos\theta}{4} \tag{1}$$

$$\text{dislocation density} = \frac{1}{D^2} \tag{2}$$

where D denotes the crystallite size, and β is the full width at half maximum. In general, in any compound, the internal strain and dislocation that cause defects are typically attributable to various processes involved during the formation of the compound. Moreover, according Chung et. al., the electrochemical performance of the $LiMn_2O_4$

electrode for cycling at 4 V region depends on the Li content being directly proportional to the strain in the crystal lattice [15]. Hence, if we could reliably measure the internal strain and the dislocation density, we would gain better understanding about the formation of compounds. The strain and dislocation density have been identified as the key parameters determining the quality of the films, thus their measurement is of fundamental importance. Since the dislocation density and strain are the manifestation of dislocation networks in the films, the decrease in the strain and dislocation density, when compared with the non-stochiometric powder sample B, indicates the formation of higher quality films at higher annealing temperatures.

The lattice strain increases with the Li concentration in the powder sample, and which is obvious because of the lattice expansion (Table 1). The strain of $Li_{1.05}Mn_2O_4$ thin film is comparable to that of $LiMn_2O_4$ powder, which shows the compensation of lithium loss by stoichiometric excess of Li. The crystallite sizes of the samples have been calculated using the Debye–Scherrer formula. The crystallite sizes for both the powder and the thin film samples were observed to be of the order of 30 nm.

3.2. Morphological studies

The scanning electron micrographs showing the morphological features of the $Li_{1+x}Mn_2O_4$ (x = 0, 0.05) thin films are shown in Fig 3. The micrographs were subjected to image processing using 'Image-J' software [16].

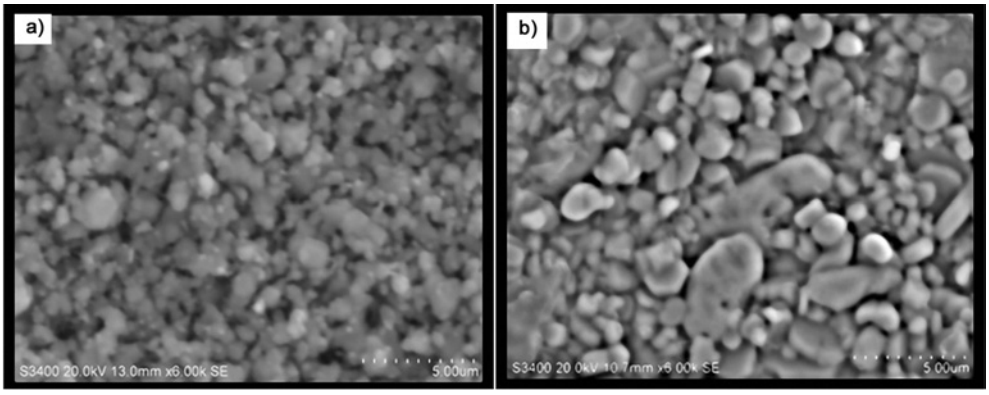

Fig. 3. Scanning electron micrograph of thin film samples of: a) $LiMn_2O_4$, b) $Li_{1.05}Mn_2O_4$

The image processing was carried out in four stages, namely de-noising, pore shape regularization, binarisation and quantification of relevant features to ascertain porosity, pore size distribution and surface texture. The de-noising has been carried out using a median filter and the pore shape regularization and binarisation were carried out using 'BinariseSEM' Java plug-in provided in the software. The porosity, pore area, pore aspect ratio and grain size were determined by the 'ComputeStats' Java plug-in provided in the software. The surface texture and roughness were com-

puted using the '3D' and 'Roughness calculation' Java plug-ins. The 3D surface texture and the pore area distribution are shown in Fig. 4, and in Table 2, the morphological parameters are given.

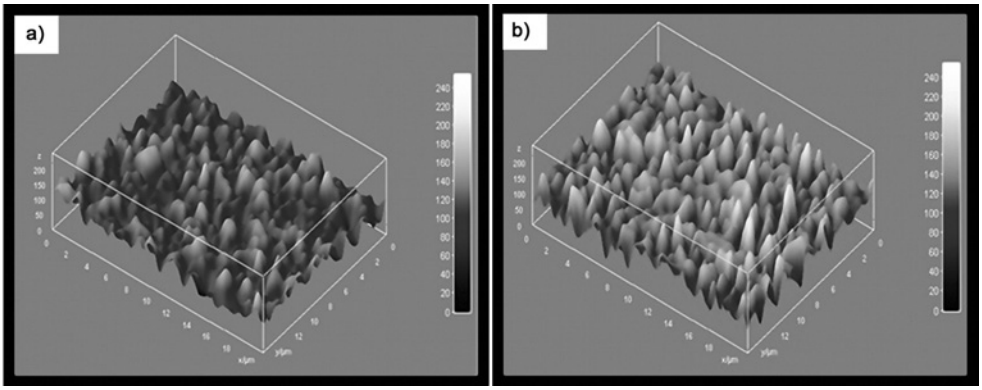

Fig. 4. 3D surface plot of thin film samples: a) $LiMn_2O_4$, b) $Li_{1.05}Mn_2O_4$

Table 2. Morphological parameters of thin films

Sample	Mean grain size [μm]	Pore area $[\mu m]^2$	Pore aspect ratio	Porosity	Pore size [μm]	Roughness [nm]	
						RMS	AM
$LiMn_2O_4$	0.708	23.207	1.632	0.377	20.455	106.654	102.324
$Li_{1.05}Mn_2O_4$	0.485	61.272	1.809	0.593	25.186	128.562	127.244

The porosity is considered to be one of the major properties influencing the electrochemical properties. For higher porosity, the electrochemically active surface area is greater, (i.e., the area of contact between the electrode and the electrolyte is greater). Hence, in order to obtain efficient electrode performance, high surface area electrodes are generally preferred. In the samples, the reduction in grain size, increase of the porosity and pore aspect ratio of thin films with increasing lithium concentration has been observed (Table 2). The observed increase in the pore aspect ratio may be considered an encouraging effect because upon increasing the pore aspect ratio, the contact area between the electrolyte and the cathode also increases, thereby improved electrochemical performance can be achieved. The root mean square roughness has also been observed to increase as Li concentration in thin films increases, and this is consistent with the effect observed by Siemen et al. [17].

3.3. Electrochemical studies

Figure 5 shows typical second cycle cyclic voltammograms of thin film electrodes $Li_{1+x}Mn_2O_4$ (x = 0, 0.05) in a solution of 9 M $LiNO_3$ under quasi-steady state condition

with low potential scan rate (0.5 mV/s). Generally for lower scan rates, the peak current would be high because electrolysis will be completed after long time [18]. On the other hand, this behaviour may also be due to the fact that the electrode is thin enough so that at the scan rate employed, the diffusion layer reaches the film edge, which is called 'finite diffusion', and causes complete oxidation or reduction. For higher scan rates, the peak current has been observed to decrease and hence it is not included in this investigation.

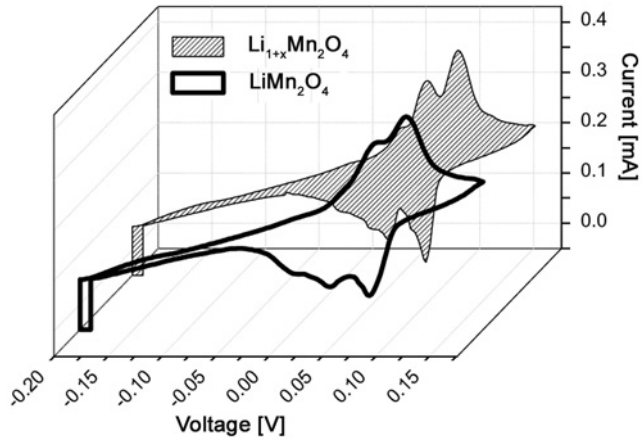

Fig. 5. Cyclic voltammogram of $Li_{1+x}Mn_2O_4$ (x = 0, 0.05) thin film in 9 M $LiNO_3$ aqueous solution

The cyclic voltammograms obtained for $LiMn_2O_4$ shown in Fig. 5 reveal two sets of well defined redox peaks in $LiNO_3$ solution being in good agreement with those obtained for the electrodes in non-aqueous solutions [19]. This indicates that intercalation of Li ions is also feasible in aqueous solutions. These four peaks are considered to be indications of the order–disorder phase transitions of $LiMn_2O_4$ due to the interactions between the electrode and Li^+ ions in the electrolyte. The presence of two peaks during discharging may be attributed to phase transitions during the insertion of Li ions in aqueous solutions [20].

The charge–discharge mechanism of $Li_xMn_2O_4$, in aqueous solution may be described as follows:

$$Li_xMn_2O_4 + \Delta x Li^+ + \Delta x e^- \underset{\text{discharging}}{\overset{\text{charging}}{\longleftrightarrow}} Li_{x+\Delta x}Mn_2O_4 \tag{3}$$

If the amount of intercalating Li ions increases, the formation of tetragonal phases should also emerge but no such redox peak corresponding to tetragonal phases have been observed. The formation of tetragonal phases is mainly because of the Jahn–Teller distortion which is an irreversible phase transition and results in diminishing of the capacity of the electrode. The absence of the lower voltage peak in the second cycle illustrates the stability of the oxide cathode in the voltage window under investigation.

In general, during intercalation of lithium ions from aqueous solutions, unwanted oxidation and reduction of water species may occur according to equation below results in a change in the pH of the electrolyte solution [21]:

$$Li_x(Host) + xH_2O \leftrightarrow Host + xLiOH(aq) + x/2H_2(g) \quad (4)$$

Hence, in order to reduce the effect of oxidation or reduction of water, the electrolyte having a higher concentration of lithium was chosen so that the chemical potential of Li^+ ions in the solution increases as the concentration of Li^+ ions in the electrolyte increases. Hence, the forward reaction of the above equation becomes less favourable. This was confirmed by constant value of pH during the experiment. The peak split in Fig. 5 was more pronounced for thin film of sample B. This shows that the formation of lithium manganese oxide has been improved in the film and the absence of extra redox couple responsible for tetragonal phase inset due to extra lithium in tetrahedral sites could be attributed to the compensation of lithium loss.

4. Conclusions

$Li_{1+x}Mn_2O_4$ (x = 0, 0.05) powders were successfully prepared by microwave processing. XRD patterns of the powder samples $Li_{1+x}Mn_2O_4$ (x = 0, 0.05), reveal the presence of a single phase compound having no impurity phases, showing that microwave processing is not associated with athermal effects and introducing impurities. XRD patterns for thin film samples reveal the formation of a compound with single phase. It is also observed that the evaporation of the $Li_{1.05}Mn_2O_4$ sample has yielded predominant (111) orientation with lesser strain. The cyclic voltammetry results, with two strong sets of red-ox peaks, also indicate the feasibility of intercalation of Li ions in aqueous solutions. The intercalation behaviour is observed to improve with increase in lithium content in the powder sample. Hence it is expected that excessive Li^+ doping can compensate for the lithium loss which occurs during evaporation of the cathode materials. It is also expected that microwave processing may be used to synthesize cathode materials for Li ion batteries in a shorter time and with good stoichiometric control.

Acknowledgements

The authors express their gratitude to the Principal and Management of Thiagarajar College of Engineering, Madurai, for their support as well as the Research Centre Imarat, India for their financial support. The SAIF-STIC, Cochin University is acknowledged for ICP-AES measurements.

References

[1] GADJOV H., GOROVA M., KOTZEVA V., AVDEEV G., UZUNOVA S., KOVACHEVA D., J. Power Sources, 134 (2004), 110.

[2] BATES J.B., DUDNEY N.J., GRUZALSKI G.R., ZUHR R.A., CHOUDHURY A., LUCK C.F., J. Power Sources, 43–44 (1993), 103.

[3] ROUGIER A., STRIEBEL K.A., WEN S.J., CAIRNS E.J., J. Electrochem. Soc., 145 (1998), 2975.
[4] FRAGNAUD P., NAGARAJAN R., SCHLEICH D.M., VUJIC D., J. Power Sources, 54 (1995), 362.
[5] SHOKOOHI F.K., TARASCON J.M., WIKENS B.J., GUYOMARD D., CHANG C.C., J. Electrochem. Soc., 139 (1992), 1845.
[6] HARISH BHAT M., CHAKRAVARTHY P., RAMAKRISHNAN A., LEVASSEUR., RAO K.J., Bull. Mater. Sci., 23 (2000), 461.
[7] YEN PEI FU., YU HSIU SU., CHENG HSIUNG LIN., SHE HUANG WU., J. Mater. Sci., 41 (2006), 1157.
[8] ALI EFTEKHARI., Electrochim. Acta, 47 (2001), 495.
[9] SPOTZ S., SKAMSER D.J., JOHNSON D.L., J. Am. Ceram. Soc., 78 (1995), 1041.
[10] RAMESH P.D., BRANDON D., SCHACHTER L., Mat. Sci. Eng., A266 (1999), 211.
[11] LI W., DAHN J.R., WAINWRIGHT D.S., Science, 264 (1994), 1115.
[12] ARORA P., POPOV B.N., WHITE R.E., J. Electrochem Soc., 145 (1998), 807.
[13] OHZUKU T., KITAGAWA M., HIRAI T., J. Electrochem. Soc., 137 (1990), 769.
[14] LALITHA S., SATHYAMOORTHY R., SENTHILARASU S., SUBBARAYAN A., NATARAJAN K., Sol. En. Mater. Sol. Cells, 82 (2004), 187.
[15] CHUNG K.Y., KIM K.B., Electrochim. Acta, 49 (2004), 3327.
[16] Research Services Branch NIMH & NINDS Image J., Image processing and analysis in Java Available via Web site: http://rsb.info.nih.gov/ij.
[17] SIMMEN F., LIPPERT T., NOVÁK P., NEUENSCHWANDER B., DÖBELI M., MALLEPELL M., WOKAUN A., Appl. Phys. A, 93 (2008), 711.
[18] LI W., MCKINNON W.R., DAHN J.R., J. Electrochem. Soc., 141 (1994), 2310.
[19] GUMMOW R.J., DE KOCK A., THACKERAY M.M., Solid State Ionics, 69 (1994), 59.
[20] WANG PEI, YANG HU, YANG HUAQUAN, J. Power Sources, 63 (1996), 275.
[21] JAYALAKSHMI M., MOHAN RAO M., SCHOLZ F., Langmuir, 19 (2003), 8403.

Received 9 May 2009
Revised 20 October 2009

Materials Science-Poland, *Vol. 28*, *No. 2*, *2010*

The effect of cryogenic treatment on the microstructure and mechanical properties of $Cu_{46}Zr_{46}Al_8$ bulk metallic glass matrix composites

G. Z. MA, D. CHEN*, Z. H. CHEN, J. W. LIU, W. LI

School of Materials Science and Engineering, Hunan University, Changsha, 410082, P. R. China

The influence of cryogenic treatment (CT) on the microstructure and mechanical properties of $Cu_{46}Zr_{46}Al_8$ glassy matrix composite fabricated by the process copper of mould suction casting. The distribution and morphology of test samples of CuZr phase changed under CT. After CT, the second phase is distributed more homogenously, and the morphology was transformed from dendrites to plates. This change in the microstructure improved the mechanical properties of the composite. Although compression fracture was still the brittle mode, the compression fracture strength was improved greatly after CT. Due to the morphological changes, the microhardness was increased about 18.55% when the treatment time was 72 h.

Keywords: *$Cu_{46}Zr_{46}Al_8$ glassy matrix composite; cryogenic treatment (CT); microstructure evolution; mechanical properties*

1. Introduction

Bulk metallic glasses (BMGs) represent an exciting class of materials with a wide range of potential applications [1]. Recently, a series of Cu–Zr and Cu–Zr–Al based BMGs or BMG composites have been found to exhibit extraordinarily high strength and good compressive ductility [2–5]. Although the localized shear transformation is still the predominant deformation mechanism, some CuZr intermetallic compounds with martensite structure or austenite-like structure formed in these materials and are believed to play an important role in improving mechanical properties [6]. The CuZr phase, as the second phase in the matrix, could affect the shear band, which is relevant for the deformation of the composite [1]. Frick et al. discovered that stress forces could induce a martensite phase transformation in nano-scaled NiTi shape memory alloys by means of nanoindentation [7]. Interestingly, the CuZr intermetallic phase shows a deformation-induced phase transformation from austenite to martensite bits

*Corresponding author, e-mail: ma97chen@hotamil.com

shape memory behaviour just like NiTi [8]. Similarly, the martensitic transformation and shape memory behaviour of the intermetallic CuZr phase have also been previously reported [9].

Traditionally, CT is widely used in the manufacture of high precision parts, and has been shown to significantly improve mechanical properties of steels such as D-2 and M-2 which was predicted due to the reduction in the amount of retained austenite structure and changed to martensite structure induced by the internal stress of CT[10]. If internal stresses caused by CT could induce martensite phase transformations in Cu–Zr and Cu–Zr–Al-based BMG and BMG composites, the mechanical property of the composite would also be improved, and the range of application would be broadened.

$Cu_{46}Zr_{46}Al_8$ was selected for this study, as among the alloys of $(Cu_{50}Zr_{50})_{100-x}Al_x$ it has the best glass-forming ability (GFA) [11, 12]. This paper aims to explore and discuss how CT changes the microstructure, and the other properties, of Cu based bulk glass composites.

2. Experimental

The $Cu_{46}Zr_{46}Al_8$ alloy was prepared by arc melting under an argon atmosphere, and then it was suction cast into a copper mould to form cylindrical rods of 4 mm in diameter. Then the samples were immersed into liquid N_2: specifically, the samples were subjected to cryogenic treatment (CT) for 2, 4, 8, 12, 24, 48, 60 and 72 h. The effects of the CT on the microstructure of $Cu_{46}Zr_{46}Al_8$ composite were investigated by X-ray diffraction (XRD) with CuK_α radiation and scanning electron microscopy (SEM, JSM-6700F). The density measurement was based on the Archimedes Principle. In order to examine the influence of the duration of the cryogenic treatment on the mechanical behaviour of the glassy matrix composite, the Vickers microhardness test and uniaxial compression test were conducted. A HBRVU-187.5 hardness tester was employed to measure the Vickers hardness of these alloys subjected to the load of 200 g for 15 s. The compressive tests were conducted under quasi-static loading at an initial strain rate of 5×10^{-4} s^{-1} at room temperature, and the fracture surfaces were examined by SEM. The dynamics of the cryogenic process on the Cu-based composite were discussed. The bars of the fluctuation of experimental error of the ultimate compression fracture strength and the Vickers hardness were not beyond 15 and 10, respectively.

3. Results and discussion

Figure1 shows the dependence of mechanical properties of the composite on the CT duration. The compression fracture strength of all CT samples increased compared with the as-cast specimens with no CT, as shown in Fig. 1a. The compression fracture strength of the untreated sample was measured five times and the average value was 1342 MPa. However, for the CT samples, the lowest compressive strength was

1540 MPa and the highest value was 1750 MPa. It is worth noting that the fracture strength of all the samples after CT was higher than the as-cast samples.

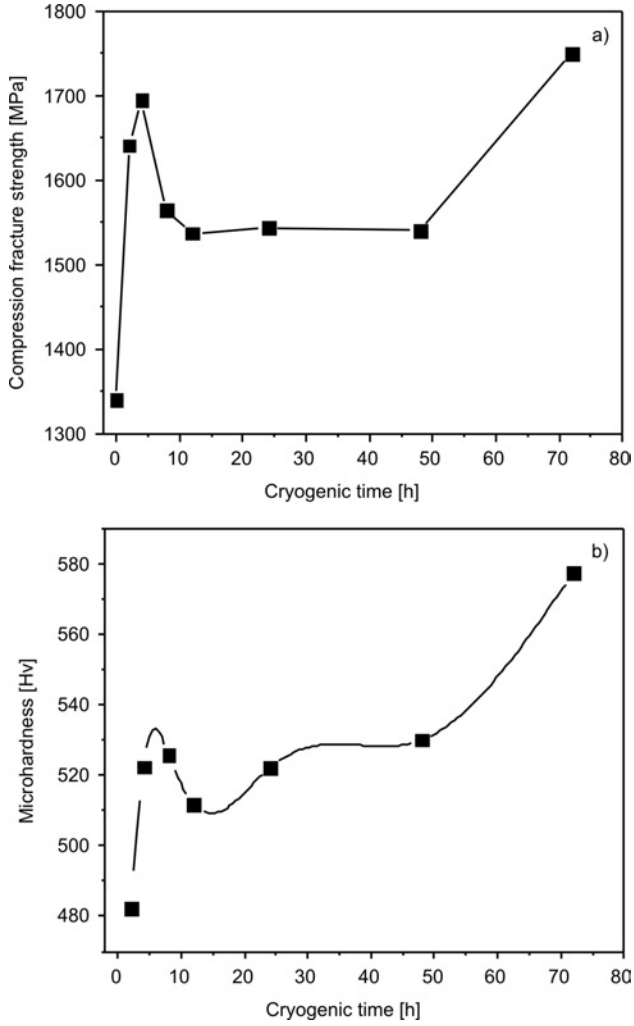

Fig. 1. Dependences of mechanical properties on the cryogenic time: a) fracture strength, b) microhardness

In order to evaluate the efficiency of atomic packing, the densities of samples before and after CT were measured. Table 1 lists the densities and microhardness of samples before and after CT. The density of all the samples increased after CT. The increase in the density indicated that the free volume was reduced, in addition to the change in the structure. The morphologies of the fracture surfaces were examined carefully. Representative SEM images were primarily observed for the samples before and after CT treatment for 72 h.

Table 1. The density and hardness before and after CT[a]

T [h]	Density [g/cm^3]	Increase of density [%]	Hardness {Hv]	Increase of hardness [%]
2	7.0923/7.0780	0.2	482.07/473.64	1.78
4	7.1090/7.0702	0.55	522.37/484.76	7.76
8	7.0991/7.0492	0.71	525.67/508.86	3.33
12	7.1114/7.0408	1.0	511.84/497.6	2.86
24	7.1320/7.0659	0.94	522.19/493.69	5.77
48	7.1167/7.1075	0.13	530.01/502.99	5.37
60	7.1888/7.1075	1.14	505.24/461.16	9.34
72	7.1470/7.1376	0.13	577.57/487.2	18.55
84	7.1439/7.1103	0.47	492.49/480.69	2.45
108	7.1765/7.1372	0.55	510.14/481.74	5.90
132	7.1888/7.1642	0.34	511.74/479.26	6.78

[a]The density and hardness represent the value after CT/before CT, increase of density and increase of hardness represent the ration of difference of density (or hardness) to the original density (or hardness),respectively.

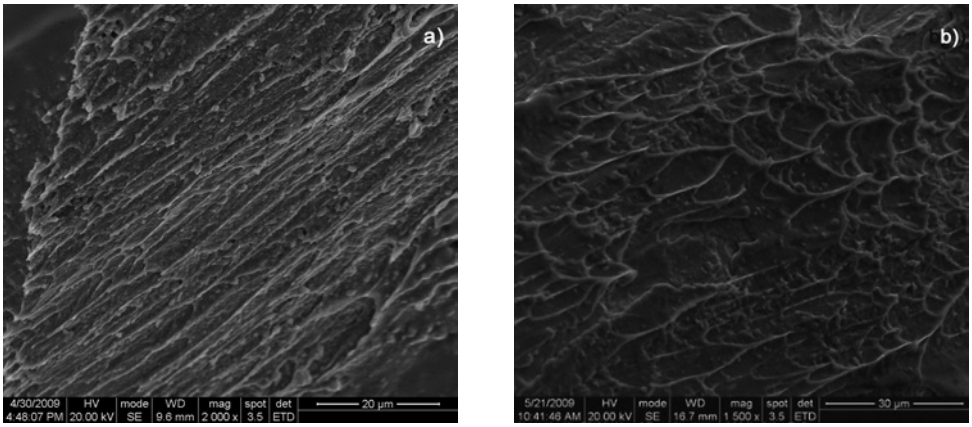

Fig. 2. SEM micrographs of fracture surfaces of: a) as-cast, b) treated for 72 h

In Figure 2, the SEM micrographs of fracture surfaces of as cast and CT samples are shown. After 72h of CT, the fracture feature consists mostly of well developed striated vein patterns, which were fine and homogeneous. Yet, in contradiction to the smooth fracture surface of Fig. 2b, the dominating features of as-cast sample are rugged planes and an elongated vein pattern with melt zone. As is well known, the fracture of the samples causes an adiabatic heating of the fracture surface [13, 14] which significantly decreases the viscosity of the samples and leads to the formation of vein patterns along the fracture planes. The well developed vein pattern of the sample subjected to 72 h CT may somewhat decrease the degree of the softening at the initial

stage of crack propagation and may contribute to the higher compressive strengths of the CT samples than the as-cast samples.

In order to understand the unique mechanical properties, the dynamics of microstructural changes was investigated. The dynamics of phase morphology induced by CT may be responsible for the enhancement of the mechanical properties. A similar phenomenon was found for AZ91 magnesium alloy [10]. In the research, CT changed the distribution and the morphology of the second phase, which resulted in a significant improvement of the mechanical properties of the alloy.

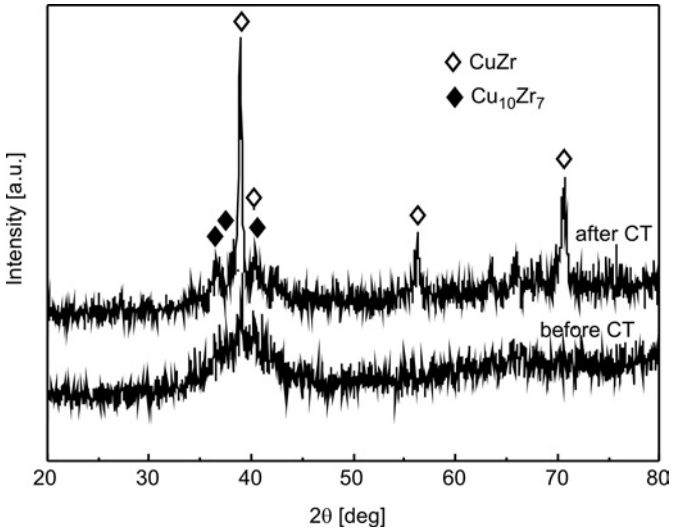

Fig. 3. XRD pattern of $Cu_{46}Zr_{46}Al_8$ BMG composites before and after CT

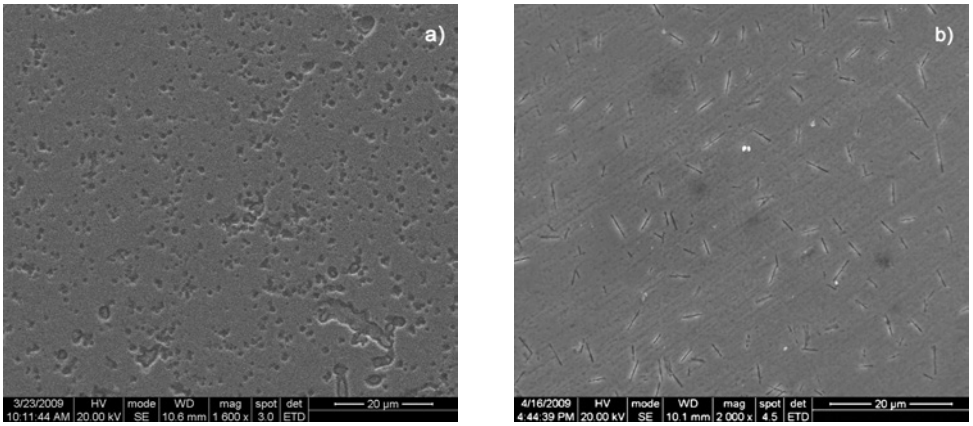

Fig. 4. SEM image of the cast glassy alloy rods$Cu_{46}Zr_{46}Al_8$ before and after CT

Figures 3 and 4 show the XRD patterns of the composite and SEM images of the sample before and after CT. In Figure 3, more crystalline peaks, which may corre-

spond to the appearance of $Cu_{10}Zr_7$ phase or monoclinic CuZr phase, were observed after CT, while only CuZr phase was seen before CT. After CT, the change of morphology was observed, as seen in Fig. 4b. There are flakes dispersed in the matrix, while only dendrite phase or rotundity grain is observed before CT, as can be seen in Fig. 4a. Furthermore, after CT, the precipitates became finer and the distribution of the second phase was more homogeneous. An important point worth noting here is that the crystalline CuZr phases exhibit quite different microstructure. The morphologies of this CuZr intermetallic compound (either *B*2 parent phase or monoclinic martensite phase) can be rather diverse, depending on the different alloy systems or on the different cooling rates, although the alloy composition might be similar. Particle sizes range from micrometer sized dendrites in a slowly solidified alloy to nanometer sized particles formed under a high cooling rate [1].

According to the binary alloy phase diagram [15] and previous investigations, $Zr_{50}Cu_{50}$ could solidify due to non-equilibrium solidification into intermetallic CuZr (*B*2) phase at 1208 K, with the decrease in temperature, and undergo eutectoid decomposition into $Cu_{10}Zr_7$ and Zr_2Cu below 988 K. But due to the sluggish diffusion kinetics of the eutectoid reaction, the CuZr (*B*2) phase transforms to a monoclinic martensitic phase, which is conducive to the improvement of mechanical properties [16, 17]. Although the CuZr phase is principally responsible for the strengthening effect on the BMG, its instability is the main reason for poor mechanical properties of these alloys. So, in order to obtain good mechanical properties, the Cu-based BMG composites should possess a stable phase microstructure. Sun [1] reported that stress forces could induce martensitic transformations in Cu–Zr–Al bulk metallic glass forming alloys and result in outstanding mechanical properties. The deformation induced martensitic transformation is believed to cause the hardening and to contribute to the high compressive deformability in Cu–Zr–(Al,Ti) [18]. The homogenization and stabilization of the internal microstructure caused by CT is the most probable reason for this observable phenomenon. In fact, CT could lead to structural change as well as to phase transformation by internal stresses and can improve the mechanical properties [19]. Some authors report that structural relaxation may be one of the microscopic mechanisms responsible for a change in the macroscopic properties and the structure of samples after CT [18]. However, at low temperatures the influence of structural relaxation is negligible [21] because its intensity I is determined by the expression

$$I \sim \exp\left(-\frac{U_i}{kT}\right) \tag{1}$$

where U_i is the mean value of the energy barrier, k is the Boltzmann constant and T is the temperature.

Therefore, the internal stress of CT changed the structure and thus leads to the improvement in the mechanical properties. These findings show $Cu_{46}Zr_{46}Al_8$ glassy matrix composite may offer unique possibilities for improving the mechanical properties of BMG composites.

4. Conclusions

In summary, CT can successfully improve the compression fracture strength, microhardness as well as the density of the $Cu_{46}Zr_{46}Al_8$ composites. The best improvements to the fracture strength and the microhardness were increases of about 30% and 18.55%, respectively: these improvements associated with microstructural changed induced by CT. After CT, the distribution and the morphology of CuZr precipitates were changed. The second phase was homogeneously distributed and the morphology was transformed from dendrite to plate forms. This microstructural modification resulted in a significant improvement of mechanical properties. This cryogenic process may provide a way of improving the properties of BMG and its composites. It may also broaden the range of potential industrial applications of BMGs in the future.

Acknowledgement

This work was sponsored by the National Natural Science Foundation of China (Grant No. 50804015).

References

[1] SUN Y.F., SHEK C.H., LI F.S., GUAN S.K., Mater. Sci. Eng. A, 31 (2008), 479.
[2] XU D.H., LOHWONGWATANA B., DUAN G., Acta Mater., 2621 (2004), 52.
[3] DAS J., TANG M.B., KIM K.B., Phys. Rev. Lett., 205501 (2005), 94.
[4] JIANG F., ZHANG Z.B., HE L., J. Mater. Res., 2638 (2006), 21.
[5] SUN Y.F., WEI B.C., WANG Y.R., Appl. Phys. Lett., 051905 (2005), 87.
[6] DAS J., PAULY S., DUHAMEL C., J. Mater. Res., 326 (2007), 22.
[7] FRICK C.P., LANG T.W., SPARK K., Acta Mater., 2223 (2006), 54.
[8] DAS J., PAULY S., BOSTROM M., DURST K., GOKEN M., ECKERT J., J. Alloys Compd., 483 (2009), 97.
[9] LIU Z.Y., AINDOW M., HRILJAC J.A., J. Metastable Nanocryst. Mater., 223 (2001), 360.
[10] ASL K.M., TARI A., KHOMAMIZADEH F., Mater. Sci. Eng. A, 523 (2009), 27.
[11] CHEUNG T.L., SHEK C.H., J. Alloys Compd., 434 (2007), 71.
[12] YU P., BAI H.Y., TANG M.B., WANG W.L., J. Non-Cryst. Solids., 351 (2005), 1328.
[13] WRIGHT W.J., SCHWARZ R.B., NIX W.D., Mater. Sci. Eng. A Strucr.Mater.: Prop. Microstructure. Process., 229 (2001), 319.
[14] LIU C.T., HEATHERLY L., EASTON D.S., Metal. Mater. Trans., 29A (1998), 181.
[15] MASSALSKI T.B., OKAMOTO H., SUBRAMANIAN P.R., KACPRZAK L., *Binary Alloy Phase Diagrams*, ASM International, 2nd Ed., 1990.
[16] SCHRYVERS D., FIRSTOV G.S., SEO J.W., HUMBEECK J.V., KOVAL Y.N., Scripta Mater., 1119 (1997), 36.
[17] DOKUKIN M.E., PEROV N.S., DOKUKIN E.B., Phys. Rev. B., 267 (2005), 368.
[18] PAULY S., DAS J., BEDNARCIK J., MATTERN N., KIM K.B., KIM D.H., ECKERT J., Scripta Mater., 60 (2009), 431.
[19] SEO J.W., SCHRYVERS D., Acta Mater., 1165 (1998), 46.
[20] ZAICHENKO S.G., PEROV N.S., GLEZER A.M., J. Magn. Magn. Mater., 297, (2000), 215.
[21] ZAICHENKO S., RPTH S., GLEZER A., J. Magn. Magn. Mater., 571, (2003), 258.

Received 22 October 2009

Contents

GUIDELINES FOR AUTHORS

Manuscripts can be sent by conventional mail or by e-mail. Submission of a manuscript to *Materials Science-Poland* implies that it is not being considered for the publication elsewhere, and the authors have a necessary authorization to publish the material contained in the paper. **The manuscripts should conform to the formal standards of the Journal which may be found in the first issue of each volume and on the web page.**

Authors are encouraged to submit electronic versions of the manuscript by e-mail, to the address of the Journal. A single PDF file should be sent, containing text, references, figures, tables etc. Alternatively, the authors can submit the manuscript by conventional mail, sending a CD with the PDF file mentioned above, to the Editor-in-Chief at his address given below.

Each submitted manuscript will be reviewed, the final decision concerning its acceptance resting with the editors. Upon acceptance, the corresponding author will be requested to submit the following material (via e-mail or by conventional mail, on CD)

- A DOC or RTF file containing the final version of the text, references, tables and figure captions. The content of the file should be identical with that of the hard copy, and should exactly match the version seen and accepted be the referee(s).
- File(s) in appropriate formats containing figures. The required formats of the drawings (plots, schemes of technological processes) must be vector files such as XLS, OPJ, cdr (Excel, Origin, CorelDraw) which may also be exported as EPS, EMF or WMF files. Drawings submitted in tiff or jpg formats (bitmaps, raster graphics), even if exported as EPS, EMF or WMF files, will not be accepted. **Bitmaps are acceptable only in the case of photographs**. The photographs (only in grayscale) should have the resolution not lower than 300 dpi (estimated for the size in which they are expected to be reproduced).
- A PDF file containing the complete manuscript (text, literature, tables, figures, etc). The file should be carefully checked as it will serve as a hard copy in case of doubts. **The contents of the PDF file should exactly match the material in other files.**

Irrespective of whether the final version is submitted by e-mail or by conventional mail, the authors should also send **via conventional mail** a signed copy of the Copyright Transfer Agreement (available on the web page of the Journal).

For detailed information consult the first issue of each volume or the web page of the Journal.

The mail should be addressed to:

Professor Juliusz Sworakowski
Editor-in-Chief, Materials Science-Poland
Politechnika Wrocławska, W-3
Wybrzeże Wyspiańskiego 27
50-370 Wrocław, Poland

Electronic correspondence should be sent to: MatSci@pwr.wroc.pl
Web page of Materials Science-Poland: www.MaterialsScience.pwr.wroc.pl

The Publisher reserves the right to make necessary alterations to the text. Each corresponding author will be supplied with one free copy of the journal. Orders for additional offprints can be placed with the Publisher.